Thermodynamic model of flue gas cooling path and implications on heavy metal recovery from MSWI fly ash

Inauguraldissertation

der Philosophisch-naturwissenschaftlichen Fakultät

der Universität Bern

vorgelegt von

Mirjam Wolffers

von Nesslau-Stein SG

Leiter der Arbeit:

Prof. Sergey V. Churakov

Dr. Urs Eggenberger

Institut für Geologie, Universität Bern

Koreferent:

Prof. Christian Ludwig

École polytechnique fédérale de Lausanne,

Paul Scherrer Institut

Thermodynamic model of flue gas cooling path and implications on heavy metal recovery from MSWI fly ash

Inauguraldissertation

der Philosophisch-naturwissenschaftlichen Fakultät

der Universität Bern

vorgelegt von

Mirjam Wolffers

von Nesslau-Stein SG

Leiter der Arbeit:
Prof. Sergey V. Churakov
Dr. Urs Eggenberger
Institut für Geologie
Universität Bern

Koreferent:
Prof. Christian Ludwig
École polytechnique fédérale de Lausanne,
Paul Scherrer Institut

Von der Philosophisch-naturwissenschaftlichen Fakultät angenommen.

Bern, 4. März 2022

Der Dekan
Prof. Dr. Zoltan Balogh

Dank

An dieser Stelle möchte ich allen danken, welche zum Gelingen dieser Arbeit beigetragen haben.

Ein grosser Dank gebührt den beiden Betreuern, welche meine Doktorarbeit begleitet haben. Im Besonderen möchte ich Urs Eggenberger danken für die enorme Unterstützung, die es überhaupt ermöglicht hat, dieses Projekt aufzugleisen. Ich erinnere mich gerne an die vielen tollen Erlebnisse aus den Jahren unserer Zusammenarbeit und schätze sehr die spannenden Erfahrungen, welche ich an der Fachstelle machen durfte. Sergey Churakov danke ich für wichtige Inputs und das Teilen der Begeisterung von thermodynamischen Berechnungen. Besonders geschätzt habe ich das Vertrauen, welches ihr meinen Leistungen entgegengebracht habt und die pragmatische Lösungsfindung, falls doch einmal etwas nicht wie geplant geklappt hat. Herzlichen Dank an Christian Ludwig (EPFL/ PSI) für das sorgfältige und aufmerksame Durchlesen als Ko-Referent und die darauffolgenden anregenden Diskussionen.

Ein grosser Dank geht auch an Dmitrii Kulik und Dan Miron (beide PSI), die mich stark unterstützt haben bei den thermodynamischen Berechnungen und beim Aufbereiten der Datenbank. Speziell herausheben möchte ich dabei die intensive Unterstützung von Dmitrii Kulik beim Aufbau des Box Flux Modells. Weiter möchte ich mich bei folgenden Personen und Organisationen bedanken: Beim Bundesamt für Umwelt, Thomas Bücherer (EWB) und Daniel Böni (KEZO) für die finanziellen Forschungsbeiträge. Bei Thomas Andres (EWB), Albert Bachmann (Saidef SA), Tino Däscher (Stadtwerk Winterthur) und Beat Schweingruber (ERZ) für das Bereitstellen von Probenmaterial und Betriebsdaten. Bei Stefan Schlumberger (ZAR) für die angenehme Zusammenarbeit und inputreiche Diskussionen. Bei Stephan Fromm und Andreas Bernhard (beide ZAR) für die gute Zusammenarbeit und den Datenaustausch. Bei Kaarina Schenk (KAA Sustainability Expertise), Leo Morf (AWEL) und Ralf Koralewska (Martin GmbH) für die Unterstützung dieses Projekts und die spannenden Diskussionen.

Einen besonderen Dank möchte ich auch den folgenden Personen aussprechen: Rainer Dähn (PSI) für die Expertise bei der Eingabe des Proposals für Strahlzeit und das Durchführen von Messungen am Synchrotron. Georg Kosakowski (PSI) für die Unterstützung bei der Datenaufbereitung. Bernard Grobéty und Christoph Neururer (beide Uni Fribourg), Barbara Lothenbach und Ellina Bernhard (beide EMPA), sowie Peter Tollan (ETH Zürich) für die analytische Unterstützung.

Ausserdem haben auch zahlreiche Personen am Geologischen Institut der Universität

Abstract

Solid residuals of municipal solid waste incineration (MSWI), i.e. bottom ash and fly ash contain significant quantities of heavy metals. Nearly 80'000 tons of MSWI fly ash is produced annually in Switzerland. From the combustion of waste wood, another 6'000t of waste wood fly ash arise annually, which show heavy metal concentrations in the range of MSWI fly ash. In Switzerland, the current practice is to stabilize and dispose of the residues from waste incineration on landfills or underground storage. For MSWI fly ash, heavy metal recovery through acid leaching will be mandatory from 2026 onwards. For waste wood fly ash, heavy metals will have to be recovered from 2024 onwards and it is a matter of discussion, whether a co-treatment with MSWI fly ash could be expedient. The heavy metals are recovered from MSWI fly ash through acid fly ash leaching (FLUWA process). The MSWI fly ash here represents a mix of the different ash fractions (boiler- and electrostatic precipitator ashes) that arise along the flue gas cooling path. With regard to the obligation of heavy metal recovery from MSWI fly ash, it has not yet been conclusively defined whether the heavy metal recovery from boiler ash is expedient from a technical and ecological point of view, as little data exists on its geochemical characteristics and heavy metal binding forms. The recovery of metals from the waste makes a valuable contribution to a sustainable closure of material cycles, as metals from primary raw material mining can partly be returned to the material cycle and the environmental pollution though land-filling is minimized. This thesis focusses on inventory of volatile heavy metals (e.g. Zn, Pb, Cu, Cd) in MSWI fly ash. Detailed characterization in combination with leaching experiments allow new insights on their chemical and mineralogical composition, heavy metal binding forms and leachability. Thermodynamic modeling was used as complementary approach to investigate ash-forming processes and transport mechanisms occurring during cooling of the flue gas. The influence of flue gas composition on phase assemblages and the formation conditions of PCDD/-F thereby represent further investigated aspects. It has been shown that the MSWI boiler ashes are significantly different materials than the electrostatic precipitator ash and that their share on the bulk fly ash is approximately 25 - 30%. The boiler ash consists mainly of acid-buffering and inert refractory minerals, as well as amorphous glass phase and shows considerably lower heavy metal concentrations than the electrostatic precipitator ash. The thermodynamic simulations predict, that Zn and Cu in the boiler ash fractions are preferably stable as silicates (Zn_2SiO_4) and oxides (e.g. ZnO, Fe_2ZnO_4, CuO), phases that have also been analytically verified. The electrostatic precipitator ash is dominated by a chloride and sulfate matrix which shows a

low acid-buffering capacity and shows much higher concentrations in the heavy metals of interest (Zn, Cd, Cu, Pb), predominantly in the form of easily soluble salts. These observations suggest that the electrostatic precipitator ash shows a higher potential for heavy metal recovery. The thermodynamic simulations confirm that the S/Cl ratio in the flue gas primarily controls the predicted equilibrium phase assemblages, while variations in O_2 concentration affects the composition of the ash to a minor extent. The thermodynamic modelling further indicate that the formation of gaseous PCDD/-F should take place at extremely reducing conditions which are not expected for typical bulk flue gas conditions. It is suggested that necessary reducing conditions may establish, e.g. in close vicinity to the combustion of plastic or other solid particles. The results of this thesis give new insights into the ash-forming processes during the cooling of the flue gas and contribute to a better understanding of speciation of heavy metals in the ash, as well as of the leachability of individual fractions of MSWI fly ash and waste wood fly ash. The data may serve as a basis for life cycle assessment and to concretize the enforcement aid for heavy metal recovery. In particular, further development of thermodynamic modelling approach opens opportunity for theoretical investigation of the combustion condition in the incineration plant, optimization of the combustion process and potential minimization of toxic organic pollutants.

Contents

Glossary

Bottom ash	The bottom ash represents the main solid residue of MSW incineration, arising at the outcome of the combustion chamber, where it is either quenched in water or collected in its dry state.
Empty pass ash	The empty pass ash (EA) represents the first solid residue arising from the flue gas path. It is the ash fraction that accumulates at the 2nd and 3rd pass (often called the empty pass) before the flue gas flows into the boiler. The EA is often disposed together with the bottom ash, but only accounts for a minor quantity.
Boiler ash	The boiler ash (BOA) consists of the different boiler ash fractions that arise at the different boiler sections.
Deposits	The term deposits, as used in this thesis, refers to the crusts that form around the heat exchanger surfaces. The deposits are released through self-cleaning mechanisms such as periodical rapping of the heat exchanger surfaces and collected together with the boiler ash, whereby they account for a minor quantity.
Electrostatic precipitator ash	The electrostatic precipitator ash (ESPA) represents the fine-grained ash collected at the electrostatic precipitator.
Fly ash	The material fly ash, as used in this thesis, is composed of a mix of the different boiler ash fractions (BOA) and the electrostatic precipitator ash (ESPA) and does not contain solid residues from dry or semi-dry flue gas cleaning.
Filter ash	The term filter ash is used in the regulation with regard to heavy metal recovery, and has not yet been conclusively defined. It is to be defined whether the term filter ash is used synonymously with fly ash, including the boiler ash. Or, whether it refers solely to the electrostatic precipitator ash, alternatively also including selected boiler ash fractions.
Air pollution control residues	The term air pollution control residues (APCr) refers in this thesis to the solid residues from dry or semi-dry flue gas cleaning systems. In other countries, where dry systems are more common, these hazardous solid residues are often collected together with the fly ash
Filter cake	The filter cake represents the solid residue arising from acid fly ash leaching and is deposited together with the bottom ash on landfill type D.

Abbreviations

ANC	Acid neutralizing capacity
BOA	Boiler ash
BSE	Backscattered electron
EA	Empty pass ash
EDS	Energy dispersive x-ray spectroscopy
Eh	Redox potential (mV)
ESP	Electrostatic precipitator
ESPA	Electrostatic precipitator ash
FA	Fly ash
FLUWA	Acid fly ash leaching
ICP-OES	Inductively coupled plasma optical emission spectroscopy
L/S	Liquid to solid ratio
MSWI	Municipal solid waste incineration
PCDD	Polychlorinated dibenzodioxins
PCDF	Polychlorinated dibenzofurans
pH	Negative logarithm of the hydrogen ion concentration
ROC	Residual oxidizable organic carbon
SEM	Secondary electron microscope
SCR	Selective catalytic reduction
SNCR	Selective non-catalytic reduction
SSA	Specific surface area
TOC	Total organic carbon
TOC400	Total organic carbon released up to 400 °C
TIC900	Total inorganic carbon released up to 900 °C
WWFA	Waste wood fly ash
XRD	X-ray diffraction
XRF	X-ray fluorescence

Part I

Introduction

Chapter 1

Background

1.1 Context

In Switzerland, municipal waste has to be thermally treated since the year 2000. Approximately 800,000 tons of bottom ash and 80,000 tons of fly ash are produced annually. From the combustion of waste wood, another 6'000t of waste wood fly ash arise annually, which show heavy metal concentrations in the range of MSWI fly ash due to paints, coatings or impregnation. The residues of the waste incineration contain heavy metals, toxic organic compounds and thus do not meet quality criteria for recycling. Current practice is to dispose of such waste directly in landfill sites. The Swiss waste ordinance (Swiss Federal Council, 2015) prescribes the recovery of metals from the incineration residues before landfilling. For MSWI fly ash, heavy metal recovery will be mandatory from 2026 onwards, e.g., through acid leaching. For waste wood fly ashes, it is probable that metals will have to be recovered in the same way as from MSWI fly ash from 2024 onwards and it is a matter of discussion, whether a co-treatment could be expedient. During thermal waste treatment, volatile heavy metals accumulate in the flue gas and precipitate in the boiler- and electrostatic precipitator ash, which are often collected together and referred to as fly ash. The fly ashes show high heavy metal concentrations (e.g. Zn, Pb, Cu, Cd), the recovery of which shows considerable environmental potential. Recovery of these heavy metals promises significant environmental and economic benefits through improved disposal quality of the remaining filter cake. The recycling of these recovered metals makes a valuable contribution to the sustainable closure of material cycles, since metals from primary raw material mining can be substituted accordingly. The heavy metals are recovered from the MSWI fly ash through acid fly ash leaching (FLUWA process). Today, the MSWI boiler ash is usually collected and treated together with the electrostatic precipitator ash. With regard to the obligation of heavy metal recovery, it has not yet been conclusively defined whether the heavy metal recovery from boiler ash is expedient, as little data exists on its geochemical characteristics. An alternative disposal route would be the disposal together with the bottom ash, as it is performed with the empty pass ash, another ash fraction arising from the flue gas cooling path. It is not known today which of these two boiler ash disposal routes are preferable from a technical and ecological point of view.

1.2   Municipal solid waste incineration

1.2.1   Municipal solid waste incineration and waste composition

Switzerland underwent a paradigm shift in waste management late in the second half of the 20 [th] century. Although the first MSWI plant started operating already in 1904, for a long time after that it was still practiced to dispose of unburned waste. As a result of increasing industrialization, the amount of waste has greatly increased and its composition has considerably changed, resulting in increasingly negative effects on the environment. With the enforcement of the Law for protection of waters (Swiss Confederation, 1972) and the Swiss Environmental Protection Act (Swiss Confederation, 1983), important milestones for sustainable waste management were set. This was followed in 1986 by the Guideline for Waste Management (BAFU, 1986), which proposed that there should remain only two types of waste: a recyclable fraction and residues suitable for sustainable landfilling. This ultimately led to a ban on landfilling the unburned waste in 2000. Today 29 MSWI plants are in operation throughout Switzerland. The Swiss Waste Ordinance (Swiss Federal Council, 2015) thereby regulates the landfilling of the solid incineration residues by defining threshold limits for the corresponding landfill types and imposes requirements for recycling. With the Resources Trialogue (Kuhn et al., 2017), solution approaches for Switzerland's waste and resource management for 2030 were created with goals for sustainable resource management: minimizing the use of energy and materials in the manufacture of products and services, optimizing the service life of products and avoiding waste wherever possible.

Today, Switzerland is one of the top waste volume generator per capita in international comparison (OECD, 2021). In 2019, around 6 million tons of municipal waste were generated, which corresponds to about 703 kg per capita (BAFU, 2020). The shares of incinerated and recycled waste are almost equal, whereby recyclable waste collected separately includes paper, cardboard, biogenic waste, waste glass, electrical and electronic equipment, textiles, PET beverage bottles, tinplate, aluminum packaging and batteries (BAFU, 2020), as well as regional different special waste collections. Each year, about 4 million tons of waste are incinerated in Switzerland, of which almost 3 million tons are municipal waste. The rest comes from construction waste, industrial and commercial waste, sewage sludge and hazardous waste. The main advantages associated with the incineration of waste compared to landfilling are: volume reduction (by 90%), mass reduction (by 75%), destruction of organic compounds associated with inertization of waste and the recovery of thermal and electric energy (Schenk, 2010). Further, it is also an efficient way to make metallic composites accessible again, thus making the metals recoverable.

The typical waste composition that is incinerated in MSWI plants is shown in Figure 1.1. Compared to the last 30 years, the relative waste composition shows significantly higher shares of biogenic waste and composite goods. The paper content has decreased significantly due to higher separate collection rates. The considerable proportion of the minerals category is largely due to cat sand (BAFU, 2014). The main part of the ferrous waste is related to food cans, while for the non-ferrous metals, aluminum is dominant
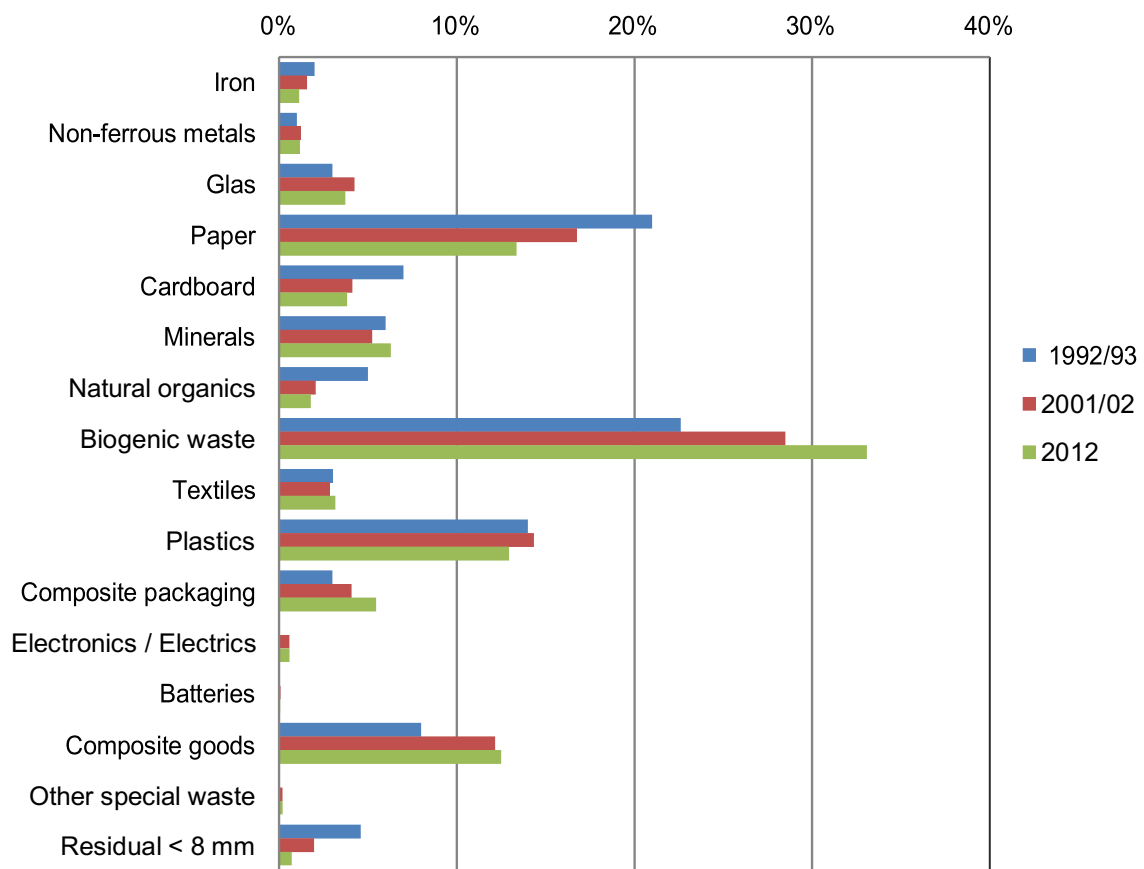
Figure 1.1: Relative composition of waste in refuse bags by waste fraction in the study municipalities in 1992/93, 2001/02, and 2012. Adapted from BAFU (2014).

Element	Use or Product
Antimony	Flame retardants, plastics (as stabilizer or catalyst), pigment (yellow or white) in e.g., plastics, ceramics, electronic components, compact discs, in alloys, vehicle brake pads, formerly in match heads, pesticides, mordants and fireworks, shooting cartridges
Cadmium	Batteries (Ni-Cd), alloys, corrosion protection, plastic stabilizer (chloride scavenger), yellow pigment for plastic
Chromium	Steel industry, alloys, leather tanning agent, yellow, red and green pigments
Copper	Electronical equipment (e.g. wires, motors), lumber/finished wood preservative, fungicide and pesticide, blue pigment
Lead	Batteries, alloys, pigment (yellow and white), ammunition, ceramic glaze, plastic stabilizer
Tin	Electronic parts (e.g. solders or electrode material), plastics and paints (as additives), food cans, polishing powder, opacifier, cosmetics, gold /bronze coloured pigment
Zinc	Steel industry (corrosion coating), as alloy in e.g. brass and bronze, yellow pigment, paper processing bleaching agent, as additive in e.g., paints, rubber products, inks, soaps, plastics, textiles, etc., luminous materials, fluorescent lights

Table 1.1: List of possible heavy metal-containing products or uses. Adapted from Chandler et al. (1997) and supplemented with Sb and Sn from BAFU (2001).

and one third thereof is represented by aluminum cans and about 3% are heavy non-ferrous metals (Cu, Zn, Sn, Pb). For the electrical and electronic equipment, the separate collection has strongly increased in the last few years, and the percentage that is disposed of in the garbage represents only 8% of the separately collected share. However, the strongly increased quantity in circulation balances out and there is no observable decrease of electrical and electronic equipment in the garbage. Mainly due to batteries and electrics / electronics (e.g. electrical appliances, cables) or special wastes (e.g. paints, Table 1.1) the heavy metal input (e.g. Zn, Cu, Pb) from municipal waste to MSWI plant is still considerable and accumulates in the residues. In addition, an important input of heavy metal to the MSWI plants also comes from various industrial wastes or automobile shredder residues (ASR). In particular, a strong increase in antimony (Sb) and tin (Sn) can be observed in the waste compared to 1991 (BAFU, 2001).

1.2.2 Combustion process and flue gas cleaning system

The main processes involved in waste incineration and the important mass streams are shown in Figure 1.2. Most MSWI plants in Switzerland are equipped with a grate furnace, boiler and electrostatic precipitator followed by a wet flue gas cleaning system, as seen in the scheme. The delivered waste is stored and homogenized in the waste bunker. The waste is conveyed to the feed funnel by crane where it enters the combustion chamber. Incineration takes place at temperatures between 800 - 1'000 °C and typical residence time on the grate is 20 - 40 min. Primary air is continuously fed into the bed from below to control the incineration temperature. Remaining incombustible solid residues are discharged to the bottom ash fraction. During incineration, small particles and volatile compounds from waste materials are transferred into the gas phase which form the flue gas. Above the firing zone is the secondary combustion chamber, where secondary air is often injected as O_2 supply.
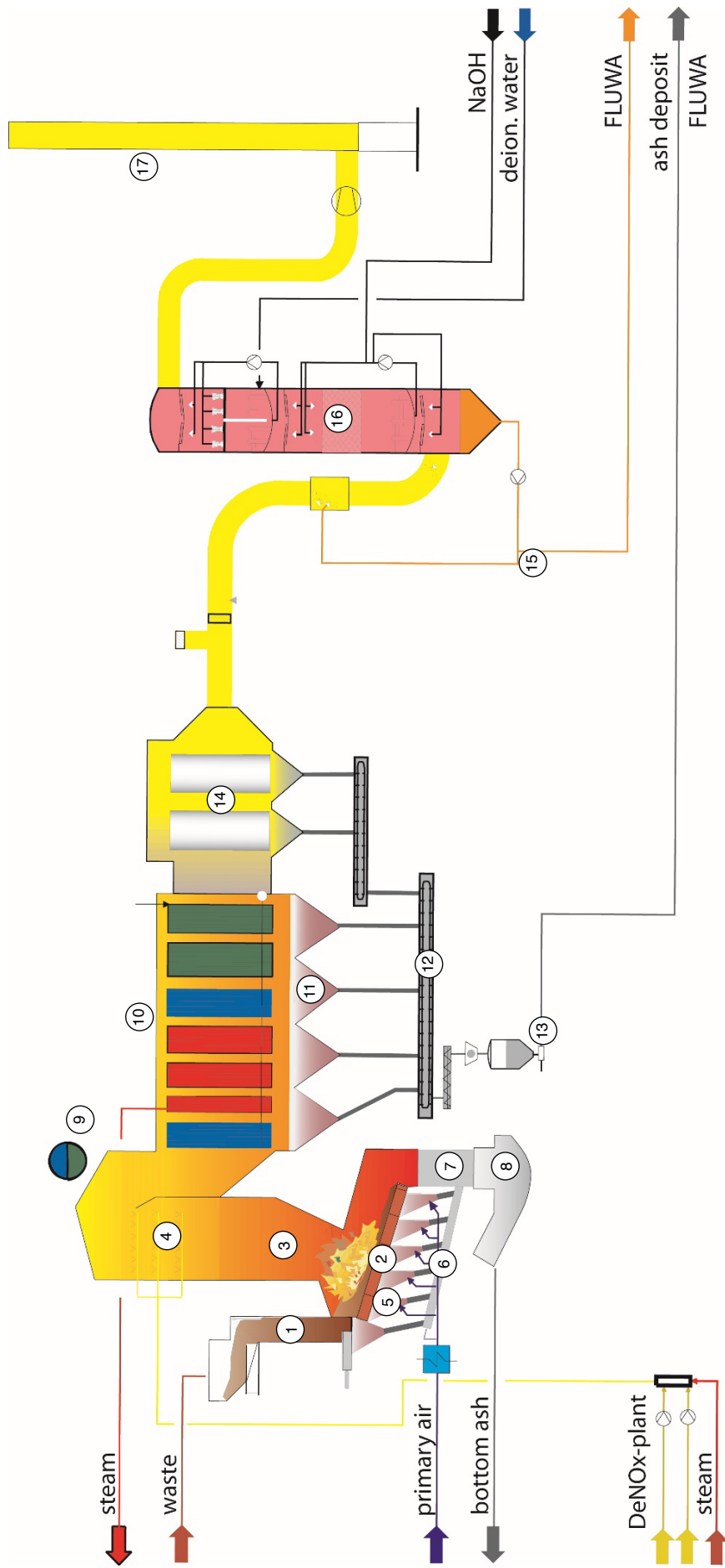
Figure 1.2: Scheme of a typical MSWI plant equipped with (1) waste feed funnel (2) grate (3) combustion chamber (4) denitrification (DeNO$_x$) (5) primary air inlet (6) air nozzles (7) bottom ash removal (8) water quench (9) steam drum (10) boiler with heat exchanger sections (blue = evaporator, red = superheater, green = economizer) (11) boiler ash hoppers (12) ash conveyor (13) pneumatic ash removal system (14) electrostatic precipitator (15) scrub water circulation (16) flue gas scrubber (17) chimney. Adapted from Hitachi Zosen INOVA, edited by Weibel (2017).

Two different processes are used to oxidize the NO$_x$ in the flue gas (BLFUW, 2002). In the so-called DeNO$_x$ process, or also termed *selective non-catalytic reduction* (SNCR), ammonia solution is injected into the secondary combustion chamber where flue gas temperatures are around 1'000 °C. In the narrow temperature window between 950 and 1'050 °C, ammonia reacts with the nitrogen oxides in the flue gas to form nitrogen and water (Beckmann et al., 2011). As an undesirable by-product of this reaction, a fraction of the ammonia burns to form NO$_x$. A minor fraction of NH$_3$ thereby escapes the reaction zone as "slip" and is found in the flue dust and exhaust gases. If the temperature drops, the nitrogen oxides are not sufficiently reduced and the NH$_3$ slip increases. The process is strongly temperature-dependent, as at higher temperatures ($> 1{,}200$ °C), NH$_3$ is combusted forming NO$_x$. The efficiency of this process is thus limited by the "slip", since excessively high NH$_3$ concentrations in the exhaust gas are impermissible. The other process termed *selective catalytic reduction* (SCR) is even more effective in reducing NO$_x$ than the SNCR. There, a catalyst is normally installed after the electrostatic precipitator to catalyze the reaction of the hot flue gas with the reducing agent (NH$_3$). This results in nitrogen oxide reduction and oxidation of organic components in the flue gas (BLFUW, 2002). By passing the boiler, the flue gas is cooled from approximately 650 °C to 250 °C. The boiler and electrostatic precipitator act as dust removal systems, where the different boiler ashes (BOA) and the electrostatic precipitator ash (ESPA) arise. In the electrostatic precipitator, the dust or mist particles suspended in the gas are electrically charged and separated at precipitation electrodes (Figure 1.3). The particles are charged by means of e.g., spray electrodes, which build up an electrostatic field by means of DC voltage. The electrically charged dust particles transfer their charges to the precipitation electrodes and remain attached to the metal plates. The dust-laden precipitation electrodes are regularly rapped and the deposited solids are removed via dust collection funnels.
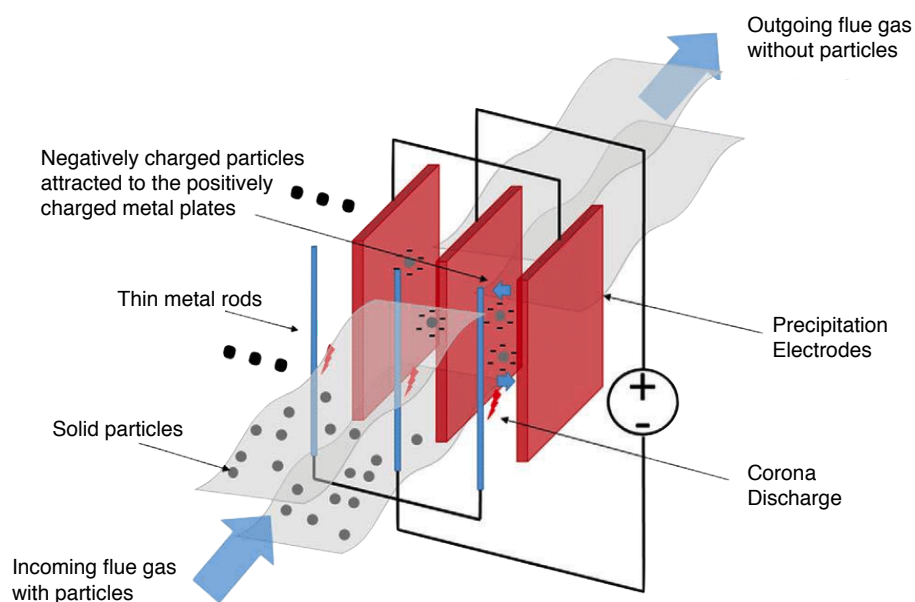
Figure 1.3: Conceptual diagram of dust removal from flue gas by flowing through electrostatic precipitator. Adapted from Becker (2010).

Gaseous compounds (mainly halogens e.g. HCl, as well as SO_2) are removed from the flue gas in a dry, semi-dry or wet flue gas cleaning system, before the clean gas (N_2, CO_2 and H_2O) is emitted through the chimney. Dry- and semi dry flue gas cleaning systems use additives as neutralizing chemicals and produce solid residues. Bicarbonate or hydrated lime are often used as adsorbents for the separation of the gaseous hydrogen chloride (HCl), hydrogen fluoride (HF) and the sulfur oxides SOx (Beckmann et al., 2011). The wet flue gas cleaning system consists of a multi-stage scrubber and the APCr arise in liquid form as scrub water (Figure 1.4). In a first stage, the flue gas is quenched with water, whereby mainly HCl, HF and NH_3 are dissolved to form the acid scrub water. In a further stage, sulfur oxides (SO_2, SO_3) and residual heavy metals are separated with the addition of NaOH, resulting in neutral or alkaline scrub water. The scrub waters can be used for heavy metal extraction (e.g. Zn, Cu, Pb, Cd) through acid fly ash leaching with the FLUWA process (Bühler and Schlumberger, 2010). When the plant is not equipped with a facility for acid leaching, the scrub waters can be discharged to surface water after precipitation of hydroxide sludge and neutralization, if quality requirements are met. Pure gypsum can be precipitated from the sulfate bearing alkaline scrub water in order to avoid landfilling of a potential secondary raw material.

Figure 1.4: Scheme of the different steps of the wet flue gas cleaning system and overview on the arising scrub waters and their possibilities for reuse. Adapted from Hitachi Zosen INOVA.

1.2.3 Heat recovery and energy production

In order to use the energy of the hot flue gas, the boiler area is equipped with heat exchanger tubes, which are combined to tube bundles and in which water or steam circulates at high pressure (approx. 40 bar). The tube bundles thereby exhibit different functions (Figure 1.5). In the economizer the feed water is preheated by the surrounding flue gas to approx. 20 - 25°C below saturated steam temperature. It is then fed to the evaporator, where the warm water is heated to the boiling temperature. Once the boiling temperature is reached, the energy amount equivalent to the vaporization heat need to be supplied to convert the wet steam into a saturated steam. Between the states of water and saturated steam exists a wet steam, a mixture of water and saturated steam. During the evaporation process, the steam temperature remains constant and steam and water have the same temperature. The wet steam is fed to the steam drum, where it is separated into water and steam. The hot water reenters the evaporator cycle and the steam is fed into the superheater. In the superheater section, the dry saturated steam is "superheated". Its temperature is thereby raised above that of the saturated steam temperature. The pressure in the superheater section corresponds to the boiler pressure, which is adjusted to the properties of the materials used and to the maximum permissible operating temperature of the steam turbine. The steam is superheated for several reasons (Mayr, 2005):

- it suppresses the formation of condensates in pipes and turbines

- the superheated steam can thus be cooled down to the saturated steam temperature without condensate forming

- superheating the steam generates a multiple of the steam volume without raising the boiler pressure - thus increasing the power of the steam turbine.

In larger plants, electricity is often generated by condensing turbines. Here, the steam, after it leaves the turbine, is condensed in a condenser and fed back to the feedwater. About 40 - 50% of the fuel energy used is converted into electricity, while the rest (about 60%) can be dissipated as waste heat. This waste heat can be decoupled from the steam via heat exchangers and be used as district heating (Mayr, 2005). The heat extraction resulting from the heat exchangers causes cooling of the flue gas as it passes through the boiler. While the temperature of flue gas is approx. 650 - 850 °C at the boiler inlet, it is cooled down to approx. 250 °C at the boiler outlet. The drop in temperature leads to precipitation of phases from the gas phase and thus result in ash-formation processes. In addition, the raw gas with its high concentration of pollutants favors the formation of corrosion phenomena. Especially at the hot tubes of the superheater, ideal corrosion conditions prevail for the flue gases. The protective evaporator, which is located upstream of the superheater on the flue gas side, and a limitation of the superheated steam temperature to 400 °C are necessary corrosion protection devices for the superheater (Mayr, 2005).
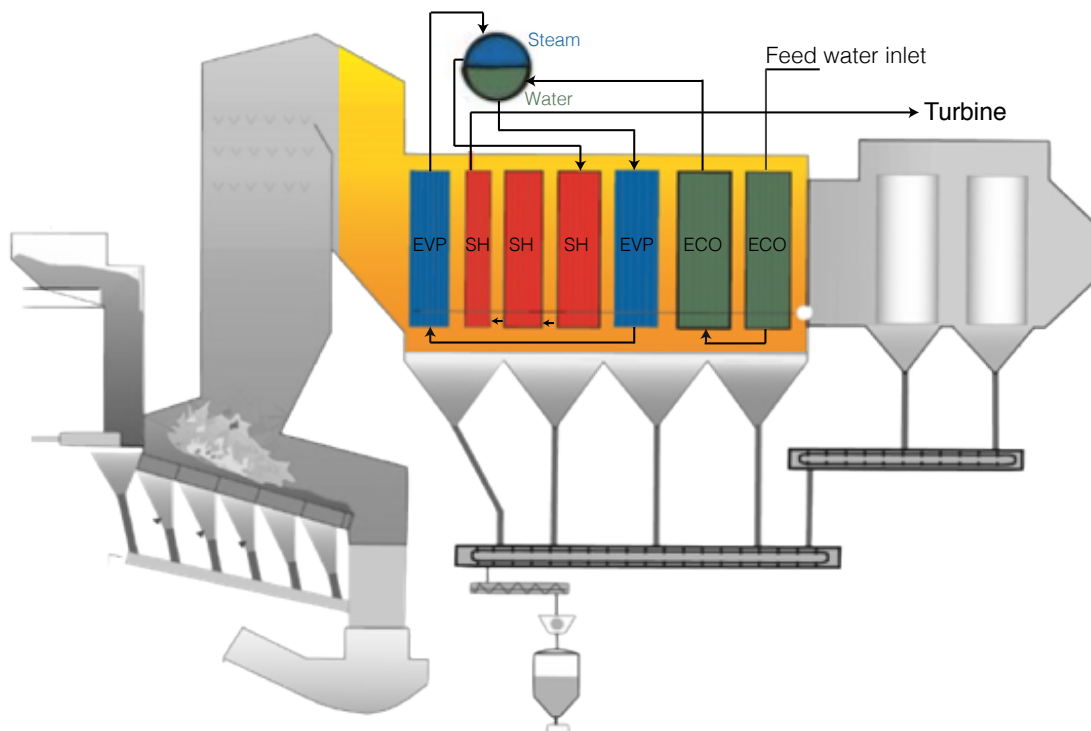
Figure 1.5: Scheme of the water-steam circuit in the boiler. EVP = evaporator, SH = superheater, ECO = economizer.

1.2.4 Incineration residues

Bottom ash

Bottom ash is the main solid residue of MSW incineration. Each year, around 800'000t of bottom ash arise in Switzerland, which corresponds to approx. 20 wt.% of the waste input. The bottom ash arises at the outcome of the combustion chamber, where it is either quenched in water or collected in its dry state. At a number of plants, the first solid residue from the flue gas path, the empty pass ash (EA), is disposed together with the bottom ash but only accounts for a minor quantity. The bottom ash is mainly composed of incombustible solid residues and unburnt organic matter (Sabbas et al., 2003). The composition of the bottom ash is mainly dependent on the waste composition and the element partitioning during incineration. Chemical elements with high boiling temperature thus accumulate in the bottom ash. The main volume fraction of bottom ash (80 - 90%) is composed of Si- and Ca- dominated crystalline compounds (e.g. melilites, wollastonite), as well as amorphous compounds (Eusden et al., 1999). However, the short residence times on the grate are often insufficient to reach a thermodynamic equilibrium state, and the reactions to form new minerals are often incomplete (Eggenberger and Mäder, 2010). The content of metallic components is in the range of 10 - 15 wt.%, whereby iron is the predominant metal. The Swiss waste ordinance (Swiss Federal Council, 2015) prescribes the recovery of non-iron metallic components from the bottom ash before landfilling. The metals from bottom ash are recovered using physical processes (e.g. magnetism, eddy current) until the non-ferrous metal content is below 1 wt.% in the grainsize fraction 2 -

16mm. Although metal depletion techniques have improved enormously in the last years, the metal-depleted residual fraction still does not meet the requirements for recycling and is disposed of in landfills. The possibilities of recycling (e.g. as substitute construction materials) or at least the partial deposition on type B deposits are subject of ongoing research.

Fly ash

The fly ash is mainly composed of precipitates from the flue gas. In Switzerland, around 80'000t of fly ash arise annually. It is composed of a mix of the different boiler ash fractions (BOA) and the electrostatic precipitator ash (ESPA). The BOA and ESPA are often collected together. The fly ash is a very fine-grained material composed of refractory minerals (e.g. quartz, feldspars), glassified melt droplets and newly formed salts (e.g. chlorides, anhydrite). It shows high metal concentrations of 10 - 15 wt.% (mainly Zn, Al, Fe, Pb), depending on waste input and partitioning of the heavy metals. Generally, industrial waste input yields higher heavy metal concentrations than incineration of household waste. Metal transfer to the fly ash fraction is favored by high incineration temperatures and also by the combustion of plastics (PVC) due to their high Cl concentration. Beside metal dependent properties (melting point, vapor pressure), the partitioning is mainly dependent on incineration conditions (oxidation states, humidity), waste composition as well as on the binding form. The transfer of heavy metals to the gas phase is thereby favored by higher furnace temperatures, as well as elevated chlorine and sulfur concentration in the flue gas (Abanades et al., 2002; Belevi and Moench, 2000; Jakob et al., 1996; Morf et al., 2000; Verhulst et al., 1996). A typical partitioning of heavy metals and nonmetals between the main mass streams is shown in Table 1.2. In addition to acid-extractable heavy metals such as Zn, Pb, Cu and Cd, the fly ash also contains considerable amounts of Sb and toxic organic compounds (e.g. PCDD/-F), which are not mobilized during acid leaching and thus accumulate in the filter cake. Untreated fly ash may be temporarily deposited in landfill type D until the end of 2025. From 2026 onwards, only filter cakes, in which the acid-extractable heavy metals have been recovered beforehand, may be deposited at landfill type D.

APCr

Depending on the flue gas cleaning system (dry or wet), solid or liquid air pollution control residues (APCr) arise. In dry and semi-dry flue gas cleaning systems, fine grained solid material arises after the injection of neutralizing additives (Sabbas et al., 2003). In other countries, where dry systems are more common, these hazardous solid residues are often collected together with the fly ash (Quina et al., 2008). APCr from semi-dry systems are similar to the residues from the dry system but usually show a lower content of unreacted lime due to a better reaction stoichiometry (Chandler et al., 1997). In wet scrubbing systems, the acid and neutral scrub waters arise as liquid APCr. The scrub waters can be used for heavy metal extraction (e.g. Zn, Cu, Pb, Cd) through acid FA

Element	Bottom Ash	Electrostatic Precipitator Ash	Flue Gas
C	1.6	0.4	98
S	34	26	40
F	34	39	27
Cl	13	20	67
Fe	99	1	0
Cu	89	10	1
Zn	51	45	4
Pb	58	37	5
Cd	12	76	12
Hg	4	24	72

Table 1.2: Observed partitioning of important nonmetals and heavy metals between the main mass streams in municipal solid waste incineration plants, if the elemental input into the furnace is taken as 100%. After Brunner and Mönch (1986).

leaching (e.g. FLUWA process (Bühler and Schlumberger, 2010)).

1.3 Waste wood incineration

1.3.1 Waste wood incineration and combustion process

In Switzerland, the demand for renewable heat and energy production has been growing enormously in Switzerland over the last decades. Particularly the energetic use of wood, as a CO_2-neutral energy source, has been strongly promoted in Switzerland in recent years and is now the second largest renewable energy source in Switzerland, after hydropower. The share of wood energy in total energy production in Switzerland was 5.3% in 2020 (BFE, 2021). About 75% of the energy volume is generated in automatic incinerators where both untreated wood and waste wood is incinerated. Each year, around 60'000t of wood ash arises from energetic use of natural wood (e.g., forest) and waste wood (e.g. coated, painted wood) through automatic firings (Stettler and Ag, 2020). However, it is necessary to distinguish between the different types of wood ash in terms of wood quality used (natural vs. waste wood) and ash fraction (bottom ash vs. fly ash). The share of fly ash from the thermal (co-)utilization of waste wood from wood-fired power plants amounted to approx. 5,000 t in 2020 (Fromm et al., 2021). In Switzerland, three large industrial wood-fired power plants with fluidized bed combustion are in operation, which are responsible for approx. 66% of the waste wood fly ash produced in Switzerland. Additionally, there are a large number of grate firing plants, which produce only a few 10t waste wood fly ash per year and plant. Grate combustion of waste wood is analogue to grate firing in MSWI plants. In fluidized bed combustion, air is injected at the bottom of the furnace in a sand bed through specially designed nozzles, which keeps a mixture of bed material (often quartz sand), ash and fuel in suspension. This creates a stationary fluidized bed in which fuel is degassed, gasified and burned (Bertsch Energy, 2012). Combustion temperatures vary, but are estimated to be > 700°C in industrial plants (Zimmermann et al., 2010). With increasing combustion temperature, ash production decreases due to mass losses by volatilization (e.g., CO_2) (Misra et al., 1993). The content of remaining organic carbon

content and toxic organic compounds depend strongly on the combustion temperature and the completeness of the combustion. Wood ash (both from natural and waste wood) is considered as waste because of the possibly high contaminant load and must be dumped on landfills, even though opportunities for recycling are being sought (e.g., in concrete production (Teixeira et al., 2019)).

1.3.2 Incineration residues

Depending on the furnace type and dedusting mechanism, wood ash can be divided into up to three different fractions: bottom ash, cyclone/boiler ash and fly ash (Obernberger, 1997). The bottom ash from wood combustion is a coarse-grained material that makes up the main part of the solid residues with about 60 - 90 wt.%. It may contain slagged parts, especially if tree bark is part of the burned material. Noncombustible metallic and mineral residues such as sand, gravel, and soil resulting from fuel contamination also make part of the bottom ash (Obernberger, 1997). Bottom ash from fluidized bed combustion also contains the remains of the bed material. Depending on the incineration plant, there is a boiler where boiler ash accumulates and/or a cyclone is installed, which serves as a dust collector. The fly ash often accumulates at fabric or hose filters. Depending on the incineration plant, the cyclone or boiler ash is collected either together with the bottom ash or with the fly ash. During incineration, heavy-metal bearing volatile compounds are transferred to the gas phase and precipitate during dedusting of the flue gas. Therefore, compared to bottom ash, waste wood fly ash is enriched in heavy metals (e.g., Zn, Pb, Cu, Cr), remaining from paints, coatings or impregnation (Huron et al., 2017; Zimmermann et al., 2010). The chemical composition of the wood incineration residues is mainly dependent on wood quality and incineration conditions (Tarelho et al., 2012; Zimmermann et al., 2010). The wood quality can be affected by wood type, compartment, growing environment and possible treatments (e.g., impregnation) prior to combustion (Etiégni and Campbell, 1991; Zimmermann et al., 2010). Due to the prevailing oxidative conditions during combustion, Cr(III) compounds may be oxidized to the very toxic and highly mobile Cr(VI) (Pohlandt-Schwandt, 1999). Thus, waste wood ashes are often severely enriched in Cr(VI) when the processed wood has been impregnated with Cr-bearing compounds. The bottom ash and fly ash from natural wood can be deposited without further treatment on landfill type D and E, according to the Swiss Waste Ordinance (Swiss Federal Council, 2015). The waste wood fly ashes, however, can only be landfilled without prior treatment until November 2023. After that, it is very likely that metals will have to be recovered in the same way as fly ash from MSWI.

1.4 Heavy metal recovery through acid leaching

1.4.1 Acid fly ash leaching (FLUWA process)

The heavy metal recovery from Swiss MSWI fly ashes will be mandatory from 2026 onwards, as prescribed in the waste ordinance (Swiss Federal Council, 2015). Acid leaching
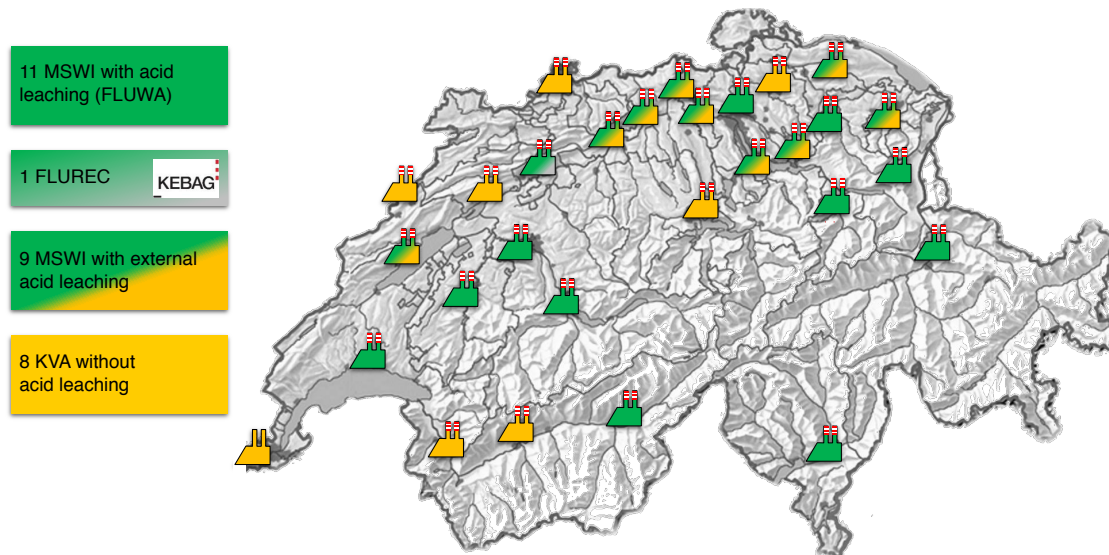
Figure 1.6: Overview of fly ash treatment method of the 29 MSWI plants in Switzerland, adapted from Weibel (2017).

with the FLUWA process (Bühler and Schlumberger, 2010) represents the state-of-the art process for heavy metal recovery from fly ash and is already installed at 12 Swiss MSWI plants (Figure 1.6). Some plants without FLUWA deliver their ashes to other plants to be treated. Currently 8 plants do not have their ashes treated yet and will have to treat their ashes either internally or externally by 2026.

In the FLUWA process, the fly ash is leached with the acid scrub water in several extraction containers that are connected with an overflow system (Figure 1.7). The heavy metals are thereby mobilized at the prevailing acid conditions and are transferred to the solution. After 45 - 60 minutes of extraction, the ash slurry is filtered by vacuum belt filtration into a filter cake with reduced heavy metal content and a heavy metal enriched filtrate. The arising filtercake is deposited on landfill type D. The heavy metal enriched filtrate is either used for direct heavy metal recovery with the FLUREC process or treated in a sewage facility where the heavy metals precipitate as a hydroxide sludge by the addition of lime. The filtered hydroxide sludge is exported abroad (dry mass 17 - 35%), where the heavy metals are recovered in smelting plants (Bühler and Schlumberger, 2010; Schlumberger et al., 2007) or will be treated in future by SwissZinc (see below). The efficiency of the FLUWA process depends on pH, Eh, liquid-to-solid ratio (LS), temperature, extraction time and leachability of fly ash. Depending on the mineralogical composition of the ash, the acid neutralizing capacity may vary. Often, additional acid must be dosed to maintain a low extraction pH value. The fly ashes show a very high reduction potential during extraction related to the presence of metallic compounds (e.g. Al^0). Oxidation of Al^0 by Cu^{2+} and Pb^{2+} at low pH value causes a reductive cementation of Pb and Cu (Weibel et al., 2017), making these metals unavailable for recovery. In order to suppress reductive cementation, an oxidizing agent (e.g. H_2O_2) has to be added. With the required recovery rates for Zn and Pb (BAFU, 2019), the use of oxidizing agents will practically become state of the art from 2026 onwards. Table 1.3 shows typical metal recovery rates
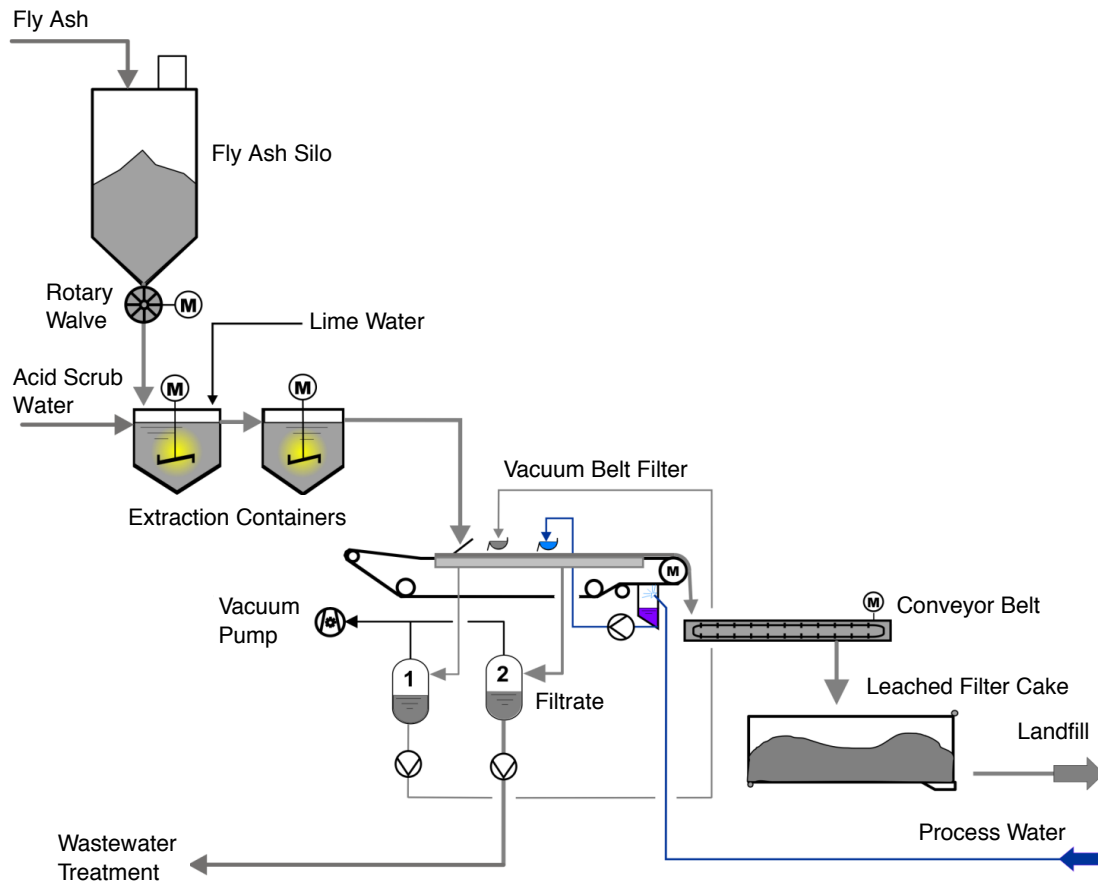
Figure 1.7: Scheme of the FLUWA process, adapted from Bühler and Schlumberger (2010).

	Recovery without use of oxidizing agent	Recovery with use of oxidizing agent
	%	%
Zn	60 - 80	60 - 80
Pb	0 - 30	50 - 90
Cu	0 - 30	40 - 80
Cd	60 - 85	85 - 95

Table 1.3: Typical ranges of recovery rates for the FLUWA process with and without oxidizing agent AWEL (2013).

for the FLUWA process with and without oxidizing agent.

In addition to the acid-extractable heavy metals such as Zn, Pb, Cu and Cd, the fly ash also contains considerable amount of Sb, which is not mobilized during acid leaching. Due to the high toxicity of Sb, especially the trivalent species, knowledge on the valence state and binding forms are essential to better estimate the hazard potential. It would be targetable to be able to mobilize the Sb during acid leaching so that it is not deposited with the filter cake.

1.4.2 Heavy metal recovery (FLUREC process)

The FLUREC process (Figure 1.8) is designed for recovering high purity Zn ($> 99.99\%$) directly from the filtrate, or from the dissolved hydroxide sludge. In a first step, Zn^0 is added to the filtrate which acts as reducing agent in order to precipitate the more noble

heavy metals Pb, Cd and Cu. This reductive separation can be described by equation 1.1:

$$Pb^{2+} + Cu^{2+} + Cd^{2+} + 3Zn^0 \rightarrow Pb^0 \downarrow + Cu^0 \downarrow + Cd^0 \downarrow + 3Zn^{2+} \qquad (1.1)$$
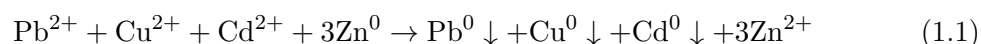
The obtained metallic cementate, which arises as by-product from the FLUREC process, serves as intermediate product for the recovery of Pb, Cu and Cd. It is sent to a Pb smelter abroad (due to its high Pb load of 50 - 70%) for further processing, where the other remaining heavy metals are recovered separately. The remaining Zn in solution is separated through solvent extraction, in which the Zn is selectively bound to a water-insoluble organic complexing phase (Schlumberger et al., 2007). This complexation step is strongly pH dependent. At low pH (pH 2.7 - 3), 99.5% of the Zn is complexed by the organic phase. Then, in a further purifying step, other metals complexed by the organic phase are separated in order to reduce interferences in the subsequent process step, where zinc is recovered electrolytically. By adding diluted sulphuric acid, the complexed Zn is released and a high-purity zinc sulphate solution is obtained. A final electrochemical step is applied in which an electrical DC potential is established in order to have Zn precipitate on Al-cathodes (electrowinning). The FLUREC process is implemented at MSWI plant Zuchwil and has a capacity to recover about 300 tons of zinc annually. The recycled Zn is fed back into the raw material cycle as a secondary raw material. With regard to the obligation of heavy metal recovery from fly ash, the industry has developed a concept in which all hydroxide sludges from Swiss FLUWAs can be processed with the FLUREC process in order to recover Zn in Switzerland. The "SwissZinc" concept envisages the decentralized production of hydroxide sludges in regional FLUWAs and subsequent Zn recovery in a joint SwissZinc plant. There, the metals are recovered from the raw material hydroxide sludge and returned to the material cycle in high quality. Over the last 10 years, an average of 11'000 tons of zinc have been imported (Figure 1.9). The total potential of all Swiss fly ashes of 2'200 t/a thus corresponds to a market share of 20%.

1.5 Remaining contaminants after treatment

1.5.1 Antimony

The high concentrations of Antimony (Sb) in fly ash are of increasing concern. Antimony is not only used in numerous metal products such as batteries, ammunition and cables, but also in non-metallic products, for example as a catalyst for the polymerization of plastics or as flame retardants (FOEN, 2007). Typical Sb concentrations in fly ashes are about 10 times higher than Sb contents in bottom ash, with ranges between about 2'000 to 5'000 ppm. Antimony is not mobilized at the conditions prevailing during acid leaching and thus accumulates in the filter cake and is deposited on landfills. Antimony is considered a toxic environmental pollutant (Gad Consulting Services, 2014) and can pose a serious risk to human health (e.g., carcinogenic (Gebel, 1997)). It is reported to exhibit a toxicity profile that shows similarities to that of arsenic (FOEN, 2007). In nature, the Sb arises as the inorganic ions Sb(III) and Sb(V), both of which are considered toxic
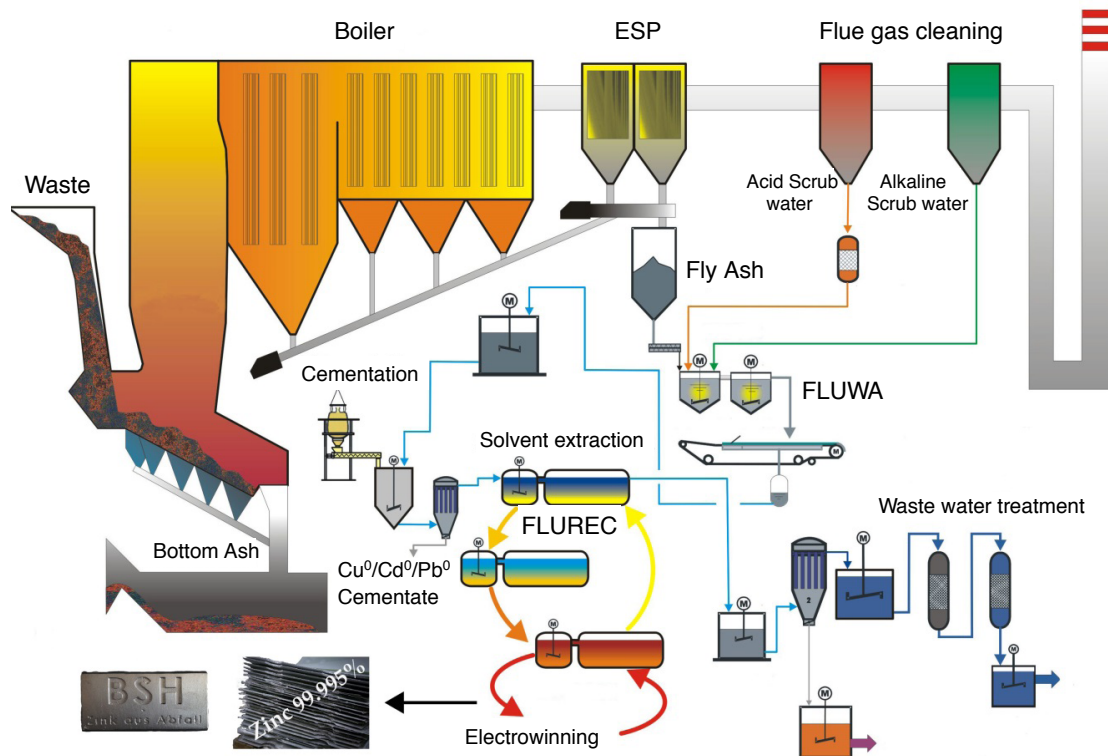
Figure 1.8: Scheme of the FLUREC process, adapted from Bühler and Schlumberger (2010).
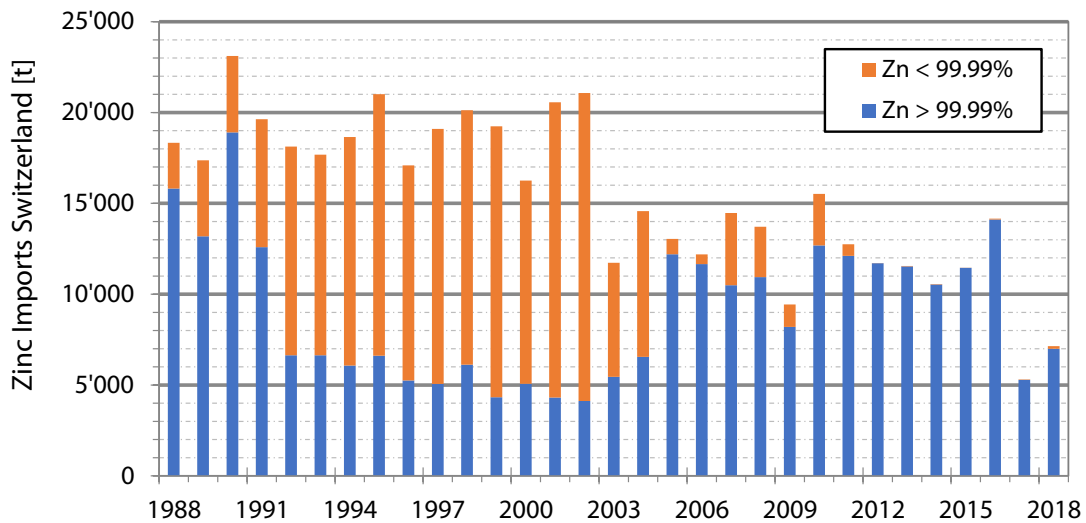
Figure 1.9: Swiss Zinc imports of the last 30 years. Since 2010, almost exclusively only zinc with a purity >99.99% is imported. Adapted from Quartier and Schlumberger (2019).

(Narukawa et al., 2005). The degree of toxicity thereby depends on the speciation and on the solubility of the Sb compounds. It was reported that the trivalent species are about 10 ten times more toxic than the pentavalent forms (Bencze, 1994). To date, very little is known about the form in which Sb is present in any of the incineration residues. The fate of antimony during incineration is highly dependent on its speciation in the waste. According to the compounds used in industry, it can be speculated that the oxidic state is predominant. Thermodynamic calculations (Paoletti et al., 2001) have predicted high volatility of antimony at incineration conditions, which is in accordance to the observation that a major fraction leaves the combustion chamber along with the flue gas and arises in the fly ash. The presence of the five-valent form has been observed in fly ash (Takaoka et al., 2005) using synchrotron-based investigations, but information about possible binding partners is missing. Better knowledge on the valence state and binding forms of Sb in fly ash is therefore essential to better estimate the hazard potential. Investigations on this topic are ongoing within the scope of this thesis.

1.5.2 Polychlorinated dibenzodioxins and -furans

Polychlorinated dibenzo-p-dioxins (PCDDs) and polychlorinated dibenzofurans (PCDFs), herein referred to as PCDD/-F are a chemical group of 210 organic, chlorinated micro-pollutants (Cunliffe and Williams, 2009) of environmental concern, as they are resistant to degradation in the environment (Dyke et al., 1997). They form as unwanted by-products in thermal processes (e.g. combustion) in presence of a chlorine source (Altarawneh et al., 2009). Each compound is composed of two benzene rings interconnected by oxygen atoms (Figure 1.10). There exist 75 PCDDs and 135 PCDFs and each individual structure is termed a congener (McKay, 2002). Due to their non-polar structure, PCDD/-Fs show a strongly hydrophobic and thus lipophilic character, explaining the low water solubility and the tendency for being adsorbed on to surfaces of particulate matter (e.g., soils) (McKay, 2002). Their chemical, physical and toxicological characteristics depend mainly on the number and position of chlorine atoms in the two benzene rings (Altarawneh et al., 2009). The 17 out of the 210 congeners are toxic, namely those where chlorine atoms occupy the positions 2,3,7,8. The congener tetrachlorodioxin 2,3,7,8-TCDD shows the highest toxicity and is classified as "probable" carcinogen (USEPA, 1994). International toxic equivalent factors (I-TEF) have been established for each of the toxic congeners (Table 1.4). Analytical results can be transformed into toxic equivalents (TEQ) by multiplying the measured concentration of each congener with its TEF. PCDD/-F and their building blocks are already present in municipal solid waste. PCDD/-F in MSW may be present as wood preservative or pesticide (McKay, 2002), whereas the organic precursors may be present in paints, organic solvents, rubbers. It is assumed that suitable combustion conditions will lead to the destruction of all PCDD/-F initially present in the MSW. Depending on the redox conditions, PCDD/-F are thermally destructed between temperatures of 350 - 600 °C (McKay, 2002; Buekens and Zhang, 2017), but for assuring total destruction of the PCDD/-F contained in the MSW, residence times of 2s at 850 °C or 1s at 1000 °C is
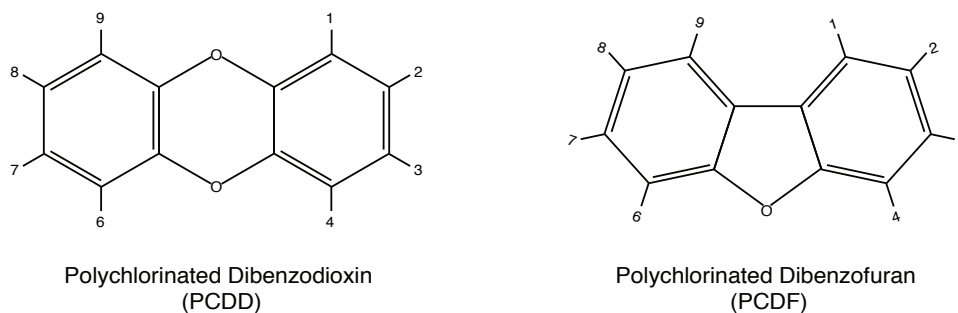
Figure 1.10: Structural formula of PCDDs (a) and PCDFs (b). The hydrogen atoms at the numbered positions can be substituted by a chlorine atom. Adapted from Altarawneh et al. (2009).

Congener	Molecular Formula	WHO-TEF	I-TEF NATO
2,3,7,8-TCDD	$C_{12}H_4Cl_4O_2$	1	1
1,2,3,7,8-PeCDD	$C_{12}H_3Cl_5O_2$	1	0.5
1,2,3,4,7,8-HxCDD	$C_{12}H_2Cl_6O_2$	0.1	0.1
1,2,3,6,7,8-HxCDD	$C_{12}H_2Cl_6O_2$	0.1	0.1
1,2,3,7,8,9-HxCDD	$C_{12}H_2Cl_6O_2$	0.1	0.1
1,2,3,4,6,7,8-HpCDD	$C_{12}HCl_7O_2$	0.01	0.01
OCDD	$C_{12}Cl_8O_2$	0.0003	0.001
2,3,7,8-TCDF	$C_{12}H_4Cl_4O$	0.1	0.1
1,2,3,7,8-PeCDF	$C_{12}H_3Cl_5O$	0.03	0.05
2,3,4,7,8-PeCDF	$C_{12}H_3Cl_5O$	0.3	0.5
1,2,3,4,7,8-HxCDF	$C_{12}H_2Cl_6O$	0.1	0.1
1,2,3,6,7,8-HxCDF	$C_{12}H_2Cl_6O$	0.1	0.1
1,2,3,7,8,9-HxCDF	$C_{12}H_2Cl_6O$	0.1	0.1
2,3,4,6,7,8-HxCDF	$C_{12}H_2Cl_6O$	0.1	0.1
1,2,3,4,6,7,8-HpCDF	$C_{12}HCl_7O$	0.01	0.01
1,2,3,4,7,8,9-HpCDF	$C_{12}HCl_7O$	0.01	0.01
OCDF	$C_{12}Cl_8O$	0.0003	0.001

Table 1.4: International toxic equivalent factors (I-TEF) and molecular formula for the different congeners.

suggested (McKay, 2002), preferably at oxidizing conditions.

However, PCDD/-F and possible precursors start forming after combustion and particularly during the cooling of the flue gas, in the boiler and the electrostatic precipitator. Despite the high research interest in PCDD/-F formation, the specific mechanisms forming these compounds remain unclear. This uncertainty is further related to the very low concentrations in combustion residues and complex analytical techniques and instrumentation for accurate analysis (Cunliffe and Williams, 2009; Stanmore, 2004). The measured concentration in the flue gas is hereby the balance between formation and destruction mechanisms, as dechlorination reactions occur. The formation of PCDD/-F in incineration plants can be divided into homogeneous and heterogeneous pathways.

- In the homogeneous pathways, PCDD/-F form from structurally related precursors in the gas phase in the presence of Cl and O at temperatures between 400 and 800 °C (Babushok and Tsang, 2003). It was thereby found that Cl present as gaseous Cl_2 was preferably implemented in PCDD/-F compared to ash-bound chlorine (Wik-

ström et al., 2004). Numerous different compounds, mainly products of incomplete combustion (PIC) can be considered as precursors. The most important precursors are reported to be monocyclic aromatic compounds (e.g. chlorinated phenols and chlorobenzenes (Figure 1.11)).

- The heterogeneous pathway involves two routes, including the well-studied *de novo* process, as well as the catalytic-assisted coupling of precursors, both taking place at temperatures between 200 and 400°C (Altarawneh et al., 2009).

  - The *de novo* synthesis relates to the formation of PCDD/-F from an unrelated organic structure such as any charred material: e.g., carbon, soot or biomass (Peng et al., 2016; Zhang et al., 2018). It involves the low-temperature gasification of particulate carbon to form carbon mono- or dioxide, as well as chlorinated carbon, the latter acting as structurally unrelated precursor for PCDD/-F (Peng et al., 2016). Catalyzed by transition metal chlorides (e.g. $CuCl_2$ (Vogg et al., 1987)), the inorganic chloride is thereby transferred to the macromolecular structure of residual carbon. The chlorinated carbon matrix is then subject to partial oxidation in order to be transformed to PCDD/-F. However, as the oxidation of residual carbon primarily results in the formation of carbon monoxide (Schwarz and Stieglitz, 1992), only a minor part of the present carbon may be transformed to PCDD/-F (Tuppurainen et al., 1998). The occurrence of the de novo synthesis on fly ash particles has been proven experimentally in different studies (Vogg and Stieglitz, 1986).

  - The catalytic-assisted coupling of precursors relates to PCDD/-F forming reactions between precursors and condensation products of volatile metals and their salts that take place on the surface of the fly ash particles during cooling of the flue gas. It is experimentally confirmed that fly ash has vastly active sites for the adsorption and condensation of e.g., chlorophenols to act as precursor for PCDD/-F formation on the surface of fly ash (Peng et al., 2016). The catalytic-assisted coupling of precursors is therefore likely to be a principal mechanism of PCDD/-F formation (Tuppurainen et al., 1998). Since the *de novo* synthesis may also lead to the formation of important precursors such as chlorinated phenols and chlorobenzes (Weber et al., 2001), it is subject to discussion whether the two heterogeneous pathways should still be regarded as separate processes, as they do not occur independently of each other.

While wet scrubbing removes most of the polar and thus water-soluble chlorophenols, removal of PCDD/-F and chlorobenzenes are negligible. PCDD/-F are removed from the flue gas through adsorption on sorbents with high specific surface, and/or by oxidation on $DeNO_x$ catalysts (Peng et al., 2016). As the remaining PCDD/-F in the flue gas is oxidized before being emitted through the chimney, the main emission of PCDD/-F from MSWI to the environment is the fly ash, where PCDD/-F are adsorbed. However, PCDD/-F are not mobilized at the conditions prevailing in the FLUWA process, leading to accumulation
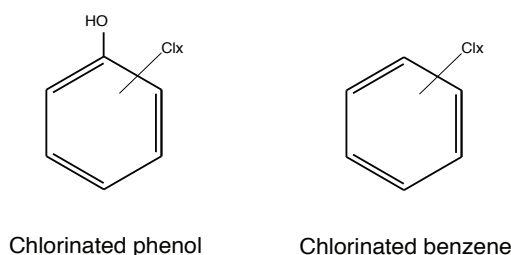
Figure 1.11: Structural formula of the most important PCDD/-F precursors, adapted from Altarawneh et al. (2009).

of PCDD/-F in the filter cake. As the mass loss during acid leaching is between 20 - 50%, the enrichment factor of PCDD/-F in filter cake is approximately 1.25 to 2. The enrichment does not change the PCDD/-F flux to the landfill. The threshold value for landfill deposition for PCDD/-F lies at 1 μg TEQ/kg, which is often exceeded. In 2020, the average PCDD/-F concentration in Swiss fly ashes (untreated) was at 0.95 μg TEQ/kg (Gaussen-Freidl and Quartier, 2020). However, it was found that PCDD/-F concentrations in the eluates of landfills were below detection limit. The mobility of PCDD/-F in landfills is strongly increased by the presence of organic compounds. Therefore, the threshold value for organic compounds is set to 20'000 mg/kg in landfill type D. Two different techniques are being developed for the thermal destruction of PCDD/-F in fly ash in Switzerland. The ExDiox process concentrates the lighter fraction where PCDD/-F is accumulated and selectively returns the fraction to the combustion chamber. The ReFire process involves returning the filter cake to the combustion chamber where the accumulated PCDD/-F is destructed thermally (Fromm et al., 2019). The latter has been proven to work out well at industrial scale and is currently improved whereby sulfur from the scrub water is precipitated as gypsum prior to the FLUWA process. The precipitated gypsum can be reused and additionally landfill volume can be saved.

Chapter 2

Scope of the thesis

2.1   Summary of open questions

Despite active research, many open questions regarding the geochemical characteristics of MSWI and waste wood fly ashes remain, which are important to optimize heavy metal recovery and to reduce hazard potential on landfills, especially with regard to the mobilization potential of heavy metals. In the present thesis, the following open questions will be addressed:

- With regard to the heavy metal recovery obligation that is to apply in Switzerland from 2026, there is a lack of knowledge as to whether heavy metal recovery from boiler ashes is expedient from a technical and ecological point of view, or whether alternative disposal routes (e.g., disposal with the bottom ash) should be examined. It is thereby unclear, whether the boiler ash is closer to the bottom ash or the ESP ash in terms of its geochemical characteristics. Since previous characterization of the MSWI ashes have been performed on the bulk fly ash mix as it is processed in the FLUWA, there is only little data on how the heavy metals are distributed among the ash fractions that arise along the flue gas cooling path. In addition, little is known on the extractability of the different ash fractions. Therefore, additional data is needed to be able to make statements regarding the efficiency of heavy metal recovery from boiler ash fractions.

- Independent of the extractability of the boiler ash, there is still little knowledge about the heavy metal binding forms present in the ash fractions. Detailed knowledge of the heavy metal binding forms (mainly Zn, Pb, Cu) is important for an efficient heavy metal recovery. With additional knowledge, process steps could possibly be adjusted to increase the heavy metal recovery. Furthermore, information on the heavy metals remaining in the filter cake and their binding forms of (e.g., Sb) are also of great importance to estimate their toxicity and mobilization potential at the landfill.

- There is little knowledge about the formation conditions of PCDD/-F along the flue gas path and about the PCDD/-F concentration in the boiler ashes. Information on the PCDD/-F concentration and congener distribution in boiler ashes are thereby

also important factors for the decision of their disposal route. Up to now, no statistically significant correlations have been observed between variables such as TOC, Cl, Cu content and the PCDD/-F concentrations in the bulk fly ash. With a detailed characterization of the different ash fractions it would be of interest to investigate possible correlations between such variables and the PCDD/-F concentration in the individual fractions.

- The heavy metal recovery obligation for the waste wood fly ashes applies from 2024 onwards. There is still little knowledge on the extractability of the waste wood fly ashes and whether a co-treatment with the MSWI FA would be expedient. In this respect it is also a matter of question how the oxidizing conditions prevailing during acid leaching would affect the Cr(VI) content in the waste wood fly ashes.

2.2   Aim of the thesis

In order to address the abovementioned open questions, this study provides a detailed investigation of the formation of MSWI fly ashes through chemical and mineralogical characterization and thermodynamic modelling. In addition, the leachability of diverse incineration residues is investigated: MSWI boiler- and ESP ashes, as well as waste wood fly ash. The key factors to optimize the acid leaching process are the knowledge of the chemical and mineralogical properties of the ash, as well as the heavy metal concentrations and their binding form. The thesis therefore focuses on the following topics:

- A detailed chemical and mineralogical characterization of the different MSWI fly ash fractions that arise along the flue gas cooling path is performed. The focus is thereby laid on the distribution of heavy metals among the different fractions and identifying possible binding forms. Further, the ash matrix affecting the leachability is investigated in detail. The efficiency of heavy metal recovery from the different ash fractions is estimated based on these findings and additional laboratory-scale leaching experiments. The results should serve as basis for the decision on the disposal route of the boiler ashes.

- In order to gain insight into the ash forming processes occurring during cooling of the flue gas, thermodynamic simulations of the cooling of the flue gas were performed at different flue gas conditions. The stability fields of the thermodynamically predicted phases (i.e. heavy metals) can thereby be investigated, as well as influences of the flue gas composition on the predicted phase assemblages. The comparison of the observed and predicted phase assemblages in the MSWI fly ash fractions should give insights into the ash forming processes and transport mechanisms occurring during cooling of the flue gas. Better knowledge of the formation of fly ashes will help to better understand and characterize these complex materials.

- A congener-specific PCDD/-F analysis of the different MSWI fly ash fractions was performed in order to locate the temperature window of PCDD/-F formation and

investigate their congener patterns, as well as correlations to TOC. The data analysis was complemented by thermodynamic modelling in order to investigate the relative stabilities of the different congeners at different flue gas conditions. The obtained data should give better insights into the formation of PCDD/-F compounds and possibly show ways to suppress their formation.

- The waste wood fly ashes are characterized in detail with respect to their heavy metal and Cr(VI) concentrations. It is further investigated in laboratory- and industrial scale experiments, whether the waste wood fly ashes are suitable for co-treatment with MSWI fly ash during acid leaching. The quality of the remaining filter cake with regard to the environmentally problematic Cr(VI) is thereby of special interest.

2.3 Thesis outline

The thesis is organized in five parts:

(i) The first part introduces to the main aspects involved in municipal solid waste incineration, focusing on waste composition, combustion process, flue gas cleaning and heat recovery. The combustion of wood and its residues are described in a subsequent section of this part. An overview is given on the state-of-the art heavy metal recovery from MSWI fly ash. The process of acid leaching and subsequent recovery of heavy metals are thereby described. At last, the remaining of contaminants in the filter cake after acid leaching is discussed.

(ii) The second part is based on two research papers that have been published in international peer-reviewed journals and two research papers being in preparation for submission. The published papers describe the mineralogical and chemical characterization of MSWI boiler- and electrostatic precipitator ashes, as well as ashes from waste wood incineration and gives implications on the heavy metal recoverability. The manuscripts in preparation focus on describing and modelling the processes occurring during flue gas cooling that lead to ash formation and contaminant build-up (e.g. PCDD/-F).

(iii) The third part contains a technical report in German that is addressed to the plant operators. It describes the different fly ash fractions and their leachability with regard to heavy metal recovery and contains data from laboratory-scale leaching experiments. The data serves as basis for implications on the heavy metal recoverability of the ash fractions, as well as on differentiation with regard to the bottom ash.

(iv) The fourth part outlines the main findings of the thesis by presenting new insights into the ash forming processes together with implications on heavy metal recovery of the different ash fractions. It also provides an outlook on aspects where additional investigation is required and outlines further studies that are planned to address these aspects.

(v) The appendix contains the supplementary material of the research papers. It further contains unpublished results and input files from the thermodynamic calculations.

References

Abanades, S., Flamant, G., Gagnepain, B., Gauthier, D., 2002. Fate of heavy metals during municipal solid waste incineration. Waste Manag. Res. 20, 55–68. https://doi.org/10.1177/0734242x0202000107

Altarawneh, M., Dlugogorski, B.Z., Kennedy, E.M., Mackie, J.C., 2009. Mechanisms for formation, chlorination, dechlorination and destruction of polychlorinated dibenzo-p-dioxins and dibenzofurans (PCDD/Fs). Prog. Energy Combust. Sci. 35, 245–274. https://doi.org/10.1016/j.pecs.2008.12.001

AWEL, 2013. Stand der Technik für die Aufbereitung von Rauchgasreinigungsrückständen aus Kehrichtverbrennungsanlagen 17–20.

Babushok, V.I., Tsang, W., 2003. Gas-phase mechanism for dioxin formation. Chemosphere 1023–1029.

Becker, K., 2010. Environmental applications of non-thermal plasmas, in: Brelles-Marino, G., E. (Ed.), Biological and Environmental Applications of Gas Discharge Plasmas. Nova Science Publishers, New York, pp. 5–32.

Beckmann, M., Karpf, R., Dütge, V., Wen, T., 2011. Vergleichende ökonomische Betrachtung verschiedener Einsatzstoffe bei Trockensorptionsverfahren zur Abgasreinigung, in: Energie Aus Abfall - Band 8. Thomé-Kozmiensky (Hrsg.), pp. 583–631.

Belevi, H., Moench, H., 2000. Factors determining the element behavior in municipal solid waste incinerators. 1. Field studies. Environ. Sci. Technol. 34, 2501–2506. https://doi.org/10.1021/es991078m

Bencze, K., 1994. Handbook on Metals in Clinical and Analytical Chemistry. New York, pp. 227–236.

Bertsch Energy, 2012. Verfahrensbeschreibung Wirbelschichtfeuerung.

BLFUW, 2002. Stand der Technik bei Abfallverbrennungsanlagen. Bundesministerium für Land- und Forstwirtschaft, Umwelt und Wasserwirtschaft.

Brunner, P.H., Mönch, H., 1986. The flux of metals through municipal solid waste incinerators. Top. Catal. 4, 105–119.

Buekens, A., Zhang, M., 2017. De novo synthesis of dioxins: a review. Int. J. Environ. Pollut. 60, 63. https://doi.org/10.1504/ijep.2016.10002958

Bühler, A., Schlumberger, S., 2010. Schwermetalle aus der Flugasche zurückgewinnen. Saure Flugaschewäsche mit dem FLUWA-Verfahren, ein zukunftsweisendes Verfahren in der Abfallverbrennung. KVA-Rückstände der Schweiz. Der Rohstoff mit Mehrwert (Bundesamt für Umwelt BAFU) 185–192

Bundesamt für Energie BFE, 2021. Schweizerische Gesamtenergiestatistik 2020.

Bundesamt für Umwelt BAFU, 2020. Abfallmengen und Recycling 2019 im Überblick.

Bundesamt für Umwelt BAFU, 2019. Vollzugshilfe für die "Rückgewinnung von Metallen aus den Filteraschen von Kehrichtverbrennungsanlagen." Bern.

Bundesamt für Umwelt BAFU, 2014. Erhebung der Kehrichtzusammensetzung 2012.

Bundesamt für Umwelt BAFU, 2001. Erhebung der Kehrichtzusammensetzung. 2001

Bundesamt für Umwelt BAFU, 1986. Leitbild für die Schweizerische Abfallwirtschaft.

Chandler, A.J., Eighmy, T.T., Hartlén, J., Hjelmar, O., Kosson, D., Sawell, S.E., van der Sloot, H.A., Vehlow, J., 1997. Municipal solid waste incinerator residues.

Cunliffe, A.M., Williams, P.T., 2009. De-novo formation of dioxins and furans and the memory effect in waste incineration flue gases. Waste Manag. 29, 739–748. https://doi.org/10.1016/j.wasman.2008.04.004

Dyke, P.H., Foan, C., Wenborn, M., Coleman, P.J., 1997. A review of dioxin releases to land and water in the UK. Sci. Total Environ. 207, 119–131. https://doi.org/10.1016/S0048-9697(97)00254-4

Eggenberger, U., Mäder, U., 2010. Charakterisierung und Alterationsreaktionen von KVA-Schlacken. KVA-Rückstände in der Schweiz - Der Rohstoff mit Mehrwert.

Etiégni, L., Campbell, A.G., 1991. Physical and chemical characteristics of wood ash. Bioresour. Technol. 37, 173–178. https://doi.org/10.1016/0960-8524(91)90207-Z

Eusden, J.D., Eighmy, T.T., Hockert, K., Holland, E., Marsella, K., 1999. Petrogenesis of municipal solid waste combustion bottom ash. Appl. Geochemistry 14, 1073–1091. https://doi.org/https://doi.org/10.1016/S0883-2927(99)00005-0

FOEN, 2007. Antimony in Switzerland: A Substance flow analysis.

Fromm, S., Eggenberger, U., Schlumberger, S., Ulrich, M., 2019. Thermische Zerstörung von Dioxinen und Furanen in sauer gewaschenen KVA Flugaschen (ReFire).

Fromm, S., Zucha, W., Schlumberger, S., Eggenberger, U., 2021. Metallrückgewinnung aus Filteraschen der thermischen Altholzverwertung.

Gad Consulting Services, 2014. Antimony, in: Encyclopedia OfToxicology. Cary, NC, pp. 274–276. https://doi.org/10.1016/B978-0-12-386454-3.00815-0

Gaussen-Freidl, B., Quartier, R., 2020. Messkampagne KVA-Asche 2020.

Gebel, T., 1997. Arsenic and antimony: comparative approach on mechanistic toxicology. Chem. Biol. Interact. 107, 131–144.

Huron, M., Oukala, S., Lardière, J., Giraud, N., Dupont, C., 2017. An extensive characterization of various treated waste wood for assessment of suitability with combustion process. Fuel 202.

Jakob, A., Stucki, S., Struis, R.P.W.J., 1996. Complete heavy metal removal from fly ash by heat treatment: Influence of chlorides on evaporation rates. Environ. Sci. Technol. 30, 3275–3283. https://doi.org/10.1021/es960059z

Kuhn, P., Reichen, S., Wassermann, E., 2017. Ressourcen Trialog: Ein Dialog über Herausforderungen und Lösungsansätze in der Abfall- und Ressourcenwirtschaft der Schweiz 2030, Schlussbericht. Aarau.

Mayr, F., 2005. Handbuch der Kesselbetriebstechnik - Kraft- und Wärmeerzeugung in Praxis und Theorie. Resch Verlag.

McKay, G., 2002. Dioxin characterisation, formation and minimisation during municipal solid waste (MSW) incineration: Review. Chem. Eng. J. 86, 343–368. https://doi.org/10.1016/S1385-8947(01)00228-5

Misra, M., Raglund, K., Baker, A., 1993. Wood ash composition as a function of furnace temperature. Biomass Bionenergy 4, 103–116.

Morf, L.S., Brunner, P.H., Spaun, S., 2000. Effect of operating conditions and input variations on the partitioning of metals in a municipal solid waste incinerator. Waste Manag. Res. 18, 4–15. https://doi.org/10.1034/j.1399-3070.2000.00085.x

Narukawa, T., Takatsu, A., Chiba, K., Riley, K.W., French, D.H., 2005. Investigation on chemical species of arsenic, selenium and antimony in fly ash from coal fuel thermal power stations. J. Environ. Monit. 7, 1342–1348. https://doi.org/10.1039/b509817c

Obernberger, I., 1997. Nutzung fester Biomasse in Verbrennungsanlagen unter besonderer Berücksichtigung des Verhaltens aschebildender Elemente. Schriftenr. Thermische Biomassenutzung.

OECD, 2021. Municipal waste. URL https://data.oecd.org/waste/municipal-waste.htm

Paoletti, F., Sirini, P., Seifert, H., Vehlow, J., 2001. Fate of antimony in municipal solid waste incineration. Chemosphere 42, 533–543. https://doi.org/10.1016/S0045-6535(00)00225-3

Peng, Y., Chen, J., Lu, S., Huang, J., Zhang, M., Buekens, A., Li, X., Yan, J., 2016. Chlorophenols in Municipal Solid Waste Incineration: A review. Chem. Eng. J. 292, 398–414. https://doi.org/10.1016/j.cej.2016.01.102

Pohlandt-Schwandt, K., 1999. Treatment of wood ash containing soluble chromate. Biomass and Bioenergy 16, 447–462. https://doi.org/10.1016/S0961-9534(99)00013-6

Quartier, R., Schlumberger, S., 2019. SwissZinc AG Projektdokumentation Mai 2019.

Quina, M.J., Santos, R.C., Bordado, J.C., Quinta-Ferreira, R.M., 2008. Characterization of air pollution control residues produced in a municipal solid waste incinerator in Portugal. J. Hazard. Mater. 152, 853–869. https://doi.org/10.1016/j.jhazmat.2007.07.055

Sabbas, T., Polettini, A., Pomi, R., Astrup, T., Hjelmar, O., Mostbauer, P., Cappai, G., Magel, G., Salhofer, S., Speiser, C., Heuss-Assbichler, S., Klein, R., Lechner, P., 2003. Management of municipal solid waste incineration residues. Waste Manag. 23, 61–88. https://doi.org/https://doi.org/10.1016/S0956-053X(02)00161-7

Schenk, K., 2010. KVA-Rückstände in der Schweiz. Der Rohstoff mit Mehrwert.

Schlumberger, S., Schuster, M., Ringmann, S., Koralewska, R., 2007. Recovery of high purity zinc from filter ash produced during the thermal treatment of waste and interting of residual materials. Waste Manag. Res. 25, 547–555.

Schwarz, G., Stieglitz, L., 1992. Formation of organohalogen compounds in fly ash by metal-catalyzed oxidation of residual carbon. Chemosphere 25, 277–282. https://doi.org/doi:10.1016/0045-6535(92)90543-z

Stanmore, B.R., 2004. The formation of dioxins in combustion systems. Combust. Flame 136, 398–427. https://doi.org/10.1016/j.combustflame.2003.11.004 Stettler, Y., Ag, H., 2020. Schweizerische Holzenergiestatistik Erhebung für das Jahr 2019.

Swiss Confederation, 1983. Bundesgesetz über den Umweltschutz (Umweltschutzgesetz, USG). 814.01.

Swiss Confederation, 1972. Allgemeine Gewässerschutzverordnung (AGSchV) vom 19. Juni 1972, AS 1972 967.

Swiss Federal Council, 2015. Ordinance on the Avoidance and the Disposal of Waste. (Waste Ordinance, ADWO). (Status of January 1st 2022).

Takaoka, M., Yamamoto, T., Tanaka, T., Takeda, N., Oshita, K., Uruga, T., 2005. Direct speciation of lead, zinc and antimony in fly ash from waste treatment facilities by XAFS spectroscopy. Phys. Scr. T T115, 943–945. https://doi.org/10.1238/Physica.Topical.115a00943

Tarelho, L.A.C., Teixeira, E.R., Silva, D.F.R., Modolo, R.C.E., Silva, J.J.F., 2012. Characteristics, management and applications of ashes from thermochemical conversion of biomass to energy, in: Proceedings of the Conference Exhibition on Biomass for Energy Jonkopin, Sweden, 29–31 May 2012.

Teixeira, E.R., Camões, A., Branco, F.G., 2019. Resources , Conservation & Recycling Valorisation of wood fl y ash on concrete. Resour. Conserv. Recycl. 145, 292–310. https://doi.org/10.1016/j.resconrec.2019.02.028

Tuppurainen, K., Halonen, I., Ruokoj, P., Tarhanen, J., Ruuskanen, J., 1998. Formation of PCDDs and PCDFs in Municipal Waste Incineration and its Inhibition Mechanisms: A Review. Chemosphere 36, 1493–1511.

USEPA, 1994. Combustion Emissions Technical Resource Document, Report No. EPA 530-R-94-014. Washington, DC.

Verholst, D., Buekens, A., Spencer, P.J., Eriksson, G., 1996. Thermodynamic behavior of metal chlorides and sulfates under the conditions of incineration furnaces. Environ. Sci. Technol. 30, 50–56. https://doi.org/10.1021/es940780+

Vogg, H., Metzger, M., Stieglitz, L., 1987. Recent findings on the formation and decomposition of PCDD/PCDF in municipal solid waste incineration. Waste Manag. Res. 5, 285–294. https://doi.org/10.1016/0734-242X(87)90080-2

Vogg, H., Stieglitz, L., 1986. Thermal Behavior Of PCDD/PCDF In Fly Ash From Municipal Incinerators. Chemisphere 15, 1373–1378.

Weber, R., Iino, F., Imagawa, T., Takeuchi, M., Sakurai, T., Sadakata, M., 2001. Formation of PCDF, PCDD, PCB, and PCN in de novo synthesis from PAH: mechanistic aspects and correlation to fluidized bed incinerators. Chemosphere 44, 1429–1438.

Weibel, G., 2017. Optimized Metal Recovery from Fly Ash from Municipal Solid Waste Incineration. PhD Thesis. University of Bern.

Weibel, G., Eggenberger, U., Schlumberger, S., Mäder, U.K., 2017. Chemical associations and mobilization of heavy metals in fly ash from municipal solid waste incineration. Waste Manag. 62, 147–159.

Wikström, E., Ryan, S., Touati, A., Tabor, D., Gullett, B.K., 2004. Origin of carbon in polychlorinated dioxins and furans formed during sooting combustion. Environ. Sci. Technol. 38, 3778–3784.

Zhang, M., Buekens, A., Li, X., 2018. Characterising boiler ash from a circulating fluidised bed municipal solid waste incinerator and distribution of PCDD/F and PCB. Environ. Sci. Pollut. Res. 25, 22775–22789. https://doi.org/10.1007/s11356-018-2402-7

Zimmermann, S., Hässig, J., Landolt, W., 2010. Literaturreview Holzasche - Wald: Nährstoffentzug durch Holzernte, Ascherückführung in den Wald, abiotische und biotische Wirkungen. Studie im Auftrag des Bundesamtes für Umwelt BAFU.

Part II

Research Papers

Chapter 3

Characterization of MSWI fly ashes along the flue gas cooling path and implications on heavy metal recovery through acid leaching

M.Wolffers[a], U. Eggenberger[a], S. Schlumberger[b], S. V. Churakov[a,c]

[a] Institute of Geological Sciences, University of Bern

[b] Zentrum für nachhaltige Abfall- und Ressourcennutzung (ZAR)

[c] Laboratory for Waste Management, Paul Scherrer Institute

3.1   Abstract

This study reports on detailed chemical and mineralogical characterization of the different municipal solid waste incineration ashes forming along the flue gas path of plants with separate dust removal and neutralization. In pursuit of optimizing heavy metal recovery through acid leaching, the metal extractability from empty pass ashes (EA), boiler ashes (BOA) and the electrostatic precipitator ashes (ESPA) was evaluated and compared. The focus was laid on matrix phases affecting leachability (e.g. alkalinity, oxidation-reduction potential), as well as on distribution and concentration of recoverable heavy metals and their binding forms. The data showed, that EA and BOA are geochemically similar and are essentially composed of two different materials: the heavy metal poor airborne ash particles and the Zn- and Pb-rich sulfate deposits that condensate on heat exchanger surfaces. Variation in relative amount and chemical composition of the deposits is responsible for fluctuations in bulk composition of EA and BOA. The ESPA shows different chemical and mineralogical characteristics than EA and BOA. The ESPA is enriched in the volatile heavy metals Zn, Pb, Cu, Cd and Sn, which are mainly incorporated in chlorides and sulfates. The high content of salt-bound and thus easily soluble heavy metals together with the lower alkalinity and lower oxidation-reduction potential indicates, that ESPA has a better leachability compared to EA and BOA. The EA and BOA, on the other hand, do not show any significant differences in leachability. The data may contribute to a basis for re-evaluating disposal routes of ash fractions with poor extraction properties.

3.2 Introduction

Heavy metal recovery from residues of municipal solid waste incineration (MSWI) is a sustainable technology for returning valuable metals back into the raw materials cycle. In Switzerland, two main types of solid residues remain after MSW incineration at 800 – 1000 °C: the bottom ash (800'000 t/y) and the fly ash (FA, 80'000 t/y) (BAFU, 2019). During incineration, volatile compounds from waste materials are transformed into the gas phase that form the flue gas. The transfer of heavy metals to the gas phase is thereby favored by higher furnace temperatures, as well as elevated chlorine and sulfur concentration in the flue gas (Verhulst et al. 1996; Abanades et al. 2009; Morf et al. 2000; Belevi and Moench 2000; Jakob et al. 1996). The first solid residue from the flue gas path is the ash arising at the 2nd and 3rd pass, also called the empty pass ash (EA), which is often disposed together with the bottom ash (Figure 3.1). After leaving the 3rd pass, the flue gas flows through the boiler, which is equipped with heat exchanger tubes. By passing the boiler, the flue gas is cooled from approximately 650 °C to 250 °C. The boiler and electrostatic precipitator act as dust removal systems, where the different BOA and the ESPA arise. BOA and ESPA are usually collected together and referred to as FA. Gaseous compounds (mainly halogens e.g. HCl, as well as SO_2) are removed from the flue gas in a dry, semi-dry or wet flue gas cleaning system, before the clean gas (N_2, CO_2 and H_2O) is emitted through the chimney. Dry- and semi dry flue gas cleaning systems use additives as neutralizing chemicals and produce solid flue gas cleaning products. In other countries, these flue gas cleaning residues are often collected together with FA and the hazardous mixture is termed air pollution control residues (APCr) (Quina, 2008; Quina, 2018). The wet flue gas cleaning system consists of a multi-stage scrubber and the APCr arise in liquid form as scrub water. In a first stage, the flue gas is quenched with water, whereby mainly HCl, HF and NH_3 are dissolved to form the acid scrub water. In a further stage, sulfur oxides (SO_2, SO_3) and residual heavy metals are separated with the addition of NaOH, resulting in neutral or alkaline scrub water. The scrub waters can be used for heavy metal extraction (e.g. Zn, Cu, Pb, Cd) through acid leaching (e.g. FLUWA process (Bühler and Schlumberger, (2010)). When the plant is not equipped with a facility for acid leaching, the scrub waters can be discharged to surface water after precipitation of hydroxide sludge and neutralization, if quality requirements are met. Pure gypsum can be precipitated from the sulfate bearing alkaline scrub water in order to avoid landfilling of a potential secondary raw material.

At present, Swiss bottom ash and FA are deposited on landfills as they do not meet the quality requirements for recycling. The Swiss waste ordinance (Swiss Federal Council, 2015) prescribes the recovery of metals from the incineration residues before landfilling. The heavy metals from bottom ash are recovered using physical processes (e.g. magnetism, eddy current) until the non-ferrous metal content is below 1 wt.%. For FA, chemical processes such as acid leaching (e.g. FLUWA process (Bühler and Schlumberger, 2010)) represent the state-of-the art for heavy metal recovery. The resulting ash slurry is filtered into a heavy metal enriched leachate that can be used for heavy metal recovery (Schlumberger
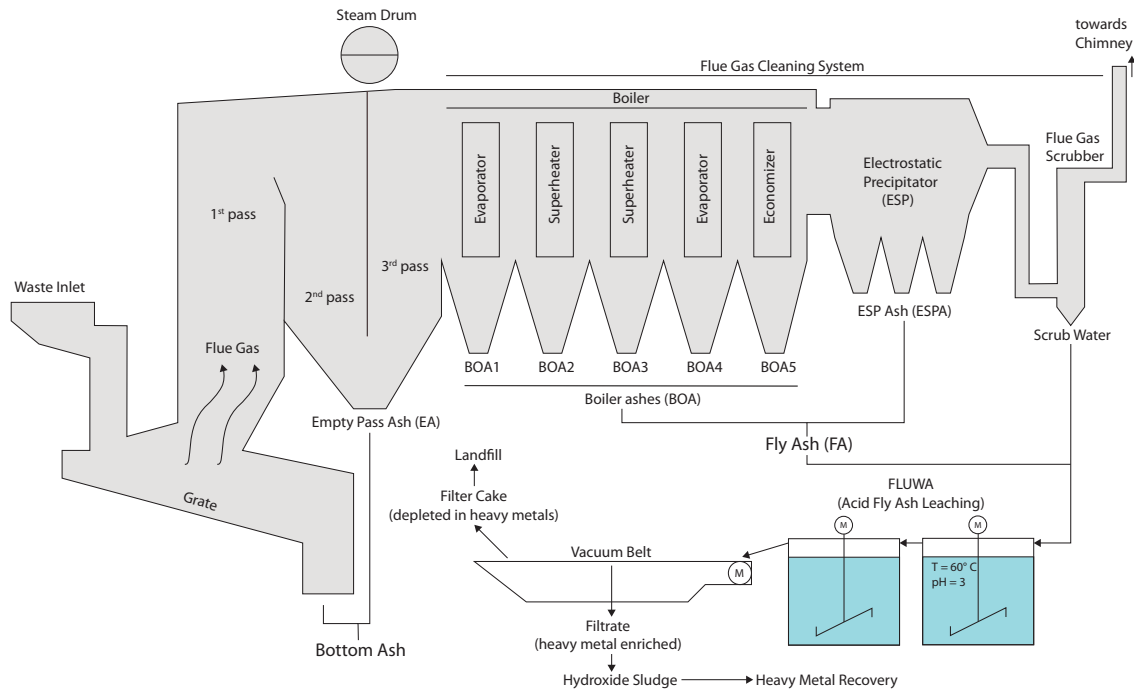
Figure 3.1: Scheme showing the different mass streams arising from incineration, on the example of a wet flue gas cleaning system combined with acid fly ash leaching (FLUWA). Adapted from Bühler and Schlumberger (2010).

et al., 2007) and a filter cake with reduced heavy metal content, which is deposited on landfills. The annual amount of filter cake deposited is often not gravimetrically recorded, but is calculated using the typical mass loss during acid leaching of approx. 25 - 30% (Bühler and Schlumberger, 2010; Weibel et al., 2021). The mobilization of the heavy metals is mainly dependent on the heavy metal binding form and the extraction conditions (e.g. pH, redox conditions (Eh), liquid to solid ratio, temperature). FA show a very high reduction potential during extraction due to the presence of metallic compounds (e.g. Al^0 in Al-foil). Oxidation of Al^0 by Cu^{2+} and Pb^{2+} during leaching at low pH value causes a reductive cementation of Pb and Cu (Weibel et al., 2017), making these metals unavailable for recovery. In order to suppress reductive cementation, an oxidizing agent is often added.

In pursuit of a circular economy, the heavy metal recovery efficiency from FA needs to be further improved. Further optimization in the heavy metal recovery rates can either be achieved by modified process conditions or by excluding ash fractions with poor extraction properties (e.g. high acid neutralizing capacity (ANC), high Al^0 content or heavy metals bound in poorly soluble form). The EA, the first ash arising at the flue gas cleaning system, is already deposited together with the bottom ash in most plants. A further step towards optimizing the heavy metal recovery process could be the exclusion of BOA fractions with poor extraction properties. As data basis for evaluating whether a separation of material flows could be expedient for better heavy metal recovery rates, it is important to understand the geochemical differences between the different ash fractions (EA, BOA and ESPA). The major part of studies on MSWI FA analyze ashes from electrostatic precipitators (e.g. Gilardoni et al., 2004; Eighmy et al., 1995; Le Forestier and Libourel, 1998; Mahieux et al., 2010; Sandell et al., 1996). In contrast, relatively few studies have addressed the
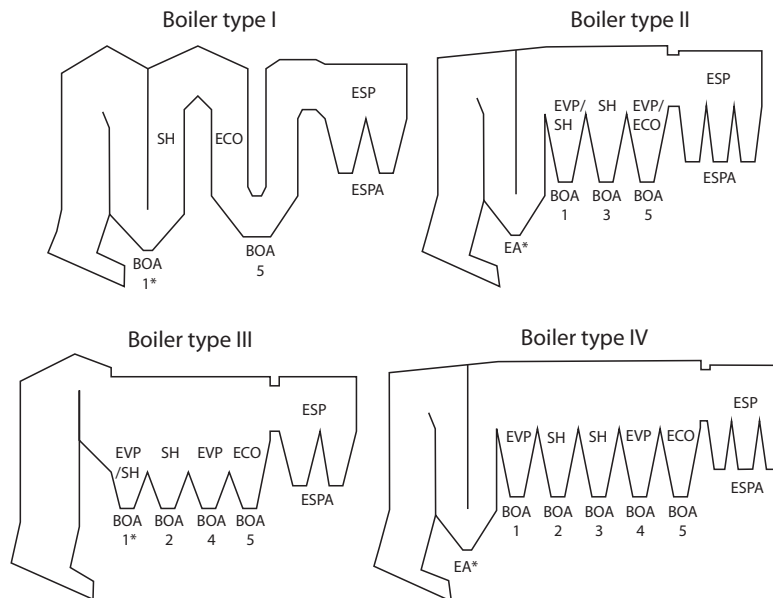
Figure 3.2: Scheme of the different boiler types considered in this study with indications on the function of the different parts. EVP = evaporator, SH = superheater, ECO = economizer, ESP = electrostatic precipitator. Ash fractions marked with * are disposed together with the bottom ash.

chemical and mineralogical characterization of MSWI BOA (De Boom and Degrez, 2015; Allegrini et al., 2014; Hsiao et al., 2006; Bodénan et al., 2010) or the characterization of different ash fractions from one plant (Keppert et al. 2012). Still, little is known about the characteristics of EA and about the differences in chemical and mineralogical composition of the ash fractions arising along the flue gas cooling path.

The present study focuses on a detailed chemical and mineralogical characterization of the different ash fractions arising along the flue gas cooling path. EA, BOA and ESPA were collected at 6 different MSWI plants in Switzerland. The investigated plants are equipped with boiler and electrostatic precipitator (ESP) as main dedusting system upstream of the flue gas scrubber (separate dust removal and neutralization). Using a broad combination of methods (XRF, XRD, SEM), the ashes were characterized with respect to the chemical and mineralogical composition of major- and minor phases. A special focus was laid on possible binding forms of the target heavy metals Zn and Pb. The ANC and the content of metallic aluminum (Al^0) were determined for each ash fraction as parameter to estimate the extraction behavior.

3.3 Materials and methods

3.3.1 Characteristics of investigated plants

The majority of MSWI plants currently in operation in Switzerland are equipped with an electrostatic precipitator as pre-deduster and a wet flue gas cleaning system downstream of the boiler (AWEL, 2013). Accordingly, the six investigated Swiss MSWI plants (A - F) have similar flue gas cleaning systems with boiler and electrostatic precipitator (ESP)

Plant-ID	Boiler type	N° of increments / sampling duration	T combustion chamber	T boiler inlet	T boiler outlet	Incinerated waste	Generated steam
			°C	°C	°C	(t/d)	(t/h)
Plant A	I	28 incr. / 14d	925	650	195	330	55
Plant B	II	35 incr. / 50d	900	590	260	355	58
Plant C	III	2 incr. / 6h	860	670	250	160	30
Plant D	IV	21 incr. / 7d	840	635	274	400	75
Plant E	IV	14 incr. / 14d	850	660	260	288	48
Plant F	IV	9 incr. / 68h	850	680	260	283	45

Table 3.1: Operation details of the investigated MSWI plants and details on the different sampling campaigns.

upstream of the flue gas scrubber, whereby dust removal and neutralization are performed separately. The plants A - E are equipped with a wet flue gas scrubber. Plant F is equipped with a dry flue gas scrubber and the neutralization residues are not collected with the FA but discharged separately. The plants show differences in boiler architecture (Figure 3.2), waste throughput capacity and operating conditions (Table 3.1). All plants incinerate municipal- as well as commercial- and industrial waste, partly also automobile shredder residues (ASR) and sewage sludge in small proportions (details in table A.1). The plant B incinerates mostly municipal waste (67%), while plant A incinerates increased amounts of industrial waste. For the other plants, the shares of municipal- and industrial waste are almost equal.

3.3.2 Estimation of mass flows

A gravimetric determination of the amount of BOA produced per boiler hopper was not possible in any of the plants. Thus, the mass flows could only be estimated. Most of the sampled plants use a system of rapping gears that operate periodically (every few hours) in order to clean the heat exchanger surfaces from deposits. It was observed that the amount of BOA arising per boiler hopper decreased towards the end of the boiler when sampling without the operation of the rapping gears. However, when sampling with the operation of the rapping gears, different quantity distributions per hopper were observed, depending on the amount of material accumulated on the heat exchanger tubes. The percentage of BOA and ESPA with respect to the FA was calculated by means of the chemical composition. By knowing the chemical composition of the FA, the mass fraction of BOA and ESPA could be calculated for each element by solving for the smallest deviation from the FA concentration. The resulting mass fractions were then averaged. This resulted in a share of BOA in relation to the total amount of FA of 25 - 30 wt.%. The quantity distribution within the boiler could not be determined because the chemical composition of the different BOA fractions was almost identical.

3.3.3 Chemical analysis

All ashes were dried at 105 °C to constant weight and ground to a particle size < 0.01 mm in a tungsten-carbide disk mill. Chemical composition of the matrix elements

was determined by wavelength dispersive X-ray fluorescence analysis (WD-XRF) using a Panalytical Axios spectrometer on pressed powder pellets (40 mm diameter, 6.40 g material and 1.44 g wax as binder). The same pellets were analyzed with a Spectro Xepos spectrometer (ED-XRF) with matrix adjusted calibration for the heavy metals of interest (Zn, Cd, Cu, Pb). TOC was analyzed externally according to DIN 19539 on the dried and fine ground ash fractions used for chemical analysis. The content of Al^0 in the ashes was calculated from H_2 gas volume determination during oxidation of Al^0 with H_2O + NaOH, as described in Zucha et al., (2020).

3.3.4   Mineralogical analysis

For mineralogical analysis, a mixture of ash material (4 g) and corundum (1 g) as internal standard was ground in a XRD-Mill McCrone from Retsch for 6 minutes at 55 Hz to a grain size of 1-10 μm. The disoriented samples were then measured using a PANalytical X'Pert Pro diffractometer (CuKα-radiation) from 5 to 60° 2θ at 0.017°/step for 40 min, with an acceleration voltage of 40 kV and an electron generating current of 40 mA. Rietveld refinements were performed with the TOPAS-Academic V6 software using the structural data (.cif files) of the Inorganic Crystal Structure Database (ICSD) as input.

3.3.5   Acid neutralizing capacity

Titration of the acid neutralizing capacity was performed on a mixture of ash (2 g) with 20 ml ultrapure water. The suspension was titrated in 40 steps using a 785 DPM Titrino device from Metrohm by adding 1 ml 1M HCl in intervals of 10 minutes under constant stirring.

3.3.6   SEM microscopy

SEM analyses were performed on a Zeiss EVO-50 XVP electron microscope (SEM) coupled with an EDAX Apollo X energy dispersive system (EDS). The ash samples were embedded in epoxy resin, polished water-free and coated with carbon to avoid surface charging. An acceleration voltage of 15 kV, high vacuum mode and a spot size of 504 nm were used for backscattered electron (BSE) images.

3.4   Results

3.4.1   Chemical composition

The evolution in bulk chemical composition of the ashes arising along the flue gas cooling path shows trends that are similar for plants A-E (Figure 3.3a). Elemental composition of EA and BOA are similar, but differ considerably from ESPA. BOA from plant F show a different trend in chemical composition and considerable differences in elemental concentrations and are therefore discussed separately. In EA and BOA, Ca is the most abundant element (> 200'000 mg/kg), followed by S (50 - 125'000 mg/kg). The EA and

BOA further show Cl and Si as main constituents, followed by Na, K, Fe, Al (detailed in Table A.2). The EA is thereby richer in Si, Al, Fe and lower in alkali, S, Cl than BOA. From BOA5 to ESPA, a major change in elemental composition can be observed, as there is a clearly visible drop in concentration of less volatile elements (Ca, Si, Al, Fe), complemented by a strong increase in more volatile elements (Cl, Na, K, Zn, Pb, Cu, Cd, Sb, Sn). The main constituents of ESPA are Cl, Ca, S, Na, K ($> 50'000$ mg/kg). Volatile heavy metals of economic interest (e.g. Zn, Cu, Sn) and potentially environmentally hazardous heavy metals (e.g. Pb, Cd, Sb) are highly enriched in ESPA compared to EA and BOA. Nevertheless, Pb- and Sb peaks are also present in BOA3. The BOA from plant F show considerably lower Ca, Cl, Si, Al concentrations than the BOA from the other plants, but higher S, Na, K, Zn, Pb, Sb, Sn concentrations. A drop in Ca and an increase in Na, K concentration is observable from the middle of the boiler on and there is a strong Pb peak for BOA3, with concentrations almost 5x higher than in ESPA. Zn concentration in BOA from the rear part of the boiler are similar or higher than the Zn concentrations in ESPA from the other plants.

The concentration in total organic carbon (TOC) is generally higher for EA and BOA than for ESPA, but show big variation between the different plants and among the different ash fractions. There is no trend observable towards a decrease in flue gas direction within EA and BOA. Similarly, for the content of Al^0, there is no clear trend observable towards a decrease in flue gas direction within EA and BOA, except for plant F (Figure 3.3b). Al^0 concentration in ESPA is significantly lower than in EA and BOA. Within EA and BOA from plant A-E, Al^0 concentrations vary between 2500 and 19'000 mg/kg, which represents 10 - 60 % of the total Al content.

The deposits which were sieved from EA and BOA are characterized by high concentrations in S, Ca, Na and K, similar to the ashes from plant F (Figure 3.4). Al, Fe, Si and Cl are present in minor concentrations. Only the deposits collected at the first boiler hopper from plants D and E show comparably high Cl concentrations. Zn, Pb, Cd concentrations are considerably higher in the deposits than in the corresponding BOA. Cu concentrations are equal or even lower in the deposits than in the bulk BOA.

3.4.2 Mineralogical composition

The evolution in mineralogical composition of the airborne ash particles from EA, BOA and ESPA is very similar for plants A - E. Therefore, mineralogical composition along the flue gas cooling path is only shown for 2 plants with different boiler architecture (Figure 3.5a,b) and for plant F, which shows different mineralogical composition (Figure 3.5c). EA and BOA show similar mineralogical composition (spectra in Figure A.1). The main components are anhydrite, silicates (e.g. the melilites gehlenite and akermanite, quartz and feldspars) and oxides (e.g. lime, hematite, perovskite). Calcite and chlorides (mainly halite) are also present in most EA and BOA, but in minor concentrations around 5 wt.%. The portion of amorphous and unidentified phases was calculated to be 40 – 50 %. The presence of amorphous or microcrystalline phases is clearly visible in the spectra by a
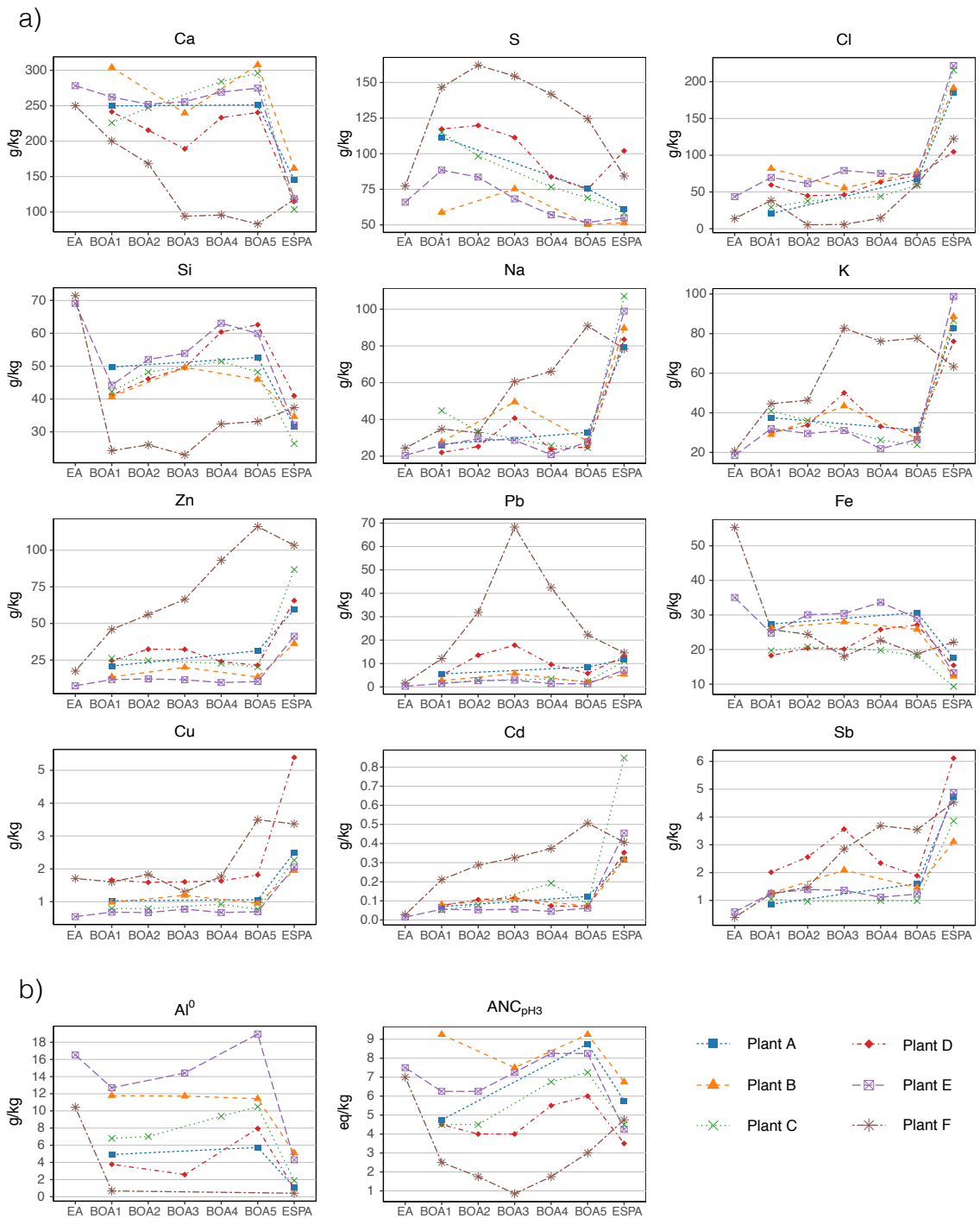
Figure 3.3: (a) Evolution of bulk elemental composition along the flue gas cooling path, from the EA to the ESPA. (b) Evolution of the parameters affecting leachability: Al^0 concentration and ANC at pH 3, which represent the pH conditions of acid leaching.
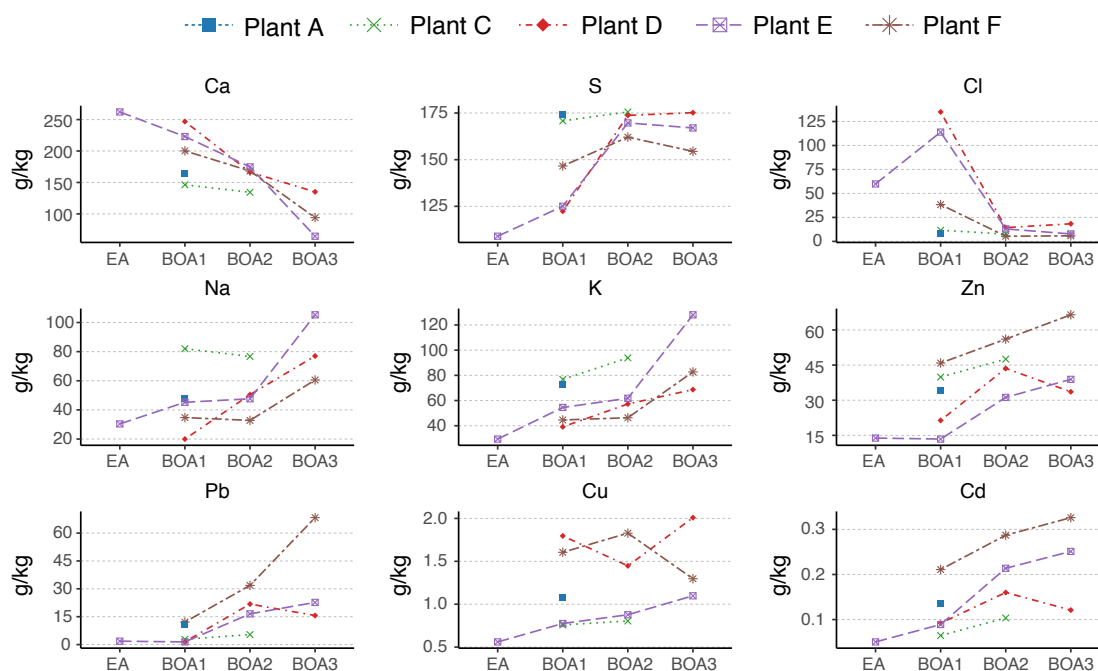
Figure 3.4: Elemental composition of the deposits from plants A, C, D and E which were separated from the airborne ash particles by sieving. For comparison, the elemental composition of BA from plant F is shown.

background bump in the range between 20 and 40° 2Theta.

The EA from plant F shows a similar mineralogical composition than the EA from plant E. However, BOA from plant F show similar mineralogy as the deposits from plant E (Figure 3.5c,d). The mineralogy is more sulfate-dominated and silicates represent minor constituents. There is a decrease in anhydrite concentration in flue gas direction, replaced by glauberite ($Na_2Ca(SO_4)_2$) as predominant sulfate from the middle of the boiler on. The complexity of the XRD spectra significantly increases from the 2nd to the 3rd boiler hopper, and associations of complex, possibly heavy metal bearing sulfate salts in minor concentrations are observed, displayed as "other sulfates". A major phase in that category is the Zn- and Cl bearing Na- sulfate d'ansite ($Na_{21}ZnCl_3(SO_4)_{10}$), which increases in concentration towards the end of the boiler and represents the only identified Cl-bearing phase. Other phases that increase towards the end of the boiler are K-bearing mixed sulfates (e.g. aphthitalite, alunite, K_2SO_4, K_2CaSO_4), which matches with the increase in K concentration from the 2nd to the 3rd pass. Pb sulfates (palmierite, anglesite), as well as Zn sulfates (K_2ZnSO_4, $ZnSO_4$) represent the heavy metal-bearing sulfates. Remarkably is the decrease in amorphous content in the ash from the last boiler hopper in BOA from plant F.

The ESPA are of different mineralogical composition than BOA and EA. The mineralogy is dominated by chlorides, matching the high Cl concentration. The spectra of the different ESPA is comparable (Figure A.1), but the absolute mineral concentrations vary from plant to plant. The mineralogy of the analyzed ESPA can be grouped into 3 types. ESPA from plant A, C and E show very high concentrations of halite (15 - 25 wt.%) and K_2ZnCl_4 (9 - 16 wt.%) and sylvite in minor concentrations. ESPA from plant D and
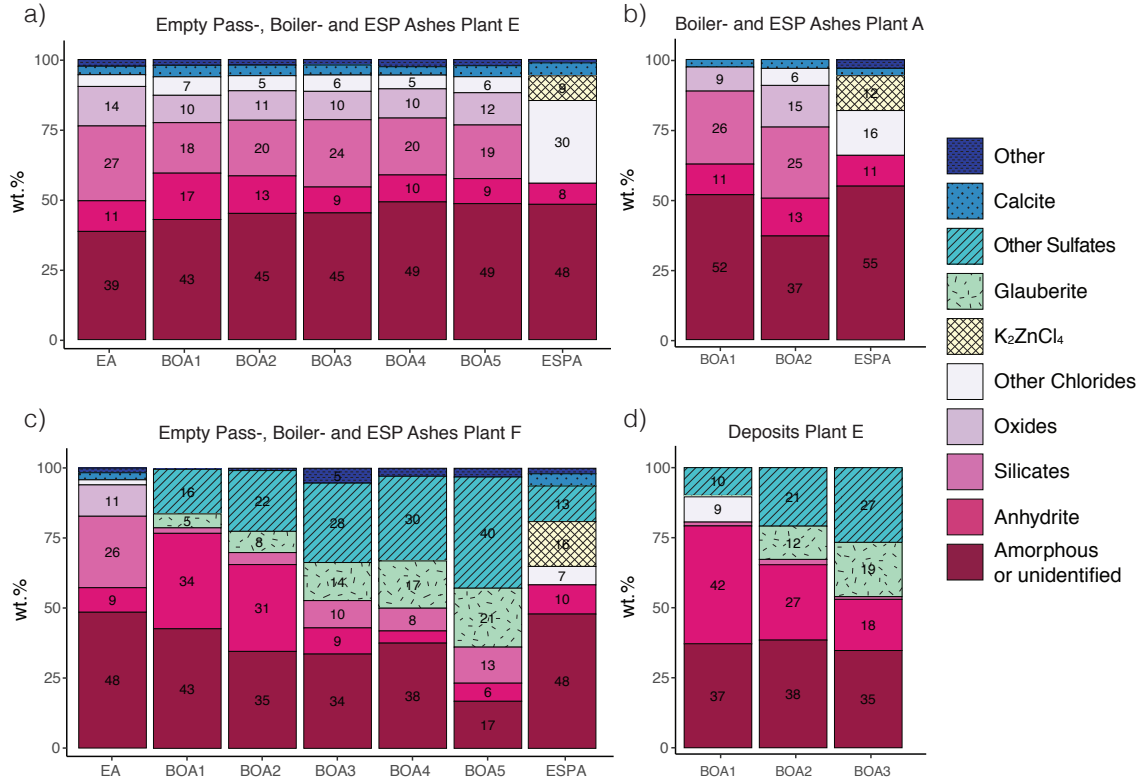
Figure 3.5: Evolution of mineralogical composition along the flue gas cooling path for airborne ash particles (a, b, c) and deposits (d) from the different incineration plants. Only concentrations > 5 wt.% are displayed as number.

F is characterized by high concentrations in K_2ZnCl_4 and d'ansite $(Na_{21}ZnCl_3(SO_4)_{10})$. Anhydrite and halite are present in concentrations around 10 wt.%. ESPA from plant B does not contain K_2ZnCl_4. Instead, sylvite, calcite and oxide concentration are elevated in ESPA from plant B compared to other ESPA. For ESPA, the calculated amount for amorphous phases is as high as for BOA (approximately 50%). Although melt droplets can occasionally reach the electrostatic precipitator, it has been observed by SEM investigations that ESPA is mainly composed of very fine crystals, probably too fine-grained ($\ll$ 1 µm) to be resolved by XRD. It is therefore assumed, that unidentified microcrystalline phases make up for the major part of the amorphous or unidentified fraction.

3.4.3   Acid neutralizing capacity

As a result of the low concentration in acid-buffering minerals (e.g. CaO, $CaCO_3$, Ca-silicates), ESPA shows lower ANC than EA and BOA (Figure 3.3b). ANC for EA and BOA are comparable and ANC of BOA from plant A-E show a slight increase towards the end of the boiler. For plant F, there is a significant drop in ANC from EA to BOA1. BOA from plant F show lower ANC than ESPA. The titration curves are shown in figures A.3 - A.8.

3.4.4 Morphology and particle chemistry

The morphological appearance of the airborne ash particles of EA and BOA is identical and only minor differences are identifiable between the different plants. The particle size distribution of EA and BOA varies from plant to plant, but remains relatively constant, with grain sizes ranging from 10 to 500 μm. It can be observed, that EA and BOA consist of three different phase types: refractory particles as well as newly formed particles in amorphous and crystalline form. The rounded shaped, porous amorphous phases represent a major part of the particles. These are mainly Fe- and Al- bearing Ca-silicates, which often contain to a lesser extent Mg, P, Ba or Ti. The chemical composition, as well as the shape and the porosity of the amorphous silicates vary broadly from particle to particle, and also compositional heterogeneities are observed within the particles. The characteristic dust rim covering the ash particles, which was previously observed in FA (Weibel et al., 2017), is not present in the BOA. However, the refractory particles often occur fully or partly covered with an amorphous or secondary formed fine crystalline phase. Among the observed refractory particles are rather inert minerals as quartz or feldspars and phases affecting the leaching behavior, as calcite and Al-foil (Figure 3.6a,b). The calcite shows marginal decomposition features by loss of CO_2. Heavy metal enriched phases were mainly observed as segregation on amorphous silicate phases in BOA. They are often associated with Fe oxides close to the composition of hematite (Fe_2O_3) that segregate from amorphous particles, as also observed by other authors (Kutchko and Kim, 2006; Weibel et al., 2017). Ba, Ti, Ni, Cr and Zn were also found to be minor constituents of the Fe oxides. Figure 3.6c shows such a coexistence of hematite and zinc ferrite (Fe_2ZnO_4) – a phase often observed in dusts from steel plants (Antrekowitsch et al., 2008). Zinc was also observed to be present as ZnO (Figure 3.6d) and Zn_2SiO_4 around quartz particles (Figure 3.6e). The observed newly formed phases are predominantly anhydrite and halite. They are found in large agglomerates, which can enclose amorphous melt droplets or refractory minerals. Often, complex mixed sulfates are found with large (Na,K)-$PbSO_4$ crystals, which were identified as fragments of deposits (Figure 3.7b).

The BOA from plant F formed concentrically around the heat exchanger surfaces in direction of flue gas, with a dendritic appearance (Figure 3.7a). Airborne ash particles accumulate between the "fingers". The formation of the large (Na,K)-$PbSO_4$ crystals in parallel layers is well visible. Locally, the (Na,K)-$PbSO_4$ is formed antiparallel to the layering, which indicates migration and recrystallisation within the deposit. Crust fragments from plant D contain the same large (Na,K)-$PbSO_4$ crystals, as well as a Zn-bearing Na,K-sulfate matrix (Figure 3.7b). The characteristic co-existence of sulfate matrices with different composition (e.g. $CaSO_4$ with (K)-Na_2SO_4) is shown in Figure 3.7c. Also more complex matrix compositions close to the composition of $K_2Na_8Ca(SO_4)_6$, $K_2Na_2Zn(SO_4)_2$ or $Na_2K_2CaZn(SO_4)_4$ were observed. ESPA shows different morphology than EA and BOA, characterized by very fine newly condensed crystals in the sub-micron scale (Figure 3.7d), with the strong tendency of the individual ash particles to form agglomerates. Refractory minerals (e.g. quartz, calcite) can be observed, which are often partly covered
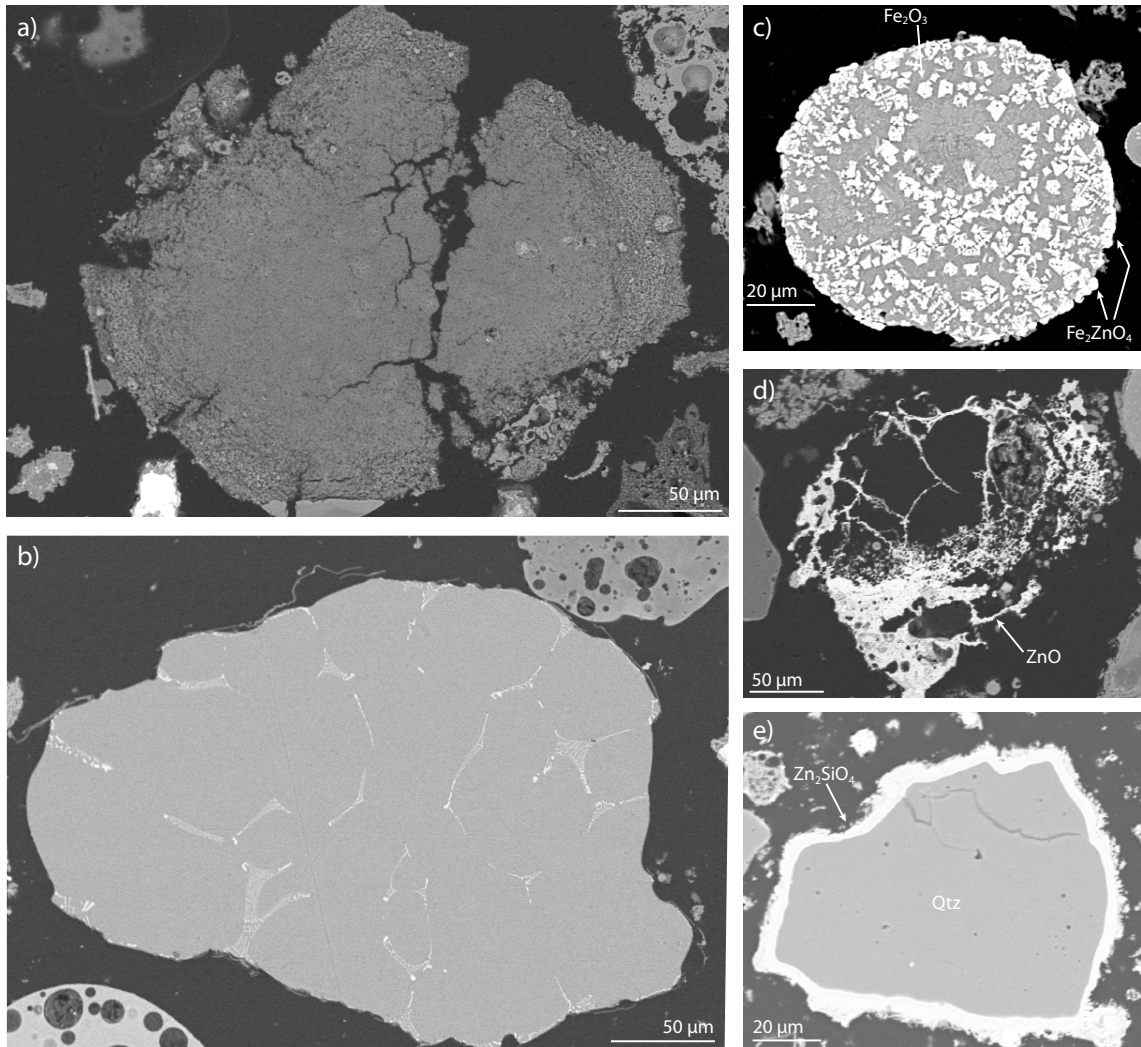
Figure 3.6: Backscattered electron (BSE) images of refractory phases in BOA: calcite (a) and Al-foil (b), and different newly formed Zn phases observed in BOA c) – e).

with the fine-grained salt crystals. Small Al-foil fragments and melt droplets were observed in minor quantities. The EDX mapping (Figure A.2) of the particle agglomerate in Figure 3.7e shows at this resolution a very homogeneous chemical composition over the entire particle agglomerate. The fine-grained ash particle matrix is composed of N, S, Ca, Zn, S, Cl and represents mixed chlorides and sulfates. $PbSO_4$ is distributed more punctually over the particle agglomerate, visible by the bright spots. The strong potential for particle agglomeration of ESPA and the very fine-grained nature of the ESPA complicates its characterization.

3.5 Discussion

3.5.1 Element partitioning and formation of the different ash fractions

The distribution of the chemical compounds along the cooling path is controlled by transport distance and formation mechanism. The fact that the Ca-, Si-, Fe-, Al-bearing glass- and refractory particles are mainly observed in EA and BOA suggests, that these particles are entrained with the flue gas and subsequently settle as they are transported through the empty pass and the boiler. However, refractory particles and melt droplets occasionally reach the electrostatic precipitator, which explains the presence of Ca and Si in ESPA. Elements which form volatile compounds with high vapor pressures (e.g chlorides and sulfates) are observed to travel further until they precipitate at the ESP. The alkali metals Na, K and the heavy metals Zn, Pb, Cd are mainly observed in newly formed particles in the ESPA, which suggests that they are transported as gaseous compounds (e.g. as chlorides or sulfates). The distribution of the elements along the flue gas cooling path from this study fits well the observations made by Belevi and Moench (2000) and Morf et al., (2000) – even though they analyzed the BOA as a whole, not divided into the different fractions. It is further assumed, that the characteristic dust rims around glass- and refractory particles observed by Weibel et al., (2017) in FA represents ESPA. This would fit to the measured chemical composition of the dust rim, being rich in Cl, Zn, S, Na, K. The accumulation of ESPA around the bigger BOA grains could either result from impact milling or during storage, regarding the strong potential for particle agglomeration around bigger grains (Figure 3.7e).

Fluctuations in the bulk elemental composition of EA and BOA are related to the amount of deposits contained in the ashes. The fact, that the deposits show higher heavy metal concentrations than the corresponding BOA shows that most heavy metals (especially Zn, Pb, Cd, Sb, Sn) tend to accumulate in the deposits rather than in the airborne BOA. Thus, the increased heavy metal contents in the BOA are mainly caused by the presence of the heavy metal enriched deposits. The macroscopic and microscopic appearance of the ashes from plant F (light brown, crumbly chunks), as well as the similar chemical and mineralogical composition, suggests that the BOA from plant F are mainly composed of heat exchanger deposits. As the EA from plant F is chemically and mineralogically similar the EA and BOA from the other plants, it is assumed, that a major part of the
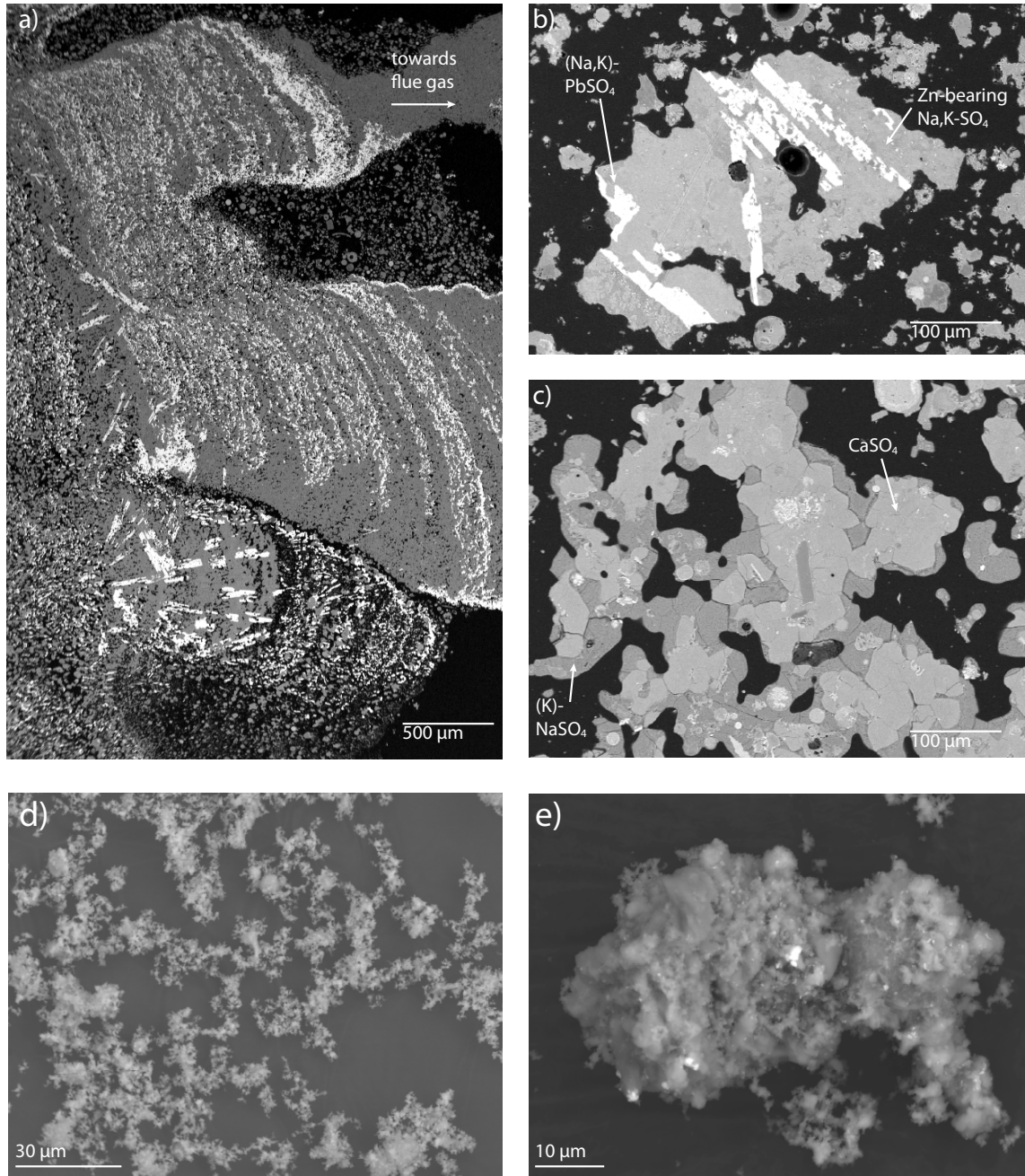
Figure 3.7: Backscattered electron (BSE) images of deposits (a - c) and ESPA (d - e). Deposit-like BOA from plant F (a), particle piece of a deposit from plant D rich in $PbSO_4$ (b), coexistence of different matrix compositions (c). Individual particles (d) and particle agglomerate (e) of ESPA.

airborne ash particles of plant F already settle from the flue gas in the empty pass.

The condensation of volatile species on the walls and heat exchanger surfaces seems to be induced by locally favorable conditions. Due to the high Na, K, S concentration in the flue gas, it is mainly alkali sulfates that condensate on the walls and heat exchanger surfaces. It was observed that the formation of alkali sulfates occurred after oxidation from SO_2 to sulfate which induced subsequent nucleation of alkali sulfates during cooling of the flue gas (Jensen et al., 2000). In some of the investigated incineration plants it was also observed that with increasing time from the last revision there was a shift of the S load in the boiler area from back to front, probably due to the deposits on the boiler walls and between the heat exchanger surfaces, which served as nucleation surface for supersaturated S compounds in the flue gas. It is therefore assumed that deposits are initially formed by local supersaturation due to the large temperature gradients between the hot flue gas and the tube surface. As soon as some layers of deposits exist, the temperature gradient decreases, but the nucleation area increases enormously, which favors the condensation of sulfate compounds. The coexistence of different sulfate matrices in the deposits might reflect differences in flue gas composition with time, resulting in a variation in composition of the condensates. Accordingly, high Zn vapor pressures may lead to the incorporation of Zn in the alkali sulfates. The conditions in the area of the superheater tubes seem to favor the condensation of $PbSO_4$, as the deposits grown on superheater tubes show the highest Pb concentration observed. The presence of $PbSO_4$ antiparallel to the layering (Figure 3.7a) indicates, that recrystallisation processes occur within the deposits. In such deposits, sulfation reactions may occur which take place on the deposit surface, as well as inside the deposit (Grabke et al., 1995). Within these sulfation reactions, condensed chlorides are transformed to sulfates by substitution of the anion. The sulfation reactions are important for corrosion processes, since the transformation of chlorides to sulfates liberates the highly corrosive Cl and enables it to travel towards the boiler tube. There, it can attack the steel tubes and form $FeCl_2$ on the tube surface. The migration of the Cl toward the boiler tube through sulfation reactions could also explain the low Cl concentrations in the deposits because only the outer layer of the deposit is removed by the operation of the rapping gears.

3.5.2 Mineralogy and effects on extractability

The mineralogical composition of the EA, BOA and ESPA strongly influences the ANC. An interesting finding is the presence of calcite particles with decomposition features, as shown in Figure 3.6a. This indicates that calcites were carried with the flue gas as refractory particles rather than that they formed secondarily from CaO. Decomposition of carbonates starts from 700 °C, but a fair number of calcites seem to persist the high temperatures. Although melilite concentrations of up to 15 wt.% were identified with XRD in the BOA, neither gehlenite nor akermanite was observed by SEM. This suggest, that these minerals are present as very fine grained, newly formed crystals, that are readily available for dissolution. As a result of the high content in calcite and Ca-silicates in EA

and BOA from plants A-E, ANC is significantly higher than in the BOA from plant F. The evolution of ANC along the flue gas cooling path stands in relation to the amount of deposits arising at the different boiler hoppers. The presence of deposits in EA and BOA results in a dilution of the strongly pH buffering ash matrix, yielding a lower ANC, since they consist mainly of sulfate salts with negligible pH buffering capacity. With decreasing amount of deposits arising in the BOA towards the end of the boiler, the ANC rises. The ashes from plant F showed a very low ANC, as they are predominantly composed of low acid-buffering sulfates. In contrast to the deposits, where Ca is mainly present as sulfates, ESPA also contains $CaCO_3$ and possibly amorphous Ca-silicates to a minor extent, which explains the higher ANC. Al represented the only identified metal in metallic form observed in EA, BOA and ESPA. Although it is likely that especially larger Al-foil particles are not transported far and settle shortly after leaving the combustion chamber, there was no trend observable that Al^0 concentration was higher in the EA or in the BOA from the first hoppers after the combustion chamber.

3.6 Conclusion

The obtained results provide important insights into the formation of the different ash fractions and its geochemical characteristics. Quenched melt droplets and refractory particles entrained by the flue gas mainly settle in the empty pass and along the boiler, whereas elements which form volatile compounds travel within the flue gas until the electrostatic precipitator, where a major part of the gaseous compounds condensate as ESPA. EA and BOA showed comparable bulk chemical and mineralogical composition. They were found to be composed of two significantly different materials: the airborne ash particles and deposits formed on the walls and heat exchanger surfaces. For the heavy metals of interest (Zn, Pb, Cu, Cd), only Zn bearing phases were found in the airborne particles of the BOA (as ZnO, Zn_2SiO_4 as rim around refractory particles, and also as segregations from amorphous phases (e.g. Fe_2ZnO_4)). It is mainly the deposits that contribute to the elevated heavy metal concentration, explained by the well-developed, large $(Na,K)-PbSO_4$ crystals and the Zn-bearing matrix sulfates. The variation in the amount and chemical composition of the deposits controls the fluctuations in the bulk composition of EA and BOA. ESPA differed considerably in chemical and mineralogical composition from EA and BOA. The ESPA is enriched in the heavy metals Zn, Pb, Cu, Cd and Sn, which are mainly incorporated in newly formed chlorides and sulfates.

Among ESPA, EA and BOA, the ESPA has the highest heavy metal concentrations. It is therefore ESPA that contribute to the elevated heavy metal concentrations in FA – and the fact, that FA is composed of 70 - 75% ESPA. The high ANC and Al^0 content in EA and BOA will result in a higher consumption of neutralizing chemicals during acid leaching compared to ESPA. In addition, ESPA shows much higher concentrations in the heavy metals of interest (Zn, Cd, Cu, Pb), predominantly in the form of easily soluble salts. These observations suggest that individual treatment of ESPA has higher potential for heavy

metal recovery. Comparing the EA and BOA, however, no significant differences could be found in the parameters affecting extractability. Therefore, no conclusive recommendation can be made as to which BOA fractions could be excluded from the acid leaching process. The mass flows could be considered as indicative criteria for excluding ash fractions, as comparatively little material is produced from the rear hoppers of the boiler.

Further optimization of the metal recovery could be achieved with a better understanding of thermodynamic and chemical equilibria along the gas cooling path. Geochemical modelling may help to reveal thermodynamic and kinetic factors controlling the formation of deposits and the geochemical interactions occurring during flue gas cooling. The application of higher-resolution instruments is suggested for a more detailed characterization of ESPA and for the investigation of possible binding partners of Cu and Cd.

Acknowledgements

3.7 References

Abanades, S., Flamant, G., Gagnepain, B., Gauthier, D., 2009. Fate of heavy metals during municipal solid waste incineration. Waste Manag. Res. 20, 55–68. https://doi.org/10.1177/0734242x0202000107

Allegrini, E., Jansson, S., Lundtorp, K., Fruergaard Astrup, T., 2014. Quality and generation rate of solid residues in the boiler of a waste-to-energy plant. J. Hazard. Mater. 270, 127–136. https://doi.org/10.1016/j.jhazmat.2014.01.048

Antrekowitsch, J., Griessacher, T., Offenthaler, D., Schnideritsch, H., 2008. Charakterisierung und Verhalten von Zink-, Blei- und Halogenverbindungen beim Recycling von Elektrolichtbogenofenstäuben. Berg- und Hüttenmännische Monatshefte, 153(5), 182–188. https://doi.org/10.1007/s00501-008-0372-7

Amt für Abfall, Wasser, Energie und Luft (AWEL), 2013. Stand der Technik für die Aufbereitung von Rauchgasreinigungsrückständen aus Kehrichtverbrennungsanlagen.

Belevi, H., Moench, H., 2000. Factors determining the element behavior in municipal solid waste incinerators. 1. Field studies. Environ. Sci. Technol. 34, 2501–2506. https://doi.org/10.1021/es991078m

Bodénan, F., Guyonnet, D., Piantone, P., Blanc, P., 2010. Mineralogy and pore water chemistry of a boiler ash from a MSW fluidized-bed incinerator. Waste Manag. 30, 1280–1289. https://doi.org/10.1016/j.wasman.2010.01.020

Bundesamt für Umwelt (BAFU), 2019. Vollzugshilfe für die «Rückgewinnung von Metallen aus den Filteraschen von Kehrichtverwertungsanlagen». Bundesamt für Umwelt, Bern. Umwelt-Vollzug Nr.1826: 21 S.

Bühler, A., Schlumberger, S., 2010. Schwermetalle aus der Flugasche zurückgewinnen. Saure Flugaschewäsche FLUWA-Verfahren- ein zukunftsweisendes Verfahren in der Abfallverbrennung. KVA-Rückstände der Schweiz. Der Rohstoff mit Mehrwert (Bundesamt für Umwelt BAFU) 185–192.

De Boom, A., Degrez, M., 2015. Combining sieving and washing, a way to treat MSWI boiler fly ash. Waste Manag. 39, 179–188. https://doi.org/10.1016/j.wasman.2015.01.040

Eighmy, T.T., Eusden, D.J., Krzanowski, J.E., Domingo, D.S., Staempfli, D., Martin, J.R., Erickson, P.M., 1995. Comprehensive Approach toward Understanding Element Speciation and Leaching Behavior in Municipal Solid Waste Incineration Electrostatic Precipitator Ash. Environ. Sci. Technol. 29, 629–646. https://doi.org/10.1021/es00003a010

Gilardoni, S., Fermo, P., Cariati, F., Gianelle, V., Pitea, D., Collina, E., Lasagni, M., 2004. MSWI fly ash particle analysis by scanning electron microscopy-energy dispersive X-ray spectroscopy. Environ. Sci. Technol. 38, 6669–6675. https://doi.org/10.1021/es0494961

Grabke, H.J., Reese, E., Spiegel, M., 1995. The effects of chlorides, hydrogen chloride, and sulfur dioxide in the oxidation of steels below deposits. Corros. Sci. 37, 1023–1043. https://doi.org/10.1016/0010-938X(95)00011-8

Hsiao, M.C., Wang, H.P., Chang, J.E., Peng, C.Y., 2006. Tracking of copper species in incineration fly ashes. J. Hazard. Mater. 138, 539–542. https://doi.org/10.1016/j.jhazmat.2006.05.087

Jakob, A., Stucki, S., Struis, R.P.W.J., 1996. Complete heavy metal removal from fly ash by heat treatment: Influence of chlorides on evaporation rates. Environ. Sci. Technol. 30, 3275–3283. https://doi.org/10.1021/es960059z

Jensen, J.R., Nielsen, L.B., Schultz-Møler, C., Wedel, S., Livbjerg, H., 2000. The nucleation of aerosols in flue gases with a high content of alkali - A laboratory study. Aerosol Sci. Technol. 33, 490–509. https://doi.org/10.1080/02786820050195340

Keppert, M., Pavlik, Z., Tydlitat, V., Volfova, P., Svarcova, S., Syc, M., Cerny R, 2012. Properties of municipal solid waste incineration ashes with respect to their separation temperature. Waste Manag. Res. 30, 1041-1048. https://doi.org/10.1177/0734242X12448513

Kutchko, B.G., Kim, A.G., 2006. Fly ash characterization by SEM-EDS. Fuel 85, 2537–2544. https://doi.org/10.1016/j.fuel.2006.05.016 Le Forestier, L., Libourel, G., 1998. Characterization of flue gas residues from municipal solid waste combustors. Environ. Sci. Technol. 32, 2250–2256. https://doi.org/10.1021/es980100t

Mahieux, P.-Y., Aubert, J.-E., Cyr, M., Coutand, M., Husson, B., 2010. Quantitative mineralogical composition of complex mineral wastes – Contribution of the Rietveld method. Waste Manag. 30, 378–388. https://doi.org/10.1016/j.wasman.2009.10.023

Morf, L.S., Brunner, P.H., Spaun, S., 2000. Effect of operating conditions and input variations on the partitioning of metals in a municipal solid waste incinerator. Waste Manag. Res. 18, 4–15. https://doi.org/10.1034/j.1399-3070.2000.00085.x

Quina, M. J., Santos, R. C., Bordado, J. C., Quinta-Ferreira, R. M., 2008. Characterization of air pollution control residues produced in a municipal solid waste incinerator in Portugal. J. Hazard. Mater. 152, 853-869. doi:10.1016/j.jhazmat.2007.07.055

Quina, M. J., Bontempi, E., Bogush, A., Schlumberger, S., Weibel, G., Braga, R., Funari, V., Hyks, J., Rasmussen, E., Lederer, J., 2018. Technologies for the management of MSW incineration ashes from gas cleaning: New perspectives on recovery of secondary raw materials and circular economy. Sci. Tot. Env. 635. 526 – 542. https://doi.org/10.1016/j.scitotenv.2018.04.150

Sandell, J.F., Dewey, G.R., Sutter, L.L., Willemin, J.A., 1996. Evaluation Of Lead-Bearing Phases In Municipal Waste Combustor Fly Ash. J. Environ. Eng.

Schlumberger, S., Schuster, M., Ringmann, S., Koralewska, R., 2007. Recovery of high purity zinc from filter ash produced during the thermal treatment of waste and interting of residual materials. Waste Manag. Res. 25, 547–555.

Swiss Federal Council, 2015. Ordinance on the Avoidance and the Disposal of Waste. (Waste Ordinance, ADWO). (Status of 1 April 2020).

Verhulst, D., Buekens, A., Spencer, P.J., Eriksson, G., 1996. Thermodynamic behavior of metal chlorides and sulfates under the conditions of incineration furnaces. Environ. Sci. Technol. 30, 50–56. https://doi.org/10.1021/es940780+

Weibel, G., Eggenberger, U., Schlumberger, S., Mäder, U.K., 2017. Chemical associations and mobilization of heavy metals in fly ash from municipal solid waste incineration. Waste Manag. 62, 147–159.

Weibel, G., Zappatini, A., Wolffers, M., Ringmann, S., 2021. Optimization of Metal Recovery from MSWI Fly Ash by Acid Leaching: Findings from Laboratory- and Industrial-Scale Experiments. Processes. 9, 352. https:// doi.org/10.3390/pr9020352

Zucha, W., Weibel, G., Wolffers, M., Eggenberger, U., 2020. Inventory of Municipal Solid Waste Incineration Fly Ash in Switzerland: Heavy Metal Recovery Potential and their Properties for Acid Leaching. Processes. 8, 1668. https://doi:.org/10.3390/pr8121668

Chapter 4

New insights into the genesis of MSWI fly ash through thermodynamic modeling

M.Wolffers[a], D. A. Kulik[b], G. D. Miron[b], U. Eggenberger[a], S. V. Churakov[a,b]

[a] Institute of Geological Sciences, University of Bern

[b] Laboratory for Waste Management, Paul Scherrer Institute

4.1 Abstract

Thermodynamic simulations of the cooling of the flue gas in a MSWI incinerator plant were performed in order to gain more insights into the stability fields of possible coexisting phases and binding partners of heavy metals in the fly ash. The simulations include the cooling of a fixed flue gas composition to investigate stability fields of solid phases, as well as dynamic simulations (a megasystem box flux model) where the flue gas composition is allowed to change with subsequent cooling by phase precipitation. There, assumptions on transport mechanisms had to be made based on field observations. Different flue gas compositions (variations in HCl, SO_2, O_2 concentration) were calculated to study the effects on phase assemblages. Of special interest were the effects of changes in temperature and gas composition on the formation of heavy metal bearing phases. It could be confirmed, that variations in the S/Cl ratio of the flue gas have greater impact on the equilibrium phase assemblages than variation in the O_2 content. For scenarios where S/Cl ratio < 1, Zn was predicted to be stable as ZnO, Fe_2ZnO_4, Zn_2SiO_4 at temperatures > approximately 300 °C (depending on HCl concentration) and as $ZnCl_2$ below this temperature. Cu was predicted to be stable as oxide at temperatures from 300 °C downwards and as $CuCl_2$ below, while Cd and Pb were predicted to be stable as chlorides from 425 °C. At molar S/Cl ratio > 1 the solids are predicted to be dominated by sulfates and the heavy metals were predicted to precipitate as sulfates already at 600 - 750 °C. The dynamic simulations using the box flux model resulted in reasonable predictions of mass streams. The assumed distinct transport mechanisms for refractory minerals and precipitated salts turned out to reproduce comparable mineralogical compositions to previously characterized ash fractions. In particular, the alkali chlorides were predicted to start forming in the boiler area at

750 °C, but were allowed to travel in suspension in the flue gas until they reached the electrostatic precipitator, resulting in a major share in the ESPA. The results confirm, that the transport mechanisms play an important role for the ash mineralogy. The created model scenarios further help to better understand the ash forming processes during cooling of the flue gas and provide information on possible mineral assemblages too fine grained or low concentrated to be detected by XRD or SEM.

4.2 Introduction

Thermal waste treatment leads to accumulation of volatile heavy metals in the fly ash and their recovery makes a valuable contribution to the sustainable closure of material cycles, as metals from primary raw material mining can partly be substituted. During incineration at 800 - 1'000 °C, volatile waste compounds with high vapor pressures and low boiling points are transformed into the gas phase that form the flue gas together with entrained dust particles. High combustion temperatures and elevated chlorine and sulfur concentrations thereby favor the transfer of heavy metals to the gas phase (Abanades et al., 2002; Verhulst et al., 1996). The hot flue gas leaves the combustion chamber to flow along the 2 nd and 3 rd pass (also called empty pass) towards the boiler, which is equipped with heat exchanger tubes (Figure 4.1a). As it passes through the boiler, the flue gas is cooled from around 650 °C to 250 °C. The boiler primarily acts as heat recovery section, but also serves as a dust separator for coarse particles. This produces the so-called boiler ash (BOA) which arises in different fractions. At 250 °C the flue gas enters the electrostatic precipitator, where dust or aerosol particles suspended in the gas are electrically charged and separated at precipitation electrodes which are periodically rapped in order to release the accumulated dust (electrostatic precipitator ash (ESPA)) to the dust collection funnels. The BOA and ESPA are usually collected together and referred to as fly ash (FA). Gaseous compounds (e.g. HCl, SO_2) are removed from the flue gas in a subsequent dry, semi-dry or wet flue gas cleaning step, before the clean gas (N_2, CO_2 and H_2O) is emitted through the chimney.

The recovery of heavy metals from MSWI fly ash will be mandatory in Switzerland from the year 2026 on (Swiss Federal Council, 2015). The FLUWA process (Bühler and Schlumberger, 2010) represents the state-of-the-art process for acid leaching, whereby the heavy metals are dissolved from the fly ash at acidic, oxidizing conditions and later precipitated into hydroxide sludge in order to be recovered by the FLUREC process (Schlumberger et al., 2007). A filter cake with reduced heavy metal content remains, which is deposited on landfills. On average, the following extraction rates can be achieved: 75% Zn, 75% Pb, 60% Cu, 90% Cd (AWEL, 2013). Despite the decent extraction rates, still considerable amounts of e.g. Pb, Zn and Cu remain in the filter cake and are deposited on landfills. Furthermore, the potentially environmentally harmful element Sb is not mobilized during the FLUWA process and accumulates in the filter cake. Since the solubility of heavy metals is strongly dependent on their binding form, detailed knowledge of the heavy metal

binding form in the fly ash is required to evaluate conditions where the accessible heavy metal mobilization can be enhanced.

Numerous studies have already been conducted to investigate the binding forms of heavy metals in MSWI FA (e.g. Bayuseno and Schmahl 2011; Weibel et al., 2017) and it was shown that the characterization of the individual ash fractions is expedient to better understand the material compared to the characterization of the fly ash mix (Wolffers et al., 2021). However, conventional methods such as powder X-ray diffraction (XRD) or secondary electron microscope (SEM) reach their limits when concentrations are low and grain sizes very small. Wet chemical methods for speciation of heavy metals in fly ash may be error prone as matrix interferences often occur (Funatsuki et al., 2012). The MSWI fly ashes are very complex materials to characterize due to their low grain size ($<$200 μm to submicron scale), their complex mineralogy and the fact that only about 50% of their components consist of crystalline phases due to the short residence time in the combustion chamber and the relatively rapid cooling. Further, heavy metals of interest such as Cu and Sb are present in low analytical concentrations (10^2 - 10^3 ppm), which also complicates the characterization.

A complementary approach by means of thermodynamic modelling was therefore applied in this study to better understand the ash-forming processes occurring during cooling of the flue gas and to gain more insight into the stability fields of possible coexisting phases and binding partners of heavy metals. The performed simulations include batch simulations, where the cooling of a fixed flue gas composition was calculated, as well as dynamic reactive transport simulations (box flux megasystem model) where the moving flue gas composition is allowed to change with subsequent cooling and phase precipitation. There, assumptions on flux rates and transport mechanisms had to be made and the obtained results could be directly compared to previous results from characterized ash fractions described in Wolffers et al., (2021). For both approaches, different flue gas compositions (reference state and variations in HCl, SO$_2$, O$_2$ concentration) were calculated to study their effect on phase assemblages. Of special interest were the effects of changes in temperature and gas composition on the formation of heavy metal bearing phases to gain insights into possible mineral associations too fine grained or low concentrated to be detected by XRD. The data are a promising complement to other characterization methods of the binding partners of the heavy metals (e.g. XRD, SEM, wet chemical methods).

4.3 Thermodynamic modeling

4.3.1 Thermodynamic modeling with GEM-selektor code

The thermodynamic calculations were performed by the method of Gibbs Energy Minimization (GEM), using the GEM-Selektor code package (Kulik et al., 2013; Wagner et al., 2012; http://gems.web.psi.ch). In GEMS, the input elemental bulk composition of the system is split into amounts of phases assuming the principle of local/partial equilibria at ambient pressure (1 bar) and various temperatures. The gas phase at such conditions

could be represented as an ideal mixture of ideal gases. For each substance (gas, liquid, solid), the standard Gibbs energy value at temperature and pressure of interest must be provided from the thermodynamic database.

4.3.2 Thermodynamic database

The IVTANTERMO thermodynamic database (Gurvich et al., 1982) was imported into GEMS format and complemented with molar volumes for the solid phases (Tables B.1 - Tables B.8), obtained from different sources (Barthelmy, 1997; Bergerhoff and Brown, 1987; Hudson Institute of Mineralogy; Jain et al., 2013). The thermodynamic data was checked against other available databases for consistency. The standard-state values of Gibbs energy or enthalpy of substances are usually given at reference pressure (1 bar or 1 atm) and temperature (298.15 K or 25 °C). For correction to elevated temperatures, the value of (absolute) entropy $S°$ at 298.15 K and the function of isobaric heat capacity vs. temperature $C_p° = f(T)$ are necessary. The most common form of $C_p° = f(T)$ is the polynomial function of temperature (Maier and Kelly, 1932). In IVTANTERMO, the following form is used (4.1):

$$C_p° = a_0 + a_1 T + a_2 T^{-2} + a_3 T^{-0.5} + a_4 T^2 \tag{4.1}$$

The polynomial coefficients are valid only in a given temperature interval; more than one of such intervals (and sets of polynomial coefficients) may be provided for a substance, e.g. if phase transitions are present. In some cases, different sets gave incorrect results at elevated temperature. In most cases, it was possible to find equivalents from the Holland-Powell database (Holland and Powell, 1998) and replace the $C_p° = f(T)$ function, otherwise the substance was not included into the chemical system. Thermodynamic data for relevant additional solids were collected from literature (Reed, 1989; Stulova et al., 1974; van Miltenburg et al., 1994) and were added as separate database. Due to missing experimental values for the majority of additional substances, the thermodynamic data (C_p, S, H) was estimated using predictive thermodynamic approaches (Glasser and Jenkins, 2016). As the phases of interest were often double or triple salts from substances contained in IVTANTERMO, their thermodynamic parameters could be estimated using the simple salt approximation (SSA) (Glasser and Jenkins, 2016; Yoder and Flora, 2005). With this method, the missing thermodynamic properties of the double or triple salts could be estimated through stochiometric additivity of the thermodynamic properties (C_p, S, H) of their simple salt constituents (results listed in Table B.10).

The chemical composition of the amorphous glass phase could be estimated on the basis of previous findings (Wolffers et al., 2021), as listed in Table 4.3. The thermodynamic properties of the amorphous glass phase were estimated in trial GEM calculations, based on the chemical potential of elements in the system.

4.3.3 Kinetic constraints

Along with nitrogen and oxygen, the sulfur dioxide gas $SO_2(g)$ is a major component of the flue gas. However, the uncatalyzed oxidation of $SO_2(g)$ is known to be very slow even at elevated temperatures (Belo et al., 2014; Christensen et al., 1998; Cullis et al., 1966; Glarborg and Marshall, 2005) and the oxidation rate of $SO_2(g)$ is known to be the limiting factor of alkali sulfate formation (Glarborg and Marshall, 2005; Jiménez and Ballester, 2007, 2005). For these reasons, it was necessary to set a kinetic constraint on the oxidation of $SO_2(g)$ in order to prevent unrealistically high oxidation rates of $SO_2(g)$. In GEMS software, metastability and kinetics can be simulated for any component using the upper- or lower additional metastability restrictions (AMR) for the mole amount of that component (Kulik et al., 2013). In a stepwise simulation, AMRs can be set as functions of time, temperature, activities of other components etc. according to kinetic laws. In this study, according to field observations, the amount of $SO_2(g)$ component in the gas phase was constrained by AMR from below according to 4.2:

$$n_q(SO_2(g)) \geq 0.4 * b_q(S) \tag{4.2}$$

where $b_q(S)$ is the total mole amount of sulfur in q-th box. As $Cl_2(g)$ and $Cl(g)$ concentrations are only observed in trace amounts in the flue gas (Christensen et al., 1998), other AMR kinetic constraints were set for the oxidation of $HCl(g)$ to $Cl_2(g)$ and $Cl(g)$ according to 4.3 and 4.4, respectively.

$$n_q(Cl_2(g)) \leq 0.0001 * b_q(Cl) \tag{4.3}$$

$$n_q(Cl(g)) \leq 0.0001 * b_q(Cl) \tag{4.4}$$

Further minor tweaks in the chemical thermodynamic system are listed in Table B.11. The use of AMRs leads to partial chemical equilibria, where not all ingredients are allowed to react completely, thus some degree of metastability remains in the computed chemical speciation.

4.3.4 Batch process simulations

In a first step, batch simulations were calculated using *Process* mode to obtain information on phase stabilities as function of temperature and flue gas composition. In the batch simulations, the cooling of a fixed flue gas composition was simulated for the temperature range of 850 °C down to 100 °C at 25 °C steps for four different flue gas compositions (scenarios, Table 4.1). A flue gas quantity of 20 kg was defined as input (19.8 kg flue gas matrix + 0.2 kg ash forming flue gas), which represents approx. 65 m^3 of hot flue gas at 850 °C. In a second step, the Box Flux simulations in the dynamic megasystem were calculated using the *GEM2MT* mode for the four different flue gas compositions in order to investigate the effect of flue gas composition on the thermodynamically stable phase assemblages in the ash fractions. The masses and compositions retrieved in the respective

	Scenario A: reference state	Scenario B: high HCl	Scenario C: high SO₂	Scenario D: low O₂
	vol.-%	vol.-%	vol.-%	vol.-%
CO_2	11	11	11	11
H_2O	15	15	15	15
HCl	0.15	0.3	0.15	0.15
N_2	66	66	66	70
O_2	7.5	7.5	7.5	3.5
SO_2	0.05	0.05	0.15	0.05

Table 4.1: Initial flue gas matrix composition of the different scenarios.

sinks were thereby considered to represent the ash fractions arising at the different boiler / ESP sections, as shown in Figure 4.1b.

4.3.5 Box-flux model of megasystem dynamics

The subsequent cooling of the flue gas was simulated based on the definition of a dynamic megasystem consisting of local-equilibrium boxes (reservoirs)are connected through the fluxes of mobile groups of phases, using an approach proposed by Kulik et al., (1993). For this study, 10 heterogeneous reactor chambers (10 boxes at different temperatures, Figure 4.1b) were defined, which are interconnected through the fluxes of physically distinct phases (e.g. gas, solids - herein referred to mobile groups of phases (MGP)). The reactor chambers (boxes) represent local-equilibrium parts of the dynamic megasystem, each existing at defined size (mass, volume), temperature and pressure, and assumed to be mixed and partially equilibrated. A similar approach has been used successfully for the simulation of sublimation in volcanic fumaroles (Churakov et al., 2000). The mass transport in the reactive box-flux megasystem is calculated by solving a system of ordinary differential equations for masses of each element in each box, defined using MGP compositions and fluxes (Kulik et al., 1993). For the context of this study, it is important that the boxes exist each at its own temperature (and ambient pressure), are connected with fluxes of different MGPs, and have "sink" fluxes removing part of solids MGP (dust, salt) out of each box via "filters". The system of differential equations connecting box masses with fluxes was integrated at each time step, then the equilibria were calculated for each box (reactor chamber) by GEM algorithm, which changed the MGP elemental compositions. At each time step, this transport-equilibration loop was repeated. This approach combines the dynamics of mass transfer between the boxes with calculations of their equilibrium phase compositions and is based on four principles (Kulik et al., 1993):

(i) rapid mixing and partial equilibration

(ii) mass transfer between the boxes is defined as MGP fluxes with flux rates assigned

(iii) MGP are allowed to react in any of the reactor chambers

(iv) the change in total free energy of the system is not constrained during the evolution

of the megasystem, i.e. the boxes can reach equilibrium, while the whole megasystem
is always out of equilibrium, though can reach a dynamic steady state

The time iterations were computed until a dynamic steady state of dynamic equilibrium
was reached in the megasystem, manifested in unchanged compositions and masses in all
boxes (i.e. respective reactor chambers). This usually occurred after a few hundred seconds
simulated time.

4.3.6 Fluxes

Different types of fluxes of matter can be considered in megasystem box-flux simulations
(Kulik et al.,1993). The simplest possible flux (of MGP) is defined in mass/time units (e.g.
in kg/s) and is called a *zero-order* flux. For example, this can be a constant source of flue
gas; a constant sink of dust; a constant flux of flue gas between box 3 and box 4. The
drawback of such flux definition (except for constant sources) is that the megasystem
containing *zero-order* fluxes between boxes may go out of balance and the matter in some
boxes can be totally depleted with time. By analogy with chemical kinetics, such issues
can be avoided if the boxes are connected with *first-order* fluxes. Such a flux is defined as a
product of the rate constant (in 1/time units) and the mass of flux matter in the outgoing
box, so the flux itself is in mass/time units. Compared with *zero-order* (constant) fluxes,
first-order fluxes increase if the source mass increase, and decrease otherwise. This is
exactly the property that allows the box-flux megasystem to evolve from a transient initial
state to a dynamic steady state when no mass is changing in any of the boxes, yet the
matter is moving fast between them, transporting also energy (as chemical energy and
heat). Based on these considerations, the fluxes of MGP between the boxes were defined
to be *first-order* fluxes, with exception for the constant-source fluxes from the equilibrium
(combustion) chamber into the first reaction chamber, defined as zero order fluxes. For a
first-order flux, the flux of MGP is assumed linearly dependent on the total mass of MGP
in the outgoing reactor chamber. Yet, there must be an overall mass conservation in the
flow-through megasystem such as that shown in Figure 4.1b. This means that the overall
mass flux between the reaction chambers is assumed constant (Table 4.2).

4.3.7 Mass-volume dependence of flue gas flux at different temperatures

As seen in Figure 4.1b, the facility has fixed volumes of compartments where the flue
gas exists at constant (ambient) pressure but different temperatures. Because of high
compressibility of gas, this means that at fixed volume of the compartments, the mass of
flue gas will be greater at lower temperature according to ideal gas law, $PV = nRT$ where
P is pressure (105 Pa), V is volume (m^3), n is the number of moles of gas, R = 8.3145
J/K/mol is the universal gas constant, and T is temperature, K. From the gas law, n =
PV/(RT); numerically, assuming the box volume V = 400 m^3, this will be

$$n(T) = 4 * 10^7/(8.3145 * T) \ mol = 4.8109 * 10^6/T \ mol \tag{4.5}$$

a)

Waste Inlet

Grate

Flue Gas

1st pass

2nd pass

3rd pass

Empty Pass Ash (EA)

Bottom Ash

System Boundaries Modelling

Evaporator

Superheater

Superheater

Evaporator

Economizer

BOA1

BOA2

BOA3

BOA4

BOA5

Boiler

Boiler ashes (BOA)

Fly Ash (FA)

Electrostatic Precipitator (ESP)

ESP Ash (ESPA)

Flue Gas Scrubber

Scrub Water

towards Chimney

b)

Volume of Boxes = 400 m³ (4m x 5m x 20m)
Mass Flux = 35 kg/s

Distribution of flux rates between reactor chambers and sinks for MGP dust* and MGP salt** if different

| Box 0 | 650°C | Equilibration |

Box 1 | 590°C
0.75* / 0.95** ; 0.25* / 0.05** → Sink 1

Box 2 | 530°C
0.75* / 0.95** ; 0.25* / 0.05** → Sink 2

Box 3 | 450°C
0.75* / 0.95** ; 0.25* / 0.05** → Sink 3

Box 4 | 350°C
0.75* / 0.95** ; 0.25* / 0.05** → Sink 4

Box 5 | 270°C
0.75* / 0.95** ; 0.25* / 0.05** → Sink 5

Box 6 | 230°C
0.25 ; 0.75 → Sink 6

Box 7 | 190°C
0.25 ; 0.75 → Sink 7

Box 8 | 150°C
0.25 ; 0.75 → Sink 8

Box 9 | 100°C → Sink

BOA1 BOA2 BOA3 BOA4 BOA5

Boiler

Electrostatic Precipitator

ESP Ash (ESPA)

Figure 4.1: Scheme of the flue gas cooling path in the incinerator plant (a), and schematic overview on megasystem box flux model and the distribution of flux rates between reservoirs and sinks for the solid *MGP dust* (*) and *MGP salt* (**) (b). The predicted solid phases in the sinks 1 - 5 thereby represent the different boiler ash fractions (BOA 1 - 5) and the ash arising at the different sections of the electrostatic precipitator (ESP) is represented by the predicted solids in sink 6 - 8, whereby their sum is considered to represent the ESPA.

Assuming the molar mass of flue gas the same as that of air (0.029 kg/mol), the mass of gas in the box will be

$$m(T) = n(T) * 0.029 = 1.39516 * 10^5/T \ kg \qquad (4.6)$$

For instance, at 650 °C (T = 923.15 K), the mass of flue gas in the box is m = 151.13 kg; at 170 °C (T = 443.15 K), m = 314.83 kg, more than twice as much.

Therefore, to maintain the mass conservation in the facility, the same mass of flue gas must enter each box per unit time. From the operation data of Energiezentrale Forsthaus, this mass flux can be assumed J_{0-1} = 35 kg/s, set as the constant-source *zero-order* flux from box 0 to box 1. However, any next flux (e.g. $J_{1-2} = J_{2-3} \ldots$) should be treated as the *first-order* flux, e.g. $J_{1-2} = k_{1-2}*m_1$ where k_{1-2} is the rate constant for the flux 1-2, and m_1 is the mass of flue gas in the (outgoing) box 1. From the condition $J_{0-1} = J_{1-2} = J_{2-3}$ = 35 kg/s and Eq. 4.6, the rate constant for the flux 1-2 will be equal to

$$k_{1-2} = J_{1-2}/m_1 = 35/(1.39516 * 10^5 * T_1) \quad 1/s = 2.5087 * 10^{-4} * T_1 \quad 1/s \qquad (4.7)$$

$$k_{q-q+1} = J_{q-q+1}/m_q \quad 1/s = 2.5087 * 10^{-4} * T_q \quad 1/s \qquad (4.8)$$

where Tq (K) is the temperature in the box. The value $1/k_{q-q+1}$ is called residence time (of flue gas) in the q-th box; it shows how much time is needed to completely replace all the gas at this flux rate (and constant mass). Calculated masses of flue gas in the boxes, flux rate constants, and residence times are given in Table 4.2.

4.3.8 MGP structure and composition

To represent the solid phase transport more realistically, the solid fraction transported between the chambers was divided into 2 MGPs: MGP "dust" and MGP "salt". Thus, three MGP were defined:

(i) the gas phase

(ii) a dust fraction which represents mainly refractory minerals and the amorphous melt droplets that settle through gravimetric forces along the boiler

(iii) newly precipitated salts which are able to travel in suspension along the boiler

The whole share of precipitated chlorides was counted as *MGP salt* , while only 50% of precipitated sulfates were counted as *MGP salt*, as (i) it is assumed that $CaSO_4$ can travel as refractory mineral as it is observed in major concentrations in the boiler ash and (ii) the transport of (alkali) sulfates may be delayed due to sticking to heat exchanger deposits. Based on field observations, it was assumed that the total mass fraction of the two solid MGP in relation to *MGP gas* makes up to 1 wt.%, whereby the shares between *MGP dust* and *MGP salt* were assumed to be equal (0.5 wt.% each). The flux of MGP

Box-Nr.	Section	Temperature °C	Mass gas in box	Mass flux	Flux rate	Residence time
		°C	kg	kg/s	1/s	s
0	Source	650	151.13	35	0.233	4
1	Boiler Section 1	590	161.64	35	0.218	5
2	Boiler Section 2	530	173.71	35	0.203	5
3	Boiler Section 3	450	192.93	35	0.183	5
4	Boiler Section 4	350	223.89	35	0.157	6
5	Boiler Section 5	270	256.86	35	0.137	7
6	ESP Section 1	230	277.28	35	0.127	8
7	ESP Section 2	170	314.83	35	0.112	9
8	ESP Section 3	130	346.06	35	0.102	10
9	Sink	100	373.89	35	0.094	11

Table 4.2: General setup of box flux model and important numbers, e.g. temperature profile, flux rates

represents the transfer of MGP from the source box (reactor chamber) to the receiving box (reactor chamber). For the solid MGP, sink fluxes were implemented for a defined share of total flux rate into a sink, thus providing a means to simulate the dust or salt removal. The remaining share of flux rate is then allowed to travel to the next reactor chamber (illustrated in Figure 4.1b, details in Table B.9). As the boiler acts as "dedusting" unit through gravimetric settling of the coarser ash particles, it was assumed that a share of 25% of the precipitated *MGP dust* is settling at each boiler section. This sums up to a total dust removal efficiency along the whole boiler area of 75%, which is in good agreement to field observations. For the newly precipitated salts, which are able to travel with the flue gas in suspension due to its small grain size, a settling of 5% at each boiler section was assumed. The dust removal efficiency at each ESP section was set to 75% for both *MGP dust* and *MGP salt*, which yields a total dust removal efficiency of 98.5%.

4.3.9 Flue gas composition

The system parameters were defined based on operational data from MSWI plant Bern Forsthaus (e.g., operating parameters, chemical data of mass streams, temperature profiles, mass flow, dimensions). The flue gas composition could be estimated based on annual mass balances and chemical analyses of the material flows arising from the flue gas (fly ash, scrub water, gas emission downstream of the electrostatic precipitator). In order to be able to calculate different flue gas scenarios, the input was subdivided into flue gas matrix (main composition of the raw gas, Table 4.1) and ash-forming flue gas fraction (Table 4.3), whereby the input was defined as elemental composition. The ash-forming flue gas fraction corresponds to the total composition of average fly ash.

4.4 Results

4.4.1 Batch simulations

The predicted thermodynamically stable phases of the batch simulations are dominated by solids, whereby almost any liquids are formed. Figure 4.2 shows the calculated stability

	Ash forming flue gas fraction	Composition of amorphous melt phase (glass)
	g/kg	g/kg
Al	29.55	27.43
Ba	2.20	0.00
Br	2.37	0.00
C	10.70	0.00
Ca	151.56	70.53
Cd	0.27	0.00
Cl	95.51	0.00
Cr	0.39	0.00
Cu	3.28	0.00
F	7.84	0.00
Fe	16.57	11.76
K	58.09	3.92
Mg	3.92	3.92
Mn	0.73	0.00
Na	75.10	23.51
Ni	0.12	0.00
O	282.02	164.58
P	3.92	3.92
Pb	9.69	0.00
S	86.66	0.00
Sb	3.94	0.00
Si	97.23	78.37
Sn	2.10	0.00
Ti	9.40	3.92
Zn	46.69	0.00
Zr	0.15	0.00

Table 4.3: Chemical composition of the ash forming flue gas fraction and estimated chemical composition of the amorphous melt phase, normalized to 1kg, expressed as g/kg.

fields of the solid major phases for the different flue gas compositions. A detailed table of all the thermodynamically stable phases as function of temperature are provided in Tables B.12 - B.15. For the solids, the main matrix phases in the reference scenario are $CaSO_4$ and the amorphous melt for the entire temperature range. In the higher temperature range > 750 °C, $CaSiO_3$(wollastonite), $CaTiO_3$, $CaTiSiO_5$(sphene), ZnO, $Ca_3P_2O_8$ are the dominant phases among the ones predicted to be thermodynamically stable. At 750 °C the formation of $NaCl$ and KCl initiates, followed by K_2SO_4, Zn_2SiO_4 at 675 °C and cristobalite (SiO_2) at 625 °C. From 600 °C on, quartz becomes the dominant SiO_2 phase. At 275 °C, Zn is preferably incorporated into $ZnCl_2$. The matrix phase assemblages of scenario B and D are comparable to that of scenario A. In scenario B, however, cristobalite and SiO_2 show higher stabilities than the Zn-silicate Zn_2SiO_4 compared to scenario A. For scenario C, the matrix phases are dominated by sulfates instead and K_2SO_4 and Na_2SO_4 are predicted to be the dominant alkali phases. The amorphous glass, $CaSO_4$, K_2SO_4 and cristobalite already form at 850 °C, followed by $ZnSO_4$ at 700 °C and Na_2SO_4 at 575 °C. From 450 °C onwards, the amorphous glass becomes less stable and K-Al-Sulfate start forming instead.

The predicted stability fields of the heavy metal bearing phases as function of temperature are presented in Figure 4.3. In the reference scenario, Zn is predicted to be present as ZnO at high temperatures until 700 °C. Then, Zn_2SiO_4 becomes the most stable Zn phase, with minor amounts of Fe_2ZnO_4 forming. At 275 °C, Zn is predicted to be present as $ZnCl_2$. The predominant form of Cu is oxidic (CuO) in the higher temperature ranges and changes to $CuCl_2$ at temperatures < 250 °C. Antimony is present as Sb_2O_4 and at 275 °C, Sb_2O_5 becomes the dominant Sb species. Lead and Cadmium are only found as chlorides and start precipitating at 425 °C. Other heavy metal phases are Cr_2O_3, Fe_2O_3, MnO_2, SnO_2, Fe_2NiO_4 and $NiSO_4$ to a minor extent. Barium is mainly bound as $BaSO_4$ and titanium as TiO_2, $NiTiO_3$, $CaTiSiO_5$. The heavy metal binding forms of Scenario D are identical to scenario A. In scenario B, it can be observed that the heavy metal bearing silicates and oxides (e.g. Zn_2SiO_4, CuO) start forming at lower temperatures compared to base scenario, while the shift towards $ZnCl_2$ initiates earlier at higher temperatures. Scenario C with the high sulfur load builds Zn, Pb, Cu, Cd predominantly as sulfates and at higher temperatures (600 - 750 °C). For Sb, the oxidic form remains the dominant species for all the four scenarios.

4.4.2 Box flux model

Evolution of gas phase composition and partitioning

The evolution of the gas concentration along the cooling path is shown in Figure 4.4. The gas phase of the reference scenario (scenario A) is dominated by $N_2 > H_2O > CO_2 > O_2$, which together account for $>99\%$ of the flue gas composition. HCl and SO_2 are the dominant Cl- and S- species. Chlorine is also present as $NaCl(g)$ and $KCl(g)$, as well as bound to heavy metals (e.g. $ZnCl_2$, and $PbCl_2$, $CuCl_2$, $CdCl_2$ in minor concentrations).
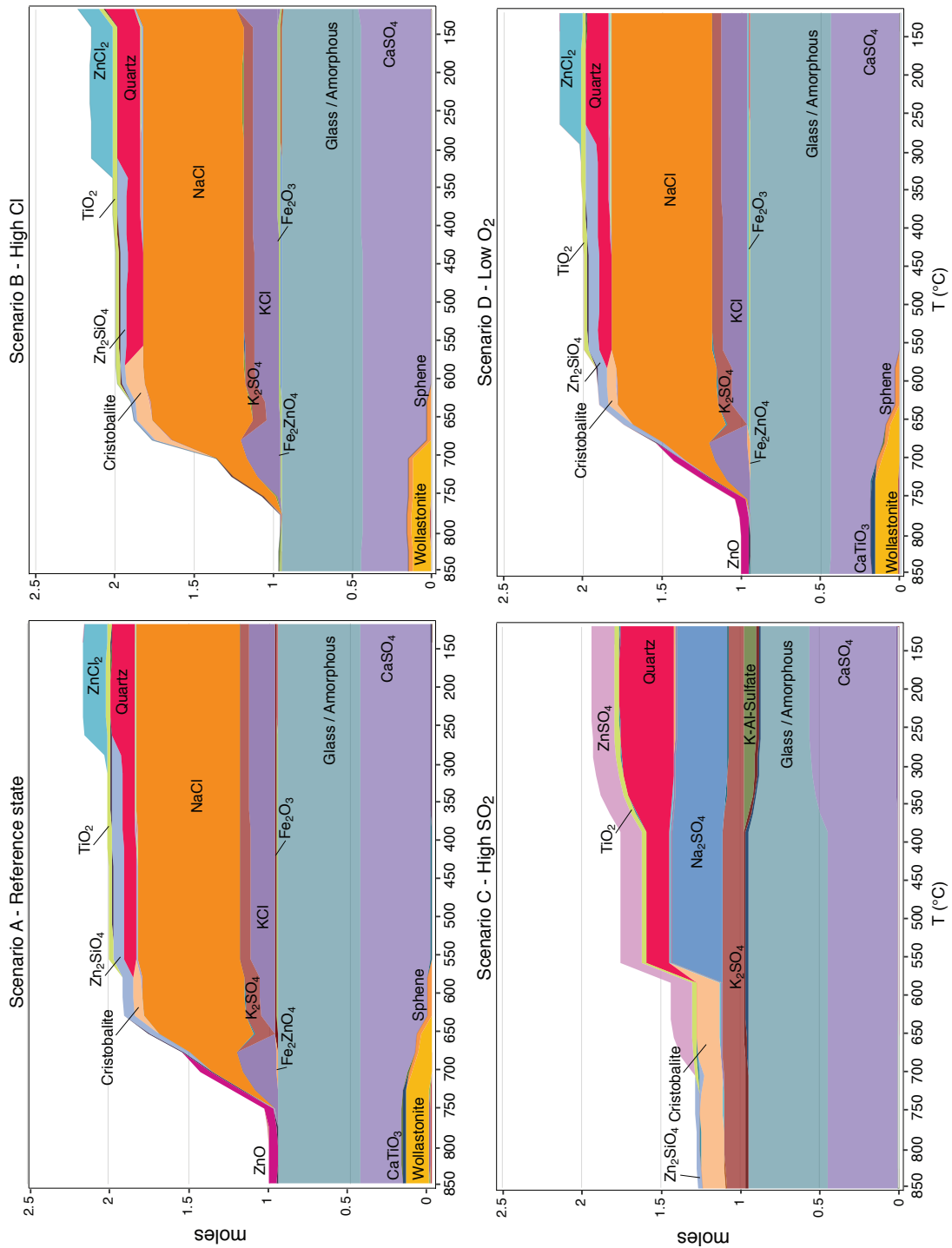
Figure 4.2: Overview of thermodynamically stable solid phases as function of temperature for the different flue gas compositions
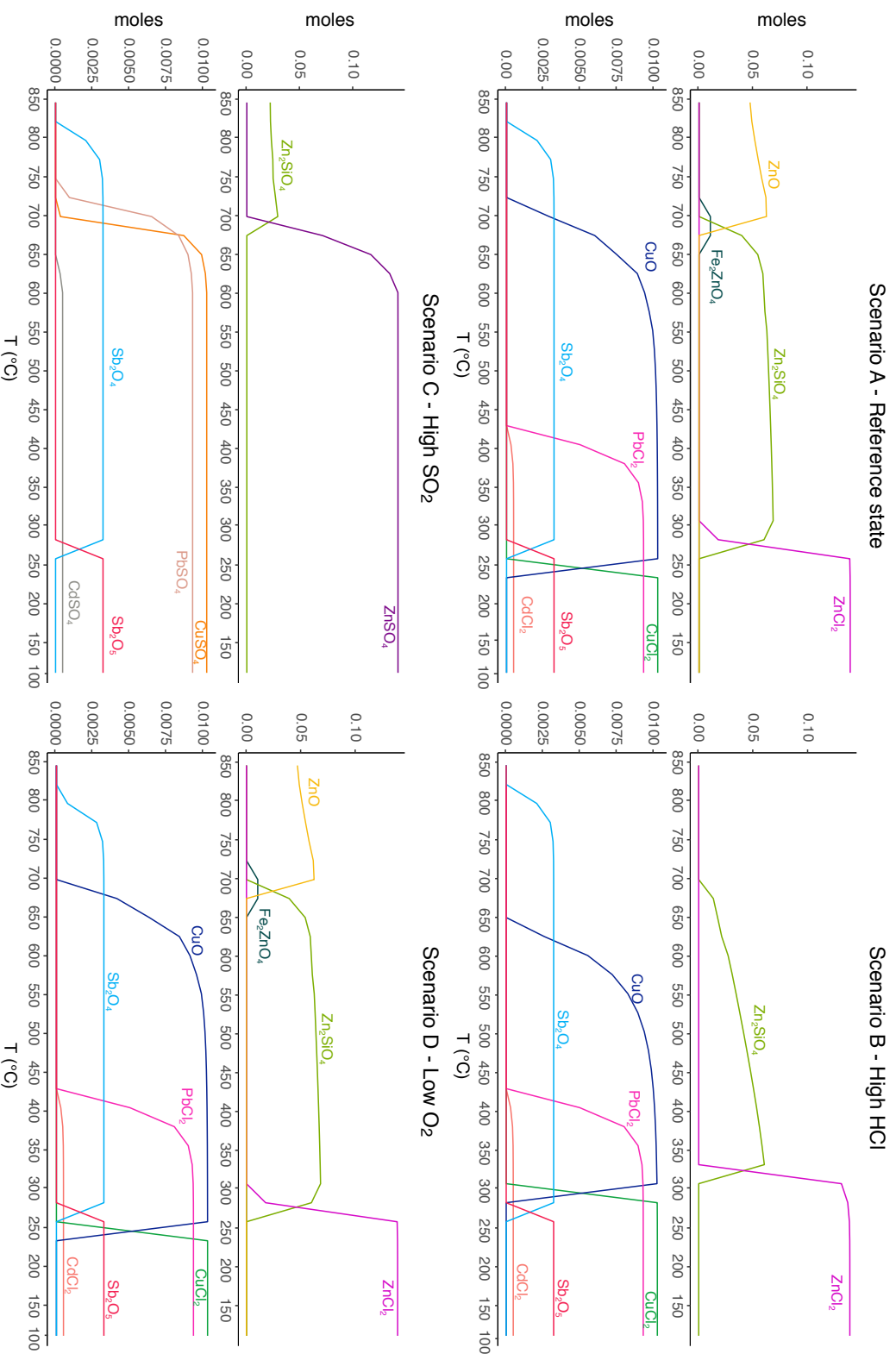
Figure 4.3: Stability fields for the heavy metals of interest as function of temperature for the different scenarios.
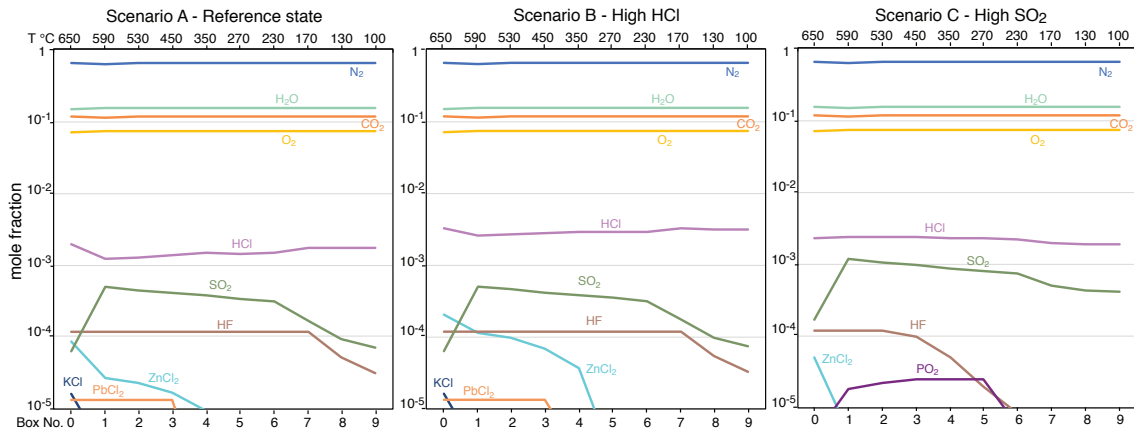
Figure 4.4: Evolution of gas phase composition during cooling of the flue gas for the different scenarios. The gas concentrations for scenario D are identical to scenario A and are therefore not shown.

As the gas cools, the concentration of KCl, NaCl and Zn-, Cu-, $CdCl_2$ decreases due to precipitation of chlorides. HF is also an important trace species. The composition of the gas phase is similar for scenario B and D, except that in scenario B, the $ZnCl_2$ concentration in the gas phase decreases more slowly due to later precipitation at higher Cl concentration. For scenario C, it can be observed that the concentration of $ZnCl_2$ drops already after equilibration and that PO_2 represents another major gas species, its concentration also dropping together with HF after box 5. Interesting is thereby also the elevated HCl vapor pressure related to the sulfate dominated system in the solids.

The partition coefficients of Cl, S and the heavy metals Zn, Pb, Cu, Cd, Sb, Sn with respect to the solid phase is shown in Figure 4.5. For the reference scenario, it can be observed, that Sb and Sn already fully partition to the solid phase at 650 °C. For Cu and Zn, partition coefficient to the solid phase is already at 0.9 and 0.8, respectively at 590 °C (Box 1) and the partition coefficient to the solid phase increases steadily until full partitioning to the solid phase is achieved at Box 5 and 6, respectively. Pb and Cd show comparable partitioning behavior, as both heavy metals show a sharp transition between full partitioning to the gas phase and sudden full partitioning to the solid phase from Box 4 onwards. While scenario D is identical to scenario A, it can be observed in scenario B that the retention of Cu and Zn in the gas phase is increased and their partitioning to the solid phase is lower compared to scenario A for Boxes 1 - 5. For scenario C it is observed that Cl fully partitions to the gas phase along all boxes and the heavy metals partition to the solid phase much earlier compared to the other scenarios – already from the first box almost all heavy metals fully partition into the solid phase. Interesting is that Cl fully partitions back to the gas phase after box 7 in scenario A, B and D, which could be associated to the low solid particle concentration compared to the boxes at higher temperature.

Evolution of ash mineralogy as function of flue gas composition

Figure 4.6a shows the predicted mineralogy of the different ash fractions for the individual scenarios (detailed tables of all the thermodynamically stable phases in Tables
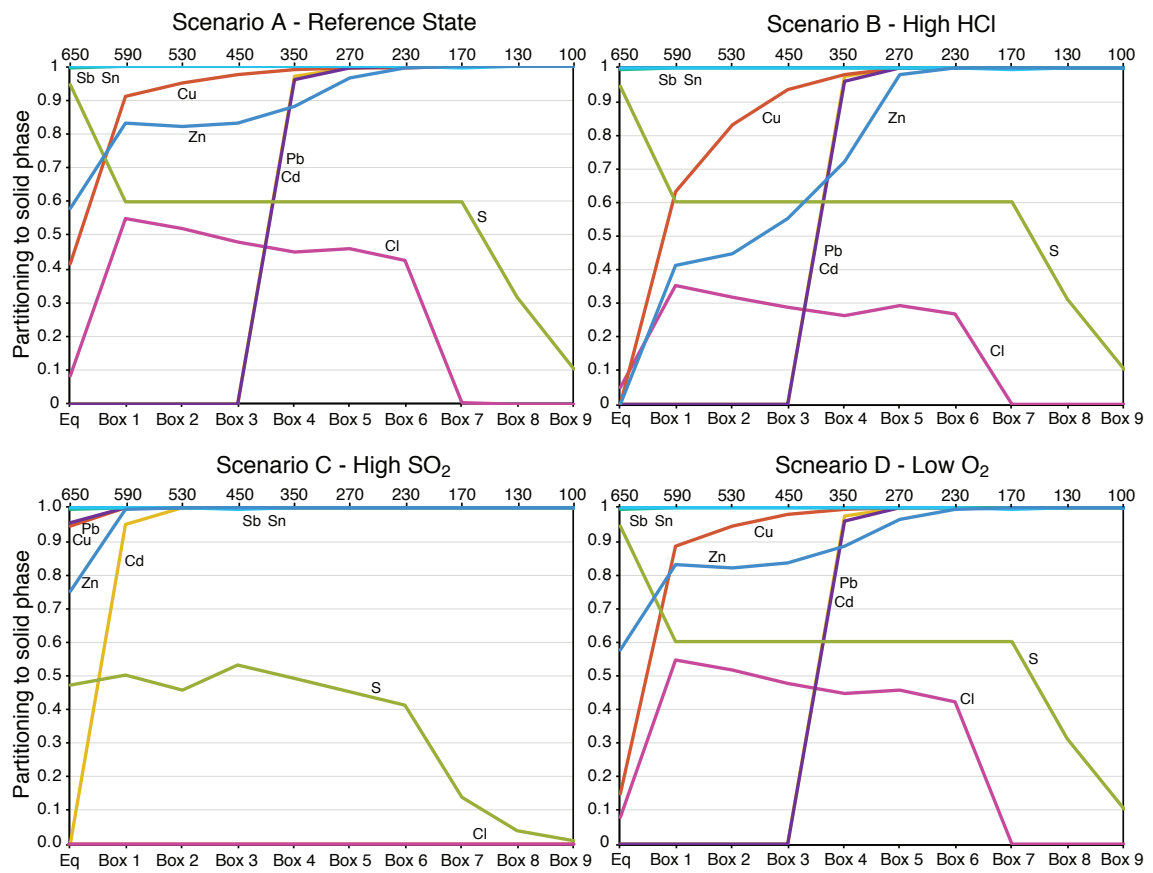
Figure 4.5: Partition coefficients of selected elements with respect to the solid phase for the different scenarios. Full partitioning to solid = 1, full partitioning to gas phase = 0.
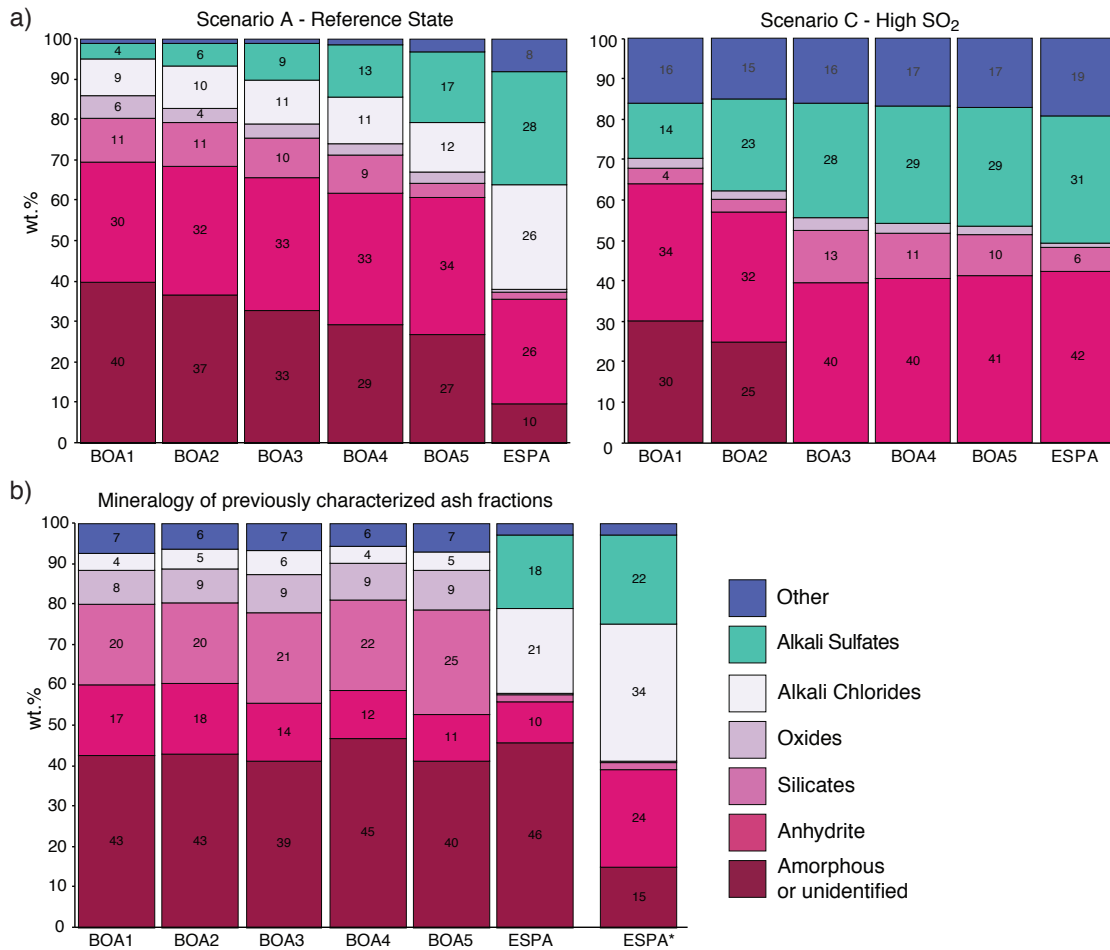
Figure 4.6: Predicted mineralogy for the different ash fractions (a) for flue gas scenario A and C vs. mineralogy of previously characterized ash fractions (b) (data from Wolffers et al., (2021)). ESPA* represents an assumption on possible mineralogical composition of the unidentified fraction based on calculated differences in chemical and mineralogical composition. The predicted mineralogy for scenarios B and D is almost identical to scenario A and are shown in figure B.1.

B.16 - B.19.). The mineralogical composition of scenario B and D are very similar to that predicted by the reference scenario and are therefore not shown. For the reference scenario, it is observed, that the mineralogy of the boiler ashes is dominated by the amorphous melt and anhydrite, followed by high shares of silicates (e.g. quartz, Zn_2SiO_4) and alkali chlorides (KCl, NaCl) while the share of alkali sulfates (mainly K_2SO_4) is increasing along the flue gas cooling path. The share of the amorphous melt phase is also gradually decreasing in flue gas direction, while its share in ESPA is substantially lower than in the boiler ash fractions. The ESPA shows thus higher shares of newly formed phases, dominated by anhydrite, alkali chlorides and alkali sulfates. For the scenario C with elevated SO_2 concentration, the predicted mineralogy is considerably different from the reference scenario. It is observed, that the amorphous glass phase only represents a thermodynamically stable phase in the first two boiler ash fractions. Anhydrite and alkali sulfates represent the dominant solid phases, together with minor amounts of silicates, oxides and other (heavy metal bearing) sulfates (e.g. $ZnSO_4$, $PbSO_4$, $CuSO_4$, $BaSO_4$, summarized as category "other").

Figure 4.7 shows the distribution of predicted heavy metal binding forms for the dif-

	BOA1	BOA2	BOA3	BOA4	BOA5	ESPA	Total amount of ash produced
	wt.%	wt.%	wt.%	wt.%	wt.%	wt.%	kg
Scenario A - Reference scenario	4	4	3	3	3	82	7.789
Scenario B - High HCl	4	4	4	4	3	81	7.921
Scenario C - High SO$_2$	5	5	5	4	4	77	6.962
Scenario D - Low O$_2$	4	4	3	3	3	82	7.795

Table 4.4: Relative distribution of masses obtained in the sinks for the different scenarios after reaching of steady state at 120 timesteps (seconds).

ferent scenarios. In the scenarios where molar S/Cl ratio < 1, the heavy metals are predominantly stable as oxides, silicates and chlorides in the boiler ashes. In the ESPA, the heavy metals are predicted to be stable as chlorides, as well as bound to sulfates to a minor extent ($ZnSO_4$, $PbSO_4$, $CuSO_4$, $CdSO_4$). In scenario C, the heavy metals are predicted to be predominantly stable as sulfates, as already predicted in the batch simulations.

Mass streams

The total amount of ash generated at steady state after 120 timesteps (corresponding to approximately 200 seconds), as well as the relative distribution of masses among the sink fluxes (Table 4.4) is similar for all the calculated scenarios. The share of ash generated at the ESP is thereby the highest with 77 - 82 wt.%, while the ash shares generated in the boiler sections are considerably lower (3 - 5 wt.%, respectively). At the incineration plants, it is often difficult to quantitatively assess the ash proportions, as they are seldom gravimetrically measured. In our previous study (Wolffers et al., 2021), it was calculated based on the chemical composition, that the share of ESPA on the total amount of ash produced is approximately 75%. The calculated amount of ESPA is thus higher than previously estimated, but overall still a reasonable value. The obtained ash concentration in the gas is similar for all scenarios, with higher ash concentrations at the beginning of the boiler (4.3 g/m^3) towards lower ash concentrations at the end of the boiler (3.8 g/m^3), as a result of subsequent ash removal.

4.5   Discussion

4.5.1   Comparison of predicted ash mineralogy from reference scenario with field observations

The flue gas represents a kinetically controlled geochemical system due to low residence times, which may locally only allow partial equilibria. In addition, the input is heterogeneous, as there are temporal differences in flue gas composition, as well as differences in amount and concentration of dust input. Nevertheless, the predicted phase assemblages for the reference scenario are in good agreement with the main trends observed in the different ash fractions measured from the previous study (Wolffers et al., 2021), comparison in Figure 4.6b). Phases that were observed in the ash but were not predicted to be ther-
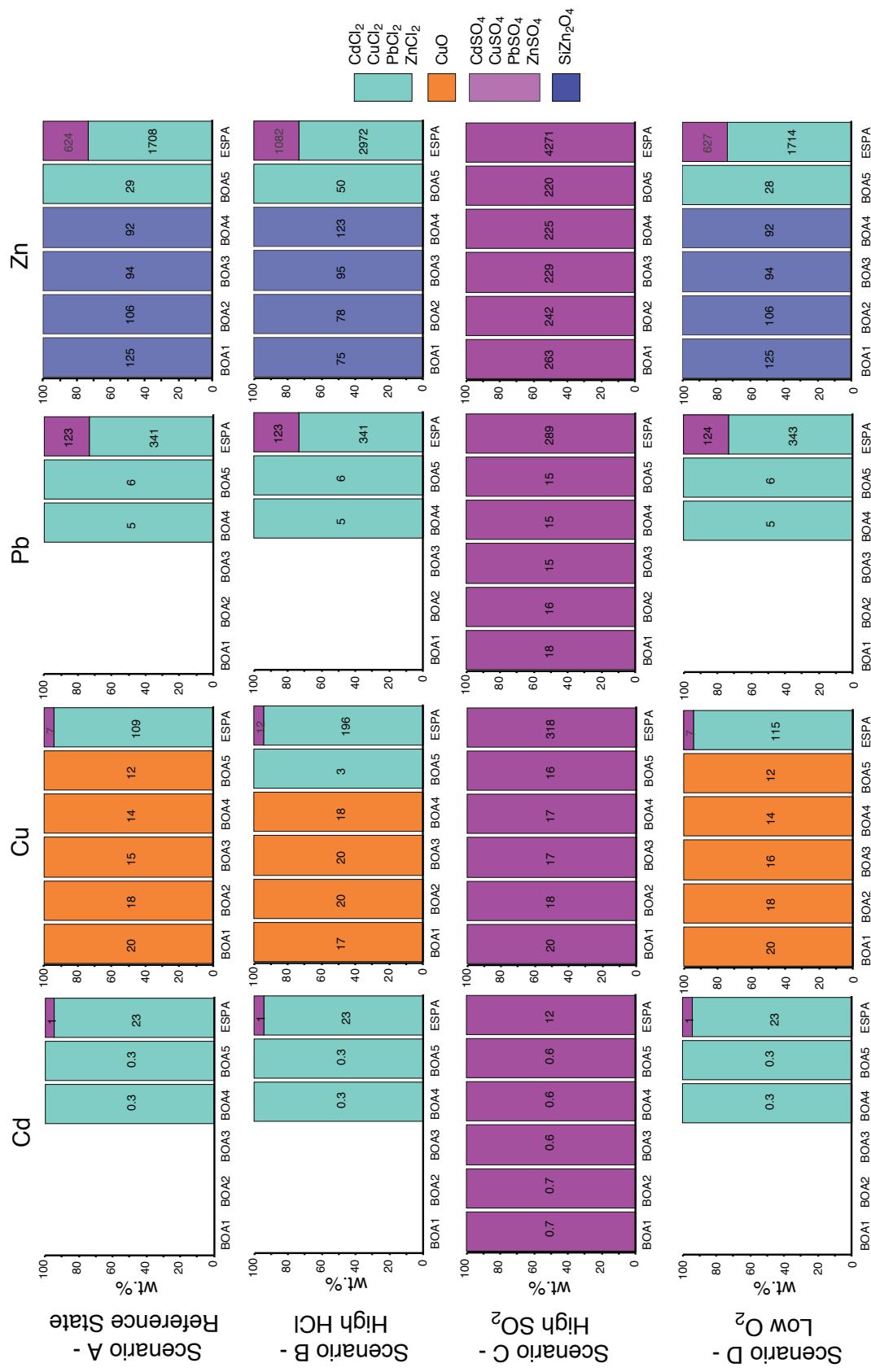
Figure 4.7: Predicted heavy metal binding forms in the different ash fractions and scenarios. The relative shares are expressed as wt.% of total solid Zn, Pb, Cu, Cd phases. The numbers displayed in the bars represent total amount in mmol.

modynamically stable at given conditions include CaO, CaCO$_3$, (Ca-)feldspars, gehlenite. These phases represent mostly refractory minerals and thus may have either traveled along the flue gas path as thermodynamically metastable compound and accumulated in the ash without being equilibrated or their formation was initiated because of locally different chemical conditions, which is assumed for gehlenite formation (Traber et al., 2002). The mentioned phases all include Ca and it is noticeable that CaSO$_4$ was predicted to form in higher quantities than observed in the ash. It is further observed that the predicted mineralogy shows higher concentrations in alkali sulfates than the characterized ash. However, it was observed that the alkali sulfates that form during passing of the boiler are often captured or preferentially form on heat exchanger deposits and are therefore only periodically released to the hoppers where the boiler ash is collected. Their produced amounts are therefore difficult to estimate and the measured concentration only represents the share that was released to the boiler ash. The characterized ESPA shows quite high share of amorphous or unidentified phases. When calculating the difference between the elements present in the determined structures and the bulk XRF chemical composition, it becomes clear that a dominant part of the amorphous or unidentified part is associated to Ca-K-Na chlorides and sulfates. The observed mineralogy was thus corrected for CaSO$_4$, NaCl, Na$_2$SO$_4$, KCl and K$_2$SO$_4$ (ESPA*, Figure 4.6b, with assumption of even distribution of alkali metals between chlorides and sulfates), which then looks very similar to the thermodynamically predicted mineralogy of the ESPA. In SEM investigations of heat exchanger deposits, it was, however observed, that the (Ca)-Alkali sulfates rarely prevail as mono salts but rather as complex mixtures of Ca, K, Na, S, Cl and heavy metals such as Zn, Pb – probably incorporating the constituents in the ratios as they are available in the flue gas (Figure 4.8). Presumably, such random sulfate/chloride assemblages also form in the ESPA, probably even as very fine-grained particles, which could explain why they could not be detected with XRD and where SEM EDX spot measurements represent multiple phases. Further, it is important to note that local conditions can vary greatly from the average composition and often probably only partial equilibrium is reached due to short residence times. Thus, there will always be differences between thermodynamically calculated stable phases and the phases observed in the ash, as kinetics often do not allow the phase to decompose once it is no longer thermodynamically stable.

4.5.2 Effects of flue gas composition on predicted matrix phase assemblages

It was observed, that the variations in the S/Cl ratio of the flue gas had greater impact on the equilibrium phase assemblages than variation in the O$_2$ content. The formation of sulfates was previously described to be directly linked to the oxidation rate of SO$_2$(g) (Glarborg and Marshall, 2005; Jiménez and Ballester, 2007; 2005) and the formation of sulfates was therefore controlled in this study by constraining the SO$_2$(g) concentration. However, the constraint primarily resulted in the limited formation of alkali sulfates and had little effect on the formation of CaSO$_4$. The strong competition between S and Cl to
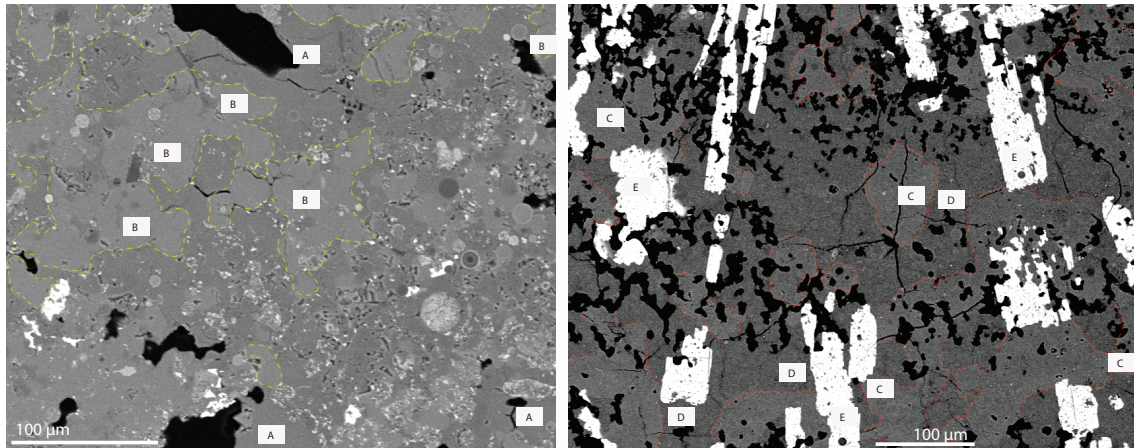
Figure 4.8: Backscattered Electron Microscope (SEM) image showing the coexistence of complex (heavy metal bearing) sulfate matrices in heat exchanger deposits of different chemical composition close to the composition of (A) = $Na_{26}K_8Ca_3(SO_4)_4$, (B) = Ca-Langbeinite $CaK_2(SO_4)_2$, (C) = $Na_2K_2Ca_1Zn_1(SO_4)_4$, (D) = $Na_4K_2Zn(SO_4)_4$, (E) = $Na_2K_2Pb(SO_4)_3$

capture the alkali metals Na and K was also observed in other studies (Christensen et al., 1998; Jiao et al., 2011; Jiménez and Ballester, 2007). The reference scenario shows a higher Cl mole fraction compared to S and therefore the chlorides are dominant. It was observed that at molar S/Cl ratio > 1 (scenario C), the sulfates become the dominant solid phases and chloride formation is suppressed. Jiao et al., (2011) also observed that the fraction of chloride formation decreased substantially with an increased SO_2 concentration. However, regardless of the S/Cl ratio, $CaSO_4$ appears to be the dominant Ca phase along with the Ca-containing glass phase, and $CaCl_2$ does not form even at high Cl contents. Although the O_2 concentration of 3.5 vol.% is low for flue gas conditions, the scenario D did not show differences in phase assemblages compared to the reference scenario. Figure 4.9 shows that the redox transition and subsequent change in phase assemblages only takes place when the activity of O_2 only substantially decreases. The observed phases such as $CaSO_4$, Fe_2O_3, Sb_2O_5 are thermodynamically stable down to O_2 concentration of 0.5 vol.%.

4.5.3   Effects of flue gas composition on predicted heavy metal binding forms

It was observed that around 250 °C, there is a substantial change in solid speciation of most heavy metals. The predicted conversion of CuO to $CuCl_2$ with decreasing temperatures is consistent with calculations by Verhulst et al., (1996). Zn is reported to be predominantly present as K_2ZnCl_4 in the ESPA (Bayuseno and Schmahl, 2011; Weibel et al., 2017; Wolffers et al., 2021), but the thermodynamic calculations predict $ZnCl_2$ to be the stable zinc chloride. It was observed that the limiting parameter to form K_2ZnCl_4 is the availability of potassium. If all available K is bound to KCl or K_2SO_4 at higher temperatures, no K_2ZnCl_4 is forming but $ZnCl_2$ instead. It was nevertheless observed that $ZnCl_2$ remained the most stable Zn chloride even if the available K, Zn or Cl content is doubled compared to what is available in the reference scenario. The formation of ZnO
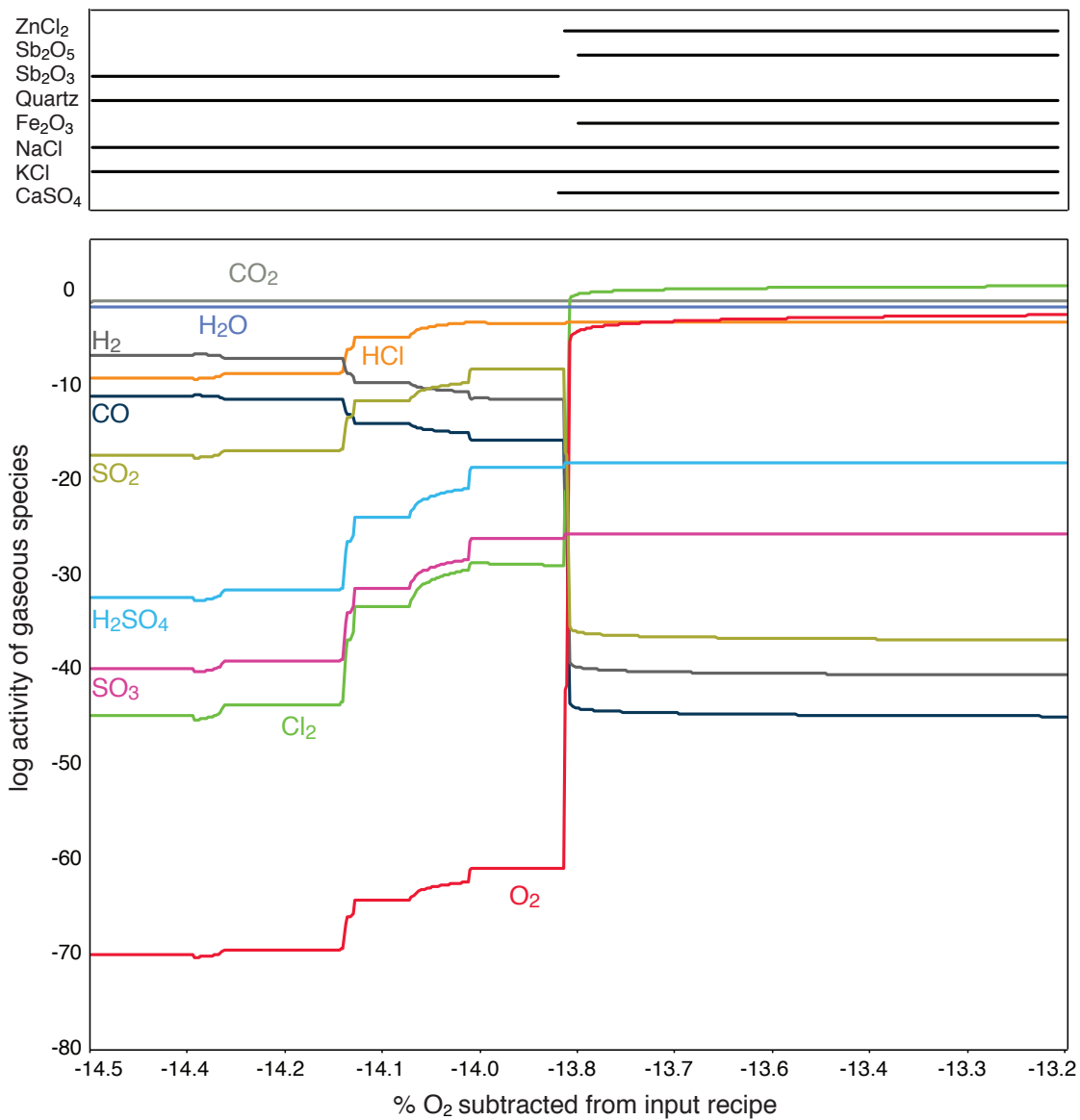
Figure 4.9: Stability of selected solid phases (top) and activity of selected gaseous species (bottom) as function of relative O_2 content in the input recipe in the region of the redox transition.

and Fe_2ZnO_4 was not predicted in the box flux simulations, probably due to lower reaction temperatures in the box flux model compared to the batch simulations. However, both phases, as well as the predicted Zn_2SiO_4, have been observed in boiler ashes (Wolffers et al., 2021). Zn_2SiO_4 was thereby observed to form reaction rims around quartz particles.

It could be confirmed that the heavy metal binding form was more sensitive to the S/Cl ratio of the flue gas composition compared to the O_2 concentration (as also observed by Lindberg et al., 2013). The shift of chloridic to sulfate binding form with increased S content was thereby also observed for Cd (Zhang et al., 2008). Jiao et al., (2011) observed that the presence of SO_2 and H_2O facilitated the conversion of gaseous metal chlorides to form sulfates, leading to earlier precipitation of e.g. $PbSO_4$ due to the reduction of the dew point. The shift of the heavy metals to sulfates with S/Cl >1 is particularly relevant for heavy metal recovery, as the heavy metals tend to be less soluble as sulfates than as chlorides. It was observed in a field experiment (Fromm et al., 2019) that increased SO_2 concentration in the flue gas has led to the preferential binding of Pb as $PbSO_4$, which was hardly extractable from the fly ash with the FLUWA process. This insight is also important with regard to increasing recycling rates of plastic, which will possibly result in lower Cl concentrations in the flue gas.

The increased HCl concentration in scenario B showed the effect on an increased retention of metals in the gas phase. This could be associated to dew point reduction, as also described in (Mkilaha et al., 2002). The prolonged retention of heavy metals in the gas phase with increased HCl concentration and the earlier shift towards formation of chlorides is an important finding when it comes to optimizing the composition of the combustion residues with respect to heavy metal extraction (e.g. fractionation of heavy metals). However, the effect was mainly observable for Cu and Zn and less for Pb, Cd, Sb, Sn.

Sb was observed to be predominantly bound as oxides, except in scenario C it was predicted to be stable as sulfate at lower temperatures. In the gas phase, Sb_4O_6 represents the dominant Sb species. However, the chloridic gaseous compound ($SbCl_3$, $SbCl_5$), as well as the penta-valent gaseous oxidic Sb compound (Sb_5O_{10}) are not present in the database, therefore statements are limited. Nevertheless, Verhulst et al., (1996) observed in thermodynamic calculations, that gaseous Sb_4O_6 was dominant over $SbCl_3$, the latter being predicted to be stable only in minor concentrations. Paoletti et al., (2001) thereby observed an increased transfer of Sb to the gas phase with increased PVC addition, possibly leading to the formation of the highly volatile $SbCl_3$. They observed, however, a rapid precipitation with cooling of the flue gas, presumably due to the conversion into the more stable oxidic or oxochloric Sb-compounds. The absence of Sb-chlorides is consistent with the observation that Sb is not mobilized during acid leaching. The presence as less soluble oxidic compound is therefore reasonable.

4.5.4 Implications on transport mechanism and mass streams

The assumptions on transport mechanisms, e.g. (i) the estimated dust removal efficiency of the boiler, as well as (ii) the assumption on the travelling of chlorides in suspension with the flue gas have resulted in reasonable results. These findings confirm the assumption, that the dust load from refractory minerals is settling faster through gravimetric forces along the boiler compared to the finely grained newly formed phases, which are able to travel with the flue gas further downstream compared to their temperature region of formation. These findings confirm, that the transport mechanism is an important factor decisive of the ash mineralogy and should also be considered when it comes to understanding the formation of pollutants (e.g. PCDD/-F) in the flue gas. Further, the assumptions on mass streams lead to ash amounts that are in good agreement with operational data. The amount of generated ash sums up to approximately 2'000 t/y, which is a reasonable value compared to the usual 2'700 - 3'000 t/y of ash generated at MSWI plant Bern Forsthaus.

4.5.5 Limitations

The designed simplified model already gives valuable insights into the prevailing processes during flue gas cooling. Nevertheless, the geochemical processes are of high complexity and aspects such as kinetics could not be fully accounted for in the present calculations. The presence of metastable $SO_2(g)$ and $Cl(g)$, $Cl_2(g)$ in the gas phase could be accounted for using kinetic constraints, which could be further tuned (e.g. through introduction of temperature dependent constraints). The thermodynamic dataset from IVTANTERMO contains a very wide range of substances and together with the additionally included ones, the used thermodynamic dataset covers the most important phases. The used dataset has been checked against the available databases (where applicable) and appears to be reasonably correct. However, it should be mentioned here, that reliable experimental data for large temperature ranges hardly exist for mixed alkali/earth alkali sulfates, and that the available data is associated with uncertainties. In addition, it was observed that important Sb phases (both gaseous and solid) are missing and it could be of great importance to include these phases for further calculations. Another complexity is represented by the conditions prevailing in the electrostatic precipitator, as the dust and mist particles suspended in the gas are electrically charged and separated at precipitation electrodes, which is difficult to simulate in our model. Nevertheless, the predicted phases are in good agreement with the observed phase assemblages and all assumptions made seem to be reasonable.

4.6 Conclusion

The performed thermodynamic calculations give valuable insights into the ash forming processes during cooling of the flue gas, which can be summarized as follows:

(i) Variations in the S/Cl ratio of the flue gas have a greater impact on the equilibrium

phase assemblages than the variation in the O_2 content, which showed only minor impact.

(ii) At molar ratio S/Cl < 1, Zn was predicted to be stable as ZnO, Fe_2ZnO_4, Zn_2SiO_4 at high temperatures, Cu as CuO. For Zn and Cu, a substantial change in heavy metal binding forms was predicted between 200 - 300 °C (depending on the HCl concentration), leading to the formation of $ZnCl_2$ and $CuCl_2$. Cd and Pb were predicted to be stable as chlorides from 425 °C. An elevated HCl concentration in the flue gas thereby resulted in increased retention of heavy metals (mainly Zn and Cu) in the gas phase and earlier shift towards formation of chlorides in the solids. The box flux model further predicted the formation of Zn-, Pb-, Cu-, Cd-sulfates in minor concentrations in the electrostatic precipitator. Sb and Sn were predicted to occurr as oxides.

(iii) The solids are dominated by sulfates at a molar ratio S/Cl > 1 in the flue gas. At these conditions, the heavy metals were predicted to start precipitating as sulfates already at 600 - 750 °C and remained in the gas phase only to a minor extent. In order to prevent excessive formation of alkali sulfates, the oxidation of $SO_2(g)$ has to be kinetically constrained when performing thermodynamic equilibrium calculations.

(iv) The dynamic simulations using the box flux model resulted in realistic predictions of mass streams and the assumed distinct transport mechanisms for refractory minerals and precipitated salts turned out to produce realistic mineralogical compositions of the ash fractions. The results confirm, that the transport mechanisms play an important role for the ash mineralogy.

The presented model thus helps to better understand the ash forming processes during cooling of the flue gas and may serve as well to obtain information on possible mineral assemblages too fine grained or low concentrated to be detected by XRD or SEM. It also shows a potential to be further developed to assess specific questions from industry, e.g. regarding the stability of corrosion-promoting phases or for optimizing the composition of the combustion residues with respect to heavy metal extraction.

Acknowledgements

4.7   References

Abanades, S., Flamant, G., Gagnepain, B., Gauthier, D., 2002. Fate of heavy metals during municipal solid waste incineration. Waste Manag. Res. 20, 55–68.

https://doi.org/10.1177/0734242x0202000107

AWEL, 2013. Stand der Technik für die Aufbereitung von Rauchgas- reinigungsrückstän-
den aus Kehrichtverbrennungsanlagen 17–20.

Barthelmy, D., 1997. Webmineral - Mineralogy Database. http://webmineral.com

Bayuseno, A.P., Schmahl, W.W., 2011. Characterization of MSWI fly ash through miner-
alogy and water extraction. Resour. Conserv. Recycl. 55, 524–534.
https://doi.org/10.1016/j.resconrec.2011.01.002

Belo, L.P., Elliott, L.K., Stanger, R.J., Spörl, R., Shah, K. V., Maier, J., Wall, T.F.,
2014. High-temperature conversion of SO_2 to SO_3: Homogeneous experiments and cat-
alytic effect of fly ash from air and oxy-fuel firing. Energy and Fuels 28, 7243–7251.
https://doi.org/10.1021/ef5020346

Bergerhoff, G., Brown, I.D., 1987. The ICSD database, Crystallographic Databases. F.H.
Allen et al. (Hrsg.), Chester.

Bühler, A., Schlumberger, S., 2010. Schwermetalle aus der Flugasche zurückgewinnen
«Saure Flugaschewäsche – FLUWA-Verfahren» ein zukunftsweisendes Verfahren in der
Abfallverbrennung. KVA-Rückstände der Schweiz. Der Rohstoff mit Mehrwert (Bundes-
amt für Umwelt BAFU) 185–192.

Christensen, K.A., Stenholm, M., Livbjerg, H., 1998. The formation of submicron aerosol
particles, HCl and SO_2 in straw-fired boilers. J. Aerosol Sci. 29, 421–444.
https://doi.org/10.1016/S0021-8502(98)00013-5

Churakov, S. V., Tkachenko, S.I., Korzhinskii, M.A., Bocharnikov, R.E., Slimiitovicli,
K.I., 2000. Evolution of composition of high-temperature fumarolic gases from Kudryavy
Volcano, Iturup, Kuril Islands: The thermodynamic modeling. Geokhimiya 38, 485–501.

Cullis, C.F., Henson, R.M., Trimm, D.L., 1966. The kinetics of the homogeneous gaseous
oxidation of sulphur dioxide. Proc. R. Soc. London. Ser. A. Math. Phys. Sci. 295,
72–83. https://doi.org/10.1098/rspa.1966.0226

Fromm, S., Eggenberger, U., Schlumberger, S., Ulrich, M., 2019. Thermische Zerstörung
von Dioxinen und Furanen in sauer gewaschenen KVA Flugaschen (ReFire).

Funatsuki, A., Takaoka, M., Oshita, K., Takeda, N., 2012. Methods of Determining Lead
Speciation in Fly Ash by X-ray Absorption Fine-Structure Spectroscopy and a Sequential
Extraction Procedure. Anal. Sci. 28, 481–490. https://doi.org/10.2116/analsci.28.481

Glarborg, P., Marshall, P., 2005. Mechanism and modeling of the formation of gaseous
alkali sulfates. Combust. Flame 141, 22–39.
https://doi.org/10.1016/j.combustflame.2004.08.014

Glasser, L., Jenkins, H.D.B., 2016. Predictive thermodynamics for ionic solids and liquids. Phys. Chem. Chem. Phys. 18, 21226–21240. https://doi.org/10.1039/c6cp00235h

Gurvich, L.V., Veits, I.V., Medvedev, V.A., et. al., 1982. Termodinamicheskie svoistva individual'nykh veshchestv (Thermodynamic Properties of Individual Compounds). Nauka, Moscow.

Holland, T.J.B., Powell, R., 1998. An internally consistent thermodynamic data set for phases of petrological interest. J. Metamorph. Geol. 16, 309–343. https://doi.org/10.1111/j.1525-1314.1998.00140.x

Hudson Institute of Mineralogy, https://www.mindat.org/

Jain, A., Ong, S.P., Hautier, G., Chen, W., Richards, W.D., Dacek, S., Cholia, S., Gunter, D., Skinner, D., Ceder, G., Persson, K.A., 2013. The Materials Project: A materials genome approach to accelerating materials innovation [WWW Document]. APL Mater. https://doi.org/doi:10.1063/1.4812323

Jiao, F., Cheng, Y., Zhang, L., Yamada, N., Sato, A., Ninomiya, Y., 2011. Effects of HCl, SO_2 and H_2O in flue gas on the condensation behavior of Pb and Cd vapors in the cooling section of municipal solid waste incineration. Proc. Combust. Inst. 33, 2787–2793. https://doi.org/10.1016/j.proci.2010.07.062

Jiménez, S., Ballester, J., 2005. Influence of operating conditions and the role of sulfur in the formation of aerosols from biomass combustion. Combust. Flame 140, 346–358. https://doi.org/10.1016/j.combustflame.2004.12.004

Jiménez, S., Ballester, J., 2007. Formation of alkali sulphate aerosols in biomass combustion. Fuel 86, 486–493. https://doi.org/10.1016/j.fuel.2006.08.005

Kulik, D.A., Chudnenko, K.V., Karpov, I.K., 1993. An Algorithm for Simulating the Evolution of a System of Local-Equilibrium Reservoirs Connected by Mobile Phase-Group Flows. Geochemisty Int. 30.

Kulik, D.A., Wagner, T., Dmytrieva, S. V., Kosakowski, G., Hingerl, F.F., Chudnenko, K. V., Berner, U.R., 2013. GEM-Selektor geochemical modeling package: revised algorithm and GEMS3K numerical kernel for coupled simulation codes. Comput. Geosci. 17, 1–24.

Lindberg, D., Backman, R., Chartrand, P., Hupa, M., 2013. Towards a comprehensive thermodynamic database for ash-forming elements in biomass and waste combustion - Current situation and future developments. Fuel Process. Technol. 105, 129–141. https://doi.org/10.1016/j.fuproc.2011.08.008

Maier, C.G., Kelley, K.K., 1932. An equation for the representation of high-temperature heat content data. J. Am. Chem. Soc. 54, 3243–3246. https://doi.org/10.1021/ja01347a029

Mkilaha, I.S., Yao, H., Naruse, I., 2002. Thermodynamic analysis of the role of chlorine and sulfur environments during combustion and incineration processes. J. Mater. Cycles Waste Manag. 4, 143–149. https://doi.org/10.1007/s10163-002-0069-z

Paoletti, F., Sirini, P., Seifert, H., Vehlow, J., 2001. Fate of antimony in municipal solid waste incineration. Chemosphere 42, 533–543. https://doi.org/10.1016/S0045-6535(00)00225-3

Reed, J.., 1989. The NBS Tables of Chemical Thermodynamic Properties: Selected Values for Inorganic and C1 and C2 Organic Substances in SI Units. National Institute of Standards and Technology. https://doi.org/https://doi.org/10.18434/M32124

Schlumberger, S., Schuster, M., Ringmann, S., Koralewska, R., 2007. Recovery of high purity zinc from filter ash produced during the thermal treatment of waste and inerting of residual materials. Waste Manag. Res. 25, 547–555. https://doi.org/10.1177/0734242X07079870

Stulova, M.I., Martynova, N.S., Susarev, M.P., 1974. Determination of the Enthalpies of Formation of the Compounds $2KCl.ZnCl_2$ and $KCl.2ZnCl_2$, translated from Zhurnal Neorganicheskoi Khimii. Russ. J. Inorg. Chem. 19, 2271–2272.

Swiss Federal Council, 2015. Ordinance on the Avoidance and the Disposal of Waste. (Waste Ordinance, ADWO). (Status of 1 April 2020).

Traber, D., Mäder, U.K., Eggenberger, U., 2002. Petrology and geochemistry of a municipal solid waste incinerator residue treated at high temperature. Schweizerische Mineral. und Petrogr. Mitteilungen 82, 1–14. https://doi.org/10.5169/seals-62348

van Miltenburg, J.C., Noiret, I., Hedoux, A., 1994. Thermodynamic properties of K_2ZnCl_4 between 5 and 350 K. Thermochim. Acta 239, 33–40. https://doi.org/10.1016/0040-6031(94)87053-5

Verhulst, D., Buekens, A., Spencer, P.J., Eriksson, G., 1996. Thermodynamic behavior of metal chlorides and sulfates under the conditions of incineration furnaces. Environ. Sci. Technol. 30, 50–56. https://doi.org/10.1021/es940780+

Wagner, T., Kulik, D., Hingerl, F.F., Dmytrieva, S.V., 2012. GEM-Selektor geochemical modeling package: TSolMod library and data interface for multicomponent phase models. Can. Mineral. 1173–1195.

Weibel, G., Eggenberger, U., Schlumberger, S., Mäder, U.K., 2017. Chemical associations and mobilization of heavy metals in fly ash from municipal solid waste incineration. Waste Manag. 62, 147–159.

Wolffers, M., Eggenberger, U., Schlumberger, S., Churakov, S.V., 2021. Characterization of MSWI fly ashes along the flue gas cooling path and implications on heavy metal

recovery through acid leaching. Waste Manag. 134, 231–240. https://doi.org/10.1016/j.wasman.2021.08.022

Wolffers, M., Weibel, G., Eggenberger, U., 2021. Waste wood fly ash treatment in switzerland: effects of co-processing with fly ash from municipal solid waste on cr(VI) reduction and heavy metal recovery. Processes 9, 1–15. https://doi.org/10.3390/pr9010146

Yoder, C.H., Flora, N.J., 2005. Geochemical applications of the simple salt approximation to the lattice energies of complex materials. Am. Mineral. 90, 488–496. https://doi.org/10.2138/am.2005.1537

Zhang, Y., Chen, Y., Meng, A., Li, Q., Cheng, H., 2008. Experimental and thermodynamic investigation on transfer of cadmium influenced by sulfur and chlorine during municipal solid waste (MSW) incineration. J. Hazard. Mater. 153, 309–319. https://doi.org/10.1016/j.jhazmat.2007.08.054

Chapter 5

PCDD/-F congener distribution along the flue gas cooling path and implications on formation temperatures and mechanisms

M.Wolffers[a], U. Eggenberger[a], D. A. Kulik[b], S. V. Churakov[a,b]

[a] Institute of Geological Sciences, University of Bern

[b] Laboratory for Waste Management, Paul Scherrer Institute

5.1 Abstract

This study performs detailed analysis of the ash fractions arising along the flue gas cooling path of five Swiss MSWI plants with respect to the PCDD/-F toxic equivalent (TEQ), congener distribution profiles, carbon fractionation and specific surface area. It is thereby assessed, whether a significant relationship between one of these variables and the congener distribution in boiler and electrostatic precipitator ashes can be determined. The study is complemented with the estimation of the thermodynamic data for the respective congeners and subsequent calculations of the relative stabilities of PCDD/-F congeners as function of temperature. The analysis shows that the TEQ values differ strongly between the analyzed plants and that the TEQ in the boiler ashes is already > 100 ng/kg in most cases. A common pattern in the distribution of PCDD/-F could be identified, with a trend towards higher relative shares of hepta- and octachlorinated PCDD/-F along the flue gas pathway. The similarity of congener distribution patterns may indicate that the formation of PCDD/-F follows a uniform mechanism (which may include multiple formation mechanisms). Thermodynamic calculations clearly show that the stability of PCDD/-F in the flue gas require strongly reducing conditions, which could only persist in a local environment. This observation can be seen as explanation why it is often impossible to find measurable relationships between the TEQ in the ashes and the operating conditions.

Congener	Molecular Formula	WHO-TEF	I-TEF NATO
2,3,7,8-TCDD	$C_{12}H_4Cl_4O_2$	1	1
1,2,3,7,8-PeCDD	$C_{12}H_3Cl_5O_2$	1	0.5
1,2,3,4,7,8-HxCDD	$C_{12}H_2Cl_6O_2$	0.1	0.1
1,2,3,6,7,8-HxCDD	$C_{12}H_2Cl_6O_2$	0.1	0.1
1,2,3,7,8,9-HxCDD	$C_{12}H_2Cl_6O_2$	0.1	0.1
1,2,3,4,6,7,8-HpCDD	$C_{12}HCl_7O_2$	0.01	0.01
OCDD	$C_{12}Cl_8O_2$	0.0003	0.001
2,3,7,8-TCDF	$C_{12}H_4Cl_4O$	0.1	0.1
1,2,3,7,8-PeCDF	$C_{12}H_3Cl_5O$	0.03	0.05
2,3,4,7,8-PeCDF	$C_{12}H_3Cl_5O$	0.3	0.5
1,2,3,4,7,8-HxCDF	$C_{12}H_2Cl_6O$	0.1	0.1
1,2,3,6,7,8-HxCDF	$C_{12}H_2Cl_6O$	0.1	0.1
1,2,3,7,8,9-HxCDF	$C_{12}H_2Cl_6O$	0.1	0.1
2,3,4,6,7,8-HxCDF	$C_{12}H_2Cl_6O$	0.1	0.1
1,2,3,4,6,7,8-HpCDF	$C_{12}HCl_7O$	0.01	0.01
1,2,3,4,7,8,9-HpCDF	$C_{12}HCl_7O$	0.01	0.01
OCDF	$C_{12}Cl_8O$	0.0003	0.001

Table 5.1: International toxic equivalent factors (I-TEF) for the different congeners

5.2 Introduction

Polychlorinated dibenzo-p-dioxins (PCDDs) and polychlorinated dibenzofurans (PCDFs), herein referred to as PCDD/-F, are a chemical group of 210 organic, chlorinated micropollutants (Cunliffe and Williams, 2009) of environmental concern, as they are resistant to degradation in the environment (Dyke et al., 1997). There exist 75 PCDDs and 135 PCDFs, and each individual structure is termed a congener (McKay, 2002). Their chemical, physical and toxicological characteristics depend mainly on the number and position of chlorine atoms around the two benzene rings (Altarawneh et al., 2009). Only 17 out of the 210 congeners are known as toxic, namely those where the positions 2,3,7,8 are occupied by chlorine atoms. The congener showing the highest toxicity is the tetrachlorodioxin 2,3,7,8-TCDD, classified as "probable" carcinogen (USEPA, 1994). International toxic equivalent factors (I-TEF) have been established for each of the toxic congeners (Table 5.1). Analytical results can be transformed into toxic equivalents (TEQ) by multiplying the measured concentration of each congener with its TEF.

PCDD/-F form as unwanted by-products in combustion processes (Altarawneh et al., 2009). With the entry into force of the Air Pollution Control Ordinance (Swiss Confederation, 1985) in 1986 and the use of efficient flue gas cleaning systems in Swiss waste incineration plants, PCDD/-F emissions via exhaust gases were drastically reduced (Fahrni, 2010). Since then, MSWI fly ash represents the main PCDD/-F input from MSWI incineration into the environment and the threshold limits for landfilling are regulated in the Waste Ordinance (Swiss Federal Council, 2015). The PCDD/-F and their chemical precursors are already present in municipal solid waste. PCDD/-F in MSW may be present as wood preservative or pesticide (McKay, 2002), whereas the organic precursors may be present in paints, organic solvents or rubbers. Favorable combustion conditions (e.g. residence times

of 2s at 850 °C (McKay, 2002)) should lead to the destruction of the PCDD/-F initially present in the MSW. However, PCDD/-F and possible precursors start forming during post-combustion and particularly during the cooling of the flue gas, in the boiler and electrostatic precipitator. Three pathways have been proposed to explain the formation of PCDD/Fs during cooling of the flue gas.

- Homogeneous synthesis, i.e. PCDD/-F formation from structurally related precursors in the gas phase in the presence of Cl and O at temperatures between 400 and 800 °C (Babushok and Tsang, 2003). It was thereby found that Cl present as gaseous Cl_2 was preferably reacting to form PCDD/-F compared to ash-bound chlorine (Wikström et al., 2004). The most important precursors for this reaction are reported to be monocyclic aromatic compounds (e.g. chlorinated phenols and chlorobenzenes (Altarawneh et al., 2009)).

- *De novo* synthesis (heterogeneous), i.e. formation of PCDD/-F from an unrelated organic structure such as any charred material: e.g., carbon, soot or biomass (Peng et al., 2016; Zhang et al., 2018) and the organic or inorganic chlorine present in the fly ash matrix at low temperatures, e.g. 200 - 400 °C (Altarawneh et al., 2009).

- Catalytic-assisted coupling of precursors (heterogeneous), i.e. reactions involving organic precursors that take place on the surface of the fly ash particles, which may be catalyzed by condensation reactions of volatile metals and their salts. It is experimentally confirmed that fly ash exposes vast number of active sites for the adsorption and condensation of e.g., chlorophenols to act as precursor for PCDD/-F formation on the surface of fly ash particles (Peng et al., 2016).

Despite active research on the PCDD/-F formation, the specific mechanisms responsible for the synthesis of these compounds remain unclear. Detailed studies of the formation mechanism are challenging due to the very low concentrations of PCDD/-F in combustion residues, which require complex analytical techniques and instrumentation for accurate analysis (Cunliffe and Williams, 2009; Stanmore, 2004). Thermodynamic modelling would be very helpful to evaluate favorable conditions for PCDD/-F formation. However, the thermodynamic properties derived from the experimental data measured for the different congeners are still incomplete for performing a comprehensive analysis (León et al., 2002). In Switzerland, only acid-leached (and thus metal-extracted) fly ash will be allowed for disposal on landfills from 2026, and the PCDD/-F limit for the disposal of treated fly ash in landfills is set to 1 μg TEQ/kg. Since there is a mass loss of about 25 - 30% during the acid leaching, the critical limit for the untreated fly ash is approx. 750 ng TEQ/kg. A recent Swiss-wide representative study of MSWI fly ashes showed that TEQ ranges between 200 and 2'500 ng/kg (Gaussen-Freidl and Quartier, 2020), confirming, that the TEQ in fly ashes may often exceed the threshold value. However, little is known about the formation mechanisms and the locations of PCDD/-F formation along the flue gas cooling path – an important missing piece of knowledge with regard to the discussion of the disposal

routes of the boiler ash (BOA). Hence, this study aims at investigating the evolution in TEQ along the flue gas cooling path: from the front part of the boiler to the electrostatic precipitator. A congener-specific evaluation is performed together with the analysis of the carbon fractionation (TOC400, ROC and TIC900) and the determination of specific surface area. It is thereby assessed, whether a significant relationship between one of these variables and the congener distribution in boiler- and electrostatic precipitator ashes (ESPA) can be determined. By identifying such relationships, key parameters for the interpretation of PCDD/-F analyses could be derived, which would enormously contribute to the mitigation of the PCDD/-F problem. The analyses are complemented with the evaluation of the standard thermodynamic properties of the different congeners. Subsequent thermodynamic calculations of the cooling of the flue gas involving the gaseous PCDD/-F congeners were conducted to gain a better understanding of their relative stabilities in the gas phase as a function of temperature.

5.3 Materials & Methods

5.3.1 Sampling and characteristics of investigated MSWI plants

The boiler- and ESP ashes from five different Swiss MSWI plants were considered in this study. The five investigated plants (A, C - E, plant B was not included in this study) have similar flue gas cleaning systems with boiler and electrostatic precipitator (ESP) upstream of the flue gas scrubber, whereby dust removal and neutralization are performed separately. All plants except plant F are equipped with a wet flue gas scrubber, while plant F is equipped with a dry flue gas scrubber and the neutralization residues are not collected with the FA but discharged separately. The plants A, C, E, F use *selective non-catalytic reduction* (SNCR) for denitrification, by means of dosing NH_3 into the secondary combustion chamber. Plant D uses *selective catalytic reduction* (SCR) for denitrification and is equipped with a catalyst downstream of the electrostatic precipitator. The plants mainly incinerate municipal- as well as commercial- and industrial waste and show differences in waste throughput capacity and operating conditions (Table 5.2). The sampling strategy, as well as the chemical and mineralogical composition of the samples, were described in a previous study (Wolffers et al., 2021). The supplementary analyses that are discussed in this study were carried out on the dried (105 °C) and analytical fine powder. The boiler ash (BOA) fractions have been numbered such, that they originate from comparable boiler sections (Figure 5.1): BOA1 originates from the boiler hoppers below the evaporator and the last superheater; BOA2 and BOA3 from hoppers below the superheaters; BOA4 from hoppers below the evaporator and BOA 5 from hoppers below the economizer. In boiler types II and III, there is no empty pass, and BOA1 is discarded together with the bottom ash.

Plant-ID	Boiler type	N° of increments / sampling duration	T combustion chamber	T boiler inlet	T boiler outlet	Share of MSW incinerated*	O₂ in Raw Gas	Denitrification System
			°C	°C	°C	%	vol.%, dry	
Plant A	I	28 incr. / 14d	925	650	195	35	10	SNCR
Plant C	III	2 incr. / 6h	860	670	250	45	8	SNCR
Plant D	IV	21 incr. / 7d	840	635	274	48	6	SCR
Plant E	IV	14 incr. / 14d	850	660	260	55	10	SNCR
Plant F	IV	9 incr. / 68h	850	680	260	45	12	SNCR

*The difference to 100% accounts for industrial- and commercial waste, as well as special waste (e.g. ASR, sewage sludge) in minor proportions

Table 5.2: Operation details of the investigated MSWI plants and details on the different sampling campaigns
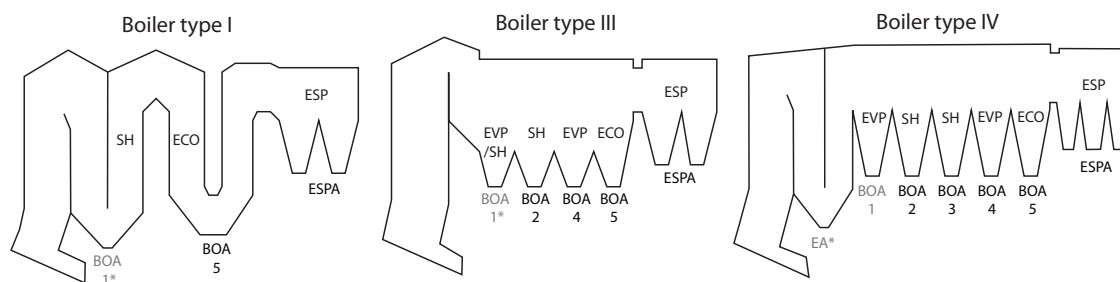
Figure 5.1: Figure 1: Scheme of the different boiler types considered in this study with indications on the function of the different parts. EVP = evaporator, SH = superheater, ECO = economizer, ESP = electrostatic precipitator. Ash fractions marked with * are disposed together with the bottom ash. The fractions where PCDD/-F analyses were made are indicated in black.

5.3.2 PCDD/-F analysis

The PCDD/-F analysis was performed on selected BOA and ESP samples (Figure 5.1). The congener-specific PCDD/-F analysis was performed according to VDI 3499 Bl.1 (VDI, 2003), where the sum of the 17 polychlorinated dibenzo-p-dioxins (PCDD) and dibenzofurans (PCDF) is analyzed according to the international toxicity equivalents (TEQ).

5.3.3 Determination of organic and inorganic carbon

Carbon fractionation was determined by the gradient method (DIN 19539:2016-12). This measurement is based on the temperature-dependent combustion of the carbon in the oxygen stream. The carbon contained in the sample is directly separated into the three fractions TOC400 (organic-bound carbon released up to 400 °C), ROC (residual oxidizable carbon) and TIC900 (inorganic carbon released up to 900 °C).

5.3.4 Determination of specific surface area

The specific surface area (SSA) was determined by nitrogen adsorption. Approximately 3g of unground sample material was thoroughly desorbed of primary adsorbed gases by heating under vacuum at 105°C for 24 h with the BELPREP – vac III pretreatment device. Adsorption isotherms were measured in equilibrium with liquid nitrogen using a BELSORP-miniX surface analyzer. The N-surface area was calculated using the Brunauer,
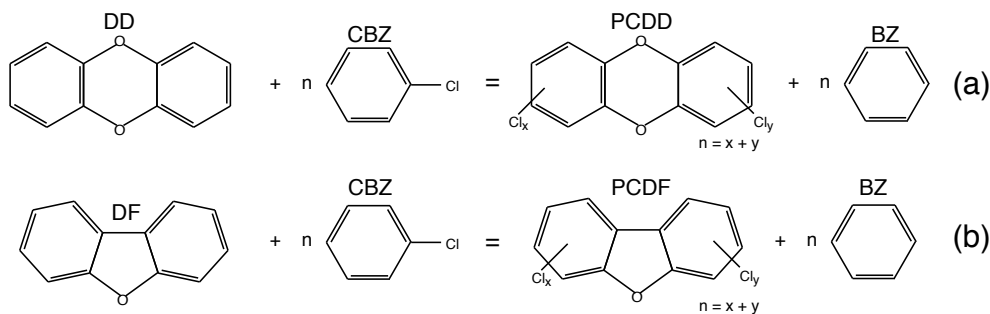
Figure 5.2: Isodesmic reactions describing the formation of PCDD (a) and PCDF (b) from structurally related precursors, adapted from (León et al., 2002) and (Wang et al., 2005).

Emmet and Teller method (BET) (Brunauer et al., 1938) for a pressure range of P/P^0 from 0.05 to 0.3.

5.4 Computational methods

5.4.1 Estimation of standard thermodynamic properties

Standard state thermodynamic properties of 17 PCDD/-F structures and their possible precursors and reactants chlorobenzol (CBZ), benzol (BZ), dibenzodioxin (DD), dibenzofuran (DF) were obtained by density functional theory (DFT) calculations using the Gaussian 09 software (Todorova et al., 2020). The unrestricted DFT calculations were conducted using the B3LYP exchange correlation functional and 6-31G(d,p) basis set. The frequency analysis was performed based on optimized structures, and used for calculation of thermochemical properties for the temperature range of 25 – 800°C. The results obtained from Gaussian provide the sum of electronic and thermal enthalpy (H), whereby $H = \varepsilon_0 + H_{corr}$. ε_0 thereby represents the total electronic energy and H_{corr} represents the thermal correction to the enthalpy (Todorova et al., 2020). The reaction enthalpies $\Delta_r H^\circ$ for the formation of the PCDD/-F congeners were thus retrieved according to Eq. 5.1: :

$$\Delta_r H^\circ_{298K} = \sum_{products} H_{298K} - \sum_{reactants} H_{298K} \tag{5.1}$$

following the respective isodesmic reactions describing the formation of PCDD (Figure 5.2a) and PCDF (Figure 5.2b).

With the use of literature values of $\Delta_f H^\circ$ (Lide, 1996; Luk'yanova et al., 1997; Sabbah, 1991) of the precursors and reactants, the gas-phase enthalpies of formation $\Delta_f H^\circ$ of the PCDD and PCDF structures could be estimated according to Eq. 5.2 and Eq. 5.3, respectively and are listed in Table 5.3.

$$\Delta_f H^\circ_{PCDD} = \Delta_r H^\circ - \Delta_f H^\circ_{BZ} + \Delta_f H^\circ_{DD} + \Delta_f H^\circ_{CBZ} \tag{5.2}$$

$$\Delta_f H^\circ_{PCDF} = \Delta_r H^\circ - \Delta_f H^\circ_{BZ} + \Delta_f H^\circ_{DF} + \Delta_f H^\circ_{CBZ} \tag{5.3}$$

The Maier-Kelley-type parameters (Maier and Kelley, 1932) were derived from the polynomial curve fitting for the calculation of C_p at high temperatures according to the isobaric heat capacity function (Eq. 5.4) and are listed in Table 5.3.

$$C_p^\circ = a_0 + a_1 T + a_2 T^{-2} + a_3 T^{-0.5} + a_4 T^2 \tag{5.4}$$

5.4.2 Uncertainties

The estimated $\Delta_f H^\circ$ values at 298.15 K agree well with values estimated in other studies (comparison in Table C.1). The estimated $\Delta_f H^\circ$ values for PCDD thereby agree within $\pm$ 2.2 kJ/mol with the values estimated in Lee et al., (2003) and within $\pm$ 20.5 kJ/mol with the values estimated in León et al., (2002) and Wang et al., (2004). The estimated $\Delta_f H^\circ$ values for PCDF agree within $\pm$ 5.9 kJ/mol with the values estimated in Wang et al., (2005). The accuracy of the estimated values is thereby primarily dependent on the accuracy of the experimental data to determine $\Delta_f H^\circ$ of the reference compounds and only to a minor extent dependent on the used basis set or the isodesmic reaction (Lee et al., 2003).

5.4.3 Setup of thermodynamic system and thermodynamic calculations

The thermodynamic calculations were performed with the Gibbs energy minimization method (GEM), using the GEM-Selektor code package (Kulik et al., 2013; Wagner et al., 2012), (http://gems.web.psi.ch) and the imported IVTANTERMO thermodynamic database (Gurvich et al., 1982). The estimated standard thermodynamic properties of selected PCDD/-F were added to the database, and their relative stabilities in the gas phase were investigated in batch simulations of the isobaric cooling of the flue gas for the different flue gas variants at different temperatures. The formation of free carbon was thereby kinetically constrained, and 30% of the available hydrogen was constrained to be present as H_2, in order to no let it take part in the reactions, as suggested in Thompson et al., (1997).

5.4.4 Flue gas composition

The ordinary flue gas composition was estimated using the annual mass balances of the investigated MSWI plant D. In order to investigate flue gas conditions favorable for PCDD/-F formation, PCDD/-F concentrations in the flue gas were calculated for different flue gas compositions (variants). The variants include an ordinary flue gas, a reduced flue gas with high Cl content, and an extremely reducing flue gas with different amounts of PVC (C_2H_3Cl) added (characteristics in Table 5.4, detailed input compositions listed in Table C.2). PVC has been identified in many studies (e.g., Zhang et al., 2021; 2015) as a possible Cl donor and a major driving source of PCDD/-F formation within a wide temperature range of 300 - 900°C.

Table 5.3: Estimated standard thermodynamic properties for the different PCDD/F congeners and their possible precursors and reactants at 1 bar, 298.15 K, with the derived Maier-Kelley-type parameters.

Congener	Sum of electronic and thermal Enthalpies H Hartree	Entropy S J/mol K	Heat capacity C_p J/mol K	Enthalpy of formation $\Delta_f H$ kJ/mol	Gibbs Energy of formation $\Delta_f G$ kJ/mol	Maier-Kelley type parameters a_0	a_1	a_2	a_3	a_4
2,3,7,8-TCDD	-2450.76	520.97	241.50	-135.643	1.676	9.670E+02	-1.130E-01	8.394E+06	-1.360E+04	1.572E-05
1,2,3,7,8-PeCDD	-2910.35	550.55	257.15	-137.243	5.031	9.722E+02	-1.179E-01	8.078E+06	-1.333E+04	1.589E-05
1,2,3,4,7,8-HxCDD	-3369.94	578.16	272.64	-137.189	10.628	9.781E+02	-1.231E-01	7.785E+06	-1.308E+04	1.609E-05
1,2,3,6,7,8-HxCDD	-3369.94	578.31	272.71	-138.630	9.142	9.773E+02	-1.229E-01	7.758E+06	-1.306E+04	1.607E-05
1,2,3,7,8,9-HxCDD	-3369.94	577.97	272.68	-137.514	10.360	9.778E+02	-1.232E-01	7.760E+06	-1.307E+04	1.619E-05
1,2,3,4,6,7,8-HpCDD	-3829.53	606.95	288.26	-137.198	15.810	9.840E+02	-1.287E-01	7.469E+06	-1.282E+04	1.648E-05
OCDD	-4289.12	634.46	303.83	-135.574	23.007	9.902E+02	-1.341E-01	7.174E+06	-1.258E+04	1.676E-05
2,3,7,8-TCDF	-2375.56	495.18	224.92	-30.828	83.599	9.333E+02	-1.123E-01	8.370E+06	-1.330E+04	1.622E-05
1,2,3,7,8-PeCDF	-2835.16	522.95	240.48	-41.216	78.707	9.413E+02	-1.196E-01	8.058E+06	-1.307E+04	1.720E-05
2,3,4,7,8-PeCDF	-2835.16	523.14	240.47	-35.054	84.812	9.379E+02	-1.167E-01	8.056E+06	-1.303E+04	1.623E-05
1,2,3,4,7,8-HxCDF	-3294.75	550.86	256.04	-43.745	81.631	9.458E+02	-1.237E-01	7.755E+06	-1.280E+04	1.707E-05
1,2,3,6,7,8-HxCDF	-3294.75	550.96	256.04	-44.966	80.380	9.458E+02	-1.239E-01	7.742E+06	-1.280E+04	1.717E-05
2,3,4,6,7,8-HxCDF	-3294.75	551.03	255.98	-38.182	87.143	9.423E+02	-1.210E-01	7.735E+06	-1.275E+04	1.616E-05
1,2,3,7,8,9-HxCDF	-3294.74	561.78	256.05	-16.052	106.068	9.564E+02	-1.320E-01	7.751E+06	-1.295E+04	1.981E-05
1,2,3,4,6,7,8-HpCDF	-3754.34	578.74	271.52	-46.458	84.379	9.506E+02	-1.283E-01	7.444E+06	-1.253E+04	1.711E-05
1,2,3,4,7,8,9-HpCDF	-3754.33	592.51	271.50	-17.676	109.057	9.610E+02	-1.360E-01	7.457E+06	-1.268E+04	1.960E-05
OCDF	-4213.92	583.61	278.63	-20.559	122.601	9.577E+02	-1.404E-01	7.165E+06	-1.242E+04	1.954E-05
Benzene (BZ)	-232.15	281.70	79.87	82.900[1]	126.066	4.849E+02	-3.975E-02	5.794E+06	-7.924E+03	7.905E-06
Chlorobenzene (CB)	-691.76	316.45	96.15	51.882[1]	98.462	4.905E+02	-4.819E-02	5.275E+06	-7.599E+03	9.642E-06
Dibenzo-p-Dioxin (DD)	-612.36	405.40	177.01	-59.413[2]	57.264	9.563E+02	-9.420E-02	1.016E+07	-1.496E+04	1.446E-05
Dibenzofuran (DF)	-537.17	378.68	160.37	47.300[3]	141.363	9.194E+02	-9.046E-02	1.016E+07	-1.463E+04	1.389E-05

[1] from Lide, (1996)
[2] from Luk'yanova et al., (1997)
[3] from Sabbah, (1991)

	Variant 1	Variant 2	Variant 3	Variant 4	Variant 5
	ordinary flue gas	reduced flue gas with high Cl content	flue gas + 0.2 wt.% PVC	flue gas + 0.33 wt.% PVC	flue gas + 0.46 wt.% PVC
	vol.%	vol.%	vol.%	vol.%	vol.%
Cl_2	0.00	0.74	0.00	0.00	0.00
CO	0.00	6.60	18.5	20.8	16.8
CO_2	6.78	0.17	2.07	0.00	0.00
H_2	9.79	9.76	17.7	22.7	24.2
H_2O	6.44	6.19	2.16	0.00	0.00
HCl	0.17	0.59	7.81	11.0	17.0
N_2	70.1	65.0	51.7	44.5	39.4
O_2	6.64	1.06	8E-18	2E-28	2E-28
SO_2	0.01	0.00	0.00	0.00	0.00
SO_3	0.00	0.01	0.00	0.00	0.00

Table 5.4: Flue gas concentrations (in vol.%) of the different variants at 1 bar, 800°C.

5.5 Results & Discussion

5.5.1 Evolution of TEQ along the flue gas cooling path

Most of the samples show TEQ values below the threshold limit of 1000 ng/kg TS (Figure 5.3). Generally, an increase in TEQ can be observed in flue gas direction, with highest values in the ESPA. However, the absolute TEQ values vary greatly between the different plants. For plant D, the TEQ of BOA3 and ESPA strongly exceeds the threshold value for landfill type C and D by multiple factors. The TEQ values of the different plants cannot be related to the operating parameters (e.g. O_2 content), as also observed by Streibel et al. (2007). It is remarkable that the TEQ in the boiler ashes are already > 100 ng/kg for most plants. It can be observed that the TEQ strongly increases from BOA4 (corresponding to approximately 375 - 450°C) and reach the highest value in the ESPA. A sharp increase in TEQ in a similar temperature range was also observed by Düwel et al., (1990), representing temperatures typical for heterogeneous catalytic reactions (Zhang et al., 2018). PCDD/-F formation thus occurred over the entire boiler section, as also observed in other studies (Allegrini et al., 2014; Düwel et al., 1990; Giugliano et al., 2001). A strong increase of PCDD/-F concentration in the gas phase was thereby observed by Giugliano et al., (2001) between the boiler inlet and the fabric filter. However, the local temperature profiles within the different boiler sections are not precisely known, and there are expected deviations from the flue gas temperature especially in the deposits, as well as in the lower part of the boiler hoppers, where the boiler ash is collected. Lower temperatures in these parts may also lead to formation of PCDD/-F in regions of higher flue gas temperature, as also mentioned in Allegrini et al., (2014). Interesting are the very low TEQ (< 50 ng/kg) in the boiler ashes from plant F. In a previous study (Wolffers et al., 2021) it was observed that these boiler ashes predominantly consist of deposits formed around heat exchanger tubes and show comparably low Cl concentrations. These deposits have longer residence times in the boiler section, as they form within the flue gas stream around the heat exchanger tubes and may be exposed to the moving flue gas over several minutes to hours/days until

Structure	Enthalpy of Formation $\Delta_f H$ this study J/mol	Difference in enthalpy of formation $\Delta_f H$ to other studies			
		Leon et al. 2002 J/mol	Lee et al. 2003 J/mol	Wang et al. 2004 J/mol	Wang et al. 2005 J/mol
2,3,7,8-TCDD	-135642.64	4'961	-1'249	-9'033	
1,2,3,7,8-PeCDD	-137242.76	7'861	1'427	-11'793	
1,2,3,4,7,8-HxCDD	-137188.84	10'815	-1'749	-14'829	
1,2,3,6,7,8-HxCDD	-138630.22	10'873	-2'555	-14'590	
1,2,3,7,8,9-HxCDD	-137275.09	11'509	1'740	-14'754	
1,2,3,4,6,7,8-HpCDD	-137197.94	14'206	1'926	-17'608	
OCDD	-135573.99	17'829	-2'227	-20'514	
2,3,7,8-TCDF	-30828.05				3'048
2,3,7,8-PeCDF	-4'315.59				4'146
2,3,4,7,8-PeCDF	-35053.63				-3'994
1,2,3,4,7,8-HxCDF	-43745.12				-5'015
1,2,3,6,7,8-HxCDF	-44969.96				-5'006
2,3,7,8,9-HxCDF	16051.77				3'992
2,3,4,6,7,8-HxCDF	-38181.77				-4'782
1,2,3,4,6,7,8-HpCDF	-46458.43				-5'898
1,2,3,4,7,8,9-HpCDF					
OCDF	20559.49				15'629

Figure 5.3: PCDD/-F concentration as TEQ for the analyzed samples, displayed in logarithmic scale (left). The threshold limit for landfills type C and D is marked in red (1000 ng/kg). The respective temperature profiles are plotted in the right figure (grey lines interpolated due to missing data).

they are mechanically removed through the rapping gears. It is thus surprising that these ashes show lower TEQ than the airborne ash particles that have residence times of only a few seconds in the boiler area. However, this is in accordance with other studies that have analyzed PCDD/-F in sieved coarse fractions of fly ash (Weidemann et al., 2016) or deposits obtained through the operation of rapping gears (Wunsch et al., 1994).

5.5.2 TOC fractionation along the flue gas cooling path

The TOC content is generally higher in the boiler ashes compared to the ESPA (Figure 5.4). The TOC400 content shows the organically bound carbon, and its distribution along the flue gas cooling path is relatively stable. The residual oxidizable carbon (ROC) is associated with coal and soot particles. The constant proportion of ROC over the respective boiler ash fractions of a plant and the subsequent decrease of the ROC content in the ESPA agrees with macroscopic observations. The TIC900 content indicates the outgassing of CO_2 from minerals, e.g. through the decomposition of calcite. The concentration distribution
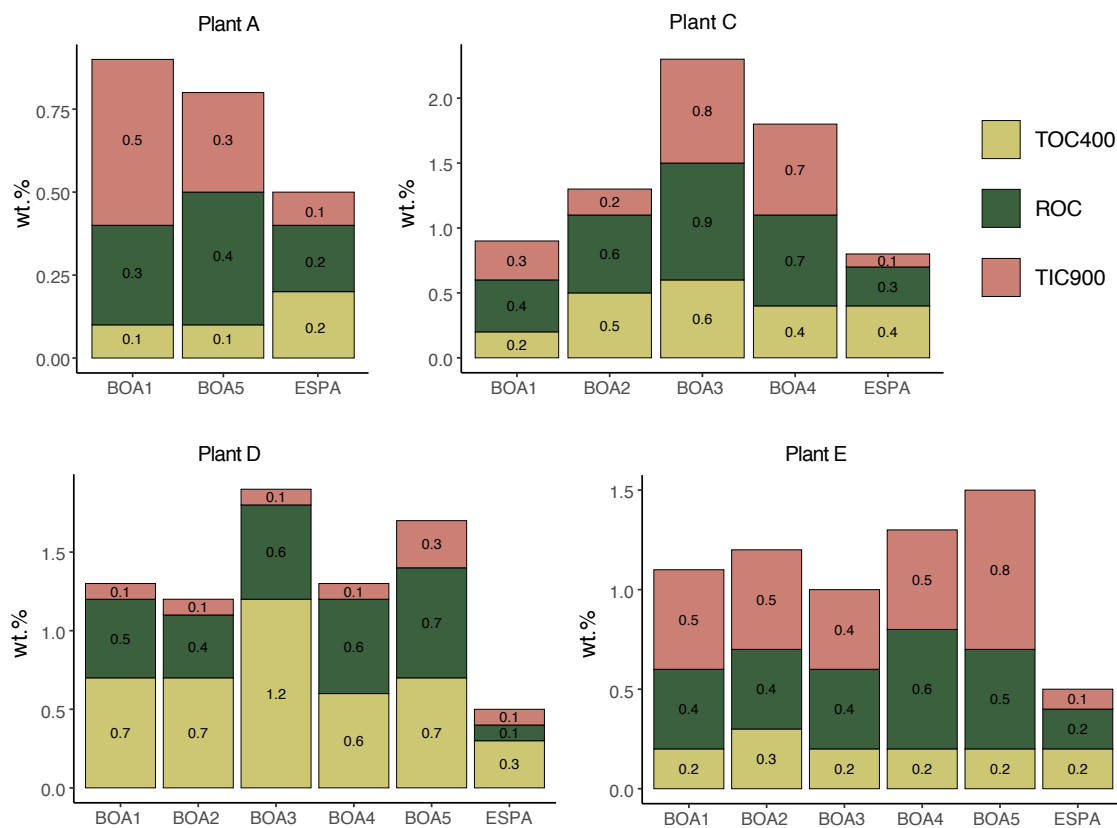
Figure 5.4: TOC400, ROC and TIC900 content of the different ash fractions. The concentrations for the plant F, were below detection limit for each carbon fraction.

is consistent with the distribution of carbonates in BOA and ESPA, where the boiler ashes show the higher concentrations (Wolffers et al., 2021). It is interesting that the TOC400 values are the highest for Plant D, which shows the highest TEQ, especially in the case of sample BOA3. For plant F, the TOC values for all analyzed ash fractions were below detection limit.

5.5.3 Correlations

The linear correlations between TEQ and the variables Cu content, TOC, carbon fractions (TOC400, ROC, TIC900) and SSA are poor (Figure 5.5). Further, no statistically significant correlations between the congener distribution and any of the carbon fractions could be observed (Table C.3). However, it is a matter of question whether the comparison of extremely low PCDD/-F concentrations in the ng/kg range with e.g., ROC concentrations in the % range represents a meaningful approach, as the two variables do not represent the same resolution. Furthermore, the investigated variables are available in excess and do not seem to represent limiting factors for the formation of PCDD/-F.

5.5.4 Congener distribution profiles

The congener concentrations of the different ash fractions are listed in Table C.4. Figure 5.6a shows the distribution pattern of the different PCDD and PCDF congeners along the
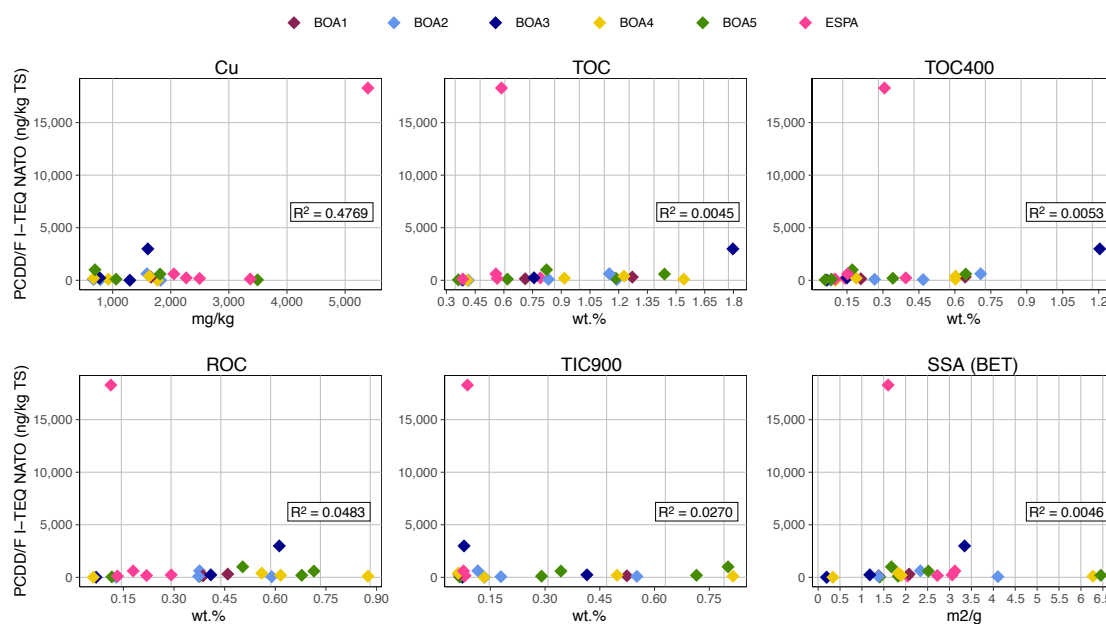
Figure 5.5: Poor correlation between TEQ and Cu content, TOC, carbon fractions and specific surface area (SSA) for the different ash fractions.

flue gas cooling path as percent share of concentration sum. Interestingly, the distribution profiles of PCDD congeners show strong similarities to the distribution of PCDF congeners. For PCDD, a trend of increasing OCDD concentration share along the flue gas path is observed for the plants D - F. OCDD also represents the dominant congener in plants A and C, but with a less clear distribution trend. The 1,2,3,4,6,7,8-HpCDD represents the second most abundant congener in most plants. For the plants D - F, a trend towards decreasing 1,2,3,4,6,7,8-HpCDD concentration with the flue gas path is observed. For the plants D - F these two most abundant congeners make almost 100% share of concentration sum towards the end of the boiler and in the ESPA. Similarly, for the PCDF, the hepta and octachlorinated 1,2,3,4,6,7,8-HpCDF and OCDF represent the most abundant congeners. An increase in the proportion of hepta- and octachlorinated PCDFs is observed along the flue gas path. In contrast to PCDDs, the concentration share of the heptachlorinated congener is dominant over OCDF in most samples, and the ratio is mostly balanced in the others. It is interesting to note that even the two samples with the extremely high TEQ (BOA3 and ESPA of plant D) show a similar trend in the distribution pattern. The relative congener distributions of the ashes of this study fit well with that of a previous study (Cunliffe and Williams, 2009). The fact that the concentration distribution pattern of PCDD and PCDF is similar could be indicative of the same formation mechanisms. The PCDD/PCDF ratio in relation to the total concentration varies between 0.3 and 6.1. The amount of PCDD dominates over the amount of PCDF in the majority of the ash fractions, but no clear trend can be detected related to the flue gas cooling path. Only in plant E, a trend towards increasing PCDD/PCDF ratio can be recognized in flue gas direction.
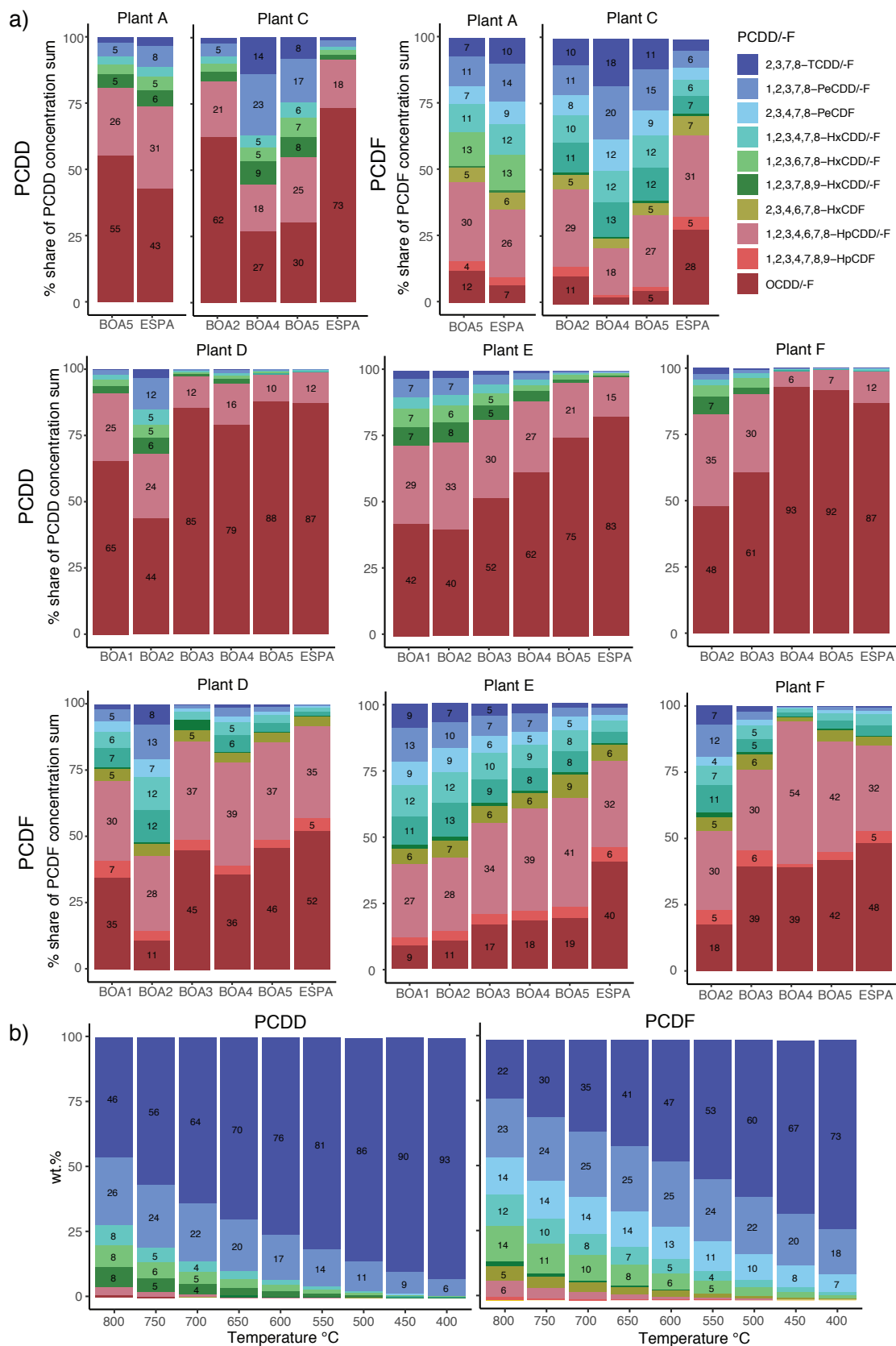
Figure 5.6: Percent share of concentration sum for the different congeners for PCDD and PCDF, determined in the different ash fractions (a) and distribution profiles obtained through thermodynamic modelling (b), results from variant 4.

5.5.5 Relative stabilities of congeners

Thermodynamic calculations show that the PCDD/-F are not stable at ordinary flue gas conditions (variant 1), showing equilibrium activities less than 10^{-265}. Even with relatively low oxygen contents for flue gas (1 vol.% O_2, (variant 2)), the PCDD/-F are thermodynamically unstable. According to the thermodynamic calculations, PCDD/-F would be stable in the flue gas at strongly reducing conditions, impossible to achieve in the bulk flue gas environment. Such conditions can only be imagined in an extremely local micro-environment with negligible O_2 fugacities ($<10^{-30}$) and high CO, H_2 and HCl concentrations in the tens of percent range. Such conditions could be obtained in variant 4 and 5 by adding the composition of PVC (C_2H_3Cl) in mass ratio $>$ 1:2 to the flue gas. If these conditions are met, equilibrium activities of PCDD/-F are strongly elevated compared to variants 1 - 3, and the PCDF congeners form in the mg/kg concentration range, while the predicted PCDD concentrations are considerably lower in the 10^{-13} mg/kg range (Table C.5). In variant 3, the PVC/flue gas mass ratio was not high enough to obtain sufficiently low O_2 activities for the PCDD/-F congeners to become thermodynamically stable. The equilibrium stabilities of PCDD/-F seem to rise strongly as soon as suitable conditions are met – leading to PCDD/-F formation in significant concentrations. The calculated concentrations for PCDF are several orders of magnitude higher than those measured. Regarding the assumption that the PCDD/-F form in micro-environments, such as burning PVC particles, once suitable conditions are reached, this may manifest a dilution or a decomposition effect. Interestingly, the PCDF activities are several orders of magnitude higher than the PCDD activities, which is also observed by Tan et al., (2001). This could be related to the fact that dioxins have two oxygen atoms in their structure, while furans have only one oxygen atom incorporated, with regard to the negligible oxygen activities. However, with higher oxygen activity (variant 3), the PCDD/-F remain thermodynamically unstable. Despite their predicted thermodynamic instability at oxidizing conditions, the PCDD/-F congeners seem to persist as thermodynamically metastable compounds in the macroscopic flue gas system once they have been formed, possibly due to slows oxidation kinetics.

5.5.6 Comparison of observed and predicted congener distribution pattern

As seen in Figure 5.6b, the observed congener distribution pattern in the ash fractions do not match well the thermodynamically predicted congener distribution pattern in the gas phase. While the hepta- and octachlorinated congeners are observed to be the dominant congeners in the ash fractions, they are only predicted to form in negligible percent shares in our calculations. For PCDD, 2,3,7,8-TCDD is predicted to be the dominant congener, together with 1,2,3,7,8-PeCDD. For PCDF, it is also the tetra- and pentachlorinated congeners that dominate the distribution pattern, together with 1,2,3,4,7,8- and 1,2,3,6,7,8-HxCDF. Generally, the predicted percent share of the lower chlorinated congeners (mainly

tetra and pentachlorinated) increase with decreasing temperatures. The presence of low-chlorinated PCDF as dominant congeners in the gas phase has already been described by several authors (Giugliano et al., 2001; Takaoka et al., 2003; Tejima et al., 2007). Nevertheless, our observation confirms that the PCDD/-F pattern in the ash cannot solely be explained through the condensation of gas phase PCDD/-F. A poor correlation between the PCDD/-F concentration in the gas phase and the PCDD/-F concentration in the solid residues was thereby also observed by Streibel et al., 2007.

5.6 Conclusion

The congener-specific PCDD/-F analyses of the different fly ash fractions represent a unique data set which helps to gain some further insights into possible formation temperatures and mechanisms along the flue gas pathway, which can be summarized into the following points:

(i) It was observed that the TEQ values differ strongly between the studied plants and that the PCDD/-F formation occurs already in the hot part of the boiler. The TEQ in the boiler ashes increased with decreasing temperature (especially after the superheater sections of the boiler at approximately 400 °C) and the ESPA clearly showed the highest TEQ. In several plants, a strong increase in TEQ can be observed from the last boiler ash to the ESPA.

(ii) No linear relationships between carbon fractionation, Cl- and Cu concentration, specific surface area and relative congener distributions could be identified for the different ash fractions. However, it is questionable, whether the comparison of extremely low PCDD/-F concentrations in the ng/kg range with e.g., ROC concentrations in the % range represents a meaningful approach, as the two variables do not represent the same resolution. Furthermore, the investigated variables are available in excess and do not seem to represent limiting factors for the formation of PCDD/-F.

(iii) A common pattern in the PCDD/-F distribution pattern could be identified, with a trend toward higher relative proportions of hepta- and octachlorinated PCDD/-F along the flue gas pathway. The fact that the distribution patterns are so similar in all investigated MSWI plants implies that the formation of PCDD/-F follows a consistent process (which may include multiple formation mechanisms). To address the question of whether the low-chlorinated congeners preferentially adhere to soot particles, a congener-specific PCDD/-F analysis of soot particles would be of interest.

(iv) The thermodynamic calculations clearly show that strongly reducing conditions are required for the stability of PCDD/-F in the flue gas, which could only be simulated in the form of an extremely local microenvironment with O_2 activities $<10^{-30}$ in the presence of non-reactive H_2 and high CO and HCl concentrations in the tens of percent range. These conditions could be obtained by adding PVC (C_2H_3Cl) in

mass ratio > 1:2 relative to the flue gas. The equilibrium stabilities of PCDD/-F were predicted to rise strongly as soon as suitable conditions are met – leading to PCDD/-F formation in significant concentrations. Such micro-environment may be associated to the close environment of the combustion of a plastic particle, and cannot be captured with coarse-resolution operating parameters such as O_2 content in the flue gas, which explains why there are no identifiable relations between the TEQ and the operating parameters. Nevertheless, despite their predicted thermodynamic instability at oxidizing conditions, the PCDD/-F congeners seem to persist as thermodynamically metastable compounds in the macroscopic flue gas system once they have been formed, possibly due to slow oxidation kinetics.

The results obtained provide a valuable data basis regarding the formation temperatures and PCDD/-F contents in the boiler ashes. The complete data set with thermodynamic data of the congeners can be used for the calculation of stabilities in other environments or different flue gas variants. With regard to the decision on the disposal route of the boiler ash, the PCDD/-F concentrations in boiler ashes should also be considered in addition to the heavy metal concentrations, binding form and leachability, especially if a subsequent dioxin destruction mechanism is applied for the filter cakes.

Acknowledgements

5.7   References

Allegrini, E., Jansson, S., Lundtorp, K., Fruergaard Astrup, T., 2014. Quality and generation rate of solid residues in the boiler of a waste-to-energy plant. J. Hazard. Mater. 270, 127–136. https://doi.org/10.1016/j.jhazmat.2014.01.048

Altarawneh, M., Dlugogorski, B.Z., Kennedy, E.M., Mackie, J.C., 2009. Mechanisms for formation, chlorination, dechlorination and destruction of polychlorinated dibenzo-p-dioxins and dibenzofurans (PCDD/Fs). Prog. Energy Combust. Sci. 35, 245–274. https://doi.org/10.1016/j.pecs.2008.12.001

Babushok, V.I., Tsang, W., 2003. Gas-phase mechanism for dioxin formation. Chemosphere 1023–1029.

Brunauer, S., Emmett, P.H., Teller, E., 1938. Adsorption of Gases in Multimolecular Layers. J. Am.Chem.Soc. 60, 309–319.
https://doi.org/https://doi.org/10.1021/ja01269a023

Cunliffe, A.M., Williams, P.T., 2009. De-novo formation of dioxins and furans and the memory effect in waste incineration flue gases. Waste Manag. 29, 739–748. https://doi.org/10.1016/j.wasman.2008.04.004

DIN 19539:2016-12, 2016. Untersuchung von Feststoffen - Temperaturabhängige Differenzierung des Gesamtkohlenstoffs (TOC400, ROC, TIC900).

Düwel, U., Nottrodt, A., Ballschmiter, K., 1990. Simultaneous sampling of PCDD/PCDF inside the combustion chamber and on four boiler levels of a waste incineration plant. Chemosphere 20, 1839–1846. https://doi.org/10.1016/0045-6535(90)90350-3

Dyke, P.H., Foan, C., Wenborn, M., Coleman, P.J., 1997. A review of dioxin releases to land and water in the UK. Sci. Total Environ. 207, 119–131. https://doi.org/10.1016/S0048-9697(97)00254-4

Fahrni, H.-P., 2010. Von der wilden Deponie zu den Verbrennungsrückständen, in: KVA-Rückstände in Der Schweiz. Der Rohstoff Mit Mehrwert (Bundesamt Für Umwelt BAFU). pp. 11–24.

Gaussen-freidl, B., Quartier, R., 2020. Messkampagne KVA-Asche 2020 Inhalt.

Giugliano, M., Cernuschi, S., Grosso, M., Aloigi, E., Miglio, R., 2001. The flux and mass balance of PCDD/F in a MSW incineration full scale plant. Chemosphere 43, 743–750. https://doi.org/10.1016/S0045-6535(00)00428-8

Gurvich, L.V., Veits, I.V., Medvedev, V.A., et. al., 1982. Termodinamicheskie svoistva individual'nykh veshchestv (Thermodynamic Properties of Individual Compounds). Nauka, Moscow.

Kulik, D.A., Wagner, T., Dmytrieva, S. V., Kosakowski, G., Hingerl, F.F., Chudnenko, K. V., Berner, U.R., 2013. GEM-Selektor geochemical modeling package: revised algorithm and GEMS3K numerical kernel for coupled simulation codes. Comput. Geosci. 17, 1–24.

Lee, J.E., Choi, W., Mhin, B.J., 2003. DFT calculation on the thermodynamic properties of polychlorinated dibenzo-p-dioxins: Intramolecular Cl-Cl repulsion effects and their thermochemical implications. J. Phys. Chem. A 107, 2693–2699. https://doi.org/10.1021/jp027133m

León, L.A., Notario, R., Quijano, J., Sánchez, C., 2002. Structures and enthalpies of formation in the gas phase of the most toxic polychlorinated dibenzo-p-dioxins. A DFT study. J. Phys. Chem. A 106, 6618–6627. https://doi.org/10.1021/jp025602e

Lide, D.R. (Ed.), 1996. CRC Handbook of Chemistry and Physics, 77th ed. CRC Press, Boca Raton, FL.

Luk'yanova, V.A., Kolesov, V.P., Avramenko, N.V., Vorob'eva, V.P., Golovkov, V.F., 1997. Standard enthalpy of formation of dibenzo-p-dioxine. Russ. J. Phys. Chem. (Engl. Transl.) 71, 338–340.

Maier, C.G., Kelley, K.K., 1932. An equation for the representation of high-temperature heat content data. J. Am. Chem. Soc. 54, 3243–3246. https://doi.org/10.1021/ja01347a029

McKay, G., 2002. Dioxin characterisation, formation and minimisation during municipal solid waste (MSW) incineration: Review. Chem. Eng. J. 86, 343–368. https://doi.org/10.1016/S1385-8947(01)00228-5

Peng, Y., Chen, J., Lu, S., Huang, J., Zhang, M., Buekens, A., Li, X., Yan, J., 2016. Chlorophenols in Municipal Solid Waste Incineration: A review. Chem. Eng. J. 292, 398–414. https://doi.org/10.1016/j.cej.2016.01.102

Sabbah, R., 1991. Thermodynamic study of fluorene and dibenzofuran. Bull. Soc. Chim. Fr 128, 350.

Smolka, A., Schmidt, K.G., 1997. Gas/particle partitioning before and after flue gas purification by an activated-carbon-filter. Chemosphere 34, 1075–1082. https://doi.org/10.1016/S0045-6535(96)00409-2

Stanmore, B.R., 2004. The formation of dioxins in combustion systems. Combust. Flame 136, 398–427. https://doi.org/10.1016/j.combustflame.2003.11.004

Streibel, T., Nordsieck, H., Neuer-Etscheidt, K., Schnelle-Kreis, J., Zimmermann, R., 2007. Experimental and statistical determination of indicator parameters for the evaluation of fly ash and boiler ash PCDD/PCDF concentration from municipal solid waste incinerators. Chemosphere 67, 155–163. https://doi.org/10.1016/j.chemosphere.2006.05.151

Swiss Confederation, 1985. Air pollution control ordinance. Bern.

Swiss Federal Council, 2015. Ordinance on the Avoidance and the Disposal of Waste. (Waste Ordinance, ADWO). (Status of 1 April 2020).

Takaoka, M., Liao, P., Takeda, N., Fujiwara, T., Oshita, K., 2003. The behavior of PCDD/Fs, PCBs, chlorobenzenes and chlorophenols in wet scrubbing system of municipal solid waste incinerator. Chemosphere 53, 153–161. https://doi.org/10.1016/S0045-6535(03)00437-5

Tan, P., Hurtado, I., Neuschütz, D., Eriksson, G., 2001. Thermodynamic modeling of pcdd/fs formation in thermal processes. Environ. Sci. Technol. 35, 1867–1874. https://doi.org/10.1021/es000218l

Tejima, H., Nishigaki, M., Fujita, Y., Matsumoto, A., Takeda, N., Takaoka, M., 2007. Characteristics of dioxin emissions at startup and shutdown of MSW incinerators. Chemosphere 66, 1123–1130. https://doi.org/10.1016/j.chemosphere.2006.06.015

Thompson, W.T., Eriksson, G., Bale, W.D., Pelton, A.D., 1997. Applications of F*A*C*T in high temperature Materials Chemistry, in: Proc.-Electrochem. Soc.

Todorova, T.K., Schreiber, M.W., Fontecave, M., 2020. Thermochemistry in Gaussian. ACS Catal. 10, 1754–1768.

USEPA, 1994. Combustion Emissions Technical Resource Document, Report No. EPA 530-R-94-014. Washington, DC.

Verein Deutscher Ingenieure (VDI), 2003. VDI 3499 Blatt 1

Wagner, T., Kulik, D., Hingerl, F.F., Dmytrieva, S.V., 2012. GEM-Selektor geochemical modeling package: TSolMod library and data interface for multicomponent phase models. Can. Mineral. 1173–1195.

Wang, Z.Y., Zhai, Z.C., Wang, L.S., 2005. Prediction of gas phase thermodynamic properties of polychlorinated dibenzo-furans by DFT. J. Mol. Struct. THEOCHEM 725, 55–62. https://doi.org/10.1016/j.theochem.2005.01.037

Wang, Z.Y., Zhai, Z.C., Wang, L.S., Chen, J.L., Kikuchi, O., Watanabe, T., 2004. Prediction of gas phase thermodynamic function of polychlorinated dibenzo-p-dioxins using DFT. J. Mol. Struct. THEOCHEM 672, 97–104. https://doi.org/10.1016/j.theochem.2003.11.030

Weidemann, E., Allegrini, E., Fruergaard Astrup, T., Hulgaard, T., Riber, C., Jansson, S., 2016. Size fractionation of waste-to-energy boiler ash enables separation of a coarse fraction with low dioxin concentrations. Waste Manag. 49, 110–113. https://doi.org/10.1016/j.wasman.2016.01.027

Wikström, E., Ryan, S., Touati, A., Tabor, D., Gullett, B.K., 2004. Origin of carbon in polychlorinated dioxins and furans formed during sooting combustion. Environ. Sci. Technol. 38, 3778–3784.

Wolffers, M., Eggenberger, U., Schlumberger, S., Churakov, S.V., 2021. Characterization of MSWI fly ashes along the flue gas cooling path and implications on heavy metal recovery through acid leaching. Waste Manag. 134, 231–240. https://doi.org/10.1016/j.wasman.2021.08.022

Wunsch, P., Leichsenring, S., Schramm, K.W., Kettrup, A., 1994. Temperature Dependence of PCDD/F-Formation in Boiler Ash. Chemosphere 29, 1235–1243.

Zhang, M., Buekens, A., Jiang, X., Li, X., 2015. Dioxins and polyvinylchloride in combustion and fires. Waste Manag. Res. 33, 630–643.
https://doi.org/10.1177/0734242X15590651

Zhang, M., Buekens, A., Li, X., 2018. Characterising boiler ash from a circulating fluidised bed municipal solid waste incinerator and distribution of PCDD/F and PCB. Environ. Sci. Pollut. Res. 25, 22775–22789.
https://doi.org/10.1007/s11356-018-2402-7

Zhang, M., Fujimori, T., Shiota, K., Li, X., Takaoka, M., 2021. Formation pathways of polychlorinated dibenzo-p-dioxins and dibenzofurans from burning simulated PVC-coated cable wires. Chemosphere 264, 128542.
https://doi.org/10.1016/j.chemosphere.2020.128542

Zhong, R., Wang, C., Zhang, Z., Liu, Q., Cai, Z., 2020. PCDD/F levels and phase distributions in a full-scale municipal solid waste incinerator with co-incinerating sewage sludge. Waste Manag. 106, 110–119.
https://doi.org/10.1016/j.wasman.2020.03.020

Chapter 6

Waste wood fly ash treatment in Switzerland: Effects of co-processing with fly ash from municipal solid waste on Cr(VI) reduction and heavy metal recovery

M.Wolffers[a], G. Weibel[a], U. Eggenberger[a]

[a] Institute of Geological Sciences, University of Bern

Abstract

In Switzerland, waste wood fly ash (WWFA) has to be treated before deposition on landfills due to its high pollutant load (Cr(VI) and other toxic heavy metals). Acid fly ash leaching, the process used for heavy metal recovery from municipal solid waste incineration fly ash (MSWIFA), represents a possible treatment for heavy metal depletion and Cr(VI) reduction in WWFA. The co-processing of WWFA with MSWIFA during acid fly ash leaching was investigated in laboratory- and industrial-scale experiments with different setups. Of interest were the effects on heavy metal recovery efficiency, successful outcome of Cr(VI) reduction and consumption of neutralizing chemicals (HCl, H_2O_2). Detailed chemical and mineralogical characterization of two WWFA types and MSWIFA showed, that MSWIFA has higher concentrations in potentially harmful elements than WWFA. However, both WWFA types showed high concentrations in Pb and Cr(VI), and therefore need treatment prior to deposition. Depending on the waste wood proportion and quality, WWFA showed chemical and mineralogical differences which affect the leaching behavior. In all experimental setups, successful Cr(VI) reduction was achieved. However, WWFA showed higher consumption of HCl and H_2O_2, the latter resulting in particularly negative effect on the recovery of Pb and Cu. Thus, co-processing of smaller WWFA portions could be expedient in order to diminish the negative effects of Pb and Cu recovery.

6.1   Introduction

The demand of renewable heat- and energy production using the CO_2 neutral energy source wood has been growing enormously in Switzerland over the last decades – leading to strongly increasing amounts of wood ashes. In Switzerland, an annual load of 60'000 t wood ash arises from automatic firings through the energetic use of natural wood (e.g. forest) and from the thermal utilization of waste wood (e.g. coated, painted wood) (Swiss Confederation, 2020). A quarter thereof represents wood ash from waste wood enriched in heavy metals and Cr(VI). Depending on incinerator plant and furnace, wood ash can be divided in up to three different fractions: grate ash, cyclone ash and filter ash (Obernberger, 1997). The coarse-grained grate ash arises directly from the grate and is equivalent to bottom ash residing from municipal solid waste incineration (MSWI). It is the biggest fraction with roughly 60 - 90 wt.% of the thermal residue (Obernberger, 1997). The cyclone ash and the filter ash arise at the flue gas cleaning system and are often collected together and referred to as wood fly ash. Compared to grate ash, wood fly ash is enriched in volatile elements (e.g. Cl, heavy metals), since their low boiling point make them evaporate during combustion and later precipitate at the flue gas cleaning system (Zimmermann et al., 2010). The chemical composition of wood ash is mainly dependent on wood quality and incineration conditions (Zimmermann et al., 2010; Tarelho et al., 2012). Factors affecting wood quality are: wood type, compartment, growing environment and possible treatments (e.g. impregnation) prior to combustion (Zimmermann et al., 2010; Etiégni et al.1991). While wood ash from natural wood may be enriched in organic pollutants (e.g. PAH, PCDD-/F (Wunderli et al., 2000)) and can contain naturally incorporated heavy metals in elevated concentrations, the contaminated waste wood ash is mostly characterized by highly elevated heavy metal concentrations (e.g. Zn, Pb, Cu, Cr) remaining from paints, coatings or impregnation (Huron et al., 2017). Due to the oxidative conditions during combustion, Cr(III) compounds are mainly oxidized to very toxic and highly mobile Cr(VI) (Pohlandt-Schwandt, 1999). Thermal residues from waste wood which have been impregnated with Cr-bearing compounds are often severely enriched in Cr(VI). In water extraction tests, studies report Cr(VI) concentrations in waste wood ash that exceed threshold value for landfilling (Pohlandt-Schwandt, 1999; Pohlandt-Schwandt et al., 2002). Because of the possibly high contaminant load, wood ash is considered as waste and has to be dumped on landfills, although opportunities for recycling are being sought (e.g. in concrete production (Teixeira et al. 2019)). The less polluted grate ash and fly ash from natural wood can be deposited without further treatment on landfill type D and E according to the Swiss Waste Ordinance (Swiss Federal Council, 2015). Waste wood fly ash (WWFA), however, has to be treated before deposition due to the elevated concentrations in Cr(VI) and possibly environmentally harmful heavy metals. As there is currently not enough capacity available in Cr(VI) reducing facilities in Switzerland to treat the entire quantity of WWFA before landfilling, waste wood fly ashes can be deposited temporarily without a prior treatment on landfill type D or E (depending on their TOC content (<2 or <5 wt.%, respectively) until end of 2023. From 2024 on, WWFA has to be treated in order to reduce Cr(VI) and

recover the heavy metals. Acid fly ash leaching with the FLUWA process (Schlumberger et al., 2007; Bühler and Schlumberger, 2010) represents a promising method for treating WWFA prior to deposition. The FLUWA process represents the state-of-the-art process in Switzerland for recovering heavy metals (mainly Zn, Cd, Pb, Cu) from the similarly generated MSWI fly ash (MSWIFA). The ash is thereby leached with acid scrub water, an acid from the flue gas cleaning system (5% HCl). Filtration of the ash slurry yields a heavy metal enriched leachate that is then precipitated to a hydroxide sludge for subsequent heavy metal recovery and a filter cake depleted in heavy metals that is deposited on landfills. Because WWFA can yield heavy metal concentrations in the same range as MSWIFA, but occur in smaller quantities, a co-treatment of both ashes could be expedient. Since 2021, all Swiss MSWIFA have to be treated before deposition (Swiss Federal Council, 2015) and depending on the heavy metal recovery guideline in revision, the use of an oxidant (e.g. hydrogen peroxide (H_2O_2)) will be necessary during the FLUWA process. Oxidizing conditions during metal extraction are a prerequisite to suppress the reductive precipitation of the redox-sensitive elements Cu, Pb, and to a minor extent, Cd. The co-processing of WWFA in the FLUWA process is already carried out at this study's investigation site Energiezentrale Bern, where it is economically favorable to co-process the arising WWFA40, a WWFA with 40% wate wood content. However, the heavy metal extraction efficiency of co-treating WWFA40 and the completeness of Cr(VI) reduction during the FLUWA process have not been investigated in detail. The aim of the study was therefore to investigate the heavy metal recovery, as well as the Cr(VI) reduction efficiency of the FLUWA process when WWFA40 is co-processed. The actual state was investigated (reducing conditions) as well as the future state (oxidizing conditions), when oxidizing conditions become state-of-the art for the FLUWA process. The industrial process was first simulated in laboratory-scale experiments in order to evaluate the leaching behavior of the different ash types (MSWIFA, WWFA40 and MFA (a mix of the two ashes to simulate the co-processing)) and to quantify the leaching efficiency in terms of heavy metal recovery and amount of neutralizing chemicals. The same experimental setups were later implemented at industrial-scale. Of special interest of the experiments was the heavy metal recovery efficiency, successful outcome of Cr(VI) reduction under reducing and oxidizing processing conditions and consumption of neutralizing chemicals (HCl, H_2O_2). The ashes used in the experiment were characterized with respect to their chemical and mineralogical composition and their acid neutralizing capacity (ANC) was determined. For comparison, the sample WWFA100 with 100% waste wood content was analyzed. To assess both the hazard potential of WWFA and the completeness of Cr(VI) reduction, the water-soluble and total content of Cr(VI) were determined for WWFA and filter cakes.

6.2 Materials and methods

6.2.1 Sample origin, sampling and sample preparation

MSWIFA and WWFA40 samples were collected in 2017 at the waste- and wood power plant Energiezentrale Bern. An annual amount of 135'000 t municipal solid waste and 65'000 t of wood (25% water content, fluidized-bed combustion) was incinerated in separate incinerators in 2017. MSW and wood are combusted separately, but treated together prior to landfilling with the FLUWA process in two consecutive extraction reactors (1 m^3 each). The co-processing of WWFA40 in the FLUWA is economically favorable since excess acidity of their scrub water is consumed by the alkalinity of the WWFA40 and the use of lime milk is minimized. At present, the FLUWA process at the incineration plant is performed under reducing conditions (without addition of H_2O_2) with MSWIFA and WWFA40 proportions in the ratio as they are produced. Adjustments of the ash ratio are made in the current process such that a favorable extraction pH of 3.8 is achieved. To perform industrial experiments at oxidizing conditions, a pumping system was installed for continuous dosing of H_2O_2. In order to understand the geochemical differences between MSWIFA and WWFA40, three representative composite samples of each ash type were investigated in terms of chemical and mineralogical composition. Sampling duration varied between one and three weeks. Samples were taken twice a day and mixed to composite samples. Additionally, three samples of WWFA40 (weekly composite samples) and their corresponding filter cakes were made available for Cr(VI) analyses. For comparison, the sample WWFA100 (100% waste wood, monthly composite sample) from a Swiss biomass power plant was investigated. Approximately 10 kg ash was collected in each sampling campaign. The ashes were homogenized and split into 1 kg working batches and dried at 105 °C until constant weight for chemical analysis and at 40 °C for mineralogical analysis.

6.2.2 Chemical analysis

Elemental composition of the ashes was obtained through energy dispersive X-ray fluorescence (ED-XRF) analysis performed on pressed powder pellets (4.0 g ash, 0.9 g wax as binder) using a Spectron Xepos spectrometer with matrix adjusted calibration. For quality control, the samples were analyzed in duplicates. The accuracy of the method was previously verified by the authors Weibel et al., (2017a) through multiple determinations of similar ash samples and the analysis of the standard reference material BCR 176R (Held et al., 2007). The ED-XRF measurements showed good reproducibilities within $< 2\%$ for the elements Cu, Zn, Cd, Sb, Pb, Br, Sn, Ba, within 5% for Al, Si, S, Cl, Ca, Ti, Mn, Fe, Cr, Sr and within $< 10\%$ for K, Na, Mg. Extract solutions were analyzed by inductively coupled plasma optical emission spectroscopy (ICP-OES) on a Thermo Scientific iCAP 700 Series after dilution with HNO_3 1% and calibrated with the multi element standards CertiPur IV and X (Merck). The analytical error accounts for $\pm 5\%$ for all elements except Na, K, Ca, Sb and S that showed $\pm 10\%$ error based on multiple measurements of certified standard solutions.

6.2.3 Mineralogical analysis

Mineralogical composition was obtained throughout X-ray powder diffraction (XRD) analysis using a Panalytical X'Pert Pro diffractometer (CuKα-radiation). 4 g of material was mixed with 1 g of internal standard (corundum) and ground dry for 6 minutes at 55 Hz in a XRD McCrone mill from Retsch. Measurement was performed on disoriented samples from 5 to 75° 2Theta at 40 kV acceleration voltage and at an electron generating current of 40 mA. An automatic divergence slit was used. For quantification, TOPAS-Academic V6 software was used (Rietveld refinement). The extended uncertainty is attributed to 50% for concentrations <1%, 20% for concentrations <5% and 10% to concentrations >5%. The structural data (.cif files) of the Inorganic Crystal Structure Database (ICSD) was used and phase concentrations and amorphous part were calculated based on the internal standard.

6.2.4 Acid neutralizing capacity

Acid neutralizing capacity (ANC) titration was performed using a 785 DPM Titrino device from Metrohm with 2 g of ash 20 ml ultrapure water. Every 10 minutes, 1 ml of HCl 1M was added under continuous stirring until the ash slurry reached a pH of 2.

6.2.5 Water-extractable Cr(VI)

The content of water-soluble Cr(VI) was determined in WWFA samples in order to make statements about the hazard potential of WWFA. Furthermore, the content of water-soluble Cr(VI) in the filter cakes was determined to examine the completeness of the Cr(VI) reduction during the FLUWA process. Cr(VI) analyses were performed on the eluates obtained with the standard eluate test F-22 (FOEN, 2017). The ash and filter cake samples were thereby eluted with ultrapure water during 24h at a liquid to solid (L/S) ratio of 10 (4 g ash, 40 ml ultrapure water). For quality control, as well as to investigate transformations in the redox state during the eluate test, Cr(III) and Cr(VI) spikes were added and the eluate test was performed two times per sample, each spiked and unspiked. Selected samples were further eluted as duplicates. For the spiking, concentration of 50 mg/kg Cr(III) in the form of $CrNO_3 \cdot 9\,H_2O$ and 10 mg/l $CrO_4{}^{2-}$ for the Cr(VI) spike were added for the eluate test. The comparison of the Cr(VI) concentrations of the two eluates per sample allowed calculating the recovery of the spike. The water-extractable Cr(VI) content in the eluates was determined spectrophotometrically with a Merck Spectroquant Pharo 100 after complexation with diphenylcarbazide (DPC) at an absorption maximum of 540 nm. For complexation, a Spectroquant chromate test set (Merck, No 1.14758) was used. No determination of Cr(VI) in the FLUWA leachate was performed as the Cr concentration in the leachates were below the detection limit in all samples.

6.2.6 Total Cr(VI)

For a more comprehensive assessment of the hazard potential of Cr(VI), the total content of Cr(VI) was determined for two WWFA samples (WWFA40_2 and WWFA100). Total Cr(VI) extraction on WWFA was performed on duplicates by hot alkaline extraction (Method 3060A (US EPA, 1996)). For quality control, the standard reference material NIST 2701 (NIST, 2009) was analyzed for total Cr(VI) content and the determined value was within the given uncertainty. The accuracy of the method on similar materials was previously verified by the authors (Weibel et al., 2016) and a reproducibility within 10% was attributed to the method based on spike recoveries and multiple measurements of the standard reference material (Weibel et al., 2017b). Analysis of Cr(VI) concentration in the extract solutions was performed with ICP-OES after the use of CHROMAFIX PS-H$^+$ cation exchange cartridges (Macherey-Nagel) in order to retain Cr(III). The effectiveness of the cartridges on similar extract solutions was tested in previous studies (Weibel et al., 2016). In order to investigate Cr redox transitions during extraction, a parallel extraction with Cr(VI) spiking was performed for each sample by adding a concentration of 100 mg/kg PbCrO$_4$.

6.2.7 Laboratory experiments

In order to investigate the effects of co-processing WWFA40 in the FLUWA process, the process was simulated in laboratory-scale at conditions feasible on industrial scale. At laboratory-scale, mass balances can be quantified precisely and process conditions (pH, Eh) can more easily be controlled. Three different ash types were used for the experiment: MSWIFA (sample MSWIFA_2), WWFA40 (sample WWFA40_2) and MFA (the ash mix of WWFA40_2 and MSWIFA_2, mixed at a ratio of 1:2, to simulate a co-treatment). Two different experimental setups were performed at laboratory-scale (Table 6.1): without the use of H$_2$O$_2$ (30%) and with a concentration of 40 l H$_2$O$_2$/t ash, which represents standard plant conditions. All experiments were performed two times in order to assure reproducibility. 150 ml of artificial acid scrub water (HCl 5% with 25 g/l Na$_2$SO$_4$) was heated in a beaker glass to 40°C before adding the ash (50 g, liquid to solid ratio L/S = 3). Due to the exothermic reaction between the scrub water and the ash, temperature rose immediately to 60°C. Under continuous stirring the ash slurry reacted for 60 minutes at 55 – 60°C. The pH and Eh-values (Ag/AgCl) were recorded temperature-compensated. The pH was controlled by adding HCl (32%). Before filtration, the pH was adjusted to a value of 3.8 with NaOH (65%). The slurry was filtered with a vacuum filter device. 100 ml of deionized water was used to wash the filter cake. For the experiments performed with H$_2$O$_2$, a concentration of 40 l/t H$_2$O$_2$ was added by 10 consecutive portions (at a 3 min interval) to the ash slurry in the first half of the experiment. The leachates were diluted with HNO$_3$ 1% and further analyzed by ICP-OES. The filter cake was weighed and dried at 105°C until constant mass was reached. The heavy metal recovery was determined from mass balance calculations.

	Ash type	Laboratory-scale			Industrial-scale		
		MSWIFA	MFA	WWFA40	MSWIFA	MFA	WWFA40
Without H_2O_2	Extraction pH	3.8	3.8	3.8	3.7 - 4.1	3.8 - 4.2	3.7 - 4.3
	Leachate pH	4.8	4.8	5.4	3.8 - 4.4	4.0 - 4.5	4.2 - 4.8
	Duration (h)	1	1	1	8	4	5
40l H_2O_2/t ash	Extraction pH	2.5	2.5	2.5	3.3 - 3.8	3.5 - 4.2	-
	Leachate pH	4.5	4.5	4.2	3.9 - 4.4	3.8 - 4.4	-
	Duration (h)	1	1	1	21	18	-
60l H_2O_2/t ash	Extraction pH	-	-	-	3.5 - 3.8	3.7 - 4.3	-
	Leachate pH	-	-	-	3.8 - 4.3	3.8 - 4.5	-
	Duration (h)	-	-	-	24	6	-

Table 6.1: Experimental Setups for laboratory- and industrial-scale experiments.

6.2.8 Industrial-scale experiments

Both the current state (reducing conditions), as well as the future state (oxidizing conditions) were investigated at industrial-scale (Table 6.1). Each ash type (MSWIFA, WWFA40 and MFA (ratio WWFA40 to MSWIFA of 1:2.5)) was treated separately without the addition of H_2O_2. Additionally, experiments with 40 and 60 l/t H_2O_2 (30%) were performed for MSWIFA and MFA. At laboratory-scale experiments it was shown that WWFA40 required higher H_2O_2 dosages for oxidizing conditions to persist. Therefore, industrial scale experiments were also conducted with 60 l/t. The efficiency of the co-treatment of WWFA40 and MSWIFA was compared to the scenarios where only WWFA40 or MSWIFA was treated solely. It was found that the treatment of wood ash solely is difficult at industrial scale due to difficulties with filtration. Therefore, the industrial-experiments with WWFA40 solely were not carried out with H_2O_2 and the focus was put on the co-treatment with MSWIFA. The different experimental setups were performed at Energiezentrale Bern on different days for time periods between 4 and 24 hours. A calculated amount of H_2O_2 was added continuously to the first extraction reactor. During each experiment, multiple samples (in 30- or 60-minute intervals, depending on the experiment duration) were taken from the input ash and from the filter cake and combined to composite samples. The pH and Eh was monitored. An average L/S-ratio of 15 was calculated on annual mass flux balances, since flow measurement of the leachate is not implemented. The ash and filter cake samples were dried at 105°C and analyzed for their elemental composition with ED-XRF in order to calculate the recovery.

6.3 Results

6.3.1 Chemical composition

The main constituents of MSWIFA are Ca, Cl, Si, S, Na ($>$75'000 mg/kg, Table 6.2). Zn, K, Al ($>$35'000 mg/kg) and Fe ($>$10'000 mg/kg) are subsidiary constituents. WWFA differ in chemical composition from MSWIFA, and there are also chemical differences between WWFA40 and WWFA100. WWFA generally shows higher Ca and Si concentrations ($>$100'000 mg/kg) than MSWIFA, followed by K, Al, Cl, S, Fe ($>$20'000 mg/kg). Notable is the higher concentration in S and heavy metals (mainly Pb, Zn, Cu) in WWFA100 compared to WWFA40, the latter showing higher concentrations in matrix elements (Ca, Si, K, Mg) in contrast. The concentrations of the main- and subsidiary constituents in the three MSWIFA samples vary within 10-20%, but Cu shows variations by more than 30%. The variations in chemical composition are smaller for WWFA40 than for MSWIFA. The element concentrations vary mostly within 10% between the three WWFA40 samples (except for about 20% for Cr, Mn and Pb). MSWIFA shows strongly elevated concentrations in the potentially harmful heavy metals Pb, Cu, Sb, Cd, some exceeding the threshold for landfilling by multiple times (Pb) or orders of magnitude (Sb, Cd). WWFA shows considerably lower Cd and Sb concentrations (lower by almost 2 and 3 orders of magnitude, respectively) but show strongly elevated Pb concentrations. In two samples of WWFA40, Pb concentration is only 10% lower than in MSWIFA. In WWFA100, Pb concentrations exceed those in MSWIFA by more than double. Zn and Cu concentrations in WWFA40 are about one third of the concentration in MSWIFA, and in WWFA100 about half. In contrast, WWFA shows higher concentrations in Ba, Cr, Fe, Mn and Ti concentrations than MSWIFA. WWFA100 further shows a very high TOC content of 74'400 mg/kg – which exceeds the threshold value for landfilling.

6.3.2 Mineralogical composition

The difference in chemical composition between MSWIFA and WWFA is also represented by a different mineralogical composition (Table 6.3). As a result of the high Cl content, Cl salts such as halite, sylvite and the Zn bearing K_2ZnCl_4 are important phases in MSWIFA. Anhydrite represents another main phase, together with several silicates (e.g. gehlenite) and calcite. Main mineralogical differences between WWFA40 and WWFA100 are in calcite and anhydrite content. WWFA40 show very high calcite concentrations (17 - 28 wt.%) and high concentration in quartz (7 - 10 wt.%). Sylvite, periclase and Ca-, Al-, Na- silicates form minor components in WWFA40. WWFA100 shows calcite, gehlenite, anhydrite and magnesite as main phases ($>$7 wt.%), followed by minor concentrations in quartz and Ca-, Al-, Na- silicates. The presence of amorphous phases is clearly visible in all spectra by a bump in the background between 20 and 40° 2Theta and was calculated to make 35 - 50% of the total content.

	MSWIFA			WWFA40			WWFA100
	MSWIFA_1	MSWIFA_2	MSWIFA_3	WWFA40_1	WWFA40_2	WWFA40_3	WWFA100
				mg/kg			
Al	39'315	45'558	37'210	46'912	44'985	42'520	32'200
Ba	1'928	1'996	1'679	5'091	4'681	5'107	5'370
Ca	165'984	170'617	163'200	288'884	285'400	307'600	235'650
Cd	277	248	311	26	23	28	71
Cl	82'120	85'100	114'500	31'140	32'800	32'530	36'050
Cr	360	350	323	582	597	443	1'221
Cu	2'131	3'411	1'771	602	683	581	1'131
Fe	18'930	20'123	12'980	22'562	22'350	20'890	26'265
K	52'045	46'290	60'030	61'974	71'182	70'050	41'475
Mg	2'529	3'024	901	20'685	20'218	20'390	11'075
Mn	820	811	876	4'274	5'327	4'296	4'856
Na	75'190	76'720	91'410	6'905	7'590	7'940	8'485
Ni	94	92	74	95	91	96	76
P	4'774	4'531	4'485	9'383	8'730	9'107	3'798
Pb	8'143	8'688	8'204	7'876	7'590	5'152	21'015
S	80'762	70'840	72'500	25'845	25'042	29'250	65'215
Sb	3'150	3'533	2'988	< 3	< 3	< 3	22
Si	101'232	107'883	86'750	144'334	148'950	126'300	129'000
Ti	11'712	11'472	8'606	n.a.	n.a.	n.a.	16'535
Zn	44'607	39'810	39'570	12'569	13'047	13'330	21'550
TOC	5'190	5'750	6'010	10'150	17'043	12'030	74'400

Table 6.2: Elemental composition of the analyzed municipal solid waste fly ash (MSWIFA) and waste wood fly ash types WWFA40 and WWFA100, determined by ED-XRF.

		MSWIFA			WWFA40			WWFA100
		wt.%			wt.%			wt.%
Phases	Formula	MSWIFA_1	MSWIFA_2	MSWIFA_3	WWFA40_1	WWFA40_2	WWFA40_3	WWFA100
Chlorides								
Halite	$NaCl$	9	-	14	<1	<1	1	1
Sylvite	KCl	3	3	5	4	4	5	-
K_2ZnCl_4	K_2ZnCl_4	4	3	3	-	-	-	-
Sulfates								
Anhydrite	$CaSO_4$	10	10	11	-	-	-	8
Silicates								
Quarz	SiO_2	3	2	2	10	10	7	5
Gehlenite	$Ca_2Al(AlSi)O_7$	7	5	3	4	2	4	9
AlphaBelite	Ca_2SiO_4	4	3	-	5	5	3	3
Albite	$NaAlSi_3O_8$	4	3	3	5	3	5	2
Sanidine	$KAlSi_3O_8$	-	-	-	-	-	-	5
Microcline	$KAlSi_3O_8$	3	4	2	-	-	-	-
Carbonates								
Calcite	$CaCO_3$	5	6	6	17	28	20	8
Magnesite	$MgCO_3$	<1	2	1	-	-	-	7
Ankerite	$CaFeCO_3$	-	-	-	-	1	-	-
Oxides								
Lime	CaO	-	-	-	2	-	4	-
Hematite	Fe_2O_3	<1	1	-	1	<1	<1	1
Rutile	TiO_2	-	-	-	2	1	3	1
Periclase	MgO	1	-	-	3	4	3	-
Mayenite	$Ca_{12}Al_{14}O_{33}$	2	2	3	-	-	-	-
Perovskite	$CaTiO_3$	2	2	2	-	-	-	-
Phosphates								
Monetite	$CaHPO_4$	5	4	3	5	6	5	2
Amorphous		37	41	43	42	35	39	49

Table 6.3: Mineralogical composition of the analyzed MSWIFA, WWFA40 and WWFA100, determined by XRD.
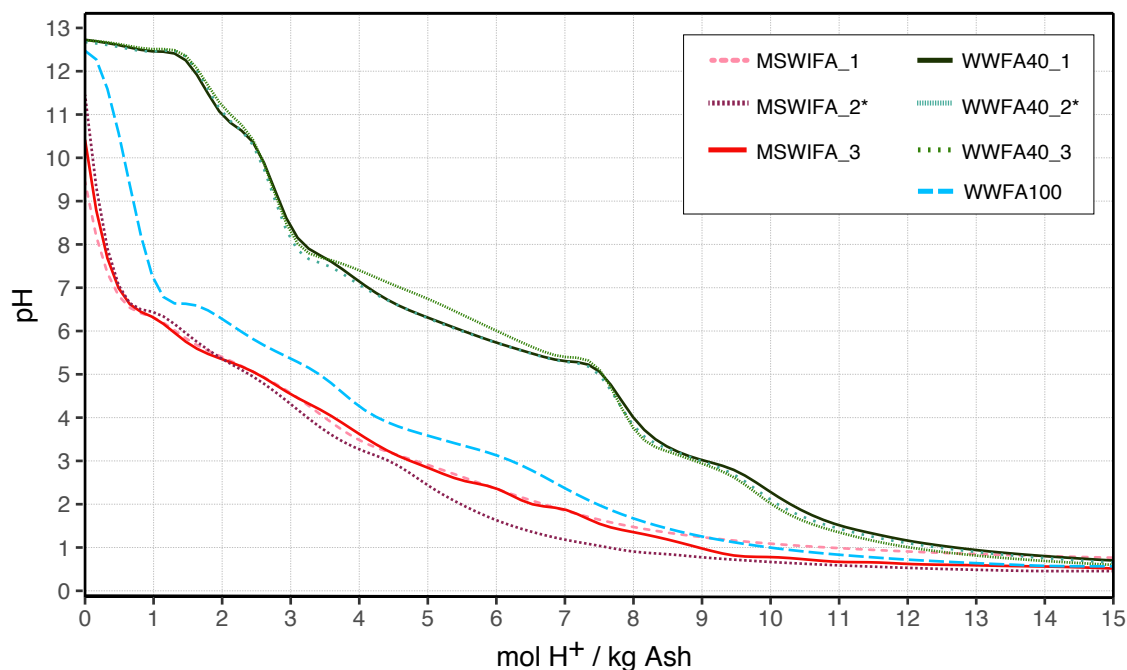
Figure 6.1: Titration curves of acid neutralizing capacity (ANC) for MSWIFA, WWFA40 and WWFA100. The samples used for the leaching experiments are indicated with *.

6.3.3 Acid neutralizing capacity

Acid neutralizing capacity (ANC) is similar for ashes of the same type, but shows differences between the ash types (Figure 6.1). The amount mol H^+ needed to reach an optimal extraction pH of 3 varies within 10% and 5%, respectively for MSWIFA and WWFA40. On average, MSWIFA consumed 4.7 mol H^+, WWFA100 6.2 mol H^+, and WWFA40 with 8.9 mol almost double the amount of H^+ to reach a pH of 3. The titration curve of WWFA40 is characterized by a small plateau at pH 12.7 and big plateau at pH 7. Although WWFA100 shows a similarly high initial pH as WWFA40, the ANC titration curve resembles more that of MSWIFA than that of WWFA40, as the plateau starting at pH 7 is less pronounced. The pH starts dropping rapidly from an initial value of 12.7 to pH 7, where calcite buffering starts. For MSWIFA, the initial pH of the titration curve is lower (pH 11.5) and drops rapidly towards pH 5 – where an almost linear decrease in pH initiates.

6.3.4 Water-extractable and total Cr(VI)

Multiple determination of the water-soluble Cr(VI) concentration of the samples revealed reproducibility within 10%. The Cr(III) spike was fully retained during all eluate tests which proves that no oxidation of Cr(III) occurred. The Cr(VI) spike was fully retained during the majority of the eluate tests. In the experiments where the Cr(VI) spike was not fully retained, redox transformations leading to reduction of Cr(VI) occurred (indicated with * in Table 6.4).

All eluates of the 6 analyzed WWFA40 samples showed water-extractable Cr(VI) con-

	WWFA40						WWFA100
	WWFA40_1	WWFA40_2	WWFA40_3	WWFA40_4	WWFA40_5	WWFA40_6	WWFA100
				mg/kg			
Water-extractable Cr(VI)	58	117	95	83	96	110	1*
Water-extractable Cr(VI) of filter cake	-	< 0.05	-	< 0.05	< 0.05	0.22	-
Total Cr(VI)	-	1*	-	-	-	-	87

Table 6.4: Water-extractable Cr(VI) and total Cr(VI) concentrations of WWFA and the filter cakes of WWFA40. Cr(VI) concentrations indicated with * are from extractions with poor Cr(VI) spike recoveries (<2%), implying erroneously low values. Where not indicated, the Cr(VI) spike was fully retained.

centrations that exceed the threshold limit for landfilling (0.5 mg/kg) by more than two orders of magnitude. The water-extractable Cr(VI) content made up for 10-20% of the Cr concentration in WWFA40. For WWFA100, the determined water-extractable Cr(VI) concentration was as low as 1 mg/kg. Since the Cr(VI) spike recovery was only 2% for WWFA100, this implies that a major part of the sample's native Cr(VI) has also been reduced. All 6 analyzed filter cakes from WWFA40, including all filter cakes from the experiments performed in this study, showed Cr(VI) concentrations below the given threshold for landfilling, independent of the applied scale (laboratory or industrial) and the redox conditions. For the hot alkaline extraction of sample WWFA40_2, none of the Cr(VI) spike was recovered, in neither of the duplicates. The total Cr(VI) concentration was expected to be similar or higher to the measured water-extractable Cr(VI) concentration. Instead, a concentration of 1 mg/kg was measured. For WWFA100, Cr(VI) spike recovery was 80% in the hot alkaline extraction and the measured total Cr(VI) concentration 87 mg/kg. The results of the double determination agreed within 3%. It is assumed that matrix interferences occurred during the hot alkaline extraction of the sample WWFA40_2 (and to a minor extent in sample WWFA100), leading to a strong diminution in Cr(VI) concentration. This might have been favored by the strongly reducing conditions during the hot alkaline extraction with WWFA40_2.

6.3.5 Laboratory-scale leaching experiments

The heavy metal recovery achieved for the two different experimental setups are shown in Figure 6.2. The reproducibility of the experiments performed in duplicates was very good (within 5 - 10%). Only for Cu, the reproducibility was within 20%, since the solubility of Cu is strongly pH dependent and a small increase in the filtrate pH value can enhance precipitation of Cu hydroxides (Hartiner, 1991). Given the attributed uncertainty of 10%, Zn recovery can be considered equal for MSWIFA and MFA, whereas it was lower by 30% for WWFA40. This lower yield is associated with a high leachate pH of 5.4 which assumedly led to Zn precipitation. For Cd, recovery is 40% lower for MFA compared to MSWIFA, whereas no Cd was recovered from WWFA40. No Pb and Cu was mobilized for any of the ash types without the use of H_2O_2. When a quantity of 40 l/t H_2O_2 was used, Zn recovery did not change. The recovery for Cd could almost be doubled from MSWIFA
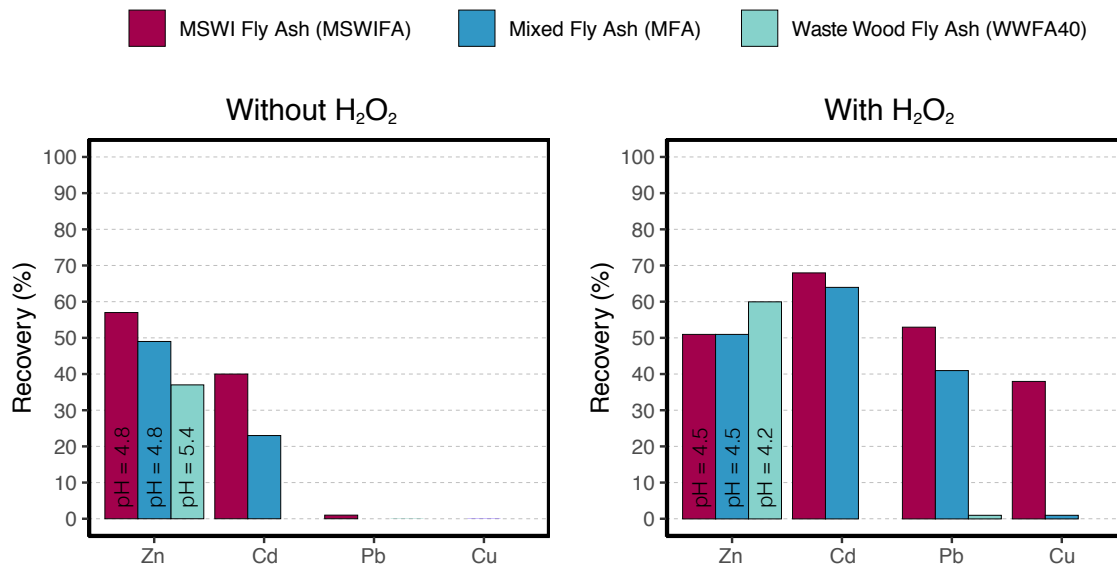
Figure 6.2: Heavy metal recovery in % for the target heavy metals Zn, Cd, Pb, Cu for the 3 different ash types in laboratory-experiments. The pH of the leachate is indicated in the bar for Zn recovery. (a) recovery without the use of H_2O_2 (b) recovery for experiments with 40 l/t H_2O_2.

and it was achieved to recover Pb (53%) and Cu (38%). This significantly higher recovery for Pb and Cu (and to a minor extent Cd) when using H_2O_2 was observed in previous studies (Weibel et al., 2017a). The recovery for MFA is equal (within the uncertainty) to that of MSWIFA for Zn and Cd. For Pb, recovery is lower by 25%, and almost no Cu was mobilized during the experiment. For WWFA40, the same recovery for Zn was achieved as for the other ash types, but any of the other heavy metals could be recovered. In the experiment with H_2O_2, the amount of HCl 32% needed to keep extraction pH at a level of 2.5 was twice as high for MFA compared to the experiments with MSWIFA (17 vs. 9 ml, respectively) and the amount needed for WWFA40 was 33 ml.

The ashes show a strong redox buffer, visible by the subsequent drop in redox potential after each H_2O_2 dosage (Figure 6.3). For MSWIFA, the redox potential dropped to strongly negative values shortly after the H_2O_2 dosage, whereas for WWFA40, Eh was still positive before the next H_2O_2 dosage. Thus, H_2O_2 consumption seems to be slower. However, the amount of H_2O_2 added was not enough to maintain oxidative conditions over the entire extraction time for MFA and WWFA40. Only for MSWIFA it was possible to maintain a stable positive redox potential over the entire experiment with 40 l/t H_2O_2.

6.3.6 Industrial-scale leaching experiments

Taking into account the attributed uncertainty of 10%, the recovery for Zn is the same for the three ash types independent of the amount of H_2O_2 added. The recovery for Cd reflect the trends observed from the laboratory experiments: a lower Cd recovery by one third for MFA and a negligible Cd recovery for WWFA40. As already observed in the laboratory experiments, the recovery for Pb and Cu are negligible without H_2O_2 (Figure 6.4a). With 40 l/t H_2O_2, 55% of Pb and 16% of Cu could be mobilized from MSWIFA,
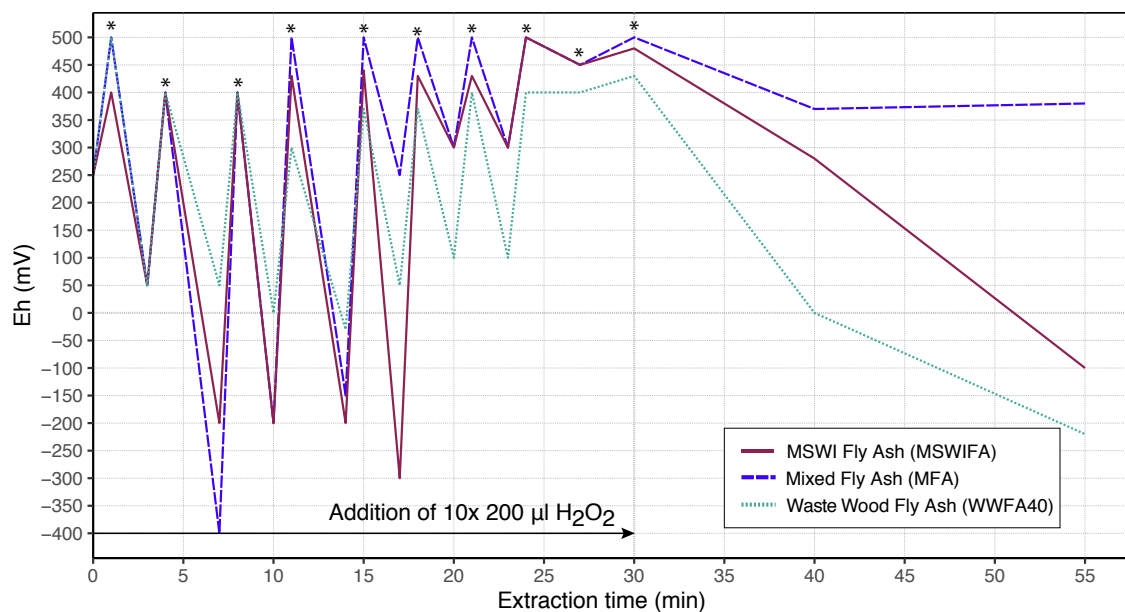
Figure 6.3: Evolution of redox potential (Eh) during laboratory-experiment with H_2O_2. Left: Eh before and after each dose of H_2O_2 (indicated with *). Right: Evolution of Eh after the last H_2O_2 dosage.

	Experiment without H_2O_2				Experiments with H_2O_2				
	Zn	Cd	Pb	Cu	Zn	Cd	Pb	Cu	
	mg/kg				mg/kg				
MSWIFA	44'710	220	6'070	1'360	43'700	260	10'700	2'500	*
					57'350	320	12'910	3'090	**
MFA	31'950	170	6'760	2'010	31'330	190	6'460	1'970	*
					31'830	160	5'710	1'770	**
WWFA40	13'890	30	5'520	630	-	-	-	-	

Table 6.5: Heavy metal concentrations of the different ashes investigated in the industrial-scale leaching experiments. The concentrations for the experiments with 40 and 60 l/t H_2O_2 are indicated with * and **, respectively.

but only 12% Pb and 3% Cu from MFA (Figure 6.4b). The recovery of both Pb and Cu is thus significantly lower for MFA compared to MSWIFA. With the higher dosage of 60 l/t H_2O_2, a higher Cd fluctuation in recovery can be observed, but considering the attributed uncertainty of 10%, the recoveries are comparable for the two ash types. For Pb recovery, a strong increase by a factor 3 can be observed for MFA, whereas Pb recovery does not increase with the higher dosage for MSWIFA. A clear increase in Cu mobilization can be observed for both ash types, which results in recoveries 2.5 and 6 times higher than with 40l, respectively. Table 6.5 lists the heavy metal concentrations of the ashes investigated in the industrial-scale leaching experiments. Considerable differences in heavy metal concentrations can be observed, which have to be taken into account when comparing the recoveries.
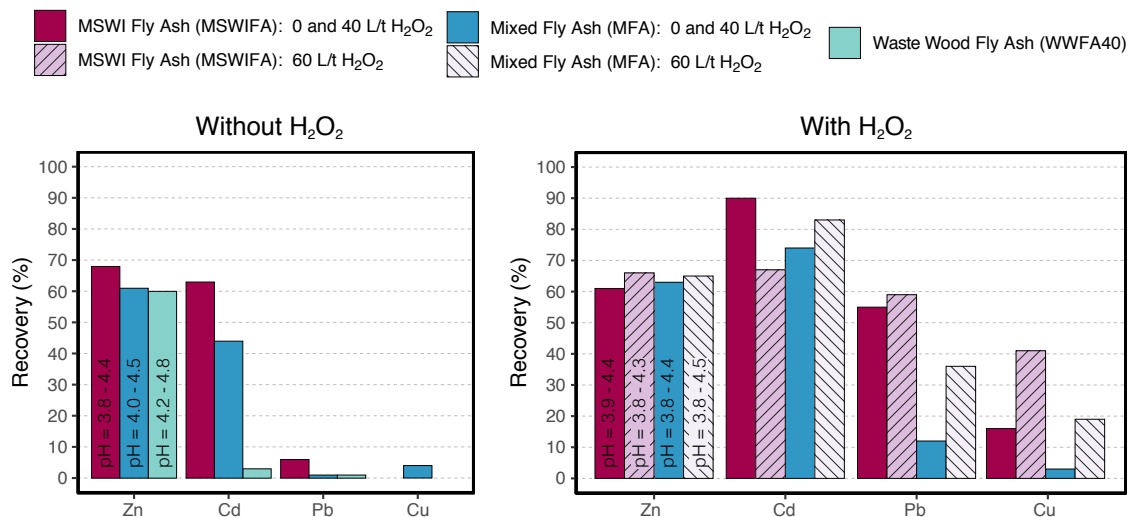
Figure 6.4: Recovery for the industrial-scale experiments (a) without and (b) with H_2O_2 (40 and 60 l/t H_2O_2). The pH of the leachate is indicated in the bar for Zn recovery. The industrial-scale experiments with H_2O_2 were not performed for WWFA40.

6.4 Discussion

6.4.1 Chemical and mineralogical differences and its effects on acid neutralizing capacity

The chemical and mineralogical characterization showed considerable differences between the ash types. As difference in matrix elements, WWFA showed significantly higher Ca and Si contents and significantly lower concentrations in Cl than MSWIFA. Within WWFA, chemical differences were also observed, depending on the waste wood content. The S content, for example, was as high as in MSWIFA for WWFA100, but less than half the concentration in WWFA40. The fluctuations in elemental composition of MSWIFA is attributed to the compositional differences in waste input. Remarkable are the constant chemical and mineralogical composition between the different WWFA40 samples, as waste wood is also a very heterogeneous feedstock (Gehrmann, 2020). This could be an effect of the low waste wood content in WWFA40. The significantly higher Cl concentration in MSWIFA is associated with the combustion of plastics (PVC). It is known that elevated Cl concentrations in the flue gas favor the evaporation and transport of heavy metals (e.g. Cd, Cu, Pb, Zn, Sb (Belevi et al., 2000; Morf et al., 2000; Luan et al., 2013)) and elevated heavy metal concentrations in MSWIFA have been observed by many authors (e.g.(Held et al., 2007; Bayuseno et al., 2011)). The high concentrations of these hazardous metals in MSWIFA are associated with the combustion of e.g. batteries, paints, alloys, plastics (EU Commission, 2002). The high Sb concentrations in MSWIFA are problematic due its high toxicity (especially of the trivalent species (Gad, 2021)). Antimony is not soluble at the low pH conditions prevailing in the FLUWA process and accumulates in the filter cake. To fully assess the hazard potential of Sb and to evaluate Sb mobilization during the FLUWA process, additional studies are in progress. The high Pb and Cr(VI) concentration in WWFA

are problematic and justify the need for treatment prior to deposition. WWFA100, the WWFA with higher waste wood content, showed significantly higher heavy metal concentrations, which reflects findings made in previous studies on WWFA (e.g. (Gehrmann, 2020)). The elevated Pb an Zn concentration in WWFA is probably due to pigments (e.g. $PbCO_3$, ZnO) from paints and coatings, whereas the high Cu content in WWFA could arise from the combustion of pickled wood products (Gras, 2006). During combustion, alkali- and alkaline earth metals in the wood transform to oxides and are subject to successive hydrogenation and carbonation during cooling (Holmberg et al., 2001), which could explain the high calcite content in WWFA40. The high Si content stands in relation to the usage of quartz sand as bed material during fluidized bed combustion (Teixeira et al. 2019). In the presence of SO_2 and O_2, CaO often forms sulfate compounds (e.g. anhydrite) (Anthony et al., 2001), as present in WWFA100. WWFA100 further showed higher TOC content (associated with incomplete combustion (Park et al., 2020)) and different matrix composition (e.g. less calcite, more sulfates) than WWFA40, the latter affecting ANC. The high ANC of WWFA40 can be explained by the very high calcite content and dissolution of Ca-silicates (e.g. gehlenite, belite). The high initial pH of all the three ash types suggests the presence of non- or microcrystalline CaO or $Ca(OH)_2$, since no CaO or lime was identified in all ashes. WWFA100 and MSWIFA both showed poorly acid buffering sulfates and chlorides as main constituents, which explains the lower amount of H^+ needed to reach the acid conditions required for the FLUWA process. Thus, although WWFA showed different chemical and mineralogical characteristics than MSWIFA, there are also different geochemical properties within WWFA, depending on their waste wood content and certainly also depending on differences in the waste wood composition.

6.4.2 Water-extractable and total Cr(VI) in WWFA and filter cakes

The measured average water-extractable Cr(VI) concentration of 93 mg/kg in WWFA40 justifies the strong need for Cr(VI) reduction prior to landfilling. The treatment of WWFA40 with the FLUWA process successfully reduced water-soluble Cr(VI). All analyzed filter cakes showed Cr(VI) concentrations below the threshold limit for landfilling, even when the experiments were performed under oxidizing conditions with H_2O_2. It was shown that acidic conditions are sufficient to dominate the reduction of water-extractable Cr(VI), as also observed in other studies (Wittbrodt et al., 1995). It was also reported that H_2O_2 can act as reductant in acidic solutions (Pettine et al., 2002). It is assumed that the water-soluble Cr(VI) is being reduced to Cr(III) during the FLUWA process, followed by precipitation as Cr(III) phase, probably as hydroxide. This is supported by the absence of dissolved Cr in the filtrate. Unfortunately, no Cr phases could be identified with XRD as the concentrations are very low and the precipitated phases possibly amorphous. It was further shown that the high Cr(VI) concentrations in the eluates were not caused by the oxidation of Cr(III) during the eluate test. However, Cr(VI) reduction occurred during the eluate test for WWFA100 due to its highly reductive character – leading to erroneously low water-extractable Cr(VI) concentrations. Similar matrix interferences occurred during the

hot alkaline extraction for WWFA40. These observations show, that spiking during Cr(VI) extraction tests with reactive material such as WWFA is indispensable. Poor Cr(VI) spike recovery is not indicative of method failure, but rather an indication for the potential of the sample to reduce the spiked Cr(VI) and not sustain its native Cr(VI) (Vitale et al., 1994). They further report that the presence of high TOC contents, as well as considerable S^{2-} or Fe^{2+} concentrations in the sample are most likely the reason for low Cr(VI) spike recovery or reduction of native Cr(VI). Although oxidative conditions prevail during combustion, it cannot be excluded that locally reducing conditions occur, where Fe^{2+} and S^{2-} persist. While no mineral phases containing Fe^{2+} and S^{2-} were observed, their presence in minor concentrations cannot be excluded. For further interpretation, a more detailed investigation on possible reductants other than C_{org} in WWFA has to be performed, with special focus on the content of Fe^{2+} and S^{2-}.

6.4.3 Leaching experiments: Heavy metal recovery and consumption of neutralizing chemicals

The laboratory-scale experiments were able to predict well the recovery trends of the industrial-scale. Differences in the recoveries between laboratory- and industrial-scale are primarily attributed to differences in pH and to element contents of the ash, as well as to a larger L/S in the industrial scale, which will increase the recovery. For WWFA40, a higher H_2O_2 dosage was needed to achieve oxidizing conditions during extraction. This could be caused due to the high content in organic matter or the presence of metals in their metallic form – leading to rapid consumption or even catalytic destruction of the added H_2O_2. The high ANC of WWFA40 led to higher acid consumption in the FLUWA compared to MSWIFA (3x higher). Thus, WWFA40 can represent a heavy metal rich replacement for the often-used pH neutralizing agent lime milk. The high acid consumption is even more pronounced when H_2O_2 is used, since the oxidation of e.g. metallic compounds consumes H^+. For the element Zn, recovery was equally high for the different ash types independent of the H_2O_2 dosage, as Zn mobility is independent of the redox conditions during extraction but controlled by pH and binding form (Weibel et al., 2018). The achieved Zn recovery was lower by 15% in the laboratory-scale experiments compared to the industrial scale experiment. It is assumed that this is due to the higher L/S used in the industrial-scale experiment (L/S of 15 compared to L/S of 3). The low Zn recovery of WWFA40 (laboratory-scale) is associated to enhanced precipitation of Zn due the high leachate pH. Remarkable is the fact that the Zn recovery seems not strongly affected by the Zn concentration in the ash. As observed in other studies (Weibel et al., 2018), the Zn yield stagnates at about 70% (in this study at about 65% in the industrial scale-experiments). It is assumed that the majority of the Zn in the ashes is readily available for dissolution (e.g. as Cl- or S-salts). The remaining 30 - 35% of the Zn seems, however, to be present in insoluble form under these conditions (e.g. as glassy particles, as Ca replacement in gehlenite or associated with iron (Weibel et al., 2018)). The recovery of Cd showed the same trends for laboratory- and industrial scale, but with lower recoveries

by 15 - 50% in the laboratory-scale. The higher recoveries in industrial-scale are again attributed to the higher L/S. The lower Cd yields in the laboratory-scale experiment without H_2O_2 are associated to the higher leachate pH. Since Cd concentration is about one order of magnitude lower than the other elements, it is subject to larger fluctuations as inhomogeneities in Cd concentration in the sample are more pronounced. The low Cd recovery from WWFA40 is attributed to the very low Cd concentration in the ash. An increase in Cd recovery can be observed for each ash type when the experiments are performed under oxidizing conditions, as observed in other studies (Weibel et al., 2018). As WWFA40 showed a higher redox buffer than MSWIFA, it is assumed that the lower Cd recoveries in the experiments without H_2O_2 are a result of reductive precipitation of Cd, since Cd recoveries are comparable to those of MSWIFA when using H_2O_2. The mobility of Pb and Cu is highly dependent on the redox conditions, as well as on the pH (especially for Cu). The recoveries for Pb and Cu for 40l H_2O_2 are higher in the laboratory-scale than in the industrial-scale. Besides differences in elemental concentrations in the ashes, the pH and redox conditions are more easily controllable in the laboratory-scale than in the industrial scale. Additionally, the industrial-scale experiment run over longer timespans and are subject to fluctuations of ash input and neutralizing chemicals. The recoveries for Pb and Cu were significantly lower for MFA compared to MSWIFA, which is attributed to the higher redox buffer of WWFA40. However, further data is required for quantifying the negative effects. The FLUWA process nevertheless represents a valuable option for treating WWFA as the heavy metal concentrations in WWFA are in the same range as for MSWIFA and WWFA shows comparable heavy metal recoveries for Zn and Cd. The negative effects of the higher consumption of H_2O_2 affecting the Pb and Cu recovery may be diminished by a co-treatment of lower WWFA ratios.

6.5 Conclusion

Heat and energy production in Switzerland using waste wood incineration is growing and new treatment pathways have to be implemented to recover heavy metals from the ashes and to reduce Cr(VI) content. Acid leaching, already established for MSWIFA, was found to be a valuable option for the treatment of WWFA. Laboratory-scale experiments were found to be suitable when evaluating the co-processing of MSWIFA and WWFA before implementing at industrial scale. Comparison of chemical and mineralogical composition of WWFA with MSWIFA showed, that WWFA can contain heavy metals (especially Pb) in elevated concentrations similar to that of MSWIFA. The investigated WWFA samples showed Cr(VI) concentrations more than 2 orders of magnitude above the threshold value for landfilling. It was found that the concentrations in heavy metals, Cr(VI) and matrix minerals differed within the two WWFA types, depending on waste wood content. The elevated heavy metal and Cr(VI) concentrations in WWFA justify the need for treatment prior to deposition. The treatment with the FLUWA process allowed to successfully reduce the Cr(VI) in the filter cake until below the threshold value for landfilling, even when the

process was performed under oxidizing conditions. The co-processing of WWFA required higher acid dosages due to its high ANC, but the Zn and Cd recovery were not negatively affected by the co-processing. Nevertheless, the co-processing of WWFA had a particularly negative effect on the recovery of the redox sensitive elements Pb and Cu, as WWFA showed a strong redox buffer and thus a higher consumption of the oxidant H_2O_2. Therefore, higher dosages of H_2O_2 are needed to maintain oxidizing conditions during the process required for Pb and Cu mobilization. The use of a stronger oxidizing agent (e.g. permanganate) could be expedient and should be further tested with regard to successful Cr(VI) reduction. Alternatively, smaller percentages of WWFA could be co-processed in existing FLUWA plants in order to diminish the negative effects due to the higher demand of neutralization chemicals. Within the next years, the implementation of co-processing the two ash types could contribute significantly to the growing demand of treatment capacities in Switzerland.

Aknowledgements

6.6   References

Anthony, E.J.; Jia, L.; Laursen, K. Strength development due to long term sulfation and carbonation/sulfation phenomena. Can. J. Chem. Eng. 2001, vol. 79, pp. 356–366. doi: 10.1002/cjce.5450790308

Bayuseno, A.P.; Schmahl, W.W. Characterization of MSWI fly ash through mineralogy and water extraction. Resour. Conserv. Recycl. 2011, vol. 55, pp. 524–534. doi: 10.1016/j.resconrec.2011.01.002

Belevi, H.; Moench H. Factors determining the element behavior in municipal solid waste incinerators. 1. Field studies. Environ. Sci. Technol. 2000, vol. 34, pp. 2501–2506. doi: 10.1021/es991078m

Bühler, A.; Schlumberger, S. Schwermetalle aus der Flugasche zurückgewinnen «Saure Flugaschewäsche - FLUWA-Verfahren» ein zukunftsweisendes Verfahren in der Abfallverbrennung. KVA-Rückstände in der Schweiz - Der Rohstoff mit Mehrwert. Bundesamt für Umwelt, BAFU, 2010, 185-192.

Etiégni, L.; Campbell, A.G. Physical and chemical characteristics of wood ash. Bioresour. Technol. 1991, vol. 37, pp. 173–178, doi: 10.1016/0960-8524(91)90207-Z

European Commission DG ENV E3. Heavy metals in waste—Final report. Project ENV.E.3/ETU/2000/0058, 2002.

Gad, S.C. Antimony. Encyclopedia of Toxicology. Volume 1. Gad Consulting Services. Cary, NC, USA. doi: 10.1016/B978-0-12-386454-3.00815-0

Gehrmann, H. J.; Mätzing, H.; Nowak, P.; Baris, D.; Seifert, H.; Dupont, C.; Defoort, F.; Peyrot, M.; Castagno, F. Waste wood characterization and combustion behaviour in pilot lab scale. J. Energy Inst. 2020, vol. 93, pp. 1634-1641. doi: 10.1016/j.joei.2020.02.001

Gras, B. Untersuchung von Holzaschen aus Kleinfeuerungsanlagen: Erkennen von Brennstoff-missbrauch. Institut für Hygiene und Umwelt, Hamburg, 2006.

Hartinger, L. Handbuch der Abwasser- und Recyclingtechnik, 2nd ed., Fachbuchverlag Leipzig: Deutschland, 1991; 978-3-446-43170-6.

Held, A.; Kramer, G.N.; Robouch, P.; Wätjen, U. The Certification of the mass fractions of As, Cd, Co, Cr, Cu, Fe, Hg, Mn, Ni, Pb, Sb, Se, Tl, V and Zn in fly ash BCR-176R. European Commission Directorate-General Joint Research Centre Institute for Reference Materials and Measurements, 2007.

Holmberg, S.L.; Claesson T. Mineralogy of granulated wood ash from a heating plant in Kalmar, Sweden. Environ. Geol. 2001, vol. 40, pp. 820–828. doi: 10.1007/s002540100261

Huron, M.; Oukala, S.; Lardière, J.; Giraud, N.; Dupont, C. An extensive characterization of various treated waste wood for assessment of suitability with combustion process. Fuel 2017, vol. 202, no. 118–128

Luan, J.; Li, R.; Zhang, Z.; Li, Y.; Zhao, Y. Influence of chlorine, sulfur and phosphorus on the volatilization behavior of heavy metals during sewage sludge thermal treatment. Waste Manag. Res. 2013, vol. 31, pp. 1012–1018. doi: 10.1177/0734242X13493955

Morf, L.S.; Brunner, P. H.; Spaun, S. Effect of operating conditions and input variations on the partitioning of metals in a municipal solid waste incinerator. Waste Manag. Res. 2000, vol. 18, pp. 4–15. doi: 10.1177/0734242X0001800102

National Institute of Standards & Technology. Certificate of analysis standard reference material 2701. Certificate of Analysis Standard Reference Material 2701, 2009.

Obernberger, I. Nutzung fester Biomasse in Verbrennungsanlagen unter besonderer Berück-sichtigung des Verhaltens aschebildender Elemente. In Schriftenreihe Thermische Bio-massenutzung; dbv-Verlag, Graz, 1997.

Park, J.H.; Eom, J.H.; Lee, S.L.; Hwang, S.W.; Kim, S.H.; Kang, S.W.; Yun, J.J.; Cho, J.S.; Lee, Y.H.; Seo D.H. Exploration of the potential capacity of fly ash and bottom ash derived from wood pellet-based thermal power plant for heavy metal removal. Science of total Environment 2020, vol. 740, doi: 10.1016/j.scitotenv.2020.140205

Pettine, M.; Campanella, L.; Millero, F.J. Reduction of Hexavalent Chromium by H2O2 in Acidic Solutions. Environ. Sci. Technol. 2002, vol. 36, pp. 901-907, doi: 10.1021/es010086b

Pohlandt-Schwandt, K.; Salthammer, T.; Marutzky, R. Reduction of soluble chromate in wood ash by formaldehyde, Biomass and Bioenergy 2002, vol. 22, pp. 139–143. doi: 10.1016/S0961-9534(01)00053-8

Pohlandt-Schwandt, K.; Treatment of wood ash containing soluble chromate. Biomass and Bioenergy 1999, vol. 16, pp. 447–462. doi: 10.1016/S0961-9534(99)00013-6

Schlumberger, S.; Schuster, M.; Ringmann, S.; Koralewska, R. Recovery of high purity zinc from filter ash produced during the thermal treatment of waste and inerting of residual materials. Waste Manag. Res. 2007, 25(6), 547-555, doi: 10.1177/0734242X07079870.

Schweizerische Eidgenossenschaft (Bundesamt für Energie), Schweizerische Holzenergiestatistik - Erhebung für das Jahr 2019, 2020.

Swiss Federal Council, Ordinance on the Avoidance and the Disposal of Waste (Waste Ordinance, ADWO), 2015 (Status of 1 April 2020).

Swiss Federal Office of Environment. Messmethoden im Abfall- und Altlastenbereich, 2017

Tarelho, L.A.C.; Teixeira, E.R.; Silva, D.F.R.; Modolo, R.C.E.; Silva, J.J.F. Characteristics, management and applications of ashes from thermochemical con- version of biomass to energy. World Bioenergy 2012, Conference Exhibition on Biomass for Energy Jonkopin, Sweden.

Teixeira, E.R.; Camooes, A.; Branco, F.G. Valorization of wood fly ash on concrete. Resources, Conservation & Recycling 2019, vol. 145, pp. 292-310, doi: 10.1016/j.resconrec.2019.02.028

US Environment Protection Agency. EPA Method 3060A. Alkaline digestion for hexavalent chromium, 1996.

Vitale, R. J.; Mussoline, G. R.; Petura, J. C.; James, B. R. Hexavalent Chromium Extractions from Soils: Evaluation of an Alkaline Digestion Method. J. Environ. Qual. 1994, vol. 23, pp. 1249–1256. doi: 10.2134/jeq1994.00472425002300060018x

Weibel, G. Optimized Metal Recovery from Fly Ash from Municipal Solid Waste Incineration. Ph.D. Thesis, University of Bern, Bern, Switzerland, 2017

Weibel, G.; Eggenberger, U.; Kulik, D.A.; Hummel, W.; Schlumberger, S.; Klink, W.; Fisch, M.; Mäder, U.K. Extraction of heavy metals from MSWI fly ash using hydrochloric acid and sodium chloride solution. Waste Manag. 2018, 76, 457–471, doi:10.1016/j.wasman.2018.03.022.

Weibel, G.; Eggenberger, U.; Schlumberger, S. and Mäder, U.K. Chemical associations and mobilization of heavy metals in fly ash from municipal solid waste incineration. Waste Manag. 2017, 62, 147–159, doi: 10.1016/j.wasman.2016.12.004.

Weibel, G.; Waber, H. N.; Eggenberger, U.; Mäder, U. K. Influence of sample matrix on the alkaline extraction of Cr(VI) in soils and industrial materials. Environ. Earth Sci. 2016, vol. 75, no. 7, pp. 1–14. doi: 10.1007/s12665-015-5236-3

Wittbrodt, P.R.; Palmer, C.D. Reduction of Cr(VI) in the Presence of Excess Soil Fulvic Acid. Environ. Sci. Technol. 1995, vol. 29, pp. 255-263, doi: 10.1021/es00001a033

Wunderli, S.; Zennegg, M.; Dolezal, I.S.; Gujer, E.; Moser, U.; Wolfensberger, M.; Hasler, P.; Noger, D.; Studer, C.; Karlaganis, G. Determination of polychlorinated dibenzo-p-dioxins and dibenzo-furans in solid residues from wood combustion by HRGC/HRMS. Chemosphere 2000, vol. 40, pp. 641–649

Zimmermann, S.; Hässig, J.; and Landolt, W. Literaturreview Holzasche - Wald: Nährstoffentzug durch Holzernte, Ascherückführung in den Wald, abiotische und biotische Wirkungen. Study commissioned by Swiss Federal Office of Environment, 2010.

Part III

Technical Report

Chapter 7

Charakterisierung der Kessel- und Elektrofilterasche im Hinblick auf die Schwermetallrückgewinnung und Abgrenzung zur Schlacke

M.Wolffers[a], U. Eggenberger[a]

[a] Institut für Geologie, Universität Bern

7.1 Ausgangslage

Die Flugaschen aus der Kehrichtverbrennungsanlage (KVA) enthalten hohe Gehalte an Metallen, deren Rückgewinnung ein erhebliches Potential zur Entlastung der Umwelt aufweist. Die rückgewonnen Metalle liefern einen wertvollen Beitrag zur nachhaltigen Schliessung von Stoffkreisläufen, indem Metalle aus dem Primärrohstoffabbau substituiert werden. Mit der Verordnung über die Vermeidung und Entsorgung von Abfällen (Abfallverordnung, VVEA, (Swiss Federal Council, 2015)) wird ab 1.01.2026 die saure Wäsche der Filterasche im Hinblick auf die Rückgewinnung der Metalle Zink (Zn) und Blei (Pb) zur Pflicht. In der Vollzugshilfe zur Rückgewinnung von Metallen aus Filteraschen von Kehrichtverbrennungsanlagen (Bundesamt für Umwelt BAFU, 2019) sind die Anforderungen für den Vollzug definiert. In der aktuellen Version der Vollzugshilfe wird die Abgrenzung der Filterasche zur Schlacke über die Metallgehalte im Filterkuchen definiert. So sollen die Gehalte der säureextrahierbaren Metalle in den Kesselaschefraktionen mit den Metallgehalten im sauer gewaschenen Filterkuchen der Filterasche verglichen werden. Liegen diese darunter, können sie zusammen mit der Schlacke abgelagert werden. Damit wird die Extrahierbarkeit der Filterasche als entscheidendes Kriterium für die Einstufung der Kesselasche herangezogen. Dies hat sich als problematisch herausgestellt, da sich die Rückgewinnungsrate im laufenden Prozess quantitativ nur schwer beurteilen lässt. Eine robustere Definition, welche Fraktionen der Flugasche als "Filterasche" im Sinne VVEA Art. 32e zu behandeln sind, wäre zielführend, da sie als Entscheidungsgrundlage dient, welche Kesselaschefraktionen als «schlackeähnlich» gelten und mit der Schlacke entsorgt werden können. In der Regel wird die abgeschiedene Leerzugasche (je nach Bauart 1. − 3.

Zug) direkt am Ofenaustritt mit der Schlacke vermischt und zusammen mit dieser in Typ D Deponien abgelagert. Dies erfolgte bisher im Rahmen der kantonalen Betriebsbewilligung der jeweiligen KVA, sofern diese Leerzugaschen „schlackenähnlich" sind. Es ist heute nicht bekannt, ob dies aus technischer und ökologischer Sicht sinnvoll ist. Die vorgeschlagene Studie soll Grundlagen und Kriterien für die Beurteilung liefern, welche Züge der Kessel-laschen als "Filterasche" im Sinne VVEA Art. 32e zu behandeln sind und welche mit der Schlacke entsorgt werden können.

Um die Unterschiede der verschiedenen Aschefraktionen zu erfassen, wurde eine orts-aufgelöste Beprobung aller Züge, vom Leerzug über die Kessel- bis zur Elektrofilterasche in 6 verschiedenen Schweizer Anlagen durchgeführt und die einzelnen Fraktionen detailliert untersucht. In Ergänzung zur chemischen und mineralogischen Charakterisierung der Frak-tionen wurden die für die Extrahierbarkeit relevanten Parameter wie Säureneutralisation-skapazität (ANC) sowie der Gehalt an metallischem Aluminium (Al^0) erhoben. Von aus-gewählten Anlagen wurden zudem FLUWA-Laborextraktionsversuche durchgeführt. Die Studie widmet sich folgenden Fragestellungen:

- Wie entwickelt sich die chemische Zusammensetzung der Rauchgasreinigungsrück-stände entlang dem Bildungspfad

- Ist die Extrahierbarkeit der relevanten Metalle abhängig vom Aschentyp (Chemie/Struktur) und wie ist diese in Bezug auf die Aschenwäsche zu beurteilen

- Welche Kriterien sollen für die Unterscheidung von Schlacke, Kessel- und Elektrofil-terasche herangezogen werden

7.2 Probenahme

7.2.1 Merkmale der untersuchten Anlagen

Die Leerzug-, Kessel- und Elektrofilteraschen wurden in 6 verschiedenen KVA in der Schweiz beprobt. Die meisten KVA, die in der Schweiz in Betrieb sind, sind mit einem Elektrofilter als Vorentstauber und einer nassen Rauchgasreinigung ausgerüstet (AWEL, 2013). Dementsprechend verfügen die sechs untersuchten Anlagen (Anlagen A - F) über vergleichbare Rauchgasreinigungssysteme mit Kessel und Elektrofilter (E-Filter) vor dem Rauchgaswäscher, wobei die Entstaubung und Neutralisation getrennt erfolgt. Die Anla-gen A - E sind mit einem nassen Rauchgaswäscher ausgestattet. Die Anlage F ist mit einem trockenen Rauchgaswäscher ausgestattet und die Neutralisationsrückstände werden separat entsorgt und nicht zusammen mit der Flugasche gesammelt. Die Anlagen zeigen unterschiedliche Bauweisen (Abbildung 7.1). In allen Anlagen werden sowohl Siedlungs- als auch Gewerbe- und Industrieabfälle verbrannt, teilweise auch Auto Shredder Rück-stände (ASR) und untergeordnet Klärschlamm (Tabelle 7.1). In der Anlage B werden hauptsächlich Siedlungsabfälle verbrannt (67 %), während in der Anlage A größere Men-gen an Industrieabfällen verbrannt werden. In den anderen Anlagen sind die Anteile von
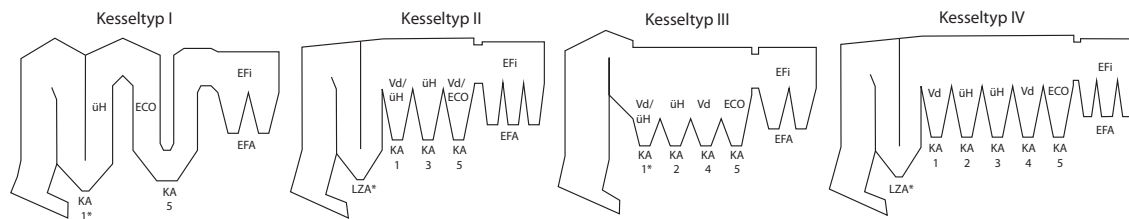
Figure 7.1: Schema der verschiedenen Kesseltypen, die in dieser Studie betrachtet werden mit Angaben der Funktion der Kesselsektionen (KA). Vd = Verdampfer, üH = Überhitzer, ECO = Economizer, EFi = Elektrofilter. Die mit * gekennzeichneten Aschefraktionen werden zusammen mit der Schlacke entsorgt.

Anlagen-ID	Kessel-Typ	Anteil Siedlungsabfall	Industrie- und Gewerbeabfall	Autoshredder Rückstände (ASR)	Klärschlamm	Menge verbrannter Abfall (t/d)	Erzeugte Dampfmenge (t/h)	T Brennkammer (°C)	T Kesseleingang (°C)	T Kesselausgang (°C)
Anlage A	I	35%	65%	3%	<1 %	330	55	925	650	195
Anlage B	II	67%	30%	2%	<1%	355	58	900	590	260
Anlage C	III	45%	54%	-	1%	160	30	860	670	250
Anlage D	IV	48%	51%	<1%	-	400	75	840	635	274
Anlage E	IV	55%	45%	-	-	288	48	850	660	260
Anlage F	IV	45%	46%	7%	1%	283	45	850	680	260

Table 7.1: Angaben zu Müllinput und Betriebsbedingungen der untersuchten Anlagen.

Anlage	Kessel Typ	Anz. Inkremente / Probenahmedauer
Anlage A	I	28 Inkr. / 14d
Anlage B	II	35 Inkr. / 6d
Anlage C	III	2 Inkr. / 6h
Anlage D	IV	21 Inkr. / 7d
Anlage E	IV	14 Inkr. / 14d
Anlage F	IV	9 Inkr. / 68h

Siedlungs- und Industrieabfällen nahezu identisch. Unterschiede in der Durchsatzmenge und weiteren Kenngrössen können ebenfalls der Tabelle 7.1 entnommen werden.

7.2.2 Probenahme und Probenvorbereitung

Aufgrund der unterschiedlichen Bauweise der Verbrennungsanlagen mussten individuelle Probenahmestrategien entwickelt und auf die verschiedenen Anlagen abgestimmt werden. Die Leerzugasche konnte nur in den Anlagen E und F beprobt werden (in letzterer nicht in der gleichen Probenahmeperiode). In den Anlagen A und C gibt es keinen Leerzug, dafür wird die erste Aschefraktion aus dem Kessel (KA1) zusammen mit der Schlacke entsorgt. Die Kesselasche-Fraktionen wurden so nummeriert, dass sie aus vergleichbaren Kesselabschnitten stammen: KA1 stammt aus den Kesseltrichtern unterhalb des Verdampfers und des letzten Überhitzers; KA2 und KA3 aus Trichtern unterhalb der Überhitzer; KA4 aus Trichtern unterhalb des Verdampfers und KA5 aus Trichtern unterhalb des Economizer (Abbildung 7.1).

Die Kesselaschen wurden entweder nach dem Stauen von Aschematerial über manuell geschlossenen Pendelklappen oder durch Aufhängen eines speziell konstruierten Probenahmehalters in den Auslass jedes Kesseltrichters entnommen. Für jedes Inkrement wurde die Probenahme für eine bestimmte Zeit (0,5 - 2h) durchgeführt, und mehrere Probenahme-

Anlage										
Anlage C	III	45%	54%	-	1%	160	30	860	670	250
Anlage D	IV	48%	51%	<1%	-	400	75	840	635	274
Anlage E	IV	55%	45%	-	-	288	48	850	660	260
~~Anlage F~~	~~IV~~	~~45%~~	~~46%~~	~~7%~~	~~1%~~	~~283~~	~~45~~	~~850~~	~~680~~	~~260~~

Anlage	Kessel Typ	Anz. Inkremente / Probenahmedauer
Anlage A	I	28 Inkr. / 14d
Anlage B	II	35 Inkr. / 50d
Anlage C	III	2 Inkr. / 6h
Anlage D	IV	21 Inkr. / 7d
Anlage E	IV	14 Inkr. / 14d
Anlage F	IV	9 Inkr. / 68h

Table 7.2: Details der Probenahme für die verschiedenen Anlagen.

Inkremente jedes Kesselbehälters wurden in einen hitzebeständigen Behälter gegeben, um über mehrere Tage bis Wochen eine Mischprobe pro Kesselbehälter zu bilden (Einzelheiten in Tabelle 7.2). Die Elektrofilterasche wurde entweder über das Notentaschungssystem in eine Mulde entleert oder vom Förderband entnommen und zu Mischproben zusammengeführt. Jede Mischprobe wurde homogenisiert und für die weitere Analyse in 1 kg-Chargen aufgeteilt. Bei ausgewählten Anlagen wurde ein Aliquot von KA1 - 3 mit einem 2-mm-Sieb gesiebt, um die luftgetragenen Aschepartikel von den blockigen Ablagerungen zu trennen. Die chemische und mineralogische Analyse wurde dann an beiden Fraktionen einzeln zusätzlich zur gesamten Asche durchgeführt, um den Unterschied zwischen den beiden Materialien zu verstehen.

7.2.3 Abschätzung der Massenströme

Eine gravimetrische Bestimmung der pro Kesselbehälter produzierten Kesselasche-Menge war in keiner der Anlagen möglich. Daher konnten die Massenströme nur geschätzt werden. Die meisten der untersuchten Anlagen verwenden ein System von Klopfvorrichtungen, die regelmäßig (alle paar Stunden) in Betrieb sind, um die Wärmetauscheroberflächen von Ablagerungen zu reinigen. Es wurde beobachtet, dass die Menge der pro Kesseltrichter anfallenden Kesselasche gegen Ende des Kessels abnahm, wenn die Probenahme ohne den Betrieb der Klopfvorrichtungen erfolgte. Bei der Probenahme mit Klopfvorrichtungen wurden jedoch unterschiedliche Mengenverteilungen pro Trichter beobachtet, je nach der Menge des auf den Wärmetauscherrohren angesammelten Materials. Der prozentuale Anteil von Kesselasche und Elektrofilterasche an der Flugasche wurde mit Hilfe der chemischen Zusammensetzung berechnet. Da die chemische Zusammensetzung der Flugasche bekannt war, konnte der Massenanteil von Kesselasche und Elektrofilterasche für jedes Element berechnet werden, indem die kleinste Abweichung von der Flugaschen-Konzentration ermittelt wurde. Die resultierenden Massenanteile wurden dann gemittelt. Daraus ergab sich ein Anteil von Kesselasche im Verhältnis zur Gesamtmenge an der Flugasche von 25 - 30 Gew.-%. Die Mengenverteilung innerhalb des Kessels konnte nicht bestimmt werden, da die chemischen Zusammensetzungen der verschiedenen Kesselasche-Fraktionen nur geringe Unterschiede aufweisen.

Figure 7.2: Probenahme im Kessel zwischen Überhitzer 1 und 2, Rauchgasrichtung nach links. Die Wächten haben sich gegen die Rauchgasrichtung ausgebildet.

7.2.4 Ofenbegehung während Sanierung

In der KVA Bern konnte im August 2019 und im April 2021 während der Ofensanierung eine Ofenbegehung gemacht werden, nachdem die Sprengreinigung erfolgt ist, aber noch vor der Sandstrahlung. Über Gerüste in der Brennkammer, im Leerzug und im Kessel konnte der Ofen von innen begangen werden und die Ofenanbackungen beprobt werden. Im Ofenraum wurde in regelmässigen Abschnitten das Krustenmaterial beprobt und im Kessel wurde jeweils Material von einem Rohrbündel gesammelt. Im Kessel bilden die Aschenansammlungen z.T. sehr grosse Wächten in Richtung des Zustroms, wie in Abbildung 7.2 zu sehen ist. Die Daten und Beobachtungen aus der Ofenbegehung sind eine weitere Bestätigung dafür, dass es sich bei den hellen Brocken in der Kesselasche um Ablagerungen von Wänden und Wärmetauscherrohren handelt.

7.3 Methodik

7.3.1 Chemische Analysen

Alle Aschen wurden bei 105 °C bis zur Gewichtskonstanz getrocknet und in einer Wolframkarbid-Scheibenmühle auf eine Partikelgröße < 0,01 mm gemahlen. Die chemische Zusammensetzung der Matrixelemente wurde mittels wellenlängendispersiver Röntgenfluoreszenzanalyse (WD-XRF) mit einem Panalytical Axios-Spektrometer an gepressten Pulverpellets (40 mm Durchmesser, 6,40 g Material und 1,44 g Wachs als Bindemittel) bestimmt. Dieselben Pellets wurden mit einem Spectro Xepos-Spektrometer (ED-XRF) mit matrixangepasster Kalibrierung für die Schwermetalle von Interesse (Zn, Cd, Cu, Pb) analysiert. Die Fraktionierung des Kohlenstoffs (TOC400, ROC, TIC900) wurde extern nach DIN 19539 an den getrockneten und fein gemahlenen Aschefraktionen analysiert, die für die chemische Analyse verwendet wurden. Die PCDD/-F Analysen wurden nach

VDI 3499 Bl.1 durchgeführt, wobei die Summe der 17 polychlorierten Dibenzo-p-Dioxine (PCDD) und Dibenzofurane (PCDF) nach den internationalen Toxizitätsäquivalenten (I-TEQ) analysiert wird. Der Gehalt an Al^0 in den Aschen wurde aus der Bestimmung des H_2 Gasvolumens während der Oxidation von Al^0 mit H_2O + NaOH berechnet, wie in Zucha et al., (2020) beschrieben.

7.3.2 Mineralogische Analysen

Für die mineralogische Analyse wurde eine Mischung aus Aschematerial (4 g) und Korund (1 g) als interner Standard in einer XRD-Mühle McCrone von Retsch 6 Minuten lang bei 55 Hz auf eine Korngröße von 1 - 10 μm gemahlen. Die desorientierten Proben wurden dann mit einem PANalytical X'Pert Pro Diffraktometer (CuKα-Strahlung) von 5 bis 60° 2θ bei 0,017°/Schritt für 40 min gemessen, mit einer Beschleunigungsspannung von 40 kV und einem Elektronenstrom von 40 mA. Rietveld-Verfeinerungen wurden mit der Software TOPAS-Academic V6 durchgeführt, wobei die Strukturdaten (.cif-Dateien) der Anorganic Crystal Structure Database (ICSD) verwendet wurden.

7.3.3 Bestimmung der spezifischen Oberfläche

Die spezifische Oberfläche (SSA) wurde durch Stickstoffadsorption bestimmt. Etwa 3 g des ungemahlenen Probenmaterials wurden durch Erhitzen unter Vakuum bei 105 °C für 24 Stunden mit dem BELPREP - vac III Vorbehandlungsgerät gründlich von den primär adsorbierten Gasen desorbiert. Die Adsorptionsisothermen wurden im Gleichgewicht mit flüssigem Stickstoff mit einem BELSORP-miniX Oberflächenanalysator gemessen. Die N-Oberfläche wurde nach der Methode von Brunauer, Emmet und Teller (BET) für einen Druckbereich von P/P0 von 0,05 bis 0,3 berechnet.

7.3.4 Rasterelektronenmikroskop

Die Rasterelektronenmikroskop (REM) Analysen wurden mit einem Zeiss EVO-50 XVP Elektronenmikroskop in Verbindung mit einem energiedispersiven EDAX Apollo X System (EDS) durchgeführt. Die Ascheproben wurden in Epoxidharz eingebettet, wasserfrei poliert und mit Kohlenstoff beschichtet, um eine Oberflächenaufladung zu vermeiden. Für die Aufnahmen mit rückgestreuten Elektronen (BSE) wurden eine Beschleunigungsspannung von 15 kV, ein Hochvakuummodus und eine Spotgröße von 504 nm verwendet.

7.3.5 Säureneutralisationskapazität

Die Titration des Säureneutralisationsvermögens wurde an einer Mischung aus Asche (2 g) und 20 ml Reinstwasser durchgeführt. Die Suspension wurde in 40 Schritten mit einem 785 DPM Titrino-Gerät von Metrohm durch Zugabe von 1 ml 1M HCl in Intervallen von 10 Minuten unter ständigem Rühren titriert.

Figure 7.3: Makroskopische Unterschiede zwischen der Kesselasche (links) und der Elektrofilterasche (rechts).

7.3.6 Extraktionsversuche

Die Extraktionsversuche wurden durch Stephan Fromm (ZAR) ausgeführt. Für die Extraktionsversuche wurden 100 g Asche mit 300 ml HCl (5%) extrahiert (Fest-Flüssig Verhältnis von 1:3), während 60 Minuten und bei einer Temperatur von 65 °C. Zur Kontrolle des pH-Wertes wurde HCl (32%) tropfenweise dosiert und zum Erreichen von oxidierenden Bedingungen in der zweiten Hälfte der Extraktion wurde jeweils insgesamt 2.9 mol H_2O_2 (30%) pro kg Asche in kleinen Mengen dosiert. Nach der Extraktion wurde die Suspension mittels Vakuumfiltration filtriert, wobei der Filterkuchen mit ca. 50 ml deionisiertem Wasser nachgewaschen wurde. Das Filtrat wurde anschliessend verdünnt und mit ICP-OES analysiert. Der Filterkuchen wurde bis zur Gewichtskonstanz getrocknet und mit XRF analysiert. Der Anreicherungsfaktor wurde über die 10 inerten Elemente Si, P, S, Ti, Cr, Fe, Ni, Sn, Sb, Ba bestimmt.

7.4 Chemische und mineralogische Charakterisierung

7.4.1 Makroskopische Eigenschaften

Bereits makroskopisch ist ein Unterschied zwischen Kessel- zu Elektrofilterasche zu erkennen (Abbildung 7.3). Die Kesselasche bildet einen grobkörnigen Mix aus flugfähigen Asche- und Russpartikeln, worin auch gröbere Bruchstücke von Rohrkrusten enthalten sind, die sich über ein 2 mm Sieb abtrennen lassen (Abbildung 7.4). Die Elektrofilterasche besteht aus einem homogenen, feinstkörnigem Aschestaub mit starker Tendenz zur Partikelagglomeration. Zudem enthält die Elektrofilterasche vereinzelt mm-grosse Russpartikel.

7.4.2 Chemische Zusammensetzung

Bezüglich der chemischen Zusammensetzung lassen sich keine grossen Unterschiede zwischen der Leerzugasche (Leerzugasche) zu den verschiedenen Kesselaschefraktionen (KA1 - KA5) beobachten (Abbildung 7.5). Beide Aschetypen zeichnen sich aus durch einen relativ hohen Calcium (Ca) Gehalt (> 200'000 mg/kg), gefolgt von Schwefel (S) (50

Figure 7.4: Durch ein 2mm Sieb lässt sich die Kesselasche grob unterteilen in rieselfähiges Material (links) und Krusten (rechts), die sich an den Wärmetauscheroberflächen gebildet haben (rechts).

- 125'000 mg/kg). Die Leerzugasche und Kesselasche weisen außerdem Chlor (Cl) und Silizium (Si) als Hauptbestandteile auf, gefolgt von Natrium (Na), Kalium (K), Eisen (Fe) und Aluminium (Al). Die Leerzugasche ist generell etwas reicher an Si, Al, Fe und niedriger an Na, K, S, Cl als die Kesselasche. Die Kesselaschen unterscheiden sich aber deutlich von der Elektrofilterasche. Von KA5 zur Elektrofilterasche ist eine große Veränderung in der Elementzusammensetzung zu beobachten, da die Konzentration der weniger flüchtigen Elemente (Ca, Si, Al, Fe) deutlich abnimmt, während die der flüchtigeren Elemente und Schwermetalle (Cl, Na, K, Zn, Pb, Cu, Cd, Sb, Sn) stark zunimmt. Die Hauptbestandteile der Elektrofilterasche sind Cl, Ca, S, Na, K (> 50'000 mg/kg). Schwermetalle von wirtschaftlichem Interesse (z. B. Zn, Cu, Sn) und potenziell umweltgefährdende Schwermetalle (z. B. Pb, Cd, Sb) sind in der Elektrofilterasche im Vergleich zu Leerzugasche und Kesselasche stark angereichert. Dennoch sind hohe Pb- und Sb-Gehalte auch in KA3 zu beobachten. Die Kesselasche der Anlage F weisen deutlich niedrigere Ca-, Cl-, Si- und Al-Konzentrationen auf als die Kesselasche der anderen Anlagen, aber höhere S-, Na-, K-, Zn-, Pb-, Sb- und Sn-Konzentrationen. Ab der Mitte des Kessels ist ein Rückgang der Ca-Konzentration und ein Anstieg der Na- und K-Konzentration zu beobachten, und es gibt einen starken Pb-Peak für KA3, mit Konzentrationen, die fast 5x höher sind als in der Elektrofilterasche. Die Zn-Konzentrationen in Kesselasche aus dem hinteren Teil des Kessels sind ähnlich oder höher als die Zn-Konzentrationen in der Elektrofilterasche aus den anderen Anlagen. Die Ablagerungen, die von der Kesselasche und Leerzugasche abgesiebt wurden, sind chemisch sehr ähnlich zu den Aschen der Anlage F und zeichnen sich durch hohe Konzentrationen an S, Ca, Na und K aus (Abbildung 7.6). Al, Fe, Si und Cl sind nur
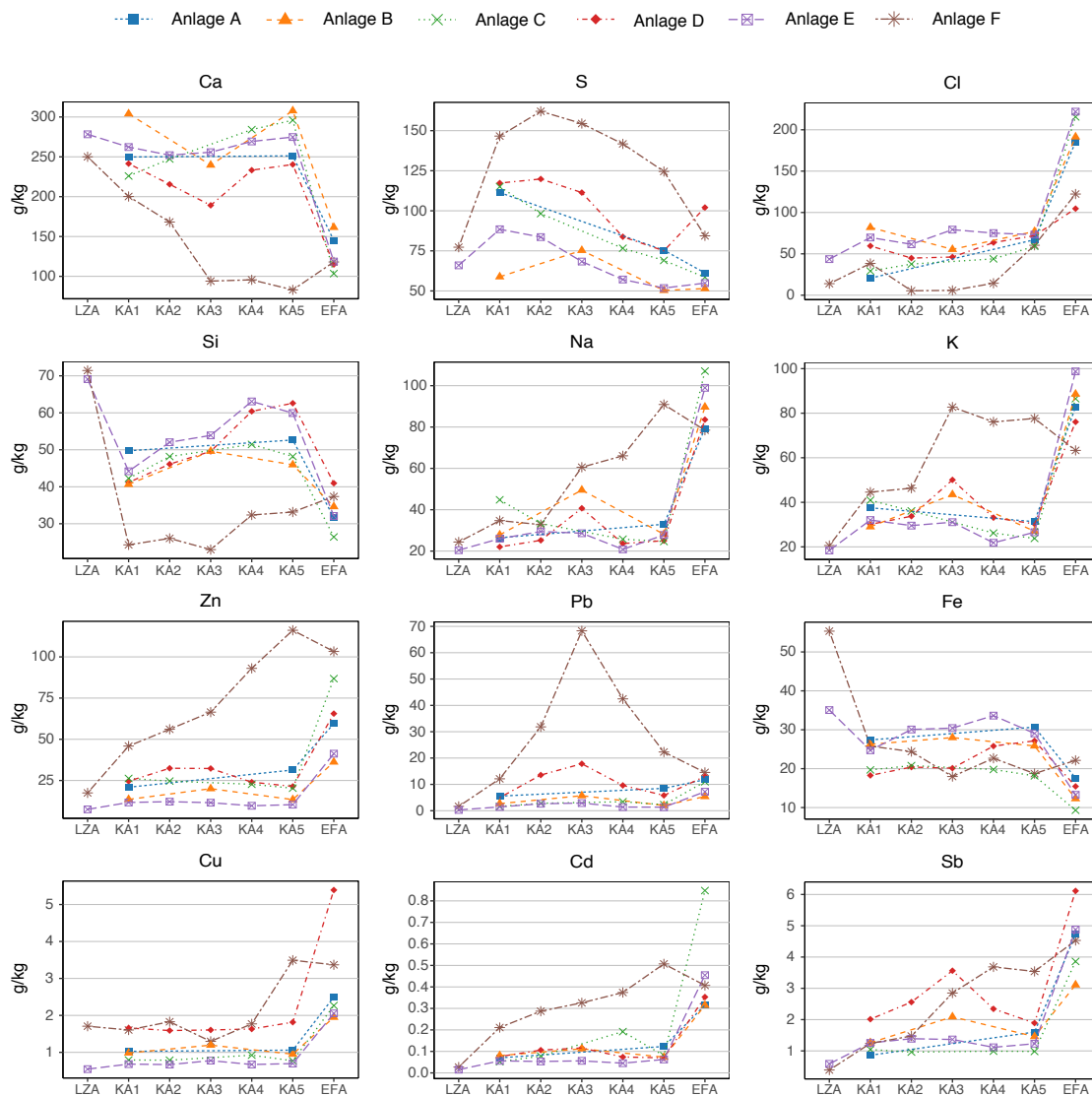
Figure 7.5: Chemische Zusammensetzung der verschiedenen Aschefraktionen, bestimmt mittels XRF. LZA = Leerzugasche, KA = Kesselasche, EFA = Elektrofilterasche.

in geringen Konzentrationen vorhanden. Nur die am ersten Kesseltrichter gesammelten Ablagerungen aus den Anlagen D und E weisen vergleichbar hohe Cl-Konzentrationen auf. Die Konzentrationen von Zn, Pb und Cd sind in den Ablagerungen deutlich höher als in den entsprechenden Kesselasche. Die Cu-Konzentrationen sind in den Ablagerungen gleich hoch oder niedriger als in der zugehörigen Kesselasche.

7.4.3 Mineralogische Zusammensetzung

Die mineralogische Zusammensetzung der Leerzug-, Kessel- und Elektrofilterasche ist für die Anlagen A - E sehr ähnlich und in Abbildung 7.7 dargestellt. Die Aschen der Anlage F weisen eine andere mineralogische Zusammensetzung auf (Abbildung 7.7c), die sehr ähnlich ist wie jene der Krusten, die von anderen Anlagen abgesiebt wurden (Abbildung 7.7d). Analog der chemischen Zusammensetzung weisen die Leerzugasche und die Kesselasche
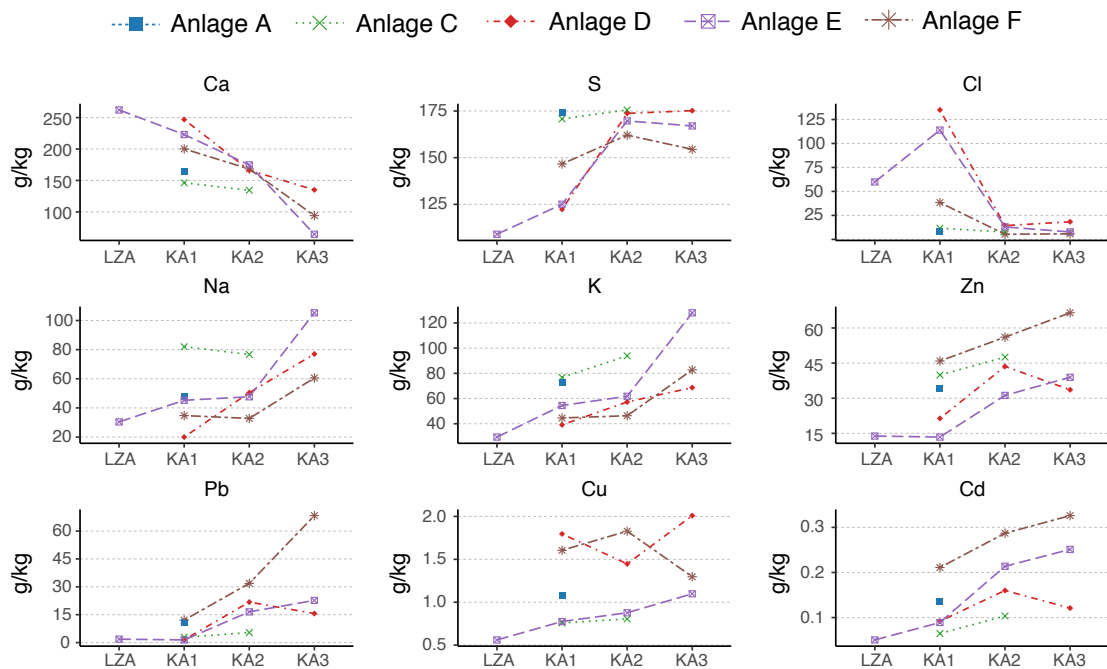
Figure 7.6: Chemische Zusammensetzung der abgesiebten Krusten. LZA = Leerzugasche, KA = Kesselasche, EFA = Elektrofilterasche.

eine vergleichbare mineralogische Zusammensetzung auf. Die Hauptbestandteile sind Anhydrit, Silikate (z. B. die Melilite Gehlenit und Akermanit, Quarz und Feldspäte) und Oxide (z. B. Kalk, Hämatit, Perowskit). Calcit und Chloride (hauptsächlich Halit) sind ebenfalls in den meisten EA und BOA vorhanden, allerdings in geringen Konzentrationen um 5 Gew.-%. Der Anteil an amorphen und nicht identifizierten Phasen wurde auf 40 - 50 % gerechnet. Die Leerzugasche der Anlage F ist vergleichbar mit den Leerzugasche und Kesselasche von anderen Anlagen. Die Mineralogie der Elektrofilterasche wird von Chloriden dominiert, was der hohen Cl-Konzentration entspricht. Die Spektren der verschiedenen Elektrofilterasche sind vergleichbar, aber die absoluten Mineralkonzentrationen variieren von Anlage zu Anlage. Die Mineralogie der analysierten Elektrofilterasche kann in 3 Typen eingeteilt werden. Die Elektrofilterasche der Anlage A, C und E weisen sehr hohe Konzentrationen von Halit (15 - 25 Gew.-%) und K_2ZnCl_4 (9 - 16 Gew.-%) sowie Sylvit in geringen Konzentrationen auf. Die Elektrofilterasche aus den Anlage D und F ist durch hohe Konzentrationen an K_2ZnCl_4 und D'Ansit ($Na_{21}ZnCl_3(SO_4)_{10}$) gekennzeichnet. Anhydrit und Halit sind in Konzentrationen um 10 Gew.-% vorhanden. Die Elektrofilterasche aus der Anlage B enthält kein K_2ZnCl_4. Stattdessen ist die Konzentration von Sylvit, Calcit und Oxiden im Vergleich zu anderen Elektrofilterasche erhöht. Der berechnete Anteil an amorphen Phasen ist in der Elektrofilterasche genauso hoch wie bei den Kesselasche (etwa 50 %). Obwohl Schmelztropfen gelegentlich den Elektrofilter erreichen, wurde bei REM-Untersuchungen festgestellt, dass die Elektrofilterasche hauptsächlich aus sehr feinen Kristallen besteht, die wahrscheinlich zu feinkörnig sind (« 1 μm), um mit Röntgenstrahlen aufgelöst zu werden. Es wird daher angenommen, dass nicht identifizierte mikrokristalline Phasen einen grossen Teil der amorphen oder nicht identifizierten Fraktion ausmachen.
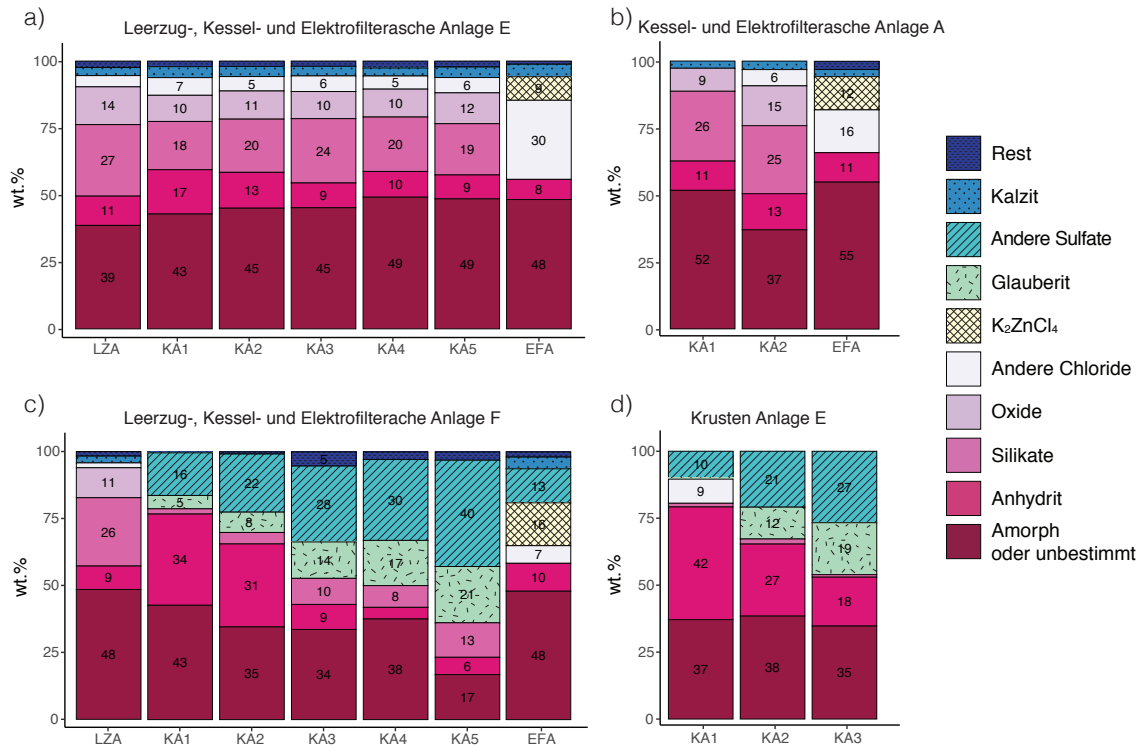
Figure 7.7: Mineralogische Zusammensetzung der verschiedenen Aschetypen und Krusten.

Die Mineralogie der Krusten ist dominiert durch Anhydrit, Glauberit und weiteren, eher komplexen Mischsulfaten, die oftmals Ca, Na, K und Zn in der Matrix aufweisen (Abbildung 7.8). Mittels Rasterelektronenmikroskop konnte beobachtet werden, dass die hohen Pb Gehalte in den Krusten hauptsächlich durch $(Na,K)-PbSO_4$ gebunden sind.

7.4.4 Kohlenstoff-Fraktionierung

Der Gehalt an organischem Kohlenstoff (TOC) ist in den Kesselaschen im Allgemeinen höher als in der Elektrofilterasche (Abbildung 7.9). Für die Anlage F lagen die Werte aller Kohlenstofffraktionen für alle analysierten Aschefraktionen unter der Nachweisgrenze. Der
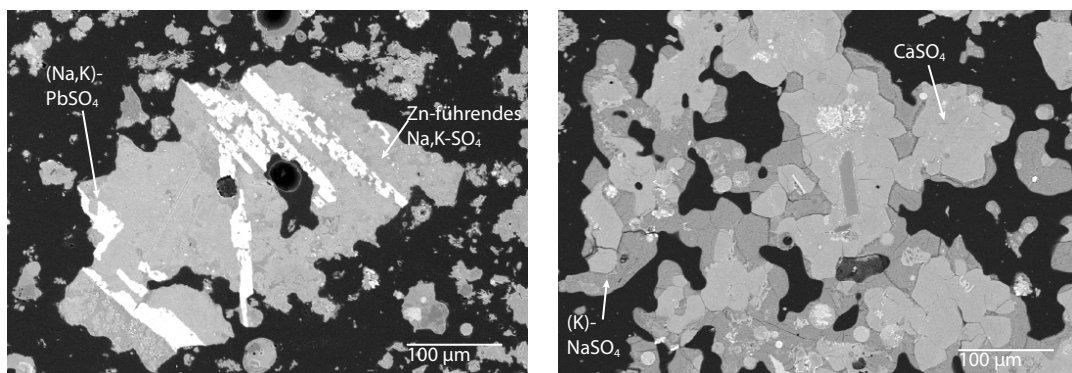
Figure 7.8: REM Aufnahmen der Krusten: Schön ausgebildete $(Na,K)-PbSO_4$ Kristalle (links) und Komplexe Mischsulfate als Matrix (links und rechts).
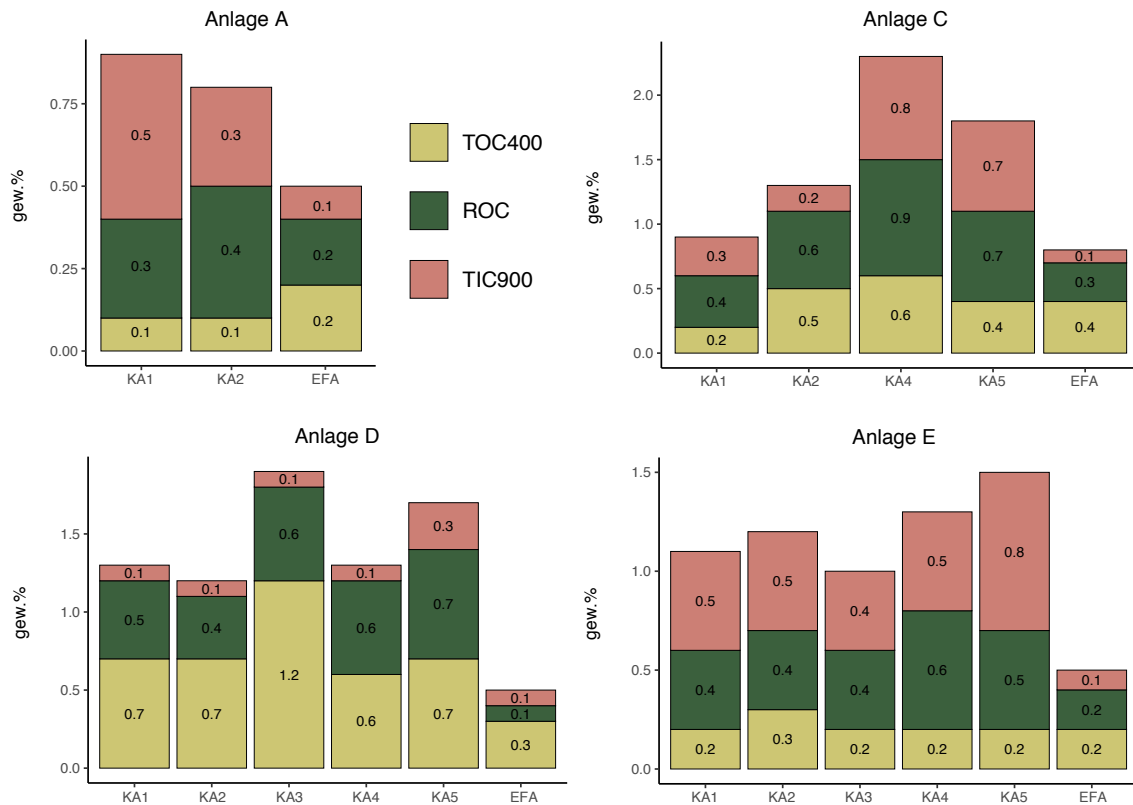
Figure 7.9: TOC Gehalt der verschiedenen Aschefraktionen aufgeschlüsselt in TOC400, ROC und TIC900. Der TOC Gehalt der Anlage F liegt unterhalb der Bestimmungsgrenze. Für die Anlage B wurde der TOC nicht bestimmt. KA = Kesselasche, EFA = Elektrofilterasche.

Gehalt an anorganischem Kohlenstoff (TIC900) weist auf die Ausgasung von CO_2 aus Mineralien hin, z.B. durch die Zersetzung von Calcit. Die Konzentrationsverteilung stimmt mit der Verteilung der Karbonate in der Kesselasche und Elektrofilterasche überein, wobei die Kesselasche tendenziell die höheren Konzentrationen aufweist. Der restlich oxidierbare Kohlenstoff (ROC) ist mit Kohle- und Rußpartikeln verbunden. Der konstante Anteil von ROC über die jeweiligen Kesselaschenfraktionen einer Anlage und die anschließende Abnahme des ROC-Gehalts in der Elektrofilterasche stimmt mit makroskopischen Beobachtungen überein. Der TOC400-Gehalt zeigt den organisch gebundenen Kohlenstoff an.

7.4.5 Spezifische Oberflächen

Die spezifischen Oberflächen korrelieren stark mit dem Russgehalt (ROC, Abbildung 7.10). Daher zeigen die Kesselaschen mit hohen Gehalten an Russpartikeln (v.a. Anlage C) hohe spezifische Oberflächen für Aschen. Bei Anlagen mit tieferen ROC Gehalten (Anlage A, E, F) zeigt sich ein Anstieg der spezifischen Oberfläche hin zur Elektrofilterasche.

7.4.6 Dioxine und Furane

Der Gehalt an polychlorierten Dibenzo-dioxinen und -furanen (PCDD/-F) in den einzelnen Kesselaschefraktionen ist für die Beurteilung von alternativen Entsorgungswegen dann relevant, wenn nach der sauren Wäsche eine Methode zur Zerstörung von Dioxinen angewen-
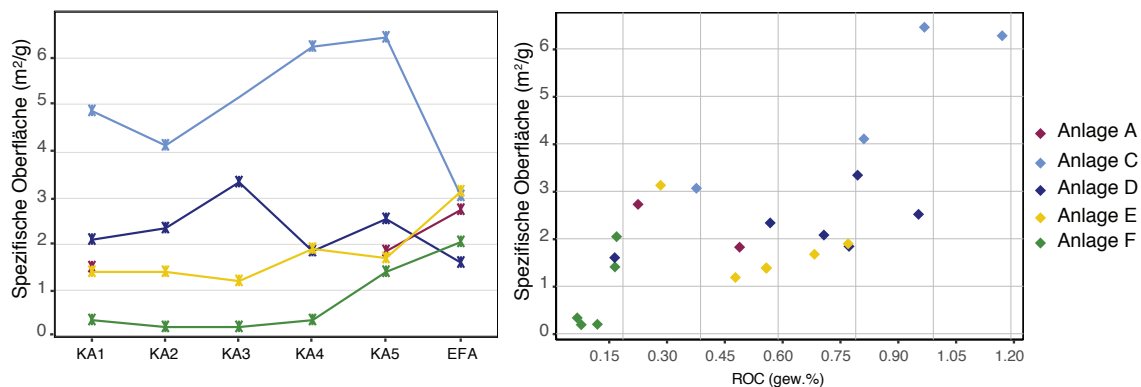
Figure 7.10: Spezifische Oberfläche der verschiedenen Aschefraktionen (links) sowie Korrelation zu TOC400 (rechts). KA = Kesselasche, EFA = Elektrofilterasche.
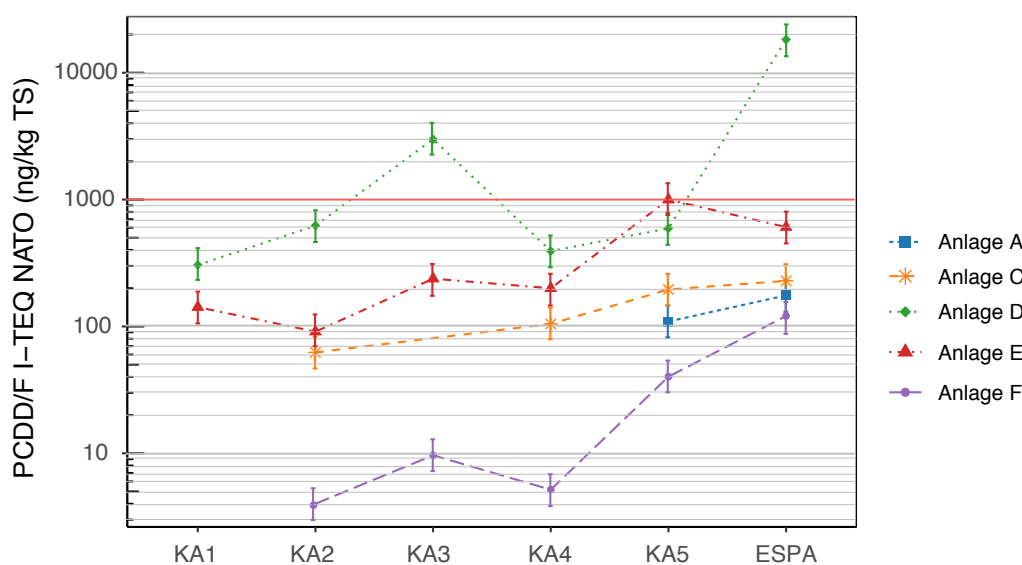
Figure 7.11: Gehalte an polychlorierten Dibenzo-dioxinen und -furanen (PCDD/-F) (als TEQ) in den verschiedenen Aschefraktionen (KA = Kesselasche, EFA = Elektrofilterasche) in logarithmischer Skala.

det wird (z.B. Refire durch Rückführung des Filterkuchens). In Abbildung 7.11 ist zu beobachten, dass die Gehalte an PCDD/-F in der Mitte des Kessels bereits über 100 ng/kg sind und gegen Ende des Kessels weiter ansteigen. Die Elektrofilterasche zeigt oftmals die höchsten Werte an PCDD/-F.

7.4.7 Extrahierbarkeit der Aschen

Anhand der mineralogischen Zusammensetzung lässt sich grob das Extraktionsverhalten ableiten. Infolge der geringen Konzentration an säurepuffernden Mineralien (z. B. CaO, $CaCO_3$, Ca-Silikate) weist die Elektrofilterasche eine deutlich niedrigere Säurepufferkapazität (ANC-Wert (englisch für Acid Neutralizing Capacity)) als die Leerzug- und Kesselaschen auf (Abbildung 7.12). Die abgebildeten Säurepufferkapazitäten bezeichnen die Menge an Säure, die während der Titration beigegeben werden musste, um einen pH-Wert von 3 zu erhalten (entspricht etwa dem pH-Wert während der sauren Wäsche). Die ANC der Leerzugasche und Kesselasche sind vergleichbar. Es ist ein leichter Anstieg der ANC
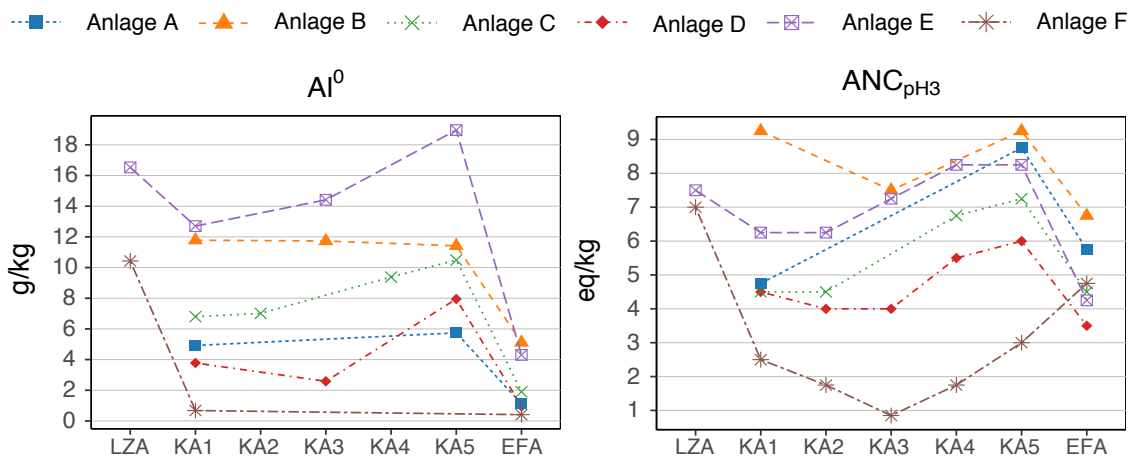
Figure 7.12: Gehalt an metallischem Aluminium (links) und Säurepufferkapazität (rechts) der verschiedenen Aschefraktionen (LZA = Leerzugasche, KA = Kesselasche, EFA = Elektrofilterasche).

zum Ende des Kessels hin zu beobachten bei den Kesselasche der Anlagen A - E, was vermutlich mit dem abnehmenden Krustengehalt gegen Ende des Kessels verbunden ist. Die Krusten weisen einen sehr tiefen ANC auf: Bei Anlage F ist ein deutlicher Abfall der ANC von Leerzugasche zu KA1 festzustellen. Die Kesselasche aus Anlage F zeigen einen sehr niedrigeren ANC, der sogar tiefer ist als jener der Elektrofilterasche. Der Gehalt an metallischem Aluminium (Al^0) kann als Proxy für den Verbrauch an Oxidationsmittel während der Extraktion gesehen werden. Das metallische Aluminium ist oftmals mit dem Gehalt an kleinen Alufoliepartikel verbunden, die als Schwebeteilchen im Verlauf des Kessels absinken und sich daher eher in den Kesselaschen als in der Elektrofilterasche anreichern, wie in Abbildung 7.12, links zu sehen ist.

Die Abbildung 7.13 zeigt die Metallausbeuten für die Metalle Zn, Pb, Cu, Cd, welche in den Laborextraktionsversuchen erzielt wurden. Es ist zu beobachten, dass die Zinkausbeute mit 58 - 83% generell hoch ist und keine grossen Unterschiede erkennbar sind zw. der Kessel- und der Elektrofilterasche. Die Bleiausbeute ist in den Kesselaschen der Anlage F (violette Balken) sehr tief (0 - 15%) trotz der sehr hohen Pb-Gehalte in den Aschen. Dies ist vermutlich auf das als schwer lösliche $PbSO_4$ gebundene Pb zurückzuführen. Für die beiden anderen Anlagen (Anlagen C und D) schwankt die Pb-Ausbeute zw. 17 - 84% und die Kesselasche zeigt nicht schlechtere Ausbeuten als die Elektrofilterasche. Bei Kupfer ist zu beobachten, dass sich das Kupfer besser aus der Elektrofilterasche mobilisieren lässt. Die Cu-Ausbeuten der Kesselasche sind deutlich tiefer für die Anlagen C und D. Bei den Kesselasche der Anlage F zeigt sich kein grosser Unterschied zur Elektrofilterasche. Die Cd Gehalte sind für alle Aschetypen konstant hoch zwischen 85 - 99%.

Der Nettosäureverbrauch zur Korrektur des pH-Wertes während der Extraktion bildet in der Tendenz genau die Säureneutralisationskapazität ab (Abbildung 7.14). So steigt der Säureverbrauch für die Kesselaschfraktionen gegen Ende des Kessels leicht an und ist dann jeweils etwas tiefer für die Elektrofilterasche.

Abbildung 7.15 zeigt die Gehalte der unbehandelten Kesselasche im Vergleich zur behandelten Elektrofilterasche. Dabei ist zu beobachten, dass insbesondere bei den Anlagen
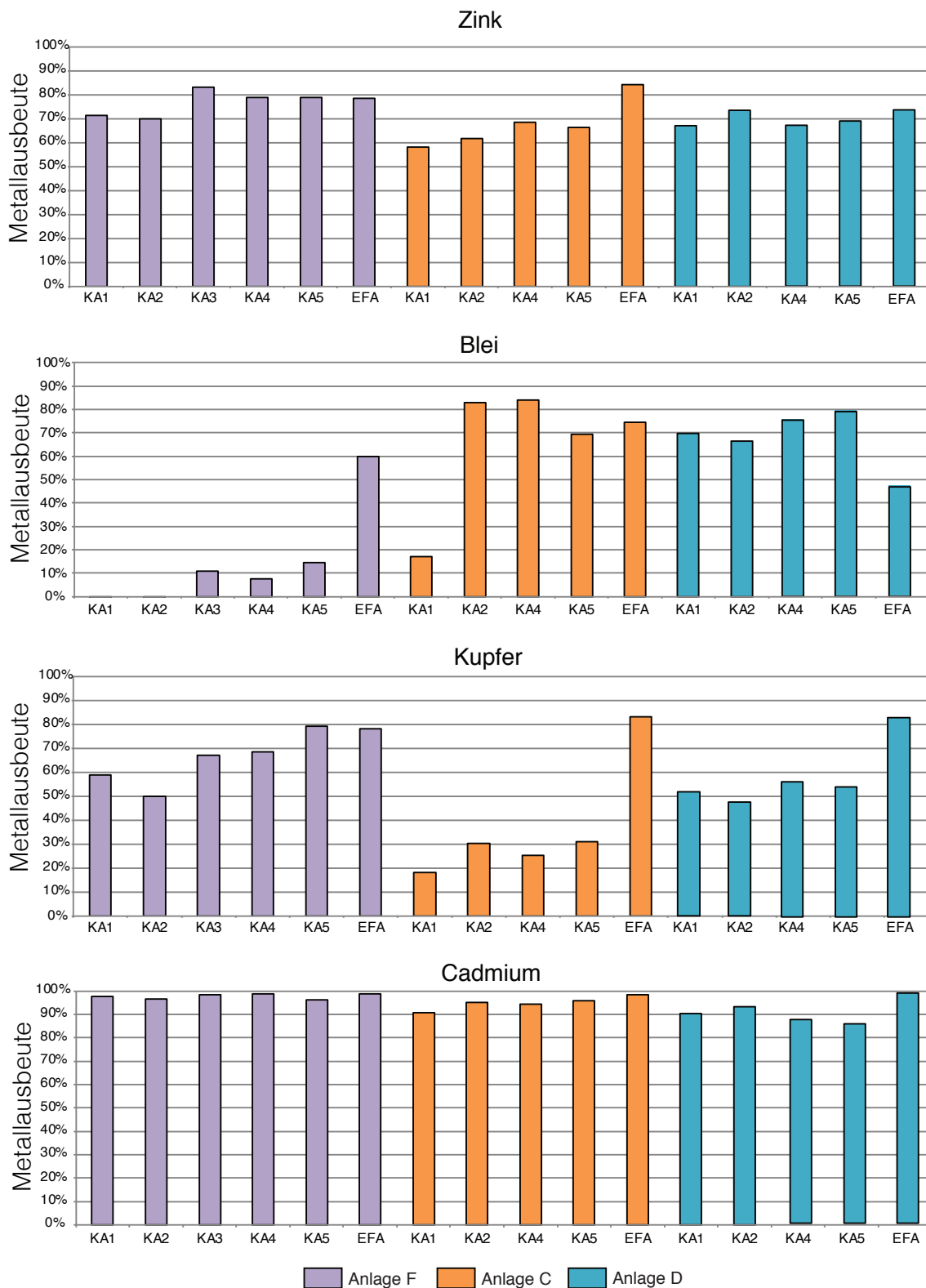
Figure 7.13: Metallausbeuten für die Metalle Zn, Pb, Cu, Cd. Violett = Anlage F, orange = Anlage C, blau = Anlage D
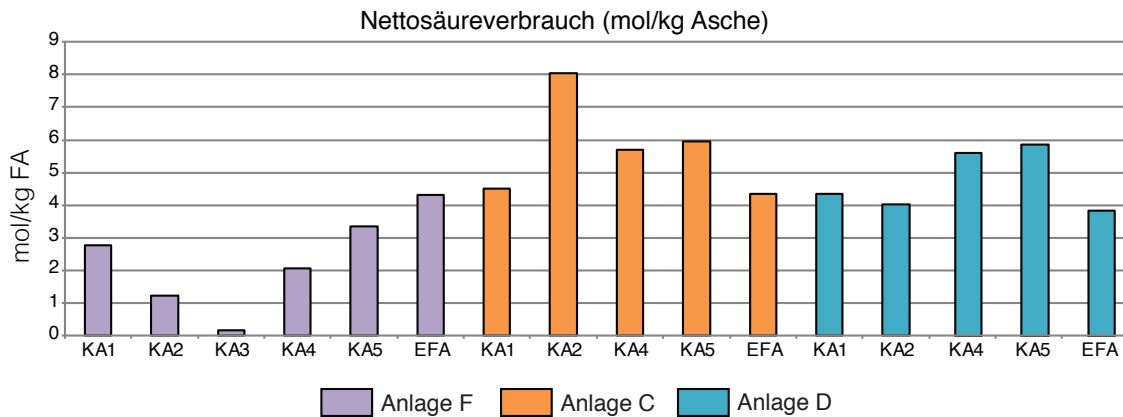
Figure 7.14: Nettosäureverbauch zur Korrektur des pH-Wertes während der Extraktion. Violett = Anlage F, orange = Anlage C, blau = Anlage D

C und D (orange und blaue Balken) die Gehalte der unbehandelten Kesselasche im selben Bereich liegt wie jene der behandelten Elektrofilterasche. Für die Anlage F (violette Balken) liegen die Gehalte deutlich darüber.

7.5 Ansätze zur Abgrenzung zur Schlacke

7.5.1 Genetischer Ansatz

Genetisch unterscheidet sich die Flugasche hauptsächlich dadurch von der Schlacke, dass deren Hauptbestandteile aus der Gasphase als neugebildete Phasen kondensiert sind. Die Schlacke besteht dagegen hauptsächlich aus den festen Rückständen der Verbrennung und deren Schmelzen. Die Kesselaschen bestehen hauptsächlich aus der Schwebefracht der Staubpartikel, beinhalten aber auch zu unterschiedlichen Anteilen neugebildete Salze, oftmals in Form von Krusten, die sich um die Wärmetauscherrohre gebildet haben. Als Einstufung, welche Kesselaschefraktionen „schlackeähnlich" sind, könnte deren Entstehung als Kriterium herangezogen werden, da die Schwermetalle oft über die Gasphase transportiert werden, und sich oftmals in angereicherter Form in neugebildeten Phasen finden. Zudem wirken sich hohe Gehalte an säurepuffernden Phasen wie CaO und $CaCO_3$ und feinen Calciumsilikaten (in Form von Gehlenite oder Schmelztropfen), die vermehrt über die Staubphase transportiert werden, negativ auf den Säureverbrauch aus. Die Abbildung 7.16 zeigt die chemischen Profile der anfallenden Verbrennungsrückstände aus der KVA: Schlacke, Leerzug-, Kessel-, Elektrofilterasche. Zur Orientierung sind auch ein paar Datenpunkte von Flugasche aus demselben Datensatz dargestellt. Das molare Verhältnis aus den Elementen Na, K, S, Cl (Hauptbestandteile neugebildete Salze) zu den Elementen Al, Ca, Si, Fe (Hauptzusammensetzung der Durchläuferminerale + Glasphase) kann als grober Indikator verwendet werden, um die die mineralische Zusammensetzung abzuleiten, welche für die Extrahierbarkeit von zentraler Bedeutung ist. Wie in Wolffers et al., (2021) beschrieben, resultiert ein hoher Anteil an Durchläuferminerale und Glasphase tendenziell in einer hohen Säureneutralisationskapazität (ANC). Aschefraktionen, die hauptsächlich
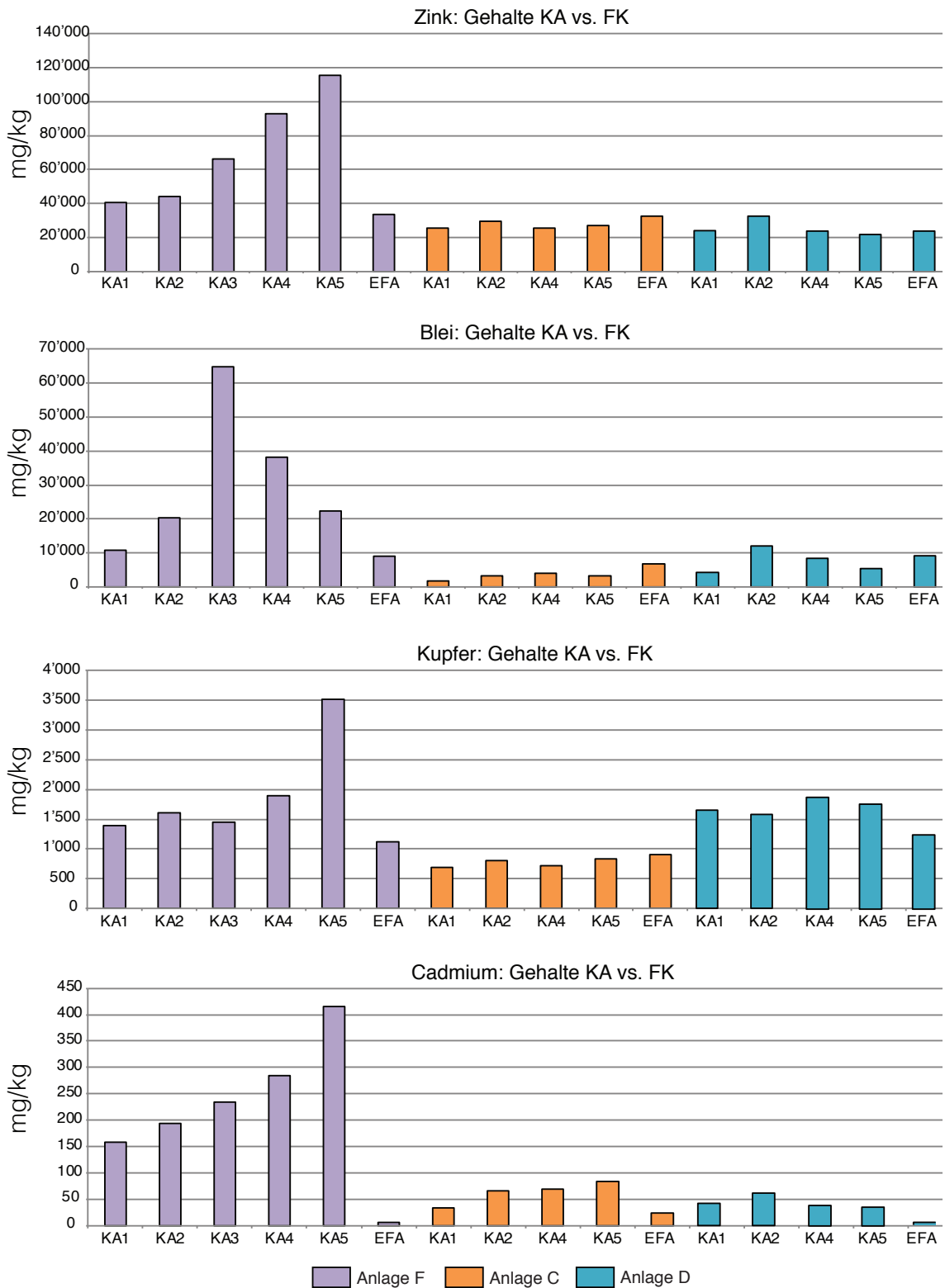
Figure 7.15: Schwermetallgehalte in der unbehandelten Kesselasche im Vergleich zu den Gehalten im Filterkuchen der Elektrofilterasche
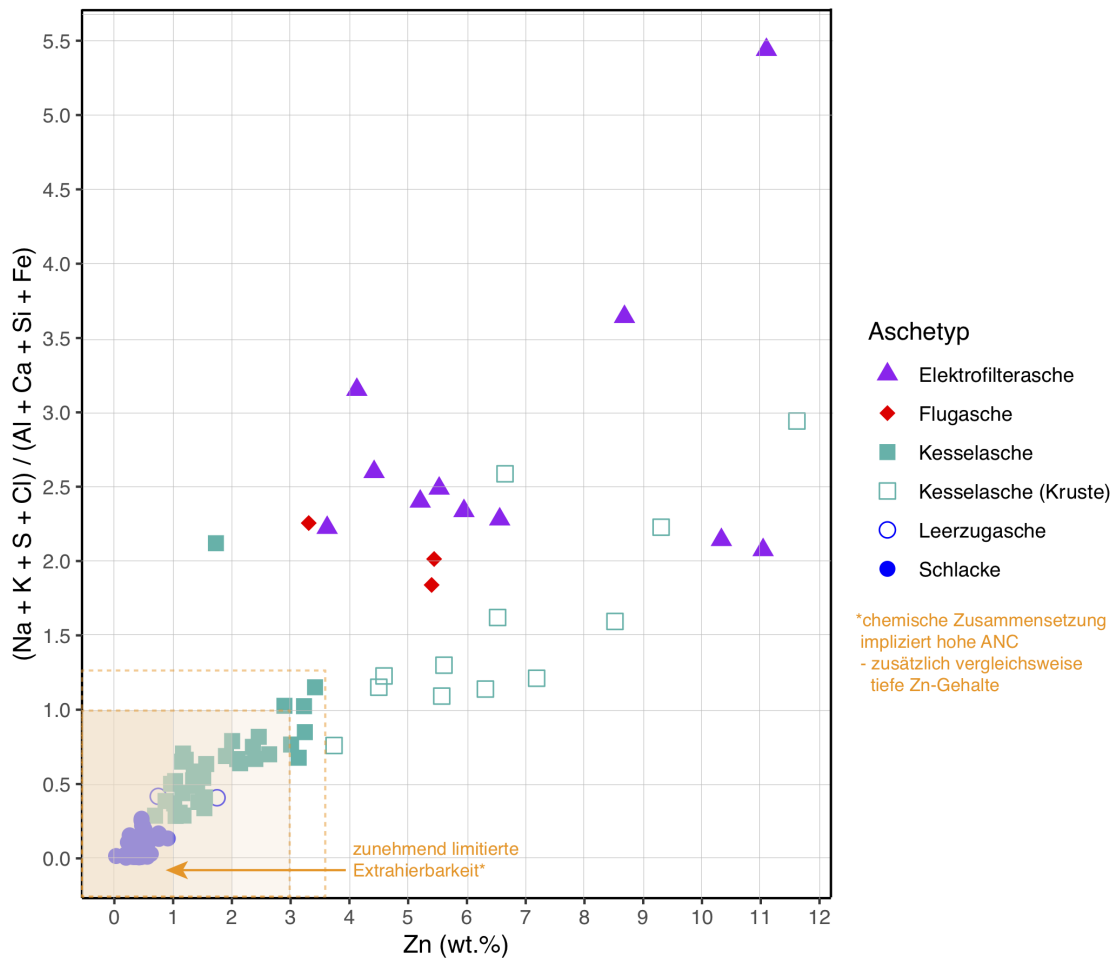
Figure 7.16: Chemische Profile der anfallenden Verbrennungsrückstände.

aus neugebildeten Salzen bestehen, zeigen eine tiefe Säureneutralisationskapazität. Für die X-Achse wurde der Zn-Gehalt gewählt als Indikator für den Gehalt an mit der Gasphase transportierten Schwermetallen. Der orange Bereich unten Links zeigt verschiedene mögliche Szenarien zur Definition von «schlackenähnlich». Die Datenpunkte unterhalb von y=1 enthalten vermehrt Staubfracht mit hoher ANC. Es gilt hierbei zu klären, bis zu welchen minimalen Zn-Gehalten eine Rückgewinnung noch sinnvoll ist. Liegt diese Definition vor, kann der orange Kasten eingegrenzt werden. Somit könnte dieser «genetische Ansatz» zur Bestimmung der «schlackenähnlichen Zusammensetzung» verwendet werden.

In Abbildung 7.17 sind die anderen relevanten Schwermetallgehalte (Pb, Cu, Cd) auf der x-Achse dargestellt. Unabhängig vom gewählten Schwermetall zeichnen sich klare Grenzen zwischen den Aschetypen ab. Zusätzlich erweist sich Zn als robustes Element für für den Einbezug der Metallrückgewinnung, im Gegensatz zu den redox- oder stark pH sensitiven Metallen wie z.B. Cu.

Abbildung 7.18 zeigt das chemische Profil aufgeschlüsselt nach Anlage und Aschetyp für die Kesselaschen. Es zeigt sich, dass die Aschen der untersuchten Anlagen verschiedene Profile zeigen (hauptsächlich bestimmt durch den Anteil an Krusten). Besonders die Anlage F, deren Kesselaschen mehrheitlich aus Krusten bestehen, hebt sich deutlich von den
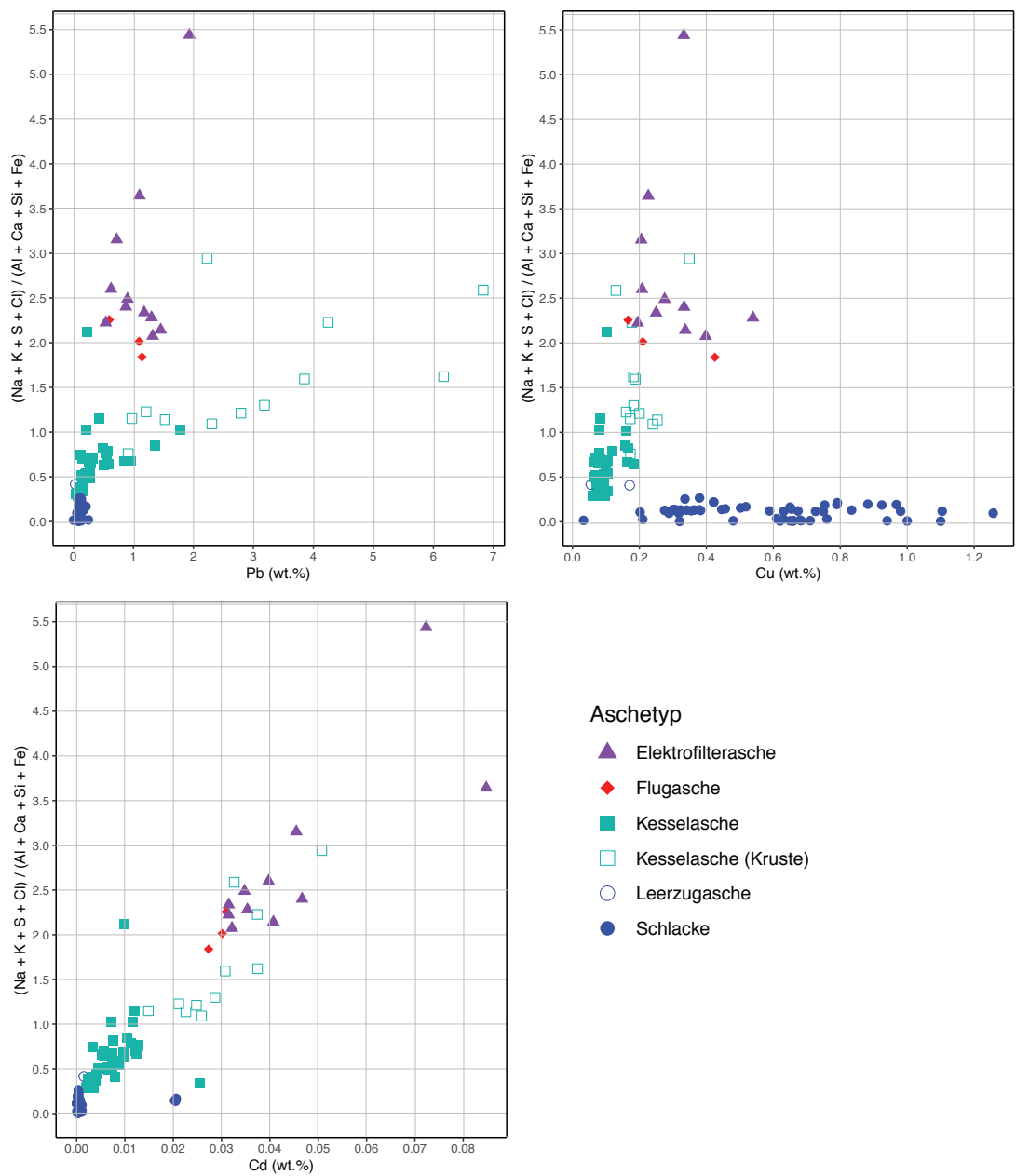
Figure 7.17: Chemisches Profil der verschiedenen Aschetypen analog Abbildung 7.16, mit Pb, Cu und Cd als Vergleich in der X-Achse
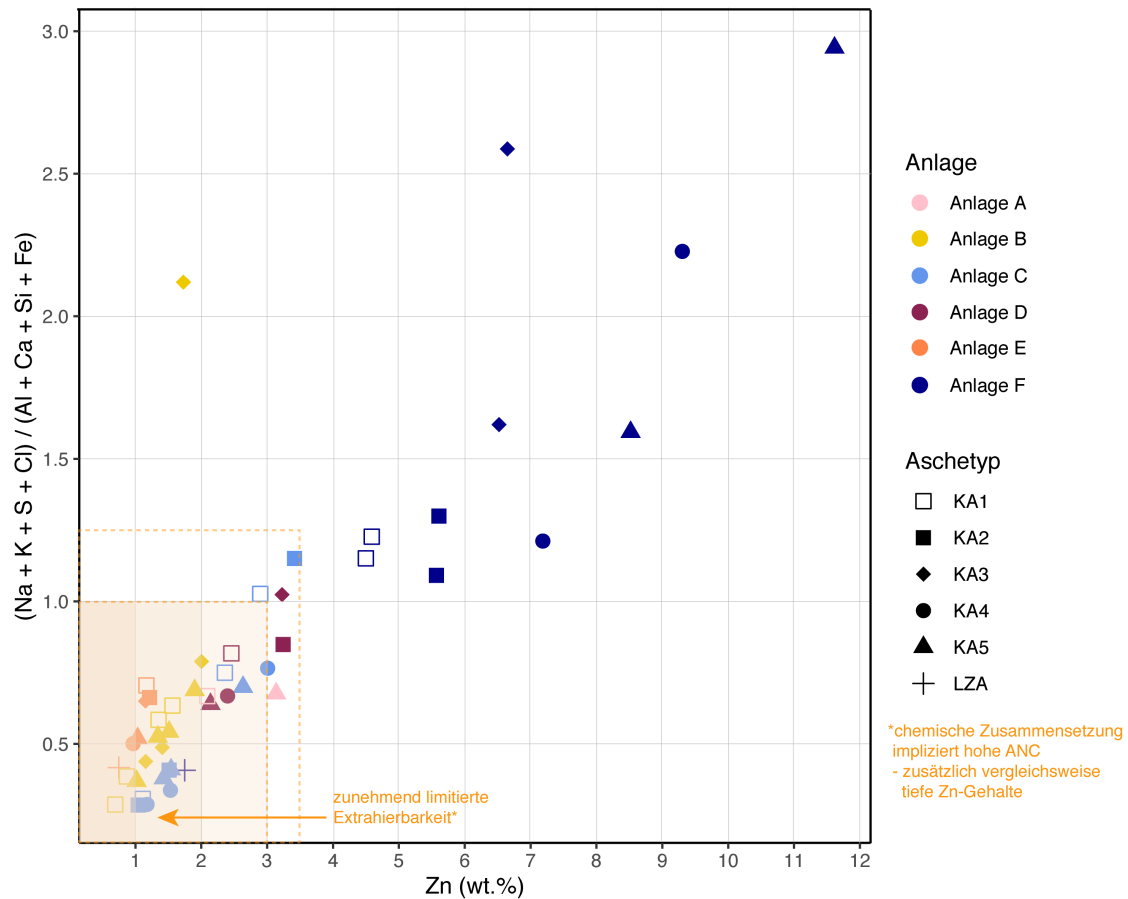
Figure 7.18: Chemisches Profil der Kesselaschen aufgeschlüsselt in Aschetyp und Anlage.

anderen Anlagen ab. Jedoch ergibt sich für die Aschefraktionen innerhalb einer Anlage keine klare Verteilung der Aschfraktionen. Tendenziell zeigt sich aber dass das Verhältnis von volatilen zu Durchläuferelementen bei KA1 - KA3 grösser ist als bei den Kesselfraktionen des hinteren Teils des Kessels (KA4 und KA5), da der Anteil an Krusten im vorderen bis mittleren Teil des Kessels oft höher ist als im hinteren Teil des Kessels. Zudem zeigen sie oft auch höhere Zn-Gehalte. Die verschiedenen orangen Bereiche unten links im Diagramm, welche mögliche Abgrenzungsszenarien zur Schlacke darstellen, zeigen, dass die Abgrenzungen stärker von der Anlage abhängt als vom Kesselaschentyp.

7.5.2 Ansatz Vergleich Schlackenstaub

Der Schlackenstaub, welcher z.B. als Endprodukt der Schlackenaufbereitung bei der ZAV Recycling AG entsteht, ist wohl jene Schlackefraktion in diesem Prozess, die in ihren Eigenschaften der Leerzug- und Kesselasche am nächsten kommt. Allerdings zeigen bereits makroskopische Untersuchengen deutliche Unterschiede zwischen den beiden Materialien: der Schlackenstaub ähnelt eher einem Feinsand, da die einzelnen Körner deutlich erkennbar sind, während die Kesselasche generell feiner ist und die Körnung von Auge nicht mehr erkennbar ist. Die chemischen Unterschiede sind in Abbildung 7.19 dargestellt. Der Schlackenstaub ist deutlich reicher an Si, Fe, Al und Cu als die Kesselasche. Die
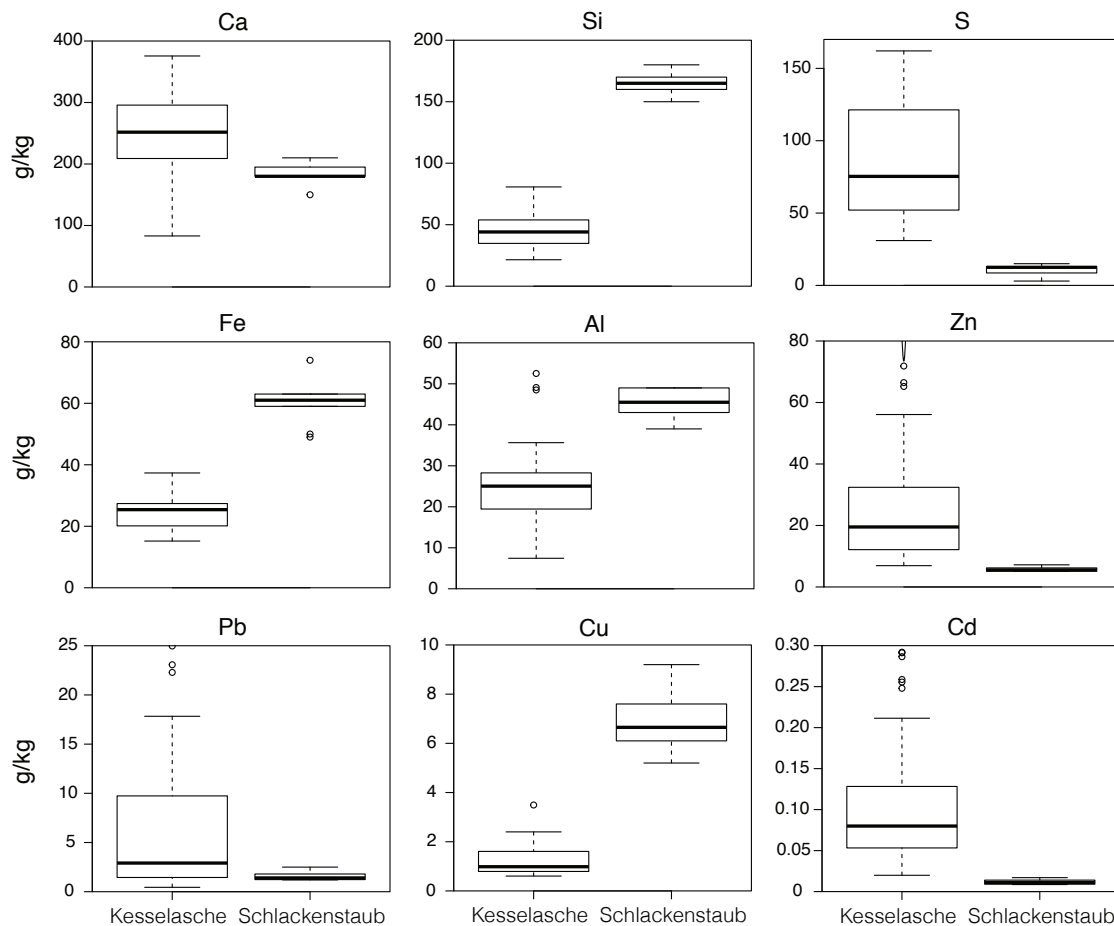
Figure 7.19: Vergleich Kesselasche zum Schlackenstaub der ZAV Recycling AG.

Kesselasche weist hingegen deutlich höhere Ca, S, Zn, Pb und Cd Werte auf. Insbesondere die höheren Gehalte an säureextrahierbaren Metallen könnten rechtfertigen, dass die Kesselasche einer Behandlung unterzogen werden sollen.

7.5.3 Ansatz zur Abschätzung der Frachten

Folgende rechnerische Frachtbetrachtungen sollen am Beispiel der KVA Bern aufzeigen, wieviel Zink im Falle einer direkten Ablagerung von unbehandelter Kesselasche auf die Deponie geht. Die bisher in der FLUWA Bern behandelte Flugasche setzt sich wie folgt zusammen:

- 30% Kesselaschen à 3.1 g/kg Zn (Mittelwert)

- 70% Elektrofilterasche à 6.8 g/kg Zn

Pro Tonne Asche, die in die FLUWA geht, stammen etwas mehr als 9kg Zn (= 16.5%) aus den Kesselaschen, von den total ca. 57 kg/t Zn. Die Extraktionsversuche im Labor zeigten, dass die Zn-Ausbeute bei den Kesselaschen vergleichbar oder nur leicht geringer als die der Elektrofilterasche sind. Es ist also eine Frage der Abwägung zwischen ökologischem Nutzen und der Wirtschaftlichkeit.

Kriterien	Bemerkungen
Schwermetallgehalte	Die Zn-, Pb-, Cu-, Cd-Gehalte sind deutlich tiefer in der Kesselasche als in der Elektrofilterasche. Zeigen die Kesselaschen einen hohen Krustengehalt, dann sind die Schwermetallgehalte vergleichbar wie jene der Elektrofilterasche.
Schwermetallausbeute	– Vergleichbar für Kesselasche und Elektrofilterasche – Cu-Ausbeute deutlich schlechter, da die Cu-Gehalte in Kesselasche deutlich tiefer sind – Pb-Ausbeute für die Krusten sind tief wegen schwerlöslichem $PbSO_4$
Säureverbrauch	Der Säureverbrauch kann vermutlich reduziert werden, wenn die Kesselasche nicht mehr mitgewaschen wird. Die Zerstörung der Säure kann aber auch ein positiver Effekt sein bei Anlagen mit viel Säure, da Elektrofilterasche kaum Säure puffert.
Oxidationsmittelverbrauch	Die Kesselasche fordert einen erhöhten Oxidationsmittelverbrauch.
Dioxine	Wenn nach der FLUWA die Dioxine nachfolgend zerstört werden (z.B. durch ReFire), sollten die Kesselasche ca. ab Mitte Kessel mitbehandelt werden, damit die erhöhten Dioxingehalte zerstört werden.
Verbleibende Schwermetallgehalte im Filterkuchen	Die Schwermetallgehalte in der Kesselasche sind oftmals ähnlich wie die Schwermetallgehalte, die nach der Wäsche im Filterkuchen der Elektrofilterasche zurückbleiben.
Massenströme	In den vorderen Kesselzügen fällt oft beträchtlich mehr Material an, aber quantitative Messungen fehlen.
Verhalten auf Deponie	Daten bezüglich Mobilisierbarkeit der Schwermetalle in unbehandelter Kesselasche wären wünschenswert.

Table 7.3: Verschiedene Kriterien die relevant sind für die Beurteilung des Entsorgungsweges der Kesselasche im Hinblick auf die Schwermetallrückgewinnung.

7.6   Zusammenfassung

Die Studie gibt einen umfassenden Überblick über die chemischen und mineralogischen Eigenschaften der Kessel- und Elektrofilteraschen im Hinblick auf die Schwermetallrückgewinnung. Die Daten zeigen, dass es sich bei den Kessel- und Elektrofilteraschen um sehr unterschiedliche Materialien handelt. Die Elektrofilteraschen zeigen deutlich höhere Schwermetallgehalte und bessere Extraktionseigenschaften, da sie einen tieferen Säuren- und Oxidationsmittelverbrauch bei der Extraktion aufweist. Die Schwermetallausbeuten für Zn und Pb sind aber vergleichbar für die Kessel- und Elektrofilteraschen. Die Frage, welche Kesselaschefraktionen bei der Extraktion mitbehandelt werden sollen, sollte gesamtheitlich betrachtet werden, da die Gewichtung der relevanten Kriterien entscheidend sind. Tabelle 7.3 gibt einen Überblick über die verschiedenen Kriterien, die für die Beurteilung des Entsorgungsweges relevant sind. Hier gilt es zu definieren, welchem Kriterium wieviel Gewicht gegeben werden soll.

Die vorliegende Datengrundlage soll nun dazu dienen, die Abgrenzung für die Definition der «schlackenähnlichen Zusammensetzung» zu definieren. Als Entscheidungskriterium sollten auch die Massenströme einbezogen werden, da oftmals bedeutend weniger Kesselaschen-Material im hinteren Teil des Kessels anfällt als im vorderen. Es sollte nun abgeklärt werden, ab welchen minimalen Zn Gehalten eine Rückgewinnung ökologischer ist als die direkte Deponierung. Am Beispiel einer oder mehreren Anlagen sollte aufgezeigt werden, wie sich die Bilanzen bei verschiedenen Szenarien verhalten. Dabei gilt es die Auswirkungen der Metallrückgewinnung auf die Umwelt den Betriebsmittelaufwänden gegenüberzustellen. Um die Mobilität der Schwermetalle in den Leerzug- und den ersten Kesselaschefraktionen zu untersuchen, könnten Säulenversuche oder Batchtests

eingesetzt werden.

7.7 Nächste Schritte

Auf Basis dieser Studie wird nun ein Projekt durchgeführt, bei welchem auf 3 - 4 Anlagen die ökologische Relevanz der Metallrückgewinnung der Kesselaschenfraktionen untersucht wird, um die aktuelle Vollzugshilfe (BAFU, 2019) zu präzisieren. Dabei wurde folgendes Vorgehen vorgeschlagen:

Probenahme:

- Ortsaufgelöste Probenahme aller anfallenden Kesselaschefraktionen, Leerzug, Elektrofilterasche und Flugasche-Mix (vorgeschlagen wird eine Mischprobe über ca. 1 Monat mit ca. 30 Inkrementen)

- Nach Möglichkeit sollen die Massenströme quantitativ erfasst werden. Anderenfalls müssen diese rechnerisch ermittelt werden

Analysen bezüglich Auswirkungen Mitbehandlung Kesselasche auf Schwermetallrückgewinnung:

- Bestimmung der chemischen Zusammensetzung mittels XRF

- Labor FLUWA Versuche mit Additionsreihen und genauer Dokumentation über den Neutralisationschemikalienverbrauch

- Über Massenströme die Zn-Frachten berechnen und Energie- und Betriebsmittelverbrauch abschätzen

Analysen bezüglich der Emissionen der Ablagerung unbehandelter Kesselasche auf die Deponie:

- VVEA Tests mit und ohne CO_2 an den einzelnen Kesselaschefraktionen, Leerzugasche sowie an generierten Filterkuchen, um Aussagen über Unterschiede in der Mobilisierbarkeit des Zn und Pb (sowie andere SM) machen zu können. Säulenexperimente an ausgewählten Leerzug- und Kesselaschenmischungen könnten zudem als Ergänzung durchgeführt werden

- Dioxinanalysen an den verschiedenen Fraktionen

Die Daten dieser weiterführenden Studie sollten dann für eine ökologische Beurteilung dienen (Ökobilanz), um die Vollzugshilfe zu präzisieren.

7.8 Referenzen

Bundesamt für Umwelt BAFU, 2019. Vollzugshilfe für die "Rückgewinnung von Metallen aus den Filteraschen von Kehrichtverbrennungsanlagen." Bern.

Swiss Federal Council, 2015. Ordinance on the Avoidance and the Disposal of Waste. (Waste Ordinance, ADWO). (Status of 1 April 2020).

Wolffers, M., Eggenberger, U., Schlumberger, S., Churakov, S.V., 2021. Characterization of MSWI fly ashes along the flue gas cooling path and implications on heavy metal recovery through acid leaching. Waste Manag. 134, 231–240. https://doi.org/10.1016/j.wasman.2021.08.022

Zucha, W., Weibel, G., Wolffers, M., Eggenberger, U., 2020. Inventory of Municipal Solid Waste Incineration Fly Ash in Switzerland: Heavy Metal Recovery Potential and their Properties for Acid Leaching. Processes.

Part IV

Closing remarks and Outlook

Chapter 8

Closing remarks and Outlook

The concluding remarks stated in this chapter outline the main findings of the thesis in terms of understanding of the ash forming processes along the flue gas cooling path, the characteristics of the different ash fractions and its implications on heavy metal recovery and formation conditions of PCDD/-F.

8.1 Ash-forming processes and transport mechanisms during the cooling of the flue gas

The findings from the thermodynamic calculations contribute enormously to gain insight into ash-forming processes and transport mechanisms occurring during the cooling of the flue gas.

- It could be confirmed that the S/Cl ratio in the flue gas has the primary control of the equilibrium phase assemblages in the system and that the O_2 concentration, as long as it is in excess, affects the composition of the ash to a minor extent. The observation that the solid phases (including heavy metals) are dominated by sulfates at S/Cl ratio > 1 is an important finding with regard to increasing recycling rates of plastic, which will possibly result in lower Cl concentrations in the flue gas. Nevertheless, it must be assumed that at local scale, different conditions than the average operating parameters (such as recorded O_2, HCl, SO_2 concentration) may prevail in the flue gas or gas-solid interface, which may represent conditions favorable for the formation of additional phases or compounds (e.g. PCDD/-F).

- The majority of phases that are predominantly observed in the ESP ash were predicted to form early at higher temperatures than the ones prevailing in the electrostatic precipitator. This implies that these phases, which are mainly newly formed salts, are able to travel as fine crystalline or amorphous particles in the flue gas stream until they reach the electrostatic precipitator. Only a minor fraction thereby settles along the boiler and accumulates in the boiler ashes. A further important finding for understanding the ash composition and mass fluxes is that the main load of glass and refractory minerals entering the boiler is transported with the flue gas and reaches the electrostatic precipitator, while only smaller shares settle along the

boiler. This finding could only be obtained through thermodynamic simulations, as the concentrations of glass- and refractory minerals in the ESP ash is strongly diluted by the high amount of newly formed salts. Therefore, thermodynamic simulations greatly support the understanding of the mineralogical composition of the ESP ash, which was found difficult to assess with XRD or SEM due to very small grain sizes and complex phase assemblages.

- The thermodynamic simulations predict that the Zn and Cu in the boiler ash fractions are preferably bound as silicates (Zn_2SiO_4) and oxides (e.g. ZnO, Fe_2ZnO_4, CuO), phases that have also been observed in the boiler ash. The heavy metals Sb, Sn are predicted to be thermodynamically stable as oxides. In the temperature regions representing the rear part of the boiler, a change towards formation of chlorides is predicted to take place for flue gas conditions where the molar S/Cl ratio is > 1. Based on the assumption that the fine-grained newly crystallized Zn-, Cu-, Pb-, Cd-chlorides mainly travel with the flue gas until they reach the electrostatic precipitator, it must be assumed that the concentrations of heavy metal chlorides in the boiler ashes are minor. It is furthermore observed, that mainly sulfates form around the heat exchanger tubes (possibly also chlorides that have been converted into sulfates as a result of sulfation reactions), which tend to incorporate Pb and Zn into their structures. These deposits are periodically released and arise as part of the boiler ashes and thereby represent significant contributions of Pb- and Zn bearing sulfates to the boiler ash.

- Thermodynamic modeling suggests that the formation of PCDD/-F via homogeneous synthesis should take place at extremely reducing conditions, which are not expected to represent bulk flue gas conditions. It is suggested, that necessary conditions for thermodynamic stability and synthesis of these species can persist locally in close vicinity of the combustion of a plastic particle. The thermodynamic calculations predict that PCDD/-F would form in large quantities at these extreme conditions (mg/kg range). Once formed, the PCDD/-F congeners seem to persist as thermodynamically metastable compounds in the macroscopic flue gas system possibly due to slow oxidation kinetics. The highest PCDD/-F concentrations have been found in the ESP ashes. It has nevertheless been observed that PCDD/-F can form at the temperatures prevailing in the boiler and concentrations of >100 ng/kg were detected in the boiler ashes. It is assumed that PCDD/-F compounds can travel with the flue gas and therefore the place of occurrence does not necessarily reflect the place of formation. It is further observed, that the PCDD/-F congener profiles of different incineration plants are very similar, which suggests that the formation of PCDD/-F seems to follow a uniform interplay of assumedly multiple formation mechanisms.

8.2 Characteristics of the different ash fractions and their leachability

The findings from the detailed chemical and mineralogical characterization of different ash fractions provide important contributions towards a better understanding of their geochemical characteristics and their leachability.

- It has been shown that the boiler ashes differ strongly from the ESP ash in composition and that their share on the bulk fly ash is approximately 25 - 30%. Essentially, there are no major differences between the empty pass ashes and the boiler ashes but a slight increase in the heavy metal content can be observed in flue gas direction. The boiler ash consists mainly of acid-buffering and inert refractory minerals and the amorphous glass phase and further shows considerably lower heavy metal concentrations than the ESP ash. Boiler ash fractions with high deposit contents show increased Pb and Zn concentrations, bound as sulfates. In contrast, the ESP ash is dominated by a sulfate and chloride matrix which shows a lower acid-buffering capacity. In addition, the ESP ash shows much higher concentrations in the heavy metals of interest (Zn, Cd, Cu, Pb), predominantly in the form of easily soluble salts. These observations suggest that the ESP ash shows a higher potential for heavy metal recovery.

- For waste wood fly ash, it is found that the concentrations in heavy metals are generally in the range of that found in MSWI fly ashes, especially for Pb, but the concentrations differ strongly with the waste wood content. The elevated heavy metal and Cr(VI) concentrations in waste wood fly ash justify the need for treatment prior to deposition. Similar to boiler ash, waste wood fly ash shows a strongly acid-buffering and also strongly self-reducing composition, which leads to an increased consumption of neutralizing and oxidizing chemicals during co-treatment with MSWI fly ash.

8.3 Implications on heavy metal recovery

The investigations on composition and leachability of the individual ash fractions at laboratory- and industrial-scale allow the following implications on heavy metal recovery.

- The ESP ashes show significantly higher heavy metal contents and lower consumption of neutralizing chemicals during extraction. Comparing the EA and BOA, no significant differences could be found in the parameters affecting extractability. Therefore, no general recommendation can be made as to which BOA fractions could be excluded from the acid leaching process. Nevertheless, the heavy metal recovery rates for Zn and Pb are comparable for the boiler- and ESP ashes. Whether heavy metal recovery is expedient from a technical and ecological point of view depends on the weighting of various factors. These factors include, but are not limited to:

- heavy metal concentrations

- heavy metal recovery rates

- consumption of neutralizing chemicals

- residual heavy metal contents in the filter cake

- PCDD/-F contents in the boiler ashes (especially if the filter cakes are additionally treated with a method of destroying PCDD/-F (e.g. ReFire process))

- mass streams of the ash fractions

- mobilization potential of the heavy metals at the landfill

As a first decision criterion, it could further help to define the minimum Zn concentration in the ash fractions where recovery is more ecological than direct landfilling.

- For waste wood fly ash, the treatment with the FLUWA process allows to successfully reduce the Cr(VI) in the filter cake below the threshold value for landfilling, even when the process is performed under oxidizing conditions. The Zn and Cd recovery are not negatively affected by the co-processing. Nevertheless, the co-processing of waste wood fly ashes require higher dosages of neutralizing chemicals and have a particularly negative effect on the recovery of the redox sensitive elements Pb and Cu, as the waste wood ashes show a strong redox buffer and thus a higher consumption of the oxidant H_2O_2. Therefore, higher dosage of H_2O_2 is needed to maintain oxidizing conditions during the process required for Pb and Cu mobilization. The use of a stronger oxidizing agent (e.g. permanganate) could be expedient and should be further tested with regard to successful Cr(VI) reduction. Alternatively, smaller percentages of waste wood fly ash could be co-processed in existing FLUWA plants in order to diminish the negative effects due to the higher demand of neutralization chemicals. Within the next years, the implementation of co-processing the two ash types could contribute significantly to the growing demand of treatment capacities in Switzerland.

8.4 Outlook

Important insights on possible heavy metal binding forms in the different ash fractions could be obtained through the complementary approach including detailed chemical and mineralogical characterization and thermodynamic modeling. Further research should focus on the following topics:

- In order to gain further insight into the heavy metal binding forms present in the different ash fractions, it would be of interest to perform XAS measurements on the different ash fractions. This would allow to study the Zn, Cu and Sb binding forms in the different ash fractions and investigate whether there are observable changes along the flue gas cooling path. For Sb, it would additionally be interesting to investigate the binding forms in the bottom ash, as little is known on the possible binding forms

of Sb in any of the MSWI solid residues. For Sb in particular, it is extremely decisive for the hazard and mobilization potential on the landfill, in which valence state and binding form it is present.

- The designed box flux model to perform thermodynamic simulations of the cooling of the flue gas represents a promising tool to assess specific questions from industry, e.g. regarding the stability of corrosion-promoting phases or for tuning the quality of the combustion residues. With respect to Sb, it was further noted that the thermodynamic database should still be supplemented with important gas species and further solids in order to perform additional thermodynamic calculations with focus on the Sb speciation at different flue gas conditions.

- Regarding the disposal routes of boiler ashes, important findings are obtained with respect to the geochemical characteristics and leachability of the different ash fractions. Further research should be carried out in order to investigate the ecological relevance of heavy metal recovery from boiler ashes and to concretize the enforcement aid for the metal recovery obligation. The suggested approach is to compare the environmental impact of heavy metal recovery with the operating costs. The use of column- and batch tests is suggested in order to simulate the mobilization potential at the landfill of the untreated empty pass- and boiler ash fractions. In addition, laboratory-scale leaching tests should be carried out to quantify the effects of boiler ash treatment on heavy metal recovery and neutralizing chemicals. Different scenarios should be tested and compared: the sole treatment of ESP ash, as well as the treatment of ESP ash with the addition of subsequent boiler ash fractions towards the empty pass ash. These data may then serve for an ecological assessment (life cycle assessment) to refine the enforcement aid.

Part V

Appendix

Appendix A

Supplementary Material
Characterization of MSWI fly ashes along the flue gas cooling path and implications on heavy metal recovery through acid leaching

Plant-ID	Boiler type	Municipal Waste	Industrial- and commercial waste	Automobile shredder residues (ASR)	Sewage sludge
Plant A	I	35%	65%	3%	<1 %
Plant B	II	67%	30%	2%	<1%
Plant C	III	45%	54%	-	1%
Plant D	IV	48%	51%	<1%	-
Plant E	IV	55%	45%	-	-
Plant F	IV	45%	46%	7%	1%

Table A.1: Data on waste input of the investigated plants.

Table A.2: Chemical data of the analyzed empty pass (EA)-, boiler (BOA)- and electrostatic precipitator ashes (ESPA).

Plant	Ash Type	Al	Ba	Br	Ca	Cd	Cl	Cr	Cu	F	Fe	K	Mg	Mn	Na	Ni	P	Pb	S	Sb	Si	Sn	Ti	Zn	TOC	Al°	ANC
													mg/kg														(eq/kg)
A	BOA1	19'919	3050	235	249'781	70	20'590	662	1'027	1'250	27'391	37'528	10'941	1'102	27'739	225	5'555	862	1'111'397	447	123'359	497'733	20'903	4'000	4'920		4.7
A	BOA5	23'764	3120	1660	251'227	123	67'083	803	1'060	9507	30'678	31'310	11'321	1'185	3599	235	8492	1603	754'407	862	134'447	526'644	31'370	5'000	5'740		8.7
A	ESPA	10'238	2360	6'840	144'953	315	185'367	606	2497	n.d.	17'576	82'830	4'048	773	33'323	194	11'797	4723	612'219	2'777	7'296	316'645	59'490	4'000	1'115		5.7
B	BOA1	25'226	3630	1090	304'026	81	81'950	1'370	984	n.d.	26'262	29'022	9'341	n.d.	27'835	585	2'684	1'260	588'814	652	188'868	40'654	13'510	4'000	11'783		9.2
B	BOA5	22'839	3730	846	239'682	112	55'390	1'220	1'195	n.d.	27'990	43'475	9'287	n.d.	5'791	642	5'704	1'391	752'282	1'100	184'490	49'605	11'530	4'000	11'730		7.5
B	BOA3	26'873	3550	1130	307'828	73	77'100	1'170	952	n.d.	28'139	10'499	n.d.	595	6'455	1'985	1'343	595	50'315	670	22'260	459'945	13'400	4'000	11'418		9.2
B	ESPA	11'851	2420	5270	161'458	315	191'360	753	1'949	n.d.	12'288	88'577	4'330	596	89'677	379	5'382	1'985	514'465	22'250	10'405	346'533	36'210	9'000	5'112		6.7
C	BOA1	25'311	2552	297	225'945	52	29'196	707	794	1032	19'680	40'933	7'980	837	5'060	207	1'634	2'832	1'150'039	1'045	422'273	154'450	26'255	6'000	6'800		4.5
C	BOA2	26'791	2666	316	247'261	78	37'616	767	788	2165	20'786	36'143	8'388	854	5'408	206	2'832	963	98'243	992	24'632	481'174	24'632	11'000	7'014		4.5
C	BOA4	30'251	2775	331	284'155	192	43'928	808	924	4038	19'791	9'445	820	25'751	228	3'411	76'618	992	51'460	583	20'376	93'040	9'380	4'000	9'380		6.7
C	BOA5	29'684	3010	542	295'989	81	59'115	679	772	7293	18'151	23'816	9'187	829	24'641	171	2'297	983	69'039	620	48'193	203'376	22'695	11'000	10'486		7.2
C	ESPA	9'945	1665	4485	103'422	848	215'595	419	2266	2810	9'306	86'516	2'874	467	107'073	191	49'929	11'005	585'546	38'860	6'816	264'427	86'810	7'000	1'902		4.5
D	BOA1	22'287	2807	811	241'476	76	59'547	504	1'660	2610	18'268	30'101	7'405	738	3'032	169	22'033	2013	177'299	634	24'570	411'163	24'570	12'000	3'780		4.5
D	BOA2	22'028	3013	525	215'508	106	44'860	527	2427	1590	20'404	33'765	7'976	800	25'206	183	13'545	1'390	119'844	851	12'752	461'121	32'415	11'000	7'014		4.0
D	BOA3	21'602	3127	832	189'129	116	461'157	543	1'606	4167	20'126	50'077	7'801	742	40'709	200	17'830	1'365	111'372	1'370	12'472	495'573	32'273	18'000	2'587		4.0
D	BOA4	26'128	3957	958	233'242	74	63'637	621	1'632	5940	25'803	33'123	8'893	929	23'643	219	9'614	1'115	83'790	876	23'990	60'406	23'990	12'000	n.d.		5.5
D	BOA5	27'871	4053	1'107	240'401	70	71'997	616	1'816	7480	27'151	30'317	9'359	916	250'043	214	5'823	1'890	75'022	751	16'870	62'591	21'400	14'000	7'950		6.0
D	ESPA	14'411	2587	3397	144'933	353	104'657	430	5'392	n.d.	15'445	76'083	4'816	632	83'581	165	13'020	102'056	409'958	26'653	7'885	65'575	65'575	4'000	955		3.5
E	EA	29'853	3275	293	278'290	15	43'595	1'140	546	n.d.	35'057	18'371	4'816	199	20'442	199	7'814	300	65'957	585	7'468	69'105	22'883	5'000	16'530		7.5
E	BOA1	24'520	2730	556	262'273	56	69'735	1'040	683	n.d.	24'724	32'035	9'866	n.d.	26'006	182	6'117	1'446	88'473	1'255	11'675	44'188	19'982	6'000	12'700		6.2
E	BOA2	25'430	2905	385	252'057	53	61'575	1'115	669	n.d.	30'074	29'553	10'360	n.d.	29'478	209	6'418	2644	83'589	1'390	12'140	52'036	20'743	7'000	n.d.		6.2
E	BOA3	27'013	3340	517	255'805	56	79'260	1'195	776	n.d.	30'431	31'077	10'421	n.d.	28'636	208	6'728	2913	68'320	1'365	11'530	53'889	22'601	6'000	14'414		7.2
E	BOA4	30'689	3275	527	269'310	45	75'105	1'245	671	n.d.	33'638	21'833	12'233	n.d.	20'846	232	7'910	1'391	57'120	1'115	9'647	63'079	24'732	8'000	n.d.		8.2
E	BOA5	32'462	2725	629	274'831	63	73'205	1'280	696	n.d.	29'064	26'565	12'347	n.d.	27'794	203	7'688	1'343	51'781	1'230	26'120	59'927	21'400	7'000	18'960		8.2
E	ESPA	9'599	2135	3785	118'579	455	221'925	839	2055	n.d.	13'271	98'763	3'401	555	98'972	178	7'222	7'222	54'865	4'880	9'632	32'106	41'260	4'000	4'302		4.2
F	EA	26'902	5055	157	250'045	27	139'940	603	1605	22250	55'347	20'600	13'819	1495	24'400	242	1'643	77'285	54'865	389	17'475	71'437	17'475	5'000	10'430		7.0
F	BOA1	12'065	2360	981	200'214	211	38'390	603	1605	n.d.	25'795	44'567	5'829	833	21'134	242	12'110	146'621	77'285	1'240	11'675	242'298	45'890	15'000	679		2.5
F	BOA2	12'295	2275	132	168'210	287	5'375	570	1828	n.d.	24'393	46'348	6'173	825	20'56	256	68'310	162'078	54'865	1'475	6'942	260'041	56'090	15'000	n.d.		1.7
F	BOA3	7'439	1830	229	94'009	326	5'790	407	1297	n.d.	17'976	82'751	3'827	586	20'566	244	1'946	544'465	28'50	1'365	66'480	230'001	66'480	15'000	n.d.		0.9
F	BOA4	10'448	2355	374	95'621	877	14'425	487	1770	n.d.	22'679	76'097	4'379	761	25'544	241	42'470	141'751	3'685	3'240	93'040	232'366	93'040	15'000	n.d.		1.7
F	BOA5	8'923	2270	3320	83'013	507	60'370	490	3493	770	18'734	77'649	3'655	644	90'901	227	2'907	124'534	2'850	3'540	116'150	231'170	116'150	15'000	n.d.		3.0
F	ESPA	13'922	2350	4'820	118'030	407	122'300	660	3369	1775	22'134	63'304	5'410	675	78'482	236	3'688	145'45	84'382	4'530	3'085	373'363	103'300	15'000	410		4.7

178
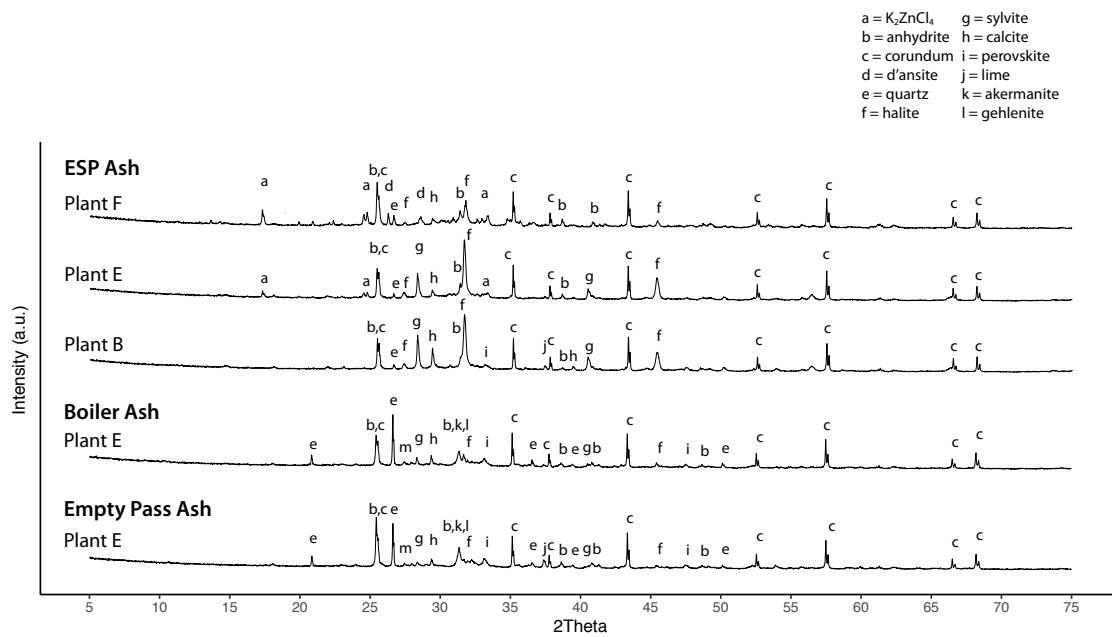
Figure A.1: XRD spectra of the different ash types arising along the flue gas cooling path. For ESP ash, the spectra for the three ash types are shown. Corundum (20 wt.%) was used as internal standard.
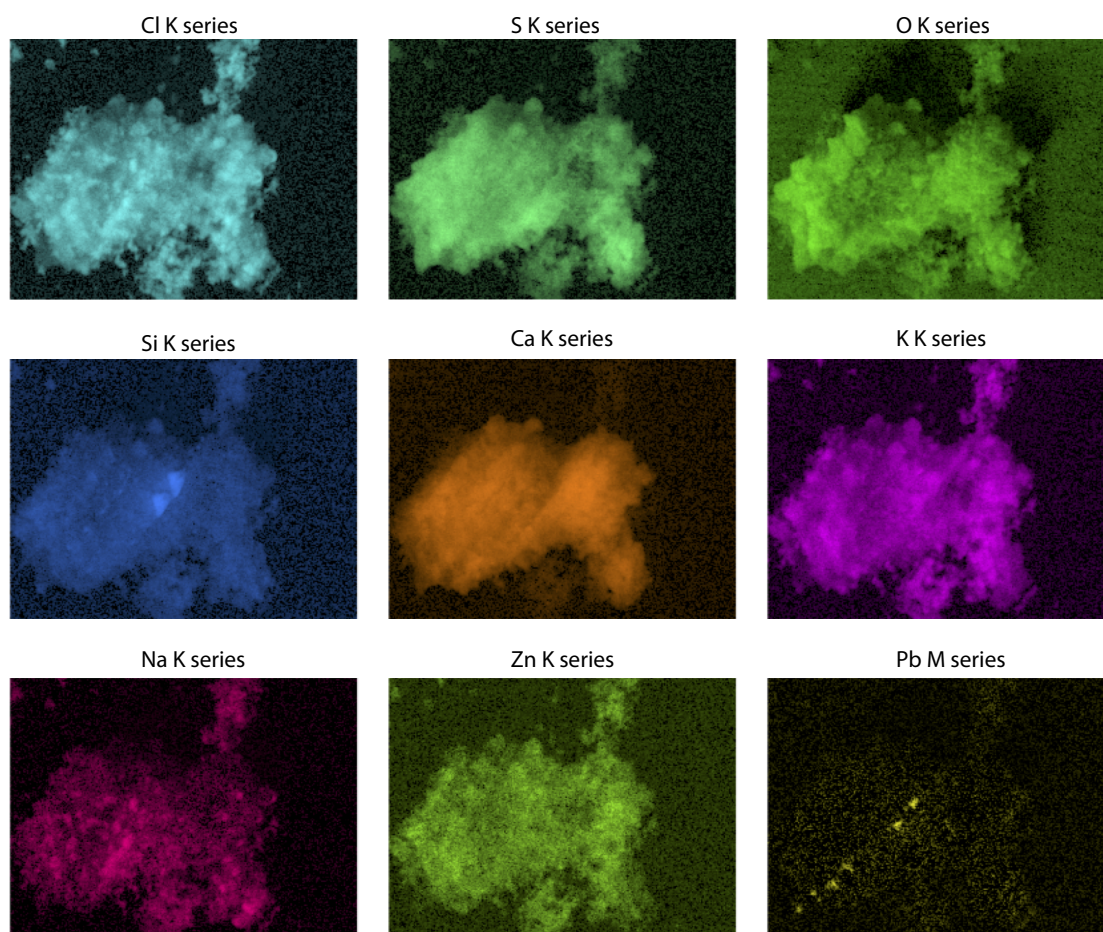
Figure A.2: EDX mapping of the particle agglomerate in ESPA shown in figure 7e of the main text.
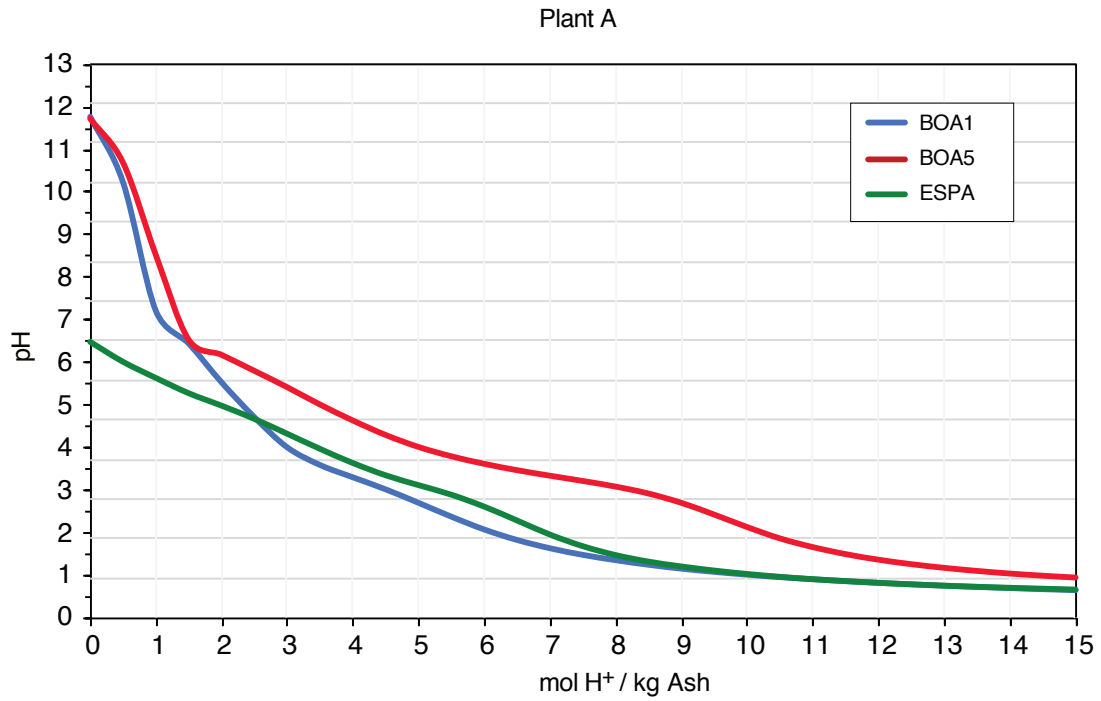
Figure A.3: Titration curve of acid neutralizing capacity (ANC) for the different ash fractions of plant A.
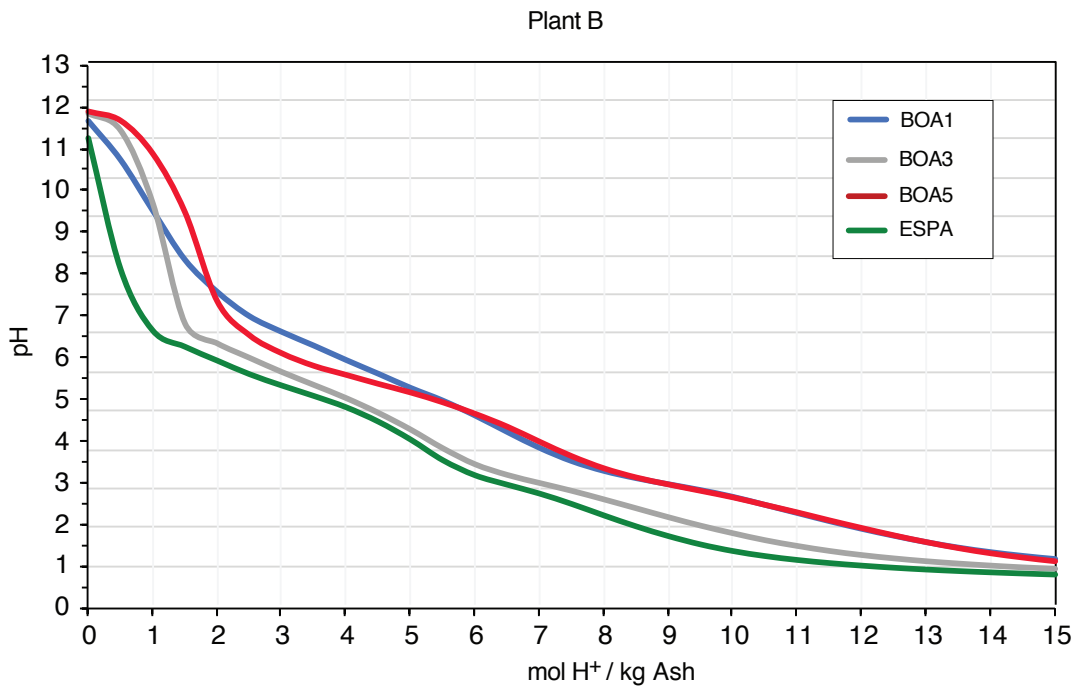
Figure A.4: Titration curve of acid neutralizing capacity (ANC) for the different ash fractions of plant B.
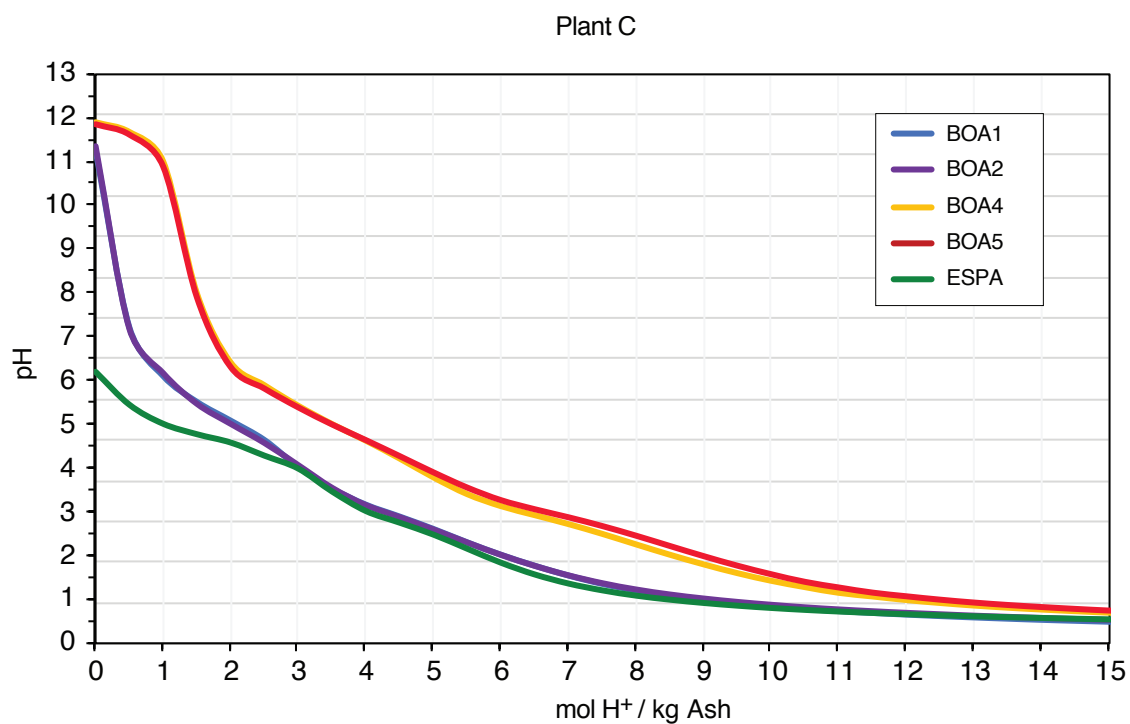
Figure A.5: Titration curve of acid neutralizing capacity (ANC) for the different ash fractions of plant C.
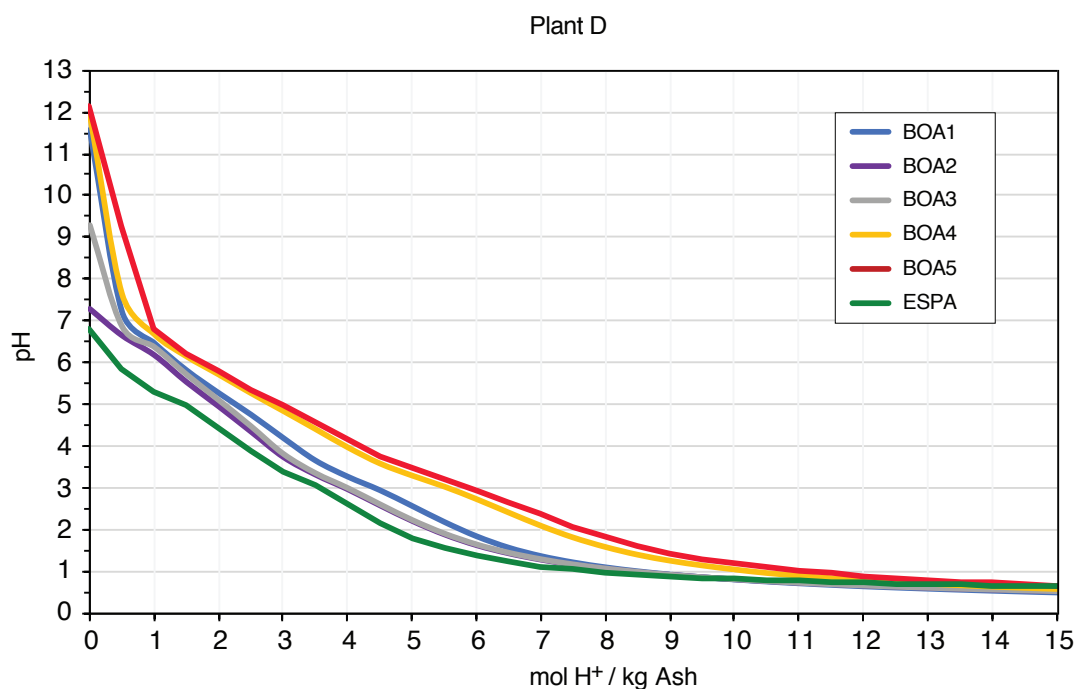
Figure A.6: Titration curve of acid neutralizing capacity (ANC) for the different ash fractions of plant D.
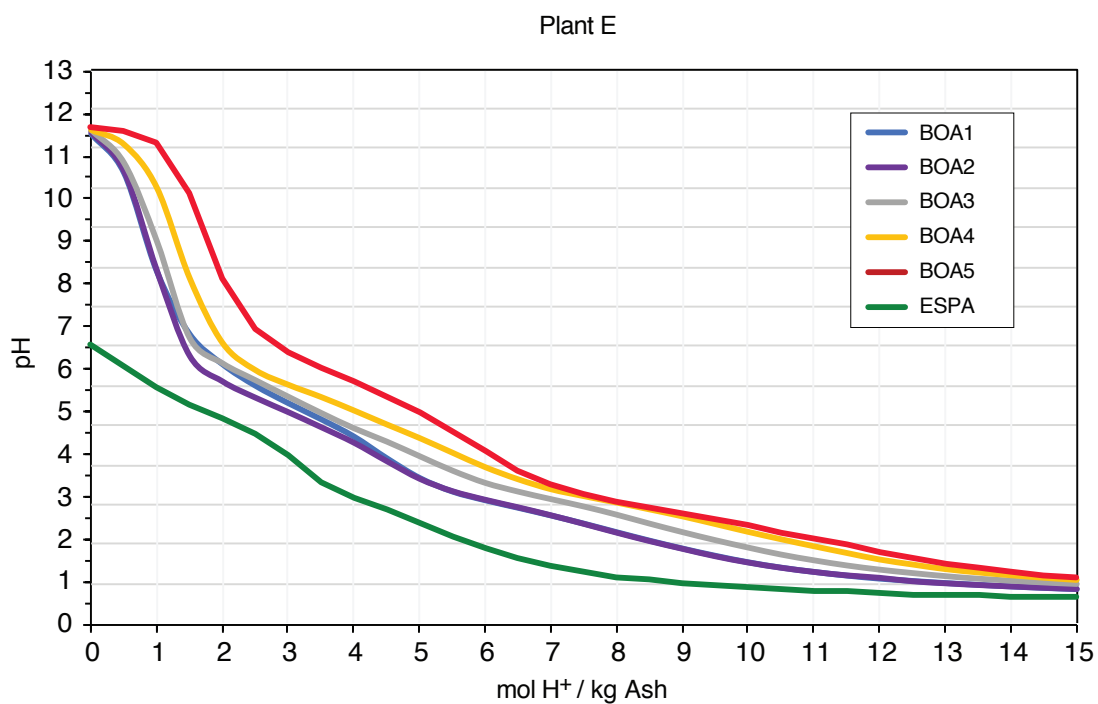
Figure A.7: Titration curve of acid neutralizing capacity (ANC) for the different ash fractions of plant E.
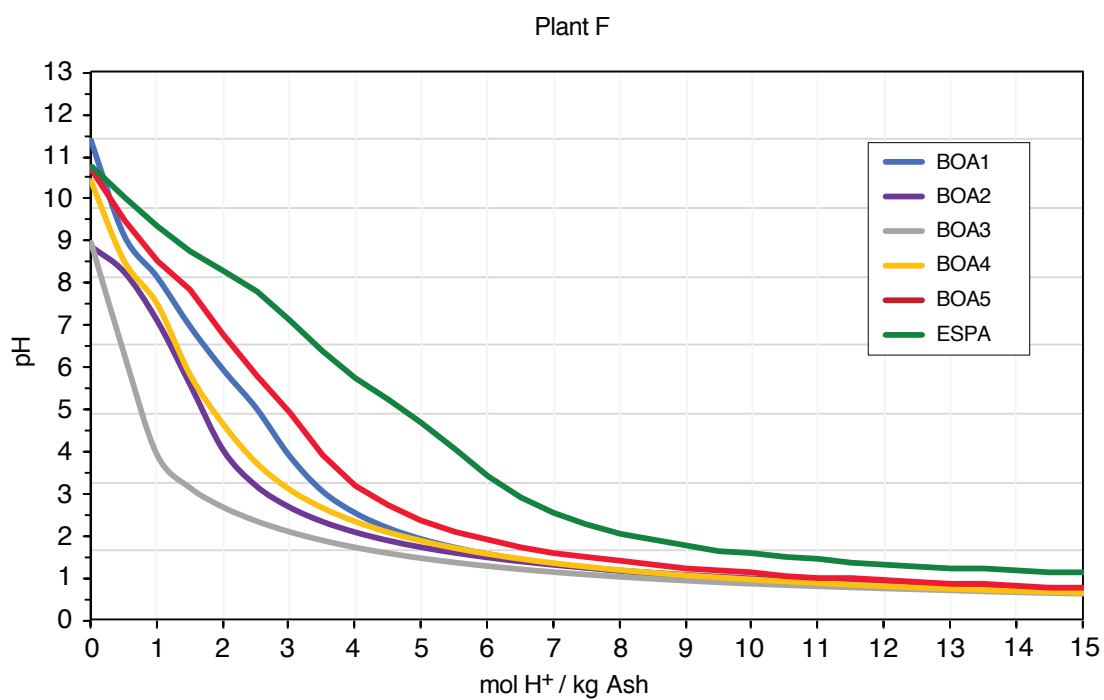
Figure A.8: Titration curve of acid neutralizing capacity (ANC) for the different ash fractions of plant F.

Appendix B

Supplementary Material
New insights into the genesis of MSWI fly ash through thermodynamic modeling

NAME	FORMULA	Mineral Name	STATE	molar volume (J/bar)	Quelle
Al	Al		c	0.993	Webmineral
Al2NiO4	Al2NiO4		c	4.108	Materialsproject
Al2O3	Al2O3	Korund	c	2.545	Webmineral
Al2S3	Al2S3		c	5.703	Materialsproject
Al2S3O12	Al2S3O12		c	12.805	Materialsproject
ANDALUSITE	Al2SiO5	Andalusit	c	5.151	Webmineral
KIANITE	Al2SiO5	Kyanit	c	4.418	Webmineral
SILLIMANITE	Al2SiO5	Sillimanit	c	4.988	Webmineral
Al2TiO5	Al2TiO5		c	5.037	Materialsproject
Al3Ni	Al3Ni		c	3.461	Materialsproject
Al3Ni2	Al3Ni2		c	4.160	Materialsproject
Al3Ti	Al3Ti		c	3.833	Materialsproject
MULLITE	Al6Si2O13	Mullit	c	10.119	Webmineral
AlAs	AlAs		c	2.838	Materialsproject
AlBr3	AlBr3		c	10.061	Materialsproject
AlCl3	AlCl3		c	6.019	Materialsproject
AlCu	AlCu	Cupalit	c	1.690	Materialsproject
AlF3	AlF3	Oskarssonit	c	2.672	Mindat
AlH3	AlH3		c	2.789	Materialsproject
AlH3	AlH3		c	2.353	Materialsproject
AlH3	AlH3		c	2.349	Materialsproject
AlH3	AlH3		c	2.056	Materialsproject
AlN	AlN		c	1.281	Materialsproject
AlNi	AlNi		c	1.444	Materialsproject
AlNi3	AlNi3		c	2.714	Materialsproject
AlO3H3	AlO3H3	Gibbsit	c	3.195	Webmineral
AlSb	AlSb		c	3.647	Materialsproject
AlTi	AlTi		c	1.952	Materialsproject
As	As	Arsen	c	1.305	Webmineral
As2Cd3	As2Cd3		c	8.169	Materialsproject
As2O3	As2O3	Claudetit	c	4.726	Webmineral
As2O5	As2O5		c	5.450	Materialsproject
As2S3	As2S3	Orpiment	c	7.050	Webmineral
As2Zn3	As2Zn3		c	6.381	Materialsproject
As4S4	As4S4	Pararealgar = As	c	3.037	Webmineral
AsCu3	AsCu3		c	3.379	Materialsproject
AsMn	AsMn		c	1.735	Materialsproject
AsNi	AsNi	Nickelin	c	1.705	Webmineral
Ba2Pb	Ba2Pb		c	8.326	Materialsproject
Ba2Sn	Ba2Sn		c	8.137	Materialsproject
Ba2TiO4	Ba2TiO4		c	7.785	Materialsproject
Ba3N2	Ba3N2		c	9.205	Materialsproject
BaBr2	BaBr2		c	6.467	Materialsproject
BaCl2	BaCl2		c	6.135	Materialsproject
BaCO3	BaCO3	Witherit	c	4.580	Webmineral
BaF2	BaF2	Frankdicksonit	c	3.582	Webmineral
BaH2	BaH2		c	3.393	Materialsproject
BaN2O6	BaN2O6	Nitrobarit	c	8.056	Webmineral
BaO	BaO		c	2.665	Materialsproject
BaO2	BaO2		c	3.140	Materialsproject
BaO2H2	BaO2H2	Ba(OH)2	c	3.868	Materialsproject
BaPb3	BaPb3		c	8.432	Materialsproject
BaS	BaS		c	4.054	Materialsproject
BaSn3	BaSn3		c	7.930	Materialsproject
BaSO4	BaSO4	Baryt	c	5.210	Webmineral

Table B.1: List of added molar volumes

NAME	FORMULA	Mineral Name	STATE	molar volume (J/bar)	Quelle
BaTiO3	BaTiO3	Barioperowskit	c	3.877	Webmineral
BaZrO3	BaZrO3		c	4.642	Materialsproject
C	C	Lonsdaleit		0.341	Webmineral
C	C	Chaoit		0.350	Webmineral
DIAMOND	C	Diamant		0.342	Webmineral
GRAPHITE	C	Graphit	c	0.533	Webmineral
Ca	Ca		c	2.547	Materialsproject
Ca12Al14O33	Ca12Al14O33	Mayenit	c	51.798	Webmineral
GEHLENITE	Ca2Al2SiO7	Gehlenit	c	9.022	Webmineral
Ca2Fe2O5	Ca2Fe2O5	Brownmillerit = Ca	c	6.791	Webmineral
AKERMANITE	Ca2MgSi2O7	Akermanit	c	9.272	Webmineral
Ca2P2O7	Ca2P2O7		c	9.032	Materialsproject
Ca2Pb	Ca2Pb		c	6.017	Materialsproject
Ca2Si	Ca2Si		c	4.999	Materialsproject
Ca2SiO4_GAMMA	Ca2SiO4_GAMMA	Calcio-Olivin	c	5.826	Mineralienatlas
Ca2Sn	Ca2Sn		c	5.828	Materialsproject
Ca3Al2O6	Ca3Al2O6		c	9.180	Materialsproject
GROSSULAR	Ca3Al2Si3O12	Grossular	c	12.529	Webmineral
MERWINITE	Ca3MgSi2O8	Werwinit	c	9.847	Webmineral
Ca3N2	Ca3N2		c	5.688	Materialsproject
Ca3P2O8	Ca3P2O8	Tuit	c	9.000	Webmineral
RANKINITE	Ca3Si2O7	Rankinit	c	9.579	Webmineral
Ca3SiO5	Ca3SiO5	Hatrurit	c	7.572	Webmineral
CaAl2	CaAl2		c	3.878	Materialsproject
CaAl2O4	CaAl2O4	Dmitryivanovit	c	3.520	Mineralienatlas
AMORTHITE	CaAl2Si2O8	Anorthit	c	10.089	Webmineral
CaAl2SiO6	CaAl2SiO6	Kushiroit	c	6.342	Mineralienatlas
CaAl4	CaAl4		c	6.402	Materialsproject
CaAl4O7	CaAl4O7	Grossit	c	9.040	Webmineral
CaBr2	CaBr2		c	6.194	Materialsproject
CaCl2	CaCl2	Hydrophilit	c	5.074	Webmineral
CaCO3	CaCO3	Kalzit	c	3.691	Webmineral
CaF2	CaF2	Fluorit	c	2.455	Webmineral
CaFe2O4	CaFe2O4	Harmunit	c	4.478	Webmineral
CaH2	CaH2			2.149	Materialsproject
CaMgO2	CaMgO2		c	2.440	Materialsproject
DIOPSIDE	CaMgSi2O6	Diopsid	c	6.636	Webmineral
MONTISELLITE	CaMgSiO4	Monticellit	c	5.116	Webmineral
CaN2O6	CaN2O6		c	7.203	Materialsproject
CaO	CaO	Lime (engl.)	c	1.662	Webmineral
CaO2	CaO2		c	2.523	Materialsproject
CaO2H2	CaO2H2	Portlandit	c	3.281	Webmineral
CaPb	CaPb		c	7.290	Materialsproject
CaPO4H	CaPO4H	Monetit	c	4.664	Webmineral
CaS	CaS	Oldhamit = (Ca,M	c	2.812	Materialsproject
CaSi	CaSi		c	2.867	Materialsproject
CaSi2	CaSi2		c	4.075	Materialsproject
PSEDOWOLLAST.].	CaSiO3	Pseudowollastonit	c	11.986	Webmineral
WOLLASTONITE	CaSiO3	Wollastonite-1A	c	3.994	Webmineral
SPHENE	CaSiTiO5	Titanit	c	5.565	Webmineral
CaSn	CaSn		c	3.703	Materialsproject
CaSO4	CaSO4	Anhydrit	c	4.593	Webmineral
CaTiO3	CaTiO3	Perowskit	c	3.369	Webmineral
CaZn	CaZn		c	3.225	Materialsproject
CaZn2	CaZn2		c	3.870	Materialsproject

Table B.2: List of added molar volumes, continued

NAME	FORMULA	Mineral Name	STATE	molar volume (J/bar)	Quelle
CaZrO3	CaZrO3	Lakargiit	c	3.805	Webmineral
Cd	Cd	Cadmium	c	1.300	Webmineral
CdBr2	CdBr2		c	6.169	Materialsproject
CdCl2	CdCl2		c	5.077	Materialsproject
CdCO3	CdCO3	Otavit	c	3.397	Webmineral
CdF2	CdF2		c	2.495	Materialsproject
CdO	CdO	Monteponit	c	1.552	Webmineral
CdO2H2	CdO2H2		c	3.193	Materialsproject
CdS	CdS	Greenockit	c	2.382	Webmineral
CdS	CdS	Hawleyit	c	2.965	Webmineral
CdSb	CdSb		c	3.662	Materialsproject
CdSO4	CdSO4		c	5.000	Materialsproject
CdTiO3	CdTiO3		c	3.697	Materialsproject
Cr	Cr	Chrom	c	0.722	Webmineral
Cr2N	Cr2N		c	1.755	Materialsproject
Cr2NiO4	Cr2NiO4		c	4.540	Materialsproject
Cr2O3	Cr2O3	Eskolait	c	2.906	Webmineral
Cr2S3O12	Cr2S3O12		c	13.369	Materialsproject
Cr5O12	Cr5O12		c	13.063	Materialsproject
Cr8O21	Cr8O21		c	26.953	Materialsproject
CrBr2	CrBr2		c	5.340	Materialsproject
CrBr3	CrBr3		c	7.399	Materialsproject
CrC6O6	CrC6O6		c	12.075	Materialsproject
CrCl2	CrCl2		c	4.488	Materialsproject
CrCl3	CrCl3		c	6.304	Materialsproject
CrF2	CrF2		c	2.505	Materialsproject
CrF3	CrF3		c	3.008	Materialsproject
CrN	CrN	Carlsbergit	c	1.084	Webmineral
CrO2	CrO2		c	1.945	Materialsproject
CrO3	CrO3		c	4.096	Materialsproject
CrPbO4	CrPbO4		c	5.642	Materialsproject
CrS	CrS		c	1.730	Materialsproject
Cu	Cu	Kupfer	c	0.711	Webmineral
Cu2O	Cu2O	Cuprit	c	2.344	Webmineral
Cu2S	Cu2S	Chalcocit	c	2.462	Webmineral
Cu3P	Cu3P		c	3.021	Materialsproject
CuCl	CuCl	Nantokit	c	2.394	Webmineral
CuCl2	CuCl2	Tolbachit	c	3.959	Webmineral
CuF	CuF		c	1.714	Materialsproject
CuF2	CuF2		c	2.136	Materialsproject
CuO	CuO	Tenorit	c	1.214	Webmineral
CuO2H2	CuO2H2	Spertiniit	c	2.474	Webmineral
CuP2	CuP2		c	2.928	Materialsproject
CuS	CuS	Covellit	c	2.043	Webmineral
CuSO4	CuSO4	Chalcocyanit	c	4.073	Webmineral
Fe	Fe		c	0.715	Webmineral
Fe2CuO4	Fe2CuO4	Cuprospinell = (Cu	c	4.619	Materialsproject
Fe2N	Fe2N		c	1.696	Materialsproject
Fe2NiO4	Fe2NiO4	Trevorit	c	4.478	Webmineral
Fe2O3	Fe2O3	Hämatit	c	3.023	Webmineral
Fe2O3_GAMMA	Fe2O3_GAMMA	Maghemit	c	2.910	Webmineral
FAYALITE	Fe2SiO4		c	4.371	Webmineral
Fe2Ti	Fe2Ti		c	2.318	Materialsproject
ULVIT	Fe2TiO4	Ulvöspinell	c	4.542	Webmineral
PSEUDOBRUKIT	Fe2TiO5	Pseudobrookit	c	5.452	Webmineral

Table B.3: List of added molar volumes, continued

NAME	FORMULA	Mineral Name	STATE	molar volume (J/bar)	Quelle
Fe2ZnO4	Fe2ZnO4		c	4.407	Webmineral
Fe3C	Fe3C	Cohenit = (Fe,Ni,C	c	2.292	Materialsproject
Fe3O4	Fe3O4	Magnetite	c	4.447	Webmineral
Fe4N	Fe4N	Roaldit = (Fe,Ni)4	c	2.986	Materialsproject
FeAl	FeAl		c	1.434	Materialsproject
FeAl2O4	FeAl2O4	Hercynit	c	4.054	Webmineral
FeAl3	FeAl3	Hollisterit	c	3.696	Mindat
FeAsS	FeAsS	Arsenopyrit	c	2.632	Webmineral
FeCl2	FeCl2	Lawrencit = (Fe,N	c	4.322	Webmineral
FeCl3	FeCl3	Molysit	c	5.258	Webmineral
FeClO	FeClO		c	3.261	Materialsproject
FeCO3	FeCO3	Siderit	c	2.994	Webmineral
FeCr2O4	FeCr2O4	Chromit	c	4.398	Webmineral
FeCu5S4	FeCu5S4	Bornit	c	9.866	Webmineral
FeCuS2	FeCuS2	Chalcopyrit	c	4.369	Webmineral
FeF2	FeF2		c	2.317	Materialsproject
FeF3	FeF3		c	3.141	Materialsproject
FeO	FeO	Wüstit	c	1.194	Webmineral
FeO2H	FeO2H	Goethit	c	2.081	Webmineral
FeO2H2	FeO2H2		c	2.643	Webmineral
FeO3H3	FeO3H3	Bernalit	c	3.301	Webmineral
FeS	FeS	Pyrrhotin = FeS b	c	2.153	Webmineral
FeS2	FeS2	Pyrit	c	2.393	Webmineral
MARCASITE	FeS2	Markasit	c	2.460	Webmineral
FeSi	FeSi	Naquit	c	1.359	Mindat
FeTi	FeTi		c	1.552	Materialsproject
ILMENITE	FeTiO3	Ilmenit	c	3.170	Webmineral
FeZnO2	FeZnO2			3.140	Webmineral
K	K		c	4.427	Materialsproject
LEUCITE	K2Al2Si4O12		c	8.868	Webmineral
ANDULARIA	K2Al2Si6O16	Adular	c	10.909	Webmineral
K2Al2Si6O16	K2Al2Si6O16	Orthoclase	c	10.909	Webmineral
MICROCLINE	K2Al2Si6O16		c	10.868	Webmineral
K2CO3	K2CO3		c	6.038	Materialsproject
K2CrO4	K2CrO4		c	7.462	Materialsproject
K2O	K2O		c	4.111	Materialsproject
K2O2	K2O2		c	4.766	Materialsproject
K2Si2O5	K2Si2O5		c	8.661	Materialsproject
K2Si4O9	K2Si4O9		c	14.939	Materialsproject
K2SiO3	K2SiO3		c	6.398	Materialsproject
K2SO4	K2SO4	Arcanit	c	6.502	Webmineral
K3AlF6	K3AlF6		c	9.936	Materialsproject
KAlO2	KAlO2		c	3.572	Materialsproject
KALCILIT	KAlSiO4	Kalsilit	c	6.037	Webmineral
KALIOPHILITE	KAlSiO4		c	5.969	Webmineral
KBr	KBr		c	4.561	Materialsproject
KCl	KCl	Sylvin	c	3.752	Webmineral
KF	KF	Carobbiit	c	2.402	Materialsproject
KH	KH		c	2.783	Materialsproject
FTORFLOGOPIT	KMg3AlSi3F2O10	Fluorphlogopit	c	14.826	Webmineral
KNO2	KNO2		c	4.691	Materialsproject
KNO3	KNO3	Niter	c	4.804	Webmineral
KO2	KO2		c	3.205	Materialsproject
KOH	KOH		c	2.651	Materialsproject
Mg	Mg		c	1.400	Mindat

Table B.4: List of added molar volumes, continued

NAME	FORMULA	Mineral Name	STATE	molar volume (J/bar)	Quelle
CORDIERITE	Mg2Al4Si5O18	Cordierit	c	23.631	Webmineral
Mg2Al4Si5O18	Mg2Al4Si5O18	Indialit	c	23.476	Webmineral
Mg2Pb	Mg2Pb		c	4.983	Materialsproject
Mg2Si	Mg2Si		c	3.883	Materialsproject
Mg2Si	Mg2Si		c	3.716	Materialsproject
KLINOENSTATIT|T	Mg2Si2O6	Klinoenstatit	c	6.255	Webmineral
Mg2SiO4	Mg2SiO4	Forsterit	c	4.366	Webmineral
Mg2TiO4	Mg2TiO4	Qandilit	c	4.467	Materialsproject
Mg3N2	Mg3N2		c	3.792	Materialsproject
Mg3P2	Mg3P2		c	6.617	Materialsproject
Mg3P2O8	Mg3P2O8	Farringtonit	c	9.544	Webmineral
Mg3Sb2	Mg3Sb2		c	8.038	Materialsproject
MgAl2O4	MgAl2O4	Spinell	c	3.971	Webmineral
MgBr2	MgBr2		c	5.530	Materialsproject
MgCl2	MgCl2		c	4.633	Materialsproject
MgCO3	MgCO3	Magnesit	c	2.827	Webmineral
MgCr2O4	MgCr2O4	Magnesiochromit	c	4.269	Webmineral
MgF2	MgF2	Sellait	c	2.013	Webmineral
MgFe2O4	MgFe2O4	Magnesioferrit	c	4.440	Webmineral
MgH2	MgH2		c	1.849	Materialsproject
MgN2O6	MgN2O6		c	6.448	Materialsproject
MgO	MgO	Periklas	c	1.118	Webmineral
MgO2H2	MgO2H2	Brucit	c	2.463	Webmineral
MgS	MgS		c	2.152	Materialsproject
MgSiO3	MgSiO3	Enstatit	c	6.264	Webmineral
MgSO4	MgSO4		c	4.162	Materialsproject
MgTi2O5	MgTi2O5	Armalcolit = (Mg,	c	5.632	Materialsproject
MgTiO3	MgTiO3	Geikielit	c	3.169	Webmineral
Mn	Mn		c	0.665	Materialsproject
Mn2Sb	Mn2Sb		c	3.018	Materialsproject
Mn3O4	Mn3O4	Hausmannit	c	4.715	Webmineral
Mn4N	Mn4N		c	3.189	Materialsproject
MnCl2	MnCl2	Scacchit	c	4.115	Webmineral
MnCO3	MnCO3	Rhodochrosit	c	3.108	Webmineral
MnF2	MnF2		c	2.494	Materialsproject
MnF3	MnF3		c	3.433	Materialsproject
MnF4	MnF4		c	3.924	Materialsproject
MnO	MnO	Manganosit	c	1.314	Webmineral
MnO2	MnO2		c	2.146	Webmineral
MnO2H	MnO2H		c	2.148	Materialsproject
MnO2H2	MnO2H2		c	2.806	Materialsproject
MnP	MnP		c	1.442	Materialsproject
MnS	MnS		c	2.551	Webmineral
MnS2	MnS2	Hauerit	c	3.417	Webmineral
MnSb	MnSb		c	2.453	Materialsproject
MnSn2	MnSn2		c	3.595	Materialsproject
MnSO4	MnSO4		c	4.565	Materialsproject
N2O3H4	N2O3H4		c	4.843	Materialsproject
N2SO4H8	N2SO4H8		c	8.104	Materialsproject
N2Zn3	N2Zn3		c	3.607	Materialsproject
Na	Na		c	2.235	Materialsproject
JADEITE	Na2Al2Si4O12	Jadeit	c	6.289	Materialsproject
LOW_ALBIT	Na2Al2Si6O16	Albit	c	10.472	Materialsproject
Na2CO3	Na2CO3	Natrit	c	4.167	Webmineral
Na2Cr2O4	Na2Cr2O4		c	2.599	Materialsproject

Table B.5: List of added molar volumes, continued

NAME	FORMULA	Mineral Name	STATE	molar volume (J/bar)	Quelle
Na2CrO4	Na2CrO4		c	6.068	Materialsproject
Na2O	Na2O		c	2.637	Materialsproject
Na2O2	Na2O2		c	3.089	Materialsproject
Na2S	Na2S		c	4.272	Materialsproject
Na2Si2O5	Na2Si2O5	Natrosilit	c	7.244	Webmineral
Na2SiO3	Na2SiO3		c	4.805	Materialsproject
Na2SO4	Na2SO4	Thénardit	c	5.277	Webmineral
Na2Ti2O5	Na2Ti2O5		c	8.970	Materialsproject
Na2Ti3O7	Na2Ti3O7		c	9.015	Materialsproject
Na2TiO3	Na2TiO3		c	4.108	Materialsproject
Na3AlF6	Na3AlF6	Kryolith	c	7.084	Webmineral
Na3As	Na3As			6.155	Materialsproject
ANDESIN	Na3Ca2Al7Si13O40	Andesit	c	8.647	Webmineral
OLIGOKLAS	Na4CaAl6Si14O40	Oligoklas	c	9.531	Webmineral
Na4SiO4	Na4SiO4		c	7.164	Materialsproject
Na5Al3F14	Na5Al3F14	Chiolite	c	15.352	Webmineral
NaAlO2	NaAlO2		c	3.072	Materialsproject
KARNEGIT	NaAlSiO4	Tief-Carnegieit	4	5.793	Materialsproject
NEFELIN-SINT.	NaAlSiO4	Nephelin	c	5.490	Webmineral
NaBr	NaBr		c	3.297	Materialsproject
BITOVNIT	NaCa4Al9Si11O40	Bytownit	c	10.660	Webmineral
LABRADOR	NaCaAl3Si5O16	Labradorit	c	9.558	Webmineral
NaCd2	NaCd2		c	4.606	Materialsproject
NaCl	NaCl	Halit	c	2.701	Webmineral
NaF	NaF	Villiaumit	c	1.495	Webmineral
NaFeO2	NaFeO2			2.653	Materialsproject
NaH	NaH		c	1.721	Materialsproject
NaNO2	NaNO2		c	3.366	Materialsproject
NaNO3	NaNO3	Nitratin	c	3.760	Webmineral
NaO2	NaO2		c	2.511	Materialsproject
NaOH	NaOH		c	2.042	Materialsproject
NFH4	NFH4		c	3.715	Materialsproject
Ni	Ni	Nickel	c	0.659	Webmineral
Ni2P	Ni2P		c	2.009	Materialsproject
Ni3P	Ni3P		c	2.626	Materialsproject
Ni3Sn	Ni3Sn	Nisnit	c	3.138	Mindat
Ni3Sn2	Ni3Sn2		c	4.595	Materialsproject
Ni3Sn4	Ni3Sn4		c	7.700	Materialsproject
Ni3Ti	Ni3Ti		c	2.814	Materialsproject
Ni5P2	Ni5P2		c	4.610	Materialsproject
NiCl2	NiCl2		c	3.567	Materialsproject
NiCO3	NiCO3	Gaspeit=(Ni,Mg,Fe	c	2.803	Materialsproject
NiF2	NiF2		c	2.077	Materialsproject
NiO	NiO	Bunsenit	c	1.097	Webmineral
NiO2H2	NiO2H2	Theophrastit	c	2.356	Webmineral
NiP2	NiP2	Negevit	c	2.480	Mindat
NiP3	NiP3		c	3.606	Materialsproject
NiS	NiS	Millerit	c	1.689	Webmineral
NiSb	NiSb	Breithauptit	c	2.066	Webmineral
NiSO4	NiSO4		c	4.014	Materialsproject
NiTi	NiTi		c	1.656	Materialsproject
NiTi2	NiTi2		c	2.699	Materialsproject
NiTiO3	NiTiO3		c	3.123	Materialsproject
NTi	NTi	Osbornit	c	1.149	Mindat
NZr	NZr		c	1.482	Materialsproject

Table B.6: List of added molar volumes, continued

NAME	FORMULA	Mineral Name	STATE	molar volume (J/bar)	Quelle
P4O10	P4O10		c	5.659	Materialsproject
Pb	Pb	Blei	c	1.827	Webmineral
Pb2CO4	Pb2CO4	Shannonit	c	5.171	Webmineral
Pb2O3	Pb2O3		c	4.906	Materialsproject
Pb2SO5	Pb2SO5	Lanarkit	c	7.500	Webmineral
Pb3O4	Pb3O4	Minium	c	7.680	Webmineral
Pb3SO6	Pb3SO6		c	10.660	Materialsproject
PbCl2	PbCl2	Cotunnit	c	4.707	Webmineral
PbCO3	PbCO3	Cerussit	c	4.059	Webmineral
PbF2	PbF2	Fluorocronit	c	3.141	Mineralienatlas
PbO	PbO	Massicot	c	2.274	Webmineral
PbO2	PbO2	Plattnerit	c	3.116	Webmineral
PbS	PbS	Galenit	c	3.149	Webmineral
PbSO4	PbSO4	Anglesit	c	4.795	Webmineral
PbTiO3	PbTiO3	Macedonit	c	3.834	Webmineral
S	S	Schwefel	c	12.358	Webmineral
Sb	Sb	Antimon	c	1.807	Webmineral
Sb2O3	Sb2O3	Senarmontit	c	5.203	Webmineral
Sb2S3	Sb2S3	Valentinit	c	5.002	Webmineral
Sb2S3O12	Sb2S3O12		c	14.251	Materialsproject
SbZn	SbZn		c	3.046	Materialsproject
Si	Si		c	1.206	Webmineral
Si2Cr	Si2Cr		c	2.150	Materialsproject
Si2H6	Si2H6		c	2.300	Materialsproject
Si2Ti	Si2Ti	Zhiqinit	c	2.558	Materialsproject
Si2Zr	Si2Zr		c	3.046	Materialsproject
Si3Cr5	Si3Cr5		c	5.685	Materialsproject
Si3Mn5	Si3Mn5		c	5.955	Materialsproject
Si3N4	Si3N4		c	4.476	Materialsproject
Si3Ti5	Si3Ti5		c	7.464	Materialsproject
Si3Zr5	Si3Zr5		c	9.380	Materialsproject
SiCdO3	SiCdO3		c	3.996	Materialsproject
SiCr	SiCr		c	1.465	Materialsproject
SiCr3	SiCr3		c	2.774	Materialsproject
SiMn	SiMn		c	1.392	Materialsproject
TEPHROITE	SiMn2O4	Tephroit	c	4.371	Webmineral
SiMn3	SiMn3		c	2.725	Materialsproject
RHODONITE	SiMnO3	Rhodonit	c	3.471	Mindat
SiNi	SiNi		c	1.463	Materialsproject
SiNi2O4	SiNi2O4	Liebenbergit	c	4.252	Webmineral
CRISTOBALITE	SiO2	Cristobalit	c	2.574	Webmineral
QUARTZ	SiO2	Quarz	c	2.268	Webmineral
TRIDIMIT	SiO2	Tridymit	c	2.554	Webmineral
SiP	SiP		c	2.844	Materialsproject
SiPb2O4	SiPb2O4		c	7.141	Materialsproject
ALAMOSITE	SiPbO3	PbSiO3	c	4.450	Webmineral
SiS	SiS		c	9.548	Materialsproject
SiS2	SiS2			5.710	Materialsproject
SiTi	SiTi		c	1.798	Materialsproject
SiZn2O4	SiZn2O4	Willemit	c	5.240	Webmineral
SiZr	SiZr		c	2.148	Materialsproject
SiZr2	SiZr2		c	3.525	Materialsproject
SiZrO4	SiZrO4	Zirkon	c	3.926	Webmineral
Sn	Sn	Zinn	c	1.629	Webmineral
Sn2S3	Sn2S3	Ottemannit	c	7.011	Webmineral

Table B.7: List of added molar volumes, continued

NAME	FORMULA	Mineral Name	STATE	molar volume (J/bar)	Quelle
SnCl2	SnCl2		c	5.313	Materialsproject
SnF2	SnF2		c	3.497	Materialsproject
SnF2	SnF2		c	3.493	Materialsproject
SnO	SnO	Romarchit	c	2.105	Webmineral
SnO2	SnO2	Cassiterit	c	2.107	Webmineral
SnS	SnS	Herzenbergit	c	2.901	Webmineral
SnS2	SnS2	Berndtit	c	4.053	Webmineral
SnSO4	SnSO4		c	5.479	Materialsproject
Ti	Ti	Titan	c	1.064	Webmineral
Ti2O3	Ti2O3	Tistarit	c	4.722	Webmineral
Ti3O5	Ti3O5		c	5.341	Materialsproject
Ti4O7	Ti4O7		c	7.158	Materialsproject
TiBr2	TiBr2		c	4.513	Materialsproject
TiBr3	TiBr3		c	7.519	Materialsproject
TiBr4	TiBr4		c	14.157	Materialsproject
TiCl2	TiCl2		c	4.428	Materialsproject
TiCl3	TiCl3		c	6.772	Materialsproject
TiF2	TiF2		c	2.109	Materialsproject
TiF3	TiF3		c	3.713	Materialsproject
TiF4	TiF4		c	4.572	Materialsproject
TiH2	TiH2		c	1.302	Materialsproject
TiO	TiO		c	1.262	Materialsproject
ANATASE	TiO2	Anatas	c	2.060	Webmineral
TiO2	TiO2	Rutil	c	1.880	Webmineral
TiS	TiS	Wassonit	c	1.796	Mindat
TiS2	TiS2		c	4.402	Materialsproject
TiZn2O4	TiZn2O4		c	4.733	Materialsproject
Zn	Zn	Zink	c	0.910	Webmineral
Zn3P2	Zn3P2		c	5.692	Materialsproject
ZnBr2	ZnBr2		c	5.883	Materialsproject
ZnCl2	ZnCl2		c	4.947	Materialsproject
ZnCO3	ZnCO3	Smithsonit	c	2.828	Webmineral
ZnF2	ZnF2		c	2.212	Materialsproject
ZnO	ZnO	Zinkit=(Zn,Mn)O	c	1.497	Materialsproject
ZnO2H2	ZnO2H2	Wülfingit	c	3.243	Webmineral
ZnP2	ZnP2		c	3.650	Materialsproject
ZnS	ZnS	Sphalerite	c	2.379	Webmineral
ZnS	ZnS	Wurtzite=(Zn,Fe)S	c	2.382	Webmineral
ZnSO4	ZnSO4	Zinkosit	c	4.157	Mineralienatlas
Zr	Zr		c	1.415	Materialsproject
ZrBr2	ZrBr2		c	5.381	Materialsproject
ZrBr3	ZrBr3		c	9.205	Materialsproject
ZrBr4	ZrBr4		c	9.782	Materialsproject
ZrCl2	ZrCl2		c	4.205	Materialsproject
ZrCl3	ZrCl3		c	7.711	Materialsproject
ZrCl4	ZrCl4		c	9.484	Materialsproject
ZrF4	ZrF4		c	3.787	Materialsproject
ZrO2	ZrO2	Baddeleyit	c	2.115	Webmineral
ZrS2	ZrS2		c	4.697	Materialsproject

Table B.8: List of added molar volumes, continued
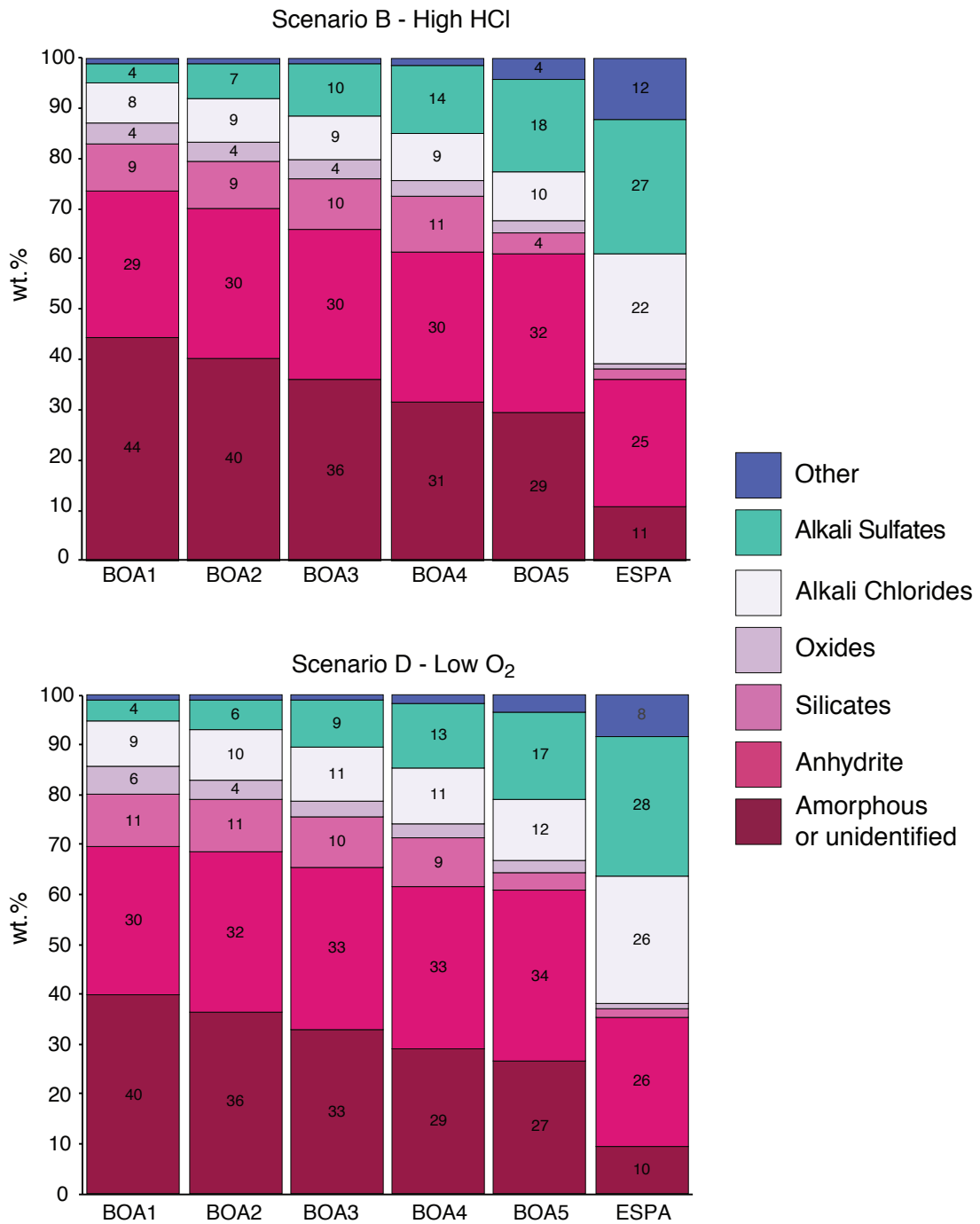
Figure B.1: Predicted mineralogy for the different ash fractions for flue gas scenario B and D.

		MGP Gas	MGP Dust		MGP Salt	
share of flux rate		99%	0.50%		0.50%	
Flux	Flux Order	share gas	share gas	share sink	share gas	share sink
0-1	0	34.89	0.182	0.000	0.182	0.000
1-2	1	0.219	0.164	0.055	0.207	0.011
2-3	1	0.203	0.152	0.051	0.193	0.010
3-4	1	0.183	0.137	0.046	0.174	0.009
4-5	1	0.157	0.118	0.039	0.150	0.008
5-6	1	0.137	0.103	0.034	0.130	0.007
6-7	1	0.127	0.032	0.095	0.032	0.095
7-8	1	0.112	0.028	0.084	0.028	0.084
8-9	1	0.102	0.025	0.076	0.025	0.076
9- sink	1	0.094	0.024	0.071	0.024	0.071

Table B.9: Detailed flux rates for the different mobile groups of phases (MGP)

Mineral Name	Formula	Constituent Simple Salts	SSA Cp J/(molK)	SSA S J/(molK)	SSA H J/mol	Literature Cp J/(molK)	Literature S J/(molK)	Literature H J/mol	Reference
Ca2Sb2O7	Ca2Sb2O7	2 CaO + Sb2O5	188	201	-2242135				
Glauberite	CaNa2(SO4)2	CaSO4 + Na2SO4	228	257	-2822393			-2829200	NBS Tables
CuZrF6	CuZrF6	CuF2 + ZrF4	170	182	-2450395				
FeSbO4	FeSbO4	0.5 Fe2O3 + 0.5 Sb2O5	104	106	-897448				
Calciolangbeinite	K2Ca2(SO4)3	2 CaSO4 + K2SO4	331	390	-4306690				
Palmierite	K2Pb(SO4)2	PbSO4 + K2SO4	236	324	-2355861		315	-2379900	NBS Tables
K2SbCl5	K2SbCl5	2 KCl + SbCl3	211	349	-1255147				
K2ZnCl4	K2ZnCl4	2 KCl + ZnCl2	170	274	-1289275	179	300	-1259654	Miltenburg (1994) (Cp, S), Hf from Stulova (1974)
Aphthitalite	K3Na(SO4)2	0.5 Na2SO4 + 1.5 K2SO4	261	338	-2850492				
K3Sb5O14	K3Sb5O14	1.5 K2O + 2.5 Sb2O5	368	457	-2972297				
KSb3O5	KSb3O5	1.5 Sb2O3 + 0.5 K2O	193	243	-1243665				
KSbO3	KSbO3	1/2 K2O + 1/2 Sb2O5	88	111	-666799				
Na2ZnCl4	Na2ZnCl4	2 NaCl + ZnCl2	168	253	-1238815				
Na3SbO4	Na3SbO4	0.5 Sb2O5 + 1.5 Na2O	156	175	-1107802				
NaSbO3	NaSbO3	0.5 Sb2O5 + 0.5 Na2O	87	100	-693234				
Pb2Sb2O7	Pb2Sb2O7	2 PbO2 + Sb2O3	227	274	-1260540				
Pb3O2Cl2	Pb3O2Cl2	PbCl2 + 2 PbO	170	272	-796595				
PbSb2O6	PbSb2O6	PbO2 + Sb2O4	176	199	-1183498				
Sb2O4	Sb2O4	Sb2O4	115	127	-907500	115	127	-907500	NBS Tables
Sb2O5	Sb2O5	Sb2O5	104	125	-971900		125	-971900	NBS Tables
Sb3O4Cl	Sb3O4Cl	4/3 Sb2O3 + 1/3 SbCl3	175	235	-1072115				
Sb4Cl2O5	Sb4Cl2O5	10/6 Sb2O3 + 2/3 SbCl3	246	339	-1435686			-1451400	NBS Tables
SbCl3	SbCl3	SbCl3	108	184	-382170	108	184	-382170	NBS Tables
SbOCl	SbOCl	1/3 SbCl3 + 1/3 Sb2O3	71	105	-363571			-374000	NBS Tables
Dansite	ZnNa21Cl3(SO4)10	3 NaCl + ZnSO4 + 9 Na2SO4	1401	1673	-14704413				NBS Tables
ZnSb2O4	ZnSb2O4	ZnO + Sb2O3	146	174	-1059003				
ZnSb2O6	ZnSb2O6	ZnO + Sb2O5	145	169	-1323359				

Table B.10: Estimated thermodynamic data of crystalline compounds added to the database, determined through SSA. Where possible, thermodynamic data from literature was used.

Correction	Phase	Value
gEx_	FG_GLASS (l)	-10000 J
gEx_	FG_GLASS (s)	-10000 J
gEx_	K-Al-Sulfate	20000 J
gEx_	Aphthitalite	20000 J
gEx_	Na_2ZnCl_4	20000 J
gEx_	$SiZn_2O_4$ (cr)	20000 J

Table B.11: Applied corrections on Gibbs Free Energy of formation for selected phases

T°C	850	825	800	775	750	725	700	675	650	625	600	575	550	525	500	475	450	425	400	375	350	325	300	275	250	225	200	175	150	125	100
BaSO4(cr)	0.0032	0.0032	0.0032	0.0032	0.0032	0.0032	0.0032	0.0032	0.0032	0.0032	0.0032	0.0032	0.0032	0.0032	0.0032	0.0032	0.0032	0.0032	0.0032	0.0032	0.0032	0.0032	0.0032	0.0032	0.0032	0.0032	0.0032	0.0032	0.0032	0.0032	0.0032
CaFe2O4(cr)	0.0106	0.0106	0.0106	0.0106	0.0106	0.0106																									
DIOPSIDE(cr)	0.0015					0.0016	0.0016	0.0016	0.0016	0.0016	0.0016	0.0016																			
MONTICELLITE(cr)	0.0001	0.0016	0.0016	0.0016	0.0016																										
WOLLASTONITE(cr)	0.1415	0.1430	0.1430	0.1430	0.1430	0.1414	0.1163	0.0760	0.0609																						
SPHENE(cr)							0.0250	0.0250	0.0250	0.0250	0.0246	0.0246																			
CaTiO3(cr)	0.0250	0.0250	0.0250	0.0250	0.0250	0.0250																									
CdCl2(cr)																			0.0003	0.0004	0.0005	0.0005	0.0005	0.0005	0.0005	0.0005	0.0005	0.0005	0.0005	0.0005	0.0005
Cr2O3(cr)	0.0008	0.0008	0.0008	0.0008	0.0008	0.0008	0.0008	0.0008	0.0008	0.0008	0.0008	0.0008	0.0008	0.0008	0.0008	0.0008	0.0008	0.0008	0.0008	0.0008	0.0008	0.0008	0.0008	0.0008	0.0008	0.0008	0.0008	0.0008	0.0007	0.0007	0.0007
Ca2P2O7(cr)																					0.0014	0.0014	0.0014	0.0014	0.0014	0.0014	0.0014	0.0014	0.0014	0.0014	0.0014
Ca3P2O8(cr)		0.0010	0.0013	0.0014	0.0014	0.0014	0.0014	0.0014	0.0014	0.0014	0.0014	0.0014	0.0014	0.0014	0.0014	0.0014	0.0014	0.0014	0.0014	0.0014											
CaSO4(cr)	0.2606	0.2561	0.2552	0.2550	0.2549	0.2565	0.2921	0.3325	0.3476	0.4085	0.4089	0.4089	0.4351	0.4351	0.4351	0.4351	0.4351	0.4351	0.4351	0.4351	0.4365	0.4365	0.4365	0.4365	0.4365	0.4365	0.4365	0.4365	0.4365	0.4365	0.4365
FG_GLASS(s)	0.5067	0.5067	0.5067	0.5067	0.5067	0.5067	0.5067	0.5067	0.5067	0.5067	0.5067	0.5067	0.5067	0.5067	0.5067	0.5067	0.5067	0.5067	0.5067	0.5067	0.5067	0.5067	0.5067	0.5067	0.5067	0.5067	0.5067	0.5067	0.5067	0.5067	0.5067
CuCl2(cr)																										0.0102	0.0102	0.0102	0.0102	0.0102	0.0102
CuO(cr)							0.0029	0.0060	0.0075	0.0089	0.0094	0.0097	0.0099	0.0100	0.0101	0.0101	0.0102	0.0102	0.0102	0.0102	0.0102	0.0102	0.0102	0.0102	0.0102						
Fe2NiO4(cr)	0.0004	0.0004	0.0004	0.0004	0.0004	0.0004	0.0004	0.0004	0.0004	0.0004																					
Fe2O3(cr)									0.0106	0.0106	0.0110	0.0110	0.0110	0.0110	0.0110	0.0110	0.0110	0.0110	0.0110	0.0110	0.0110	0.0110	0.0110	0.0110	0.0110	0.0110	0.0110	0.0110	0.0110	0.0110	0.0110
Fe2ZnO4(cr)							0.0106	0.0106																							
KCl(cr)					0.0203	0.1411	0.2074	0.2427		0.0917	0.0968	0.0987	0.1519	0.1554	0.1555	0.1556	0.1556	0.1556	0.1556	0.1556	0.1584	0.1584	0.1584	0.1584	0.1584	0.1592	0.1592	0.1592	0.1592	0.1592	0.1592
K2SO4(cr)									0.1308	0.0890	0.0885	0.0885	0.0624	0.0600	0.0600	0.0600	0.0600	0.0600	0.0600	0.0600	0.0586	0.0586	0.0586	0.0586	0.0586	0.0582	0.0582	0.0582	0.0582	0.0582	0.0582
Mg-Langbeinite														0.0008	0.0008	0.0008	0.0008	0.0008	0.0008	0.0008	0.0008	0.0008	0.0008	0.0008	0.0008	0.0008	0.0008	0.0008	0.0008	0.0008	0.0008
CLINOENSTATIT													0.0008																		
MnO2(cr)	0.0027	0.0027	0.0027	0.0027	0.0027	0.0027	0.0027	0.0027	0.0027	0.0027	0.0027	0.0027	0.0027	0.0027	0.0027	0.0027	0.0027	0.0027	0.0027	0.0027	0.0027	0.0027	0.0027	0.0027	0.0027	0.0027	0.0027	0.0027	0.0027	0.0027	0.0027
NaCl(cr)					0.0033	0.0768	0.1857	0.2860	0.5874	0.6302	0.6324	0.6333	0.6337	0.6338	0.6339	0.6339	0.6339	0.6339	0.6339	0.6339	0.6339	0.6339	0.6339	0.6339	0.6339	0.6339	0.6339	0.6339	0.6339	0.6339	0.6339
NiSO4(cr)																										0.0004	0.0004	0.0004	0.0004	0.0004	0.0004
NiTiO3(cr)											0.0004	0.0004	0.0004	0.0004	0.0004	0.0004	0.0004	0.0004	0.0004	0.0004	0.0004	0.0004	0.0004	0.0004	0.0004						
PbCl2(cr)																			0.0050	0.0080	0.0089	0.0092	0.0093	0.0093	0.0093	0.0093	0.0093	0.0093	0.0093	0.0093	0.0093
Sb2O4(cr)			0.0021	0.0030	0.0032	0.0032	0.0032	0.0032	0.0032	0.0032	0.0032	0.0032	0.0032	0.0032	0.0032	0.0032	0.0032	0.0032	0.0032	0.0032	0.0032	0.0032	0.0032	0.0032							
Sb2O5(cr)																									0.0032	0.0032	0.0032	0.0032	0.0032	0.0032	0.0032
CRISTOBALITE(cr)										0.0562	0.0554	0.0536	0.0005																		
QUARTZ(cr)											0.0002	0.0010	0.0786	0.0798	0.0791	0.0784	0.0777	0.0771	0.0765	0.0760	0.0755	0.0751	0.0747	0.0833	0.1442	0.1442	0.1442	0.1442	0.1440	0.1431	0.1401
SiZn2O4(cr)								0.0401	0.0551	0.0598	0.0608	0.0618	0.0636	0.0644	0.0651	0.0658	0.0665	0.0671	0.0677	0.0682	0.0687	0.0691	0.0695	0.0609							
SiZrO4(cr)								0.0003	0.0003	0.0003	0.0003	0.0003	0.0003	0.0003	0.0003	0.0003	0.0003	0.0003	0.0003	0.0003	0.0003	0.0003	0.0003	0.0003	0.0003	0.0003	0.0003	0.0003	0.0003	0.0003	0.0003
SnO2(cr)	0.0035	0.0035	0.0035	0.0035	0.0035	0.0035	0.0035	0.0035	0.0035	0.0035	0.0035	0.0035	0.0035	0.0035	0.0035	0.0035	0.0035	0.0035	0.0035	0.0035	0.0035	0.0035	0.0035	0.0035	0.0035	0.0035	0.0035	0.0035	0.0035	0.0035	0.0035
TiO2(cr)													0.0246	0.0246	0.0246	0.0246	0.0246	0.0246	0.0246	0.0246	0.0246	0.0246	0.0246	0.0246	0.0246	0.0250	0.0250	0.0250	0.0250	0.0250	0.0250
ZnCl2(cr)																								0.0179	0.1414	0.1417	0.1418	0.1418	0.1418	0.1418	0.1418
ZnO(cr)	0.0478	0.0495	0.0523	0.0555	0.0588	0.0627	0.0632																								
ZrO2(cr)	0.0003	0.0003	0.0003	0.0003	0.0003	0.0003	0.0003																								

Table B.12: Predicted stable phases for scenario A – reference state from batch simulations.

T°C	850	825	800	775	750	725	700	675	650	625	600	575	550	525	500	475	450	425	400	375	350	325	300	275	250	225	200	175	150	125	100
BaSO4(cr)	0.0032	0.0032	0.0032	0.0032	0.0032	0.0032	0.0032	0.0032	0.0032	0.0032	0.0032	0.0032	0.0032	0.0032	0.0032	0.0032	0.0032	0.0032	0.0032	0.0032	0.0032	0.0032	0.0032	0.0032	0.0032	0.0032	0.0032	0.0032	0.0032	0.0032	0.0032
CaFe2O4(cr)		0.0106	0.0073																												
DIOPSIDE(cr)	0.0016	0.0016	0.0016	0.0016	0.0016	0.0016	0.0016	0.0016	0.0016	0.0016																					
WOLLASTONIT	0.1163	0.1163	0.1163	0.1163	0.1163	0.1160	0.1160																								
SPHENE(cr)	0.0250	0.0250	0.0250	0.0250	0.0250	0.0250	0.0250	0.0250	0.0246	0.0246																					
CdCl2(cr)																			0.0003	0.0004	0.0005	0.0005	0.0005	0.0005	0.0005	0.0005	0.0005	0.0005	0.0005	0.0005	0.0005
Cr2O3(cr)	0.0007	0.0008	0.0008	0.0008	0.0008	0.0008	0.0008	0.0008	0.0008	0.0008	0.0008	0.0008	0.0008	0.0008	0.0008	0.0007	0.0007	0.0007	0.0007	0.0007	0.0007	0.0007	0.0007	0.0007	0.0007	0.0007	0.0007	0.0007	0.0007	0.0007	0.0007
Ca2P2O7(cr)																	0.0014	0.0014	0.0014	0.0014	0.0014	0.0014	0.0014	0.0014	0.0014	0.0014	0.0014	0.0014	0.0014	0.0014	0.0023
Ca3P2O8(cr)	0.0004	0.0004	0.0011	0.0013																											
CaSO4(cr)	0.2963	0.2952	0.2857	0.2817	0.2922	0.2925	0.2925	0.4085	0.4089	0.4089	0.4351	0.4351	0.4351	0.4351	0.4351	0.4351	0.4351	0.4351	0.4365	0.4365	0.4365	0.4365	0.4365	0.4365	0.4365	0.4365	0.4365	0.4365	0.4365	0.4365	0.4608
FG_GLASS(s)	0.5067	0.5067	0.5067	0.5067	0.5067	0.5067	0.5067	0.5067	0.5067	0.5067	0.5067	0.5067	0.5067	0.5067	0.5067	0.5067	0.5067	0.5067	0.5067	0.5067	0.5067	0.5067	0.5067	0.5067	0.5067	0.5067	0.5067	0.5067	0.5067	0.5067	0.4651
CuCl2(cr)																		0.0102	0.0102	0.0102	0.0102	0.0102	0.0102	0.0102	0.0102	0.0102	0.0102	0.0102	0.0102	0.0102	0.0102
CuO(cr)										0.0026	0.0055	0.0072	0.0082	0.0089	0.0094	0.0096	0.0098	0.0100	0.0101	0.0101	0.0102	0.0102	0.0102								
Fe2NiO4(cr)	0.0003	0.0003	0.0004	0.0004	0.0004	0.0004	0.0004	0.0004																							
Fe2O3(cr)	0.0107	0.0107	0.0034		0.0106	0.0106	0.0106	0.0106	0.0110	0.0110	0.0110	0.0110	0.0110	0.0110	0.0110	0.0110	0.0110	0.0110	0.0110	0.0110	0.0110	0.0110	0.0110	0.0110	0.0110	0.0110	0.0110	0.0110	0.0110	0.0110	0.0126
K_AlSulfate(cr)																															0.0151
KCl(cr)					0.0213	0.1419	0.2080	0.2431	0.0839	0.0927	0.1492	0.1543	0.1550	0.1554	0.1555	0.1555	0.1555	0.1555	0.1583	0.1583	0.1583	0.1583	0.1583	0.1583	0.1592	0.1592	0.1592	0.1592	0.1592	0.1592	0.2595
K2SO4(cr)								0.0886	0.0886	0.0886	0.0624	0.0600	0.0600	0.0600	0.0600	0.0600	0.0600	0.0600	0.0586	0.0586	0.0586	0.0586	0.0586	0.0586	0.0582	0.0582	0.0582	0.0582	0.0582	0.0582	
Mg-Langbeinite								0.0008	0.0008	0.0008	0.0008	0.0008	0.0008	0.0008	0.0008	0.0008	0.0008	0.0008	0.0008	0.0008	0.0008	0.0008	0.0008	0.0008	0.0008	0.0008	0.0008	0.0008	0.0008	0.0008	0.0020
CLINOENSTATIT											0.0008																				
MnO2(cr)	0.0027	0.0027	0.0027	0.0027	0.0027	0.0027	0.0027	0.0027	0.0027	0.0027	0.0027	0.0027	0.0027	0.0027	0.0027	0.0027	0.0027	0.0027	0.0027	0.0027	0.0027	0.0027	0.0027	0.0027	0.0027	0.0027	0.0027	0.0027	0.0027	0.0027	0.0027
NaCl(cr)	0.0027	0.0027	0.0027	0.0027	0.0784	0.1492	0.1867	0.4381	0.6257	0.6303	0.6324	0.6333	0.6337	0.6338	0.6339	0.6339	0.6339	0.6339	0.6339	0.6339	0.6339	0.6339	0.6339	0.6339	0.6339	0.6339	0.6339	0.6339	0.6339	0.6339	0.6354
NiSO4(cr)																									0.0004	0.0004	0.0004	0.0004	0.0004	0.0004	0.0004
NiTiO3(cr)				0.0004	0.0004	0.0004	0.0004	0.0004	0.0004	0.0004	0.0004	0.0004	0.0004	0.0004	0.0004	0.0004	0.0004	0.0004	0.0004	0.0004	0.0004	0.0004	0.0004	0.0004							
PbCl2(cr)																			0.0050	0.0080	0.0089	0.0092	0.0093	0.0093	0.0093	0.0093	0.0093	0.0093	0.0093	0.0093	0.0093
Sb2O4(cr)			0.0021	0.0030	0.0032	0.0032	0.0032	0.0032	0.0032	0.0032	0.0032	0.0032	0.0032	0.0032	0.0032	0.0032	0.0032	0.0032	0.0032	0.0032	0.0032	0.0032	0.0032	0.0032							
Sb2O5(cr)																									0.0032	0.0032	0.0032	0.0032	0.0032	0.0032	0.0032
CRISTOBALITE)								0.1023	0.0987	0.0948	0.1150	0.1127																			
QUARTZ(cr)													0.1092	0.1057	0.1023	0.0990	0.0958	0.0928	0.0899	0.0873	0.0848	0.0826	0.1442	0.1442	0.1442	0.1442	0.1442	0.1442	0.1440	0.1431	0.1816
SiZn2O4(cr)									0.0616	0.0594	0.0570	0.0543	0.0514	0.0484	0.0452	0.0419	0.0385	0.0351	0.0315	0.0276	0.0216	0.0177	0.0137								
SiZrO4(cr)					0.0003	0.0003	0.0003	0.0003	0.0003	0.0003	0.0003	0.0003	0.0003	0.0003	0.0003	0.0003	0.0003	0.0003	0.0003	0.0003	0.0003	0.0003	0.0003	0.0003	0.0003	0.0003	0.0003	0.0003	0.0003	0.0003	0.0003
SnO2(cr)	0.0035	0.0035	0.0035	0.0035	0.0035	0.0035	0.0035	0.0035	0.0035	0.0035	0.0035	0.0035	0.0035	0.0035	0.0035	0.0035	0.0035	0.0035	0.0035	0.0035	0.0035	0.0035	0.0035	0.0035	0.0035	0.0035	0.0035	0.0035	0.0035	0.0035	0.0035
TiO2(cr)	0.0246	0.0246	0.0246	0.0246	0.0246	0.0246	0.0246	0.0246	0.0246	0.0246	0.0246	0.0246	0.0246	0.0246	0.0246	0.0246	0.0246	0.0246	0.0246	0.0246	0.0246	0.0246	0.0246	0.0246	0.0250	0.0250	0.0250	0.0250	0.0250	0.0250	0.0262
ZnCl2(cr)																							0.1339	0.1398	0.1414	0.1417	0.1418	0.1418	0.1418	0.1418	0.1418
ZrO2(cr)	0.0003	0.0003	0.0003	0.0003																											

Table B.13: Predicted stable phases for scenario B – High HCl from batch simulations.

T°C	850	825	800	775	750	725	700	675	650	625	600	575	550	525	500	475	450	425	400	375	350	325	300	275	250	225	200	175	150	125	100
BaSO4(cr)	0.0032	0.0032	0.0032	0.0032	0.0032	0.0032	0.0032	0.0032	0.0032	0.0032	0.0032	0.0032	0.0032	0.0032	0.0032	0.0032	0.0032	0.0032	0.0032	0.0032	0.0032	0.0032	0.0032	0.0032	0.0032	0.0032	0.0032	0.0032	0.0032	0.0032	0.0032
CdSO4(cr)										0.0003	0.0005	0.0005	0.0005	0.0005	0.0005	0.0005	0.0005	0.0005	0.0005	0.0005	0.0005	0.0005	0.0005	0.0005	0.0005	0.0005	0.0005	0.0005	0.0005	0.0005	0.0005
Cr2O3(cr)	0.0008	0.0008	0.0008	0.0008	0.0008	0.0008	0.0008	0.0008	0.0008	0.0008	0.0008	0.0008	0.0008	0.0008	0.0008	0.0008	0.0008	0.0008	0.0008	0.0007	0.0007	0.0007	0.0007	0.0007	0.0007	0.0007	0.0007	0.0007	0.0007	0.0007	0.0007
Ca2P2O7(cr)																					0.0020	0.0044	0.0052	0.0056	0.0058	0.0059	0.0059	0.0059	0.0059	0.0059	0.0059
CaSO4(cr)	0.4393	0.4393	0.4393	0.4393	0.4393	0.4393	0.4393	0.4393	0.4393	0.4393	0.4393	0.4393	0.4393	0.4393	0.4393	0.4393	0.4393	0.4393	0.4393	0.4393	0.4832	0.5174	0.5364	0.5461	0.5508	0.5530	0.5538	0.5542	0.5543	0.5543	0.5543
FG_GLASS(s)	0.5067	0.5067	0.5067	0.5067	0.5067	0.5067	0.5067	0.5067	0.5067	0.5067	0.5067	0.5067	0.5067	0.5067	0.5067	0.5067	0.5067	0.5067	0.5067	0.5067	0.4309	0.3689	0.3362	0.3196	0.3116	0.3079	0.3064	0.3058	0.3056	0.3056	0.3056
CuSO4(cr)							0.0003	0.0087	0.0099	0.0101	0.0102	0.0102	0.0102	0.0102	0.0102	0.0102	0.0102	0.0102	0.0102	0.0102	0.0102	0.0102	0.0102	0.0102	0.0102	0.0102	0.0102	0.0102	0.0102	0.0102	0.0102
Fe2O3(cr)	0.0110	0.0110	0.0110	0.0110	0.0110	0.0110	0.0110	0.0110	0.0110	0.0110	0.0110	0.0110	0.0110	0.0110	0.0110	0.0110	0.0110	0.0110	0.0110	0.0110	0.0138	0.0162	0.0174	0.0180	0.0183	0.0185	0.0185	0.0185	0.0185	0.0185	0.0185
K_AlSulfate(cr)																					0.0276	0.0501	0.0620	0.0681	0.0710	0.0723	0.0729	0.0731	0.0732	0.0732	0.0732
K2SO4(cr)	0.1232	0.1307	0.1344	0.1363	0.1371	0.1375	0.1377	0.1377	0.1378	0.1378	0.1378	0.1378	0.1378	0.1378	0.1378	0.1378	0.1378	0.1378	0.1378	0.1378	0.1231	0.1112	0.1049	0.1017	0.1001	0.0994	0.0991	0.0990	0.0990	0.0990	0.0990
Mg-Langbeinite	0.0008	0.0008	0.0008	0.0008	0.0008	0.0008	0.0008	0.0008	0.0008	0.0008	0.0008	0.0008	0.0008	0.0008	0.0008	0.0008	0.0008	0.0008	0.0008	0.0008	0.0030	0.0048	0.0057	0.0062	0.0065	0.0066	0.0066	0.0066	0.0066	0.0066	0.0066
MnO2(cr)	0.0027	0.0027	0.0027	0.0027	0.0027	0.0027	0.0027	0.0027	0.0027	0.0027	0.0027	0.0027	0.0027	0.0027	0.0027	0.0027	0.0027	0.0027	0.0027	0.0027	0.0027	0.0027	0.0027	0.0027	0.0027	0.0027	0.0027	0.0027	0.0027	0.0027	0.0027
Na2SO4(cr)													0.3170	0.3170	0.3170	0.3170	0.3170	0.3170	0.3170	0.3170	0.3183	0.3195	0.3201	0.3204	0.3205	0.3205	0.3206	0.3206	0.3206	0.3206	0.3206
NiSO4(cr)								0.0004	0.0004	0.0004	0.0004	0.0004	0.0004	0.0004	0.0004	0.0004	0.0004	0.0004	0.0004	0.0004	0.0004	0.0004	0.0004	0.0004	0.0004	0.0004	0.0004	0.0004	0.0004	0.0004	0.0004
NiTiO3(cr)	0.0004	0.0004	0.0004	0.0004		0.0004	0.0004																								
PbSO4(cr)						0.0009	0.0065	0.0083	0.0090	0.0092	0.0093	0.0093	0.0093	0.0093	0.0093	0.0093	0.0093	0.0093	0.0093	0.0093	0.0093	0.0093	0.0093	0.0093	0.0093	0.0093	0.0093	0.0093	0.0093	0.0093	0.0093
Sb2O4(cr)			0.0020	0.0030	0.0032	0.0032	0.0032	0.0032	0.0032	0.0032	0.0032	0.0032	0.0032	0.0032	0.0032	0.0032	0.0032	0.0032	0.0032	0.0032	0.0032	0.0032	0.0032								
Sb2O5(cr)																								0.0032	0.0032	0.0032	0.0032	0.0032	0.0032	0.0032	0.0032
CRISTOBALITE(cr)	0.1442	0.1442	0.1442	0.1442	0.1442	0.1419	0.1152	0.1442	0.1442	0.1442	0.1442	0.1442																			
QUARTZ(cr)													0.1442	0.1442	0.1442	0.1442	0.1442	0.1442	0.1442	0.1442	0.2200	0.2819	0.3146	0.3313	0.3393	0.3430	0.3445	0.3450	0.3450	0.3441	0.3412
SiZn2O4(cr)	0.0219	0.0222	0.0230	0.0244	0.0247	0.0269	0.0290	0.0246	0.0250	0.0250	0.0250	0.0250	0.0250	0.0250	0.0250	0.0250	0.0250	0.0250	0.0250	0.0250	0.0272	0.0290	0.0300	0.0304	0.0307	0.0308	0.0308	0.0308	0.0308	0.0308	0.0308
SiZrO4(cr)	0.0003	0.0003	0.0003	0.0003	0.0003	0.0003	0.0003	0.0003	0.0003	0.0003	0.0003	0.0003	0.0003	0.0003	0.0003	0.0003	0.0003	0.0003	0.0003	0.0003	0.0003	0.0003	0.0003	0.0003	0.0003	0.0003	0.0003	0.0003	0.0003	0.0003	0.0003
SnO2(cr)	0.0035	0.0035	0.0035	0.0035	0.0035	0.0035	0.0035	0.0035	0.0035																						
SnSO4(cr)										0.0035	0.0035	0.0035	0.0035	0.0035	0.0035	0.0035	0.0035	0.0035	0.0035	0.0035	0.0035	0.0035	0.0035	0.0035	0.0035	0.0035	0.0035	0.0035	0.0035	0.0035	0.0035
TiO2(cr)	0.0027	0.0024	0.0016	0.0002																											
ZnSO4(cr)								0.0711	0.1163	0.1340	0.1417	0.1417	0.1418	0.1418	0.1418	0.1418	0.1418	0.1418	0.1418	0.1418	0.1418	0.1418	0.1418	0.1418	0.1418	0.1418	0.1418	0.1418	0.1418	0.1418	0.1418

Table B.14: Predicted stable phases for scenario C – High SO$_2$ from batch simulations

Table B.15: Predicted stable phases for scenario D – Low O_2 from batch simulations

T°C	850	825	800	775	750	725	700	675	650	625	600	575	550	525	500	475	450	425	400	375	350	325	300	275	250	225	200	175	150	125	100
BaSO4(cr)	0.0032	0.0032	0.0032	0.0032	0.0032	0.0032	0.0032	0.0032	0.0032	0.0032	0.0032	0.0032	0.0032	0.0032	0.0032	0.0032	0.0032	0.0032	0.0032	0.0032	0.0032	0.0032	0.0032	0.0032	0.0032	0.0032	0.0032	0.0032	0.0032	0.0032	0.0032
CaFe2O4(cr)	0.0106	0.0106	0.0106	0.0106	0.0106	0.0106																									
DIOPSIDE(cr)	0.0015	0.0016	0.0016	0.0016	0.0016	0.0016	0.0016	0.0016	0.0016	0.0016	0.0016	0.0016																			
MONTICELLITE(cr)	0.0001		0.0016	0.0016	0.0016																										
WOLLASTONITE(cr)	0.1414	0.1430	0.1430	0.1430	0.1430	0.1414	0.1163	0.0759	0.0609																						
SPHENE(cr)						0.0250	0.0250	0.0250	0.0250	0.0250	0.0246	0.0246																			
CaTiO3(cr)	0.0250	0.0250	0.0250	0.0250	0.0250	0.0250	0.0250	0.0250	0.0250	0.0250																					
CdCl2(cr)																			0.0003	0.0004	0.0004	0.0005	0.0005	0.0005	0.0005	0.0005	0.0005	0.0005	0.0005	0.0005	0.0005
Cr2O3(cr)	0.0008	0.0008	0.0008	0.0008	0.0008	0.0008	0.0008	0.0008	0.0008	0.0008	0.0008	0.0008	0.0008	0.0008	0.0008	0.0008	0.0008	0.0008	0.0008	0.0008	0.0008	0.0008	0.0008	0.0008	0.0008	0.0008	0.0008	0.0008	0.0008	0.0007	0.0007
Ca2P2O7(cr)	0.0014	0.0014	0.0014	0.0014	0.0014	0.0014	0.0014	0.0014	0.0014	0.0014	0.0014	0.0014	0.0014	0.0014	0.0014	0.0014	0.0014	0.0014	0.0014	0.0014	0.0014	0.0014	0.0014	0.0014	0.0014	0.0014	0.0014	0.0014	0.0014	0.0014	0.0014
Ca3P2O8(cr)	0.0009	0.0013																													
CaSO4(cr)	0.2606	0.2563	0.2552	0.2550	0.2549	0.2565	0.2921	0.3326	0.3476	0.4085	0.4089	0.4089	0.4351	0.4351	0.4351	0.4351	0.4351	0.4351	0.4351	0.4351	0.4365	0.4365	0.4365	0.4365	0.4365	0.4365	0.4365	0.4365	0.4365	0.4365	0.4365
FG_GLASS(s)	0.5067	0.5067	0.5067	0.5067	0.5067	0.5067	0.5067	0.5067	0.5067	0.5067	0.5067	0.5067	0.5067	0.5067	0.5067	0.5067	0.5067	0.5067	0.5067	0.5067	0.5067	0.5067	0.5067	0.5067	0.5067	0.5067	0.5067	0.5067	0.5067	0.5067	0.5067
CuCl2(cr)																								0.0102	0.0102	0.0102	0.0102	0.0102	0.0102	0.0102	0.0102
CuO(cr)							0.0041	0.0063	0.0083	0.0090	0.0095	0.0098	0.0100	0.0100	0.0101	0.0101	0.0102	0.0102	0.0102	0.0102	0.0102	0.0102	0.0102								
Fe2NiO4(cr)	0.0004	0.0004	0.0004	0.0004	0.0004	0.0004	0.0004	0.0004	0.0004																						
Fe2O3(cr)					0.0106	0.0106	0.0106	0.0106	0.0106	0.0106	0.0110	0.0110	0.0110	0.0110	0.0110	0.0110	0.0110	0.0110	0.0110	0.0110	0.0110	0.0110	0.0110	0.0110	0.0110	0.0110	0.0110	0.0110	0.0110	0.0110	0.0110
Fe2ZnO4(cr)						0.0106	0.0106																								
KCl(cr)					0.0202	0.1410	0.2073	0.2426	0.1307	0.0917	0.0968	0.0987	0.1519	0.1554	0.1555	0.1556	0.1556	0.1556	0.1556	0.1556	0.1584	0.1584	0.1584	0.1584	0.1584	0.1592	0.1592	0.1592	0.1592	0.1592	0.1592
K2SO4(cr)								0.0890	0.0885	0.0886	0.0624	0.0600	0.0600	0.0600	0.0600	0.0600	0.0600	0.0600	0.0600	0.0600	0.0586	0.0586	0.0586	0.0586	0.0586	0.0582	0.0582	0.0582	0.0582	0.0582	0.0582
Mg-Langbeinite																															
CLINOENSTATIT													0.0008																		
MnO2(cr)	0.0027	0.0027	0.0027	0.0027	0.0027	0.0027	0.0027	0.0027	0.0027	0.0027	0.0027	0.0027	0.0027	0.0027	0.0027	0.0027	0.0027	0.0027	0.0027	0.0027	0.0027	0.0027	0.0027	0.0027	0.0027	0.0027	0.0027	0.0027	0.0027	0.0027	0.0027
NaCl(cr)	0.0027	0.0027	0.0027	0.0033	0.0768	0.1857	0.2860	0.5873	0.6302	0.6324	0.6333	0.6337	0.6338	0.6339	0.6339	0.6339	0.6339	0.6339	0.6339	0.6339	0.6339	0.6339	0.6339	0.6339	0.6339	0.6339	0.6339	0.6339	0.6339	0.6339	0.6339
NiSO4(cr)																								0.0004	0.0004	0.0004	0.0004	0.0004	0.0004	0.0004	0.0004
NiTiO3(cr)										0.0004	0.0004	0.0004	0.0004	0.0004	0.0004	0.0004	0.0004	0.0004	0.0004	0.0004	0.0004	0.0004	0.0004								
PbCl2(cr)																				0.0050	0.0080	0.0089	0.0092	0.0093	0.0093	0.0093	0.0093	0.0093	0.0093	0.0093	0.0093
Sb2O4(cr)	0.0008	0.0008	0.0008	0.0008	0.0008	0.0008	0.0008	0.0008	0.0008	0.0008	0.0008	0.0008	0.0008	0.0008	0.0008	0.0008	0.0008	0.0008	0.0008	0.0008	0.0008	0.0008	0.0008								
Sb2O5(cr)																								0.0032	0.0032	0.0032	0.0032	0.0032	0.0032	0.0032	0.0032
CRISTOBALITE(cr)								0.0401	0.0551	0.0562	0.0556	0.0546	0.0003																		
QUARTZ(cr)												0.0001	0.0787	0.0798	0.0791	0.0784	0.0777	0.0771	0.0765	0.0760	0.0755	0.0751	0.0747	0.0833	0.1442	0.1442	0.1442	0.1442	0.1440	0.1431	0.1401
SiZn2O4(cr)									0.0598	0.0608	0.0618	0.0636	0.0644	0.0651	0.0658	0.0665	0.0671	0.0677	0.0682	0.0687	0.0691	0.0695	0.0609								
SiZrO4(cr)								0.0003	0.0003	0.0003	0.0003	0.0003	0.0003	0.0003	0.0003	0.0003	0.0003	0.0003	0.0003	0.0003	0.0003	0.0003	0.0003	0.0003	0.0003	0.0003	0.0003	0.0003	0.0003	0.0003	0.0003
SnO2(cr)	0.0035	0.0035	0.0035	0.0035	0.0035	0.0035	0.0035	0.0035	0.0035	0.0035	0.0035	0.0035	0.0035	0.0035	0.0035	0.0035	0.0035	0.0035	0.0035	0.0035	0.0035	0.0035	0.0035	0.0035	0.0035	0.0035	0.0035	0.0035	0.0035	0.0035	0.0035
TiO2(cr)											0.0246	0.0246	0.0246	0.0246	0.0246	0.0246	0.0246	0.0246	0.0246	0.0246	0.0246	0.0246	0.0246	0.0246	0.0250	0.0250	0.0250	0.0250	0.0250	0.0250	0.0250
ZnCl2(cr)																								0.0180	0.1414	0.1417	0.1418	0.1418	0.1418	0.1418	0.1418
ZnO(cr)	0.0478	0.0495	0.0523	0.0554	0.0587	0.0627	0.0634																								
ZrO2(cr)	0.0003	0.0003	0.0003	0.0003	0.0003	0.0003	0.0003																								

(kg)	BaSO4	DIOPSIDE	Ca2P2O7	Ca3P2O8	CaSO4	FG_GLASS	SPHENE	CdCl2	CdSO4	Cr2O3	CuCl2	CuO	CuSO4	Fe2NiO4	Fe2O3	K_AlSulfate	KCl	K2SO4	KSbS2O8	Mg-Langbeinite
KA1	0.002432	0.000683	0.000000	0.000856	0.097596	0.130913	0.009531	0.000000	0.000227	0.000000	0.001599	0.000000	0.000000	0.000000	0.003475	0.000000	0.011084	0.012937	0.000000	0.000000
KA2	0.002222	0.000000	0.000000	0.000690	0.092443	0.105520	0.000000	0.000000	0.000183	0.000000	0.001388	0.000000	0.000000	0.000000	0.002801	0.000000	0.010288	0.016389	0.000000	0.000305
KA3	0.002098	0.000000	0.000000	0.000574	0.087269	0.087895	0.000000	0.000000	0.000152	0.000000	0.001205	0.000000	0.000000	0.000000	0.002333	0.000000	0.008744	0.024554	0.000000	0.000288
KA4	0.002069	0.000000	0.000410	0.000000	0.086210	0.076500	0.000000	0.000000	0.000132	0.000000	0.001072	0.000000	0.000000	0.000000	0.002031	0.000000	0.007439	0.033652	0.000000	0.000284
KA5	0.002018	0.000000	0.000352	0.000000	0.084072	0.065826	0.000000	0.000055	0.000113	0.000000	0.000928	0.000000	0.000000	0.000000	0.001747	0.000000	0.005773	0.042826	0.000000	0.000277
EFA	0.022693	0.000000	0.005328	0.000000	1.658677	0.611368	0.004123	0.000285	0.000095	0.014709	0.001061	0.000000	0.000000	0.000000	0.019256	0.030088	0.207082	1.116128	0.000273	0.009240

(kg)	MnO2	NaCl	Na2SO4	NiSO4	NiTiO3	PbCl2	PbSO4	Sb2O4	Sb2O5	Sb2S3O12	CRISTOBALITE	QUARTZ	SiZn2O4	SiZrO4	SnO2	SnS2O8	SrSO4	TiO2	ZnCl2	ZnSO4
KA1	0.000465	0.019063	0.000000	0.000000	0.000129	0.000000	0.001955	0.000000	0.006343	0.000000	0.000000	0.027920	0.000000	0.000000	0.001045	0.000363	0.002607	0.000000	0.000000	0.000000
KA2	0.000375	0.019488	0.000000	0.000000	0.000104	0.000000	0.001576	0.000000	0.007471	0.000000	0.000027	0.023520	0.000000	0.000000	0.000842	0.000293	0.002269	0.000000	0.003130	0.000000
KA3	0.000312	0.020565	0.000000	0.000000	0.000087	0.000000	0.001312	0.005865	0.000000	0.000000	0.000000	0.021004	0.000000	0.000000	0.000701	0.000244	0.002244	0.000000	0.000000	0.000000
KA4	0.000272	0.022672	0.000000	0.000000	0.000076	0.000000	0.001142	0.004525	0.000000	0.000000	0.000000	0.020432	0.000000	0.000000	0.000610	0.000212	0.002212	0.000000	0.000000	0.000000
KA5	0.000234	0.024711	0.000000	0.000065	0.000000	0.000000	0.000983	0.008634	0.000000	0.000000	0.000000	0.000000	0.000000	0.000000	0.000525	0.000183	0.001953	0.000000	0.003854	0.000000
EFA	0.002320	0.636008	0.000000	0.000646	0.000000	0.094730	0.037381	0.009673	0.000760	0.000000	0.000000	0.104749	0.000000	0.000000	0.004914	0.000616	0.001812	0.020453	0.232717	0.110808

Table B.16: Predicted stable phases for scenario A – reference state from Box Flux Model simulations.

(kg)	BaSO4	DIOPSIDE	Ca2P2O7	Ca3P2O8	CLINOENSTATIT	CaSO4	FG_GLASS	SPHENE	CdCl2	CdSO4	Cr2O3	CuCl2	CuO	CuSO4	FeO3	K_AlSulfate	KCl	K2SO4	KSbS2O8	Mg-Langbeinite
KA1	0.002205	0.000000	0.000000	0.000992	0.000367	0.098681	0.151922	0.000000	0.000000	0.000000	0.000262	0.000000	0.001347	0.000000	0.004033	0.000000	0.006808	0.013732	0.000000	0.000000
KA2	0.002015	0.000000	0.000000	0.000801	0.000000	0.090145	0.122453	0.000000	0.000000	0.000000	0.000211	0.000000	0.001606	0.000000	0.003250	0.000000	0.004915	0.021405	0.000000	0.000354
KA3	0.001902	0.000000	0.000000	0.000667	0.000000	0.085099	0.102000	0.000000	0.000000	0.000000	0.000175	0.000000	0.001596	0.000000	0.002707	0.000000	0.003042	0.029429	0.000000	0.000335
KA4	0.001876	0.000000	0.000476	0.000000	0.000000	0.084090	0.088776	0.000000	0.000049	0.000000	0.000150	0.000000	0.001491	0.000000	0.002356	0.000000	0.001125	0.038581	0.000000	0.000330
KA5	0.001830	0.000000	0.000409	0.000000	0.000000	0.082004	0.076389	0.000000	0.000055	0.000000	0.000127	0.000350	0.000000	0.000000	0.002028	0.000000	0.000000	0.042880	0.000000	0.000322
EFA	0.020576	0.000000	0.007101	0.000000	0.000000	1.635396	0.688533	0.000000	0.004122	0.000285	0.001073	0.026311	0.000000	0.001898	0.023306	0.049978	0.000000	0.814740	0.001378	0.012652

(kg)	MnO2	NaCl	Na2SO4	NiSO4	NiTiO3	PbCl2	PbSO4	Sb2O4	Sb2O5	Sb2S3O12	CRISTOBALITE	QUARTZ	SiZn2O4	SiZrO4	SnO2	SnS2O8	SrSO4	TiO2	ZnCl2	ZnSO4
KA1	0.000540	0.020586	0.000000	0.000000	0.000150	0.000000	0.000000	0.002268	0.000000	0.000000	0.015227	0.000000	0.016614	0.000000	0.001212	0.000000	0.000421	0.004507	0.000000	0.000000
KA2	0.000435	0.021043	0.000000	0.000000	0.000121	0.000000	0.000000	0.001828	0.000000	0.000000	0.000023	0.011346	0.017404	0.000000	0.000977	0.000000	0.000340	0.003633	0.000000	0.000000
KA3	0.000362	0.022205	0.000000	0.000000	0.000101	0.000000	0.000000	0.001523	0.000000	0.000000	0.000000	0.007679	0.021136	0.000000	0.000814	0.000000	0.000283	0.003026	0.000000	0.000000
KA4	0.000315	0.024480	0.000000	0.000000	0.000088	0.001428	0.000000	0.001326	0.000000	0.000000	0.000000	0.004226	0.027512	0.000000	0.000708	0.000000	0.000246	0.002634	0.000000	0.000000
KA5	0.000271	0.025793	0.003959	0.000044	0.000000	0.001620	0.000000	0.001141	0.000000	0.000000	0.000000	0.010019	0.000000	0.000000	0.000610	0.000000	0.000212	0.002305	0.006802	0.000000
EFA	0.002692	1.403592	0.867829	0.000750	0.000000	0.094715	0.037375	0.000000	0.011225	0.000083	0.000000	0.131200	0.000000	0.000000	0.005701	0.000718	0.002103	0.024106	0.405064	0.174683

Table B.17: Predicted stable phases for scenario B – High HCl from Box Flux Model simulations.

(kg)	BaSO4	Ca2P2O7	CaSO4	FG_GLASS	CdSO4	Cr2O3	CuSO4	Fe2O3	K_AlSulfate	K2SO4	KSb2O8	Mg-Langbeinite	MnO2
KA1	0.002539	0.000000	0.116189	0.102629	0.000144	0.000177	0.003148	0.002724	0.000000	0.046641	0.000000	0.000643	0.000364
KA2	0.002319	0.000000	0.106139	0.082722	0.000140	0.000143	0.002880	0.002196	0.000000	0.042607	0.000000	0.000587	0.000294
KA3	0.002190	0.000000	0.126420	0.000000	0.000132	0.000118	0.002719	0.004986	0.028689	0.029956	0.000000	0.004228	0.000245
KA4	0.002160	0.000000	0.124701	0.000000	0.000130	0.000105	0.002682	0.004340	0.028299	0.029549	0.000000	0.004171	0.000213
KA5	0.002106	0.000000	0.121609	0.000000	0.000127	0.000090	0.002615	0.003734	0.027597	0.028816	0.000000	0.004067	0.000183
EFA	0.023688	0.077131	2.279656	0.000000	0.002465	0.000876	0.050802	0.037056	0.536085	0.559611	0.000620	0.079008	0.001819

(kg)	Na2SO4	NiSO4	PbSO4	Sb2O4	Sb2S3O12	CRISTOBALITE	QUARTZ	SiZrO4	SnO2	SnS2O8	SrSO4	TiO2	ZnSO4
KA1	0.000000	0.000101	0.005424	0.001532	0.000000	0.013461	0.000000	0.000000	0.000819	0.000000	0.000165	0.003097	0.042441
KA2	0.032563	0.000082	0.004961	0.001235	0.000000	0.010850	0.000000	0.000000	0.000660	0.000000	0.000133	0.002496	0.039081
KA3	0.031534	0.000068	0.004683	0.001029	0.000000	0.040716	0.000000	0.000000	0.000550	0.000000	0.000111	0.003301	0.036903
KA4	0.031106	0.000059	0.004620	0.000000	0.000896	0.035437	0.000000	0.000000	0.000571	0.000571	0.000096	0.002873	0.036401
KA5	0.030334	0.000051	0.004505	0.000000	0.000771	0.030493	0.000000	0.000000	0.000000	0.000492	0.000083	0.002472	0.035498
EFA	0.589255	0.000506	0.087515	0.000000	0.012754	0.302587	0.000000	0.000000	0.000000	0.008428	0.001421	0.024529	0.689573

Table B.18: Predicted stable phases for scenario C – High SO$_2$ from Box Flux Model simulations.

(kg)	BaSO4	DIOPSIDE	Ca2P2O7	Ca3P2O8	CaSO4	FG_GLASS	SPHENE	CdCl2	CdSO4	Cr2O3	CuCl2	CuO	CuSO4	Fe2NiO4	Fe2O3	K_AlSulfate	KCl	K2SO4	KSbS2O8	Mg-Langbeinite
KA1	0.002433	0.000683	0.000000	0.000856	0.097625	0.130999	0.009538	0.000000	0.000000	0.000228	0.000000	0.001613	0.000000	0.000000	0.003477	0.000000	0.011019	0.013223	0.000000	0.000000
KA2	0.002223	0.000000	0.000000	0.000690	0.092472	0.105589	0.000000	0.000000	0.000000	0.000183	0.000000	0.001441	0.000000	0.000000	0.002803	0.000000	0.010218	0.016668	0.000000	0.000306
KA3	0.002098	0.000000	0.000000	0.000575	0.087296	0.087952	0.000000	0.000000	0.000000	0.000153	0.000000	0.001263	0.000000	0.000000	0.002335	0.000000	0.008665	0.024839	0.000000	0.000288
KA4	0.002070	0.000000	0.000410	0.000000	0.086237	0.076550	0.000000	0.000049	0.000000	0.000132	0.000000	0.001124	0.000000	0.000000	0.002032	0.000000	0.007347	0.033955	0.000000	0.000285
KA5	0.002018	0.000000	0.000353	0.000000	0.084098	0.065869	0.000000	0.000055	0.000000	0.000114	0.000000	0.000974	0.000000	0.000000	0.001748	0.000000	0.005667	0.043144	0.000000	0.000278
EFA	0.022698	0.000000	0.005422	0.000000	1.660461	0.609698	0.000000	0.004145	0.000286	0.001090	0.015424	0.000000	0.001113	0.000000	0.019363	0.031598	0.200612	1.119285	0.001248	0.009437

(kg)	MnO2	NaCl	Na2SO4	NiSO4	NiTiO3	PbCl2	PbSO4	Sb2O4	Sb2O5	Sb2S3O12	CRISTOBALITE	QUARTZ	SiZn2O4	SiZrO4	SnO2	SnS2O8	SrSO4	TiO2	ZnCl2	ZnSO4
KA1	0.000465	0.019069	0.000000	0.000000	0.000129	0.000000	0.000000	0.001956	0.000000	0.000000	0.006352	0.000000	0.027919	0.000000	0.001045	0.000000	0.000363	0.000000	0.000000	0.000000
KA2	0.000375	0.019494	0.000000	0.000000	0.000104	0.000000	0.000000	0.001577	0.000000	0.000000	0.000000	0.007505	0.023531	0.000000	0.000843	0.000000	0.000293	0.003132	0.000000	0.000000
KA3	0.000312	0.020571	0.000000	0.000000	0.000087	0.000000	0.000000	0.001313	0.000000	0.000000	0.000000	0.005865	0.021034	0.000000	0.000702	0.000000	0.000244	0.002609	0.000000	0.000000
KA4	0.000272	0.022678	0.000000	0.000000	0.000076	0.001436	0.000000	0.001143	0.000000	0.000000	0.000000	0.004517	0.020484	0.000000	0.000611	0.000000	0.000212	0.002271	0.003868	0.000000
KA5	0.000234	0.024718	0.000000	0.000000	0.000065	0.001629	0.000000	0.000983	0.000000	0.000000	0.000000	0.008639	0.000000	0.000000	0.000526	0.000000	0.000183	0.001954	0.003868	0.000000
EFA	0.002321	1.444872	0.636235	0.000647	0.000000	0.095255	0.037588	0.000000	0.009679	0.000027	0.000000	0.105769	0.000000	0.000000	0.004917	0.000617	0.001813	0.020503	0.233571	0.101179

Table B.19: Predicted stable phases for scenario D – Low O$_2$ from Box Flux Model simulations

Appendix C

Supplementary Material
PCDD/-F congener distribution along the flue gas
cooling path and implications on formation
temperatures and mechanisms

	Variant 1 ordinary flue gas	Variant 2 reduced flue gas with high Cl content	Variant 3 flue gas + 0.2 wt.% PVC	Variant 4 flue gas + 0.33 wt.% PVC	Variant 5 flue gas + 0.46 wt.% PVC
	vol.%	vol.%	vol.%	vol.%	vol.%
Cl_2	0.00	0.74	0.00	0.00	0.00
CO	0.00	6.60	18.5	20.8	16.8
CO_2	6.78	0.17	2.07	0.00	0.00
H_2	9.79	9.76	17.7	22.7	24.2
H_2O	6.44	6.19	2.16	0.00	0.00
HCl	0.17	0.59	7.81	11.0	17.0
N_2	70.1	65.0	51.7	44.5	39.4
O_2	6.64	1.06	8E-18	2E-28	2E-28
SO_2	0.01	0.00	0.00	0.00	0.00
SO_3	0.00	0.01	0.00	0.00	0.00

	Enthalpy of formation $\Delta_f H$ this study	Difference in enthalpy of formation $\Delta_f H$ to other studies			
		Leon et al. 2002	Lee et al. 2003	Wang et al. 2004	Wang et al. 2005
Structure	J/mol	J/mol	J/mol	J/mol	J/mol
2,3,7,8-TCDD	-135642.64	4'961	-1'249	-9'033	
1,2,3,7,8-PeCDD	-137242.76	7'861	-1'427	-11'793	
1,2,3,4,7,8-HxCDD	-137188.84	10'815	-1'749	-14'829	
1,2,3,6,7,8-HxCDD	-138630.22	10'873	-1'559	-14'590	
1,2,3,7,8,9-HxCDD	-137514.40	11'089	-1'740	-14'754	
1,2,3,4,6,7,8-HpCDD	-137197.94	14'206	-1'926	-17'608	
OCDD	-135573.99	17'829	-2'227	-20'514	
2,3,7,8-TCDF	-30828.05				-3'048
1,2,3,7,8-PeCDF	-41215.59				-4'166
2,3,4,7,8-PeCDF	-35053.63				-3'994
1,2,3,4,7,8-HxCDF	-43745.12				-5'015
1,2,3,6,7,8-HxCDF	-44965.96				-5'006
1,2,3,7,8,9-HxCDF	-16051.77				-3'992
2,3,4,6,7,8-HxCDF	-38181.77				-4'782
1,2,3,4,6,7,8-HpCDF	-46458.43				-5'898
1,2,3,4,7,8,9-HpCDF	-17675.52				-4'866
OCDF	-20559.49				-5'629

Table C.1: Difference of the calculated $\Delta_f H$ value in relation to other studies

5

	Variant 1	Variant 2	Variant 3	Variant 4	Variant 5
	ordinary flue gas	reduced flue gas with high Cl content	flue gas + 0.2 wt.% PVC	flue gas + 0.33 wt.% PVC	flue gas + 0.46 wt.% PVC
	mol/kg	mol/kg	mol/kg	mol/kg	mol/kg
Al	0.00922	0.00922	0.00738	0.00615	0.00492
Ba	0.00016	0.00016	0.00013	0.00011	0.00009
Br	0.00029	0.00029	0.00024	0.00020	0.00016
C	2.56257	2.56257	8.45021	12.37531	16.30041
Ca	0.03795	0.03795	0.03036	0.02530	0.02024
Cd	0.00002	0.00002	0.00002	0.00002	0.00001
Cl	0.08324	0.83242	3.26667	5.38896	7.51125
Cr	0.00008	0.00008	0.00006	0.00005	0.00004
Cu	0.00051	0.00051	0.00041	0.00034	0.00027
F	0.00409	0.00409	0.00328	0.00273	0.00218
Fe	0.00300	0.00300	0.00240	0.00200	0.00160
H	12.32910	12.32910	19.46352	24.21979	28.97607
K	0.01477	0.01477	0.01181	0.00985	0.00788
Mg	0.00155	0.00155	0.00124	0.00103	0.00083
Mn	0.00014	0.00014	0.00011	0.00009	0.00007
N	52.95412	52.95412	42.36329	35.30274	28.24220
Na	0.03262	0.03262	0.02610	0.02175	0.01740
Ni	0.00002	0.00002	0.00002	0.00001	0.00001
O	12.85379	12.85379	10.28303	8.56919	6.85536
P	0.00128	0.00128	0.00102	0.00085	0.00068
Pb	0.00046	0.00046	0.00037	0.00031	0.00025
S	0.04160	0.04160	0.03328	0.02773	0.02218
Sb	0.00032	0.00032	0.00026	0.00021	0.00017
Si	0.03256	0.03256	0.02605	0.02171	0.01737
Sn	0.00018	0.00018	0.00014	0.00012	0.00009
Ti	0.00199	0.00199	0.00159	0.00132	0.00106
Zn	0.00709	0.00709	0.00567	0.00473	0.00378
Zr	0.00002	0.00002	0.00001	0.00001	0.00001

Table C.2: Input molar composition of the different variants, expressed as mol/kg

	2,3,7,8-TCDD	1,2,3,7,8-PeCDD	1,2,3,4,7,8-HxCDD	1,2,3,6,7,8-HxCDD	1,2,3,7,8,9-HxCDD	1,2,3,4,6,7,8-HpCDD	OCDD	2,3,7,8-TCDF	1,2,3,7,8-PeCDF	2,3,4,7,8-PeCDF	1,2,3,4,7,8-HxCDF	1,2,3,6,7,8-HxCDF	1,2,3,7,8,9-HxCDF	2,3,4,6,7,8-HxCDF	1,2,3,4,6,7,8-HpCDF	1,2,3,4,7,8,9-HpCDF	OCDF
2,3,7,8-TCDD	1.0	0.9	0.5	0.4	0.6	0.1	0.6	0.8	0.7	0.6	0.4	0.4	0.0	0.0	0.5	0.3	0.5
1,2,3,7,8-PeCDD	0.9	1.0	0.7	0.5	0.7	0.1	0.7	0.8	0.8	0.7	0.6	0.5	0.0	0.0	0.5	0.3	0.6
1,2,3,4,7,8-HxCDD	0.5	0.7	1.0	0.9	0.9	0.4	0.9	0.7	0.8	0.8	0.9	0.8	0.3	0.0	0.5	0.1	0.8
1,2,3,6,7,8-HxCDD	0.4	0.5	0.9	1.0	0.9	0.6	0.9	0.7	0.7	0.8	0.8	0.8	0.4	0.1	0.5	0.1	0.7
1,2,3,7,8,9-HxCDD	0.6	0.7	0.9	0.9	1.0	0.6	1.0	0.8	0.9	0.8	0.8	0.8	0.4	0.1	0.5	0.1	0.8
1,2,3,4,6,7,8-HpCDD	0.1	0.1	0.4	0.6	0.6	1.0	0.6	0.3	0.4	0.4	0.5	0.6	0.7	0.4	0.3	0.1	0.5
OCDD	0.6	0.7	0.9	0.9	1.0	0.6	1.0	0.8	0.9	0.8	0.8	0.8	0.4	0.1	0.6	0.1	0.8
2,3,7,8-TCDF	0.8	0.8	0.7	0.7	0.8	0.3	0.8	1.0	1.0	0.9	0.7	0.8	0.2	0.0	0.6	0.2	0.8
1,2,3,7,8-PeCDF	0.7	0.8	0.8	0.7	0.9	0.4	0.9	1.0	1.0	0.8	0.8	0.9	0.3	0.0	0.6	0.2	0.8
2,3,4,7,8-PeCDF	0.6	0.7	0.8	0.8	0.8	0.4	0.8	0.9	0.8	1.0	0.9	0.9	0.3	0.2	0.5	0.2	0.9
1,2,3,4,7,8-HxCDF	0.4	0.6	0.9	0.8	0.8	0.5	0.8	0.7	0.8	0.9	1.0	0.9	0.4	0.2	0.5	0.1	0.9
1,2,3,6,7,8-HxCDF	0.4	0.5	0.8	0.8	0.8	0.6	0.8	0.8	0.9	0.9	0.9	1.0	0.4	0.2	0.5	0.1	0.9
1,2,3,7,8,9-HxCDF	0.0	0.0	0.3	0.4	0.4	0.7	0.4	0.2	0.3	0.3	0.4	0.4	1.0	0.4	0.1	0.0	0.4
2,3,4,6,7,8-HxCDF	0.0	0.0	0.0	0.1	0.1	0.4	0.1	0.0	0.0	0.2	0.2	0.2	0.4	1.0	0.1	0.1	0.2
1,2,3,4,6,7,8-HpCDF	0.5	0.5	0.5	0.5	0.5	0.3	0.6	0.6	0.6	0.5	0.5	0.5	0.1	0.1	1.0	0.0	0.3
1,2,3,4,7,8,9-HpCDF	0.3	0.3	0.1	0.1	0.1	0.1	0.1	0.2	0.2	0.2	0.1	0.1	0.0	0.1	0.0	1.0	0.2
OCDF	0.5	0.6	0.8	0.7	0.8	0.5	0.8	0.8	0.8	0.9	0.9	0.9	0.4	0.2	0.3	0.2	1.0
TOC400	0.0	0.0	0.0	0.0	0.0	0.1	0.0	0.0	0.0	0.0	0.0	0.0	0.2	0.0	0.0	0.0	0.0
ROC	0.3	0.3	0.2	0.1	0.1	0.0	0.1	0.2	0.2	0.2	0.2	0.2	0.0	0.0	0.1	0.2	0.2
ROC/TOC	0.1	0.1	0.2	0.2	0.2	0.1	0.2	0.2	0.2	0.4	0.4	0.3	0.1	0.3	0.1	0.1	0.4
TIC900	0.4	0.3	0.2	0.2	0.3	0.1	0.3	0.3	0.2	0.4	0.3	0.2	0.1	0.1	0.1	0.2	0.4
TOC	0.0	0.0	0.0	0.1	0.0	0.1	0.0	0.0	0.0	0.1	0.1	0.1	0.1	0.3	0.0	0.0	0.1
SSA	0.5	0.5	0.2	0.1	0.1	0.0	0.1	0.4	0.3	0.3	0.1	0.1	0.1	0.0	0.3	0.2	0.1
Cl	0.0	0.0	0.0	0.0	0.0	0.0	0.0	0.0	0.0	0.0	0.0	0.0	0.0	0.1	0.0	0.0	0.0
Cu	0.1	0.1	0.3	0.3	0.3	0.3	0.3	0.2	0.2	0.3	0.4	0.3	0.2	0.2	0.0	0.1	0.4

Table C.3: Correlation coefficient (R2) matrix for the different congeners and carbon fractionation, SSA, Cl and Cu concentration.

Table C.4: PCDD/-F congener concentrations (ng/kg TS) in the analyzed ash fractions

Plant	Position	2,3,7,8-TCDD	1,2,3,7,8-PeCDD	1,2,3,4,7,8-HxCDD	1,2,3,6,7,8-HxCDD	1,2,3,7,8,9-HxCDD	1,2,3,4,6,7,8-HpCDD	OCDD	2,3,7,8-TCDF	1,2,3,7,8-PeCDF	2,3,4,7,8-PeCDF	1,2,3,4,7,8-HxCDF	1,2,3,6,7,8-HxCDF	1,2,3,7,8,9-HxCDF	2,3,4,6,7,8-HxCDF	1,2,3,4,6,7,8-HpCDF	1,2,3,4,7,8,9-HpCDF	OCDF
								ng/kg TS										
A	BOA5	17	37	23	28	37	190	410	56	90	53	86	100	6	42	240	28	97
A	ESPA	25	60	26	39	47	230	320	110	160	97	130	150	12	69	290	35	74
C	BOA2	7	16	10	10	12	71	210	50	58	39	52	58	5	27	150	18	54
C	BOA4	24	40	8	9	15	31	46	86	97	57	59	63	3	18	85	5	12
C	BOA5	43	88	30	38	41	130	160	110	150	91	120	120	7	47	260	16	48
C	ESPA	32	78	37	53	56	550	2'200	110	160	110	150	170	20	180	760	120	700
D	BOA1	16	87	84	120	130	1'200	3'100	84	200	160	270	320	22	200	1'300	290	1'500
D	BOA2	53	180	83	73	94	370	660	430	740	370	700	690	45	240	1'600	200	620
D	BOA3	170	980	1'300	1'800	1'800	28'000	200'000	280	770	600	1'900	2'200	190	2'800	23'000	2'400	28'000
D	BOA4	38	160	130	180	220	2'200	11'000	71	200	110	300	370	17	210	2'300	200	2'100
D	BOA5	31	190	190	270	290	4'900	42'000	110	260	150	420	470	47	480	5'000	430	6'200
D	ESPA	480	2'600	5'400	11'000	8'500	280'000	2'100'000	930	2'400	3'300	9'400	11'000	1'800	22'000	220'000	31'000	330'000
E	BOA1	17	37	24	37	39	160	230	94	130	90	120	110	13	61	280	33	88
E	BOA2	11	28	17	27	33	140	170	43	61	55	71	79	8	41	170	21	65
E	BOA3	34	84	79	110	120	690	1'200	83	130	110	180	150	23	110	600	68	290
E	BOA4	27	85	70	78	130	910	2'100	60	110	71	140	130	14	92	600	58	280
E	BOA5	49	200	270	570	420	6'900	25'000	160	350	560	830	820	110	920	4'300	450	2'000
E	ESPA	42	140	160	300	250	5'600	31'000	160	280	220	420	440	63	620	3'300	560	4'100
F	BOA2	<1	<1	1	2	3	16	22	4	7	2	4	6	<1	3	17	<3	<10
F	BOA3	<1	<2	3	6	4	49	100	5	7	5	11	11	<2	13	68	14	88
F	BOA4	<1	<2	2	3	4	52	850	<1	<1	1	3	4	<1	3	130	<3	94
F	BOA5	3	5	11	12	12	440	5'400	4	12	11	25	32	4	41	400	28	400
F	ESPA	3	12	21	44	32	860	6'400	22	55	46	160	140	17	120	1'200	180	1'800

209

	Scenario 1	Scenario 2	Scenario 3	Scenario 4	Scenario 5
	ordinary flue gas	reduced flue gas with high Cl content	flue gas + 0.2 wt.% PVC	flue gas + 0.33 wt.% PVC	flue gas + 0.46 wt.% PVC
			mg/kg		
2378-TCDD	0	0	0	1.56E-13	3.22E-13
12378-PeCDD	0	0	0	8.87E-14	1.24E-13
123478-HxCDD	0	0	0	2.58E-14	2.45E-14
123678-HxCDD	0	0	0	2.86E-14	2.71E-14
123789-HxCDD	0	0	0	2.59E-14	2.46E-14
1234678-HpCDD	0	0	0	1.14E-14	7.30E-15
OCDD	0	0	0	2.69E-15	1.18E-15
2378-TCDF	0	0	0	17.33	39.90
23478-PeCDF	0	0	0	17.53	27.37
12378-PeCDF	0	0	0	10.89	17.01
123478-HxCDF	0	0	0	9.28	9.83
123678-HxCDF	0	0	0	10.72	11.35
123789-HxCDF	0	0	0	1.30	1.38
234678-HxCDF	0	0	0	4.19	4.44
1234678-HpCDF	0	0	0	4.93	3.55
1234789-HpCDF	0	0	0	0.87	0.62
OCDF	0	0	0	3.30E-03	1.61E-03

Table C.5: Calculated equilibrium concentrations for the different PCDD/-F congeners at 800°C.

Appendix D

Erklärung